UHF ANTENNA DESIGN FOR AFIT RANDOM NOISE RADAR

THESIS

Matthew T. Ludwig, Second Lieutenant, USAF

AFIT/GE/ENG/12-28

DEPARTMENT OF THE AIR FORCE
AIR UNIVERSITY

AIR FORCE INSTITUTE OF TECHNOLOGY

Wright-Patterson Air Force Base, Ohio

AFIT/GE/ENG/12-28

UHF ANTENNA DESIGN FOR AFIT RANDOM NOISE RADAR

THESIS

Presented to the Faculty

Department of Electrical and Computer Engineering

Graduate School of Engineering and Management

Air Force Institute of Technology

Air University

Air Education and Training Command

In Partial Fulfillment of the Requirements for the

Degree of Master of Science in Electrical Engineering

Matthew T. Ludwig, BS

Second Lieutenant, USAF

March 2012

AFIT/GE/ENG/12-28

UHF ANTENNA DESIGN FOR AFIT RANDOM NOISE RADAR

Matthew T. Ludwig, BS

Second Lieutenant, USAF

Approved:

_____	_____
Peter Collins, Ph.D., USAF (Chairman)	Date
_____	_____
Michael Temple, Ph.D., USAF (Member)	Date
_____	_____
Geoffrey Akers, Lt Col, USAF (Member)	Date

Abstract

The capability to see one's enemy without letting them know they're being watched presents a major advantage of battle space awareness. The great military strategist Sun Tzu said "the expert leaves no trace … thus, he is master of his enemy's fate." As purely random noise is completely indistinguishable from the background noise of the radio frequency (RF) spectrum, a radar system based on such a waveform would fulfill this extreme low probability of intercept (LPI) posture. While the AFIT system remains a research platform, its characteristics has application in a wide variety radar system sizes and scenarios. The primary advantages of wideband random noise radar (RNR) are the LPI properties of the waveform and the high density of information in the radar snapshots. The increased information capacity is derived from the ultrawideband (UWB) used for the radar waveform. The size of the bandwidth directly impacts the range resolution of the radar measurements.

Many system elements can degrade the bandwidth performance of the RNR, including filtering, sampling and antenna bandwidth. The design of a small UHF antenna for an UWB RNR system was undertaken in order to improve system bandwidth and reduce overall system size. The Vivaldi dipole antenna class showed the greatest potential for high performance in this specific application. After extensive computer simulation, three designs were built using two printed circuit board antenna construction methods. The antipodal chopped Vivaldi dipole antenna, built with a milling machine,

achieved a wider bandwidth and more uniform spectral performance characteristics. Though current results show improvement over the current log-periodic antenna (LPA) used on the system, greater performance could possibly be achieved with higher fidelity construction methods.

The chopped Vivaldi dipole antenna can be classified as a highly efficient, electrically small antenna optimized for UWB applications, due to the combination of small size as well as a nearly uniform frequency response and low dispersion in the UHF bandwidth. Though designed for AFIT's Noise Network (NoNET) system, a UHF UWB RNR, the antenna could be applied to a variety of UHF systems looking to optimize the trade-off between size and power budgets.

Acknowledgments

First and foremost I would like to thank my advisor Dr. Collins for his guidance in both research and design on this project, as well as throughout AFIT courses. Thank you to Mr. McNeely for his extensive help in building the antennas and making accurate measurements. Thank you as well to AFRL for the sponsorship of my thesis as well as the use of the UHF ridged horn antennas and accompanying data. Finally, I would like to thank my friends and family for their support.

Matthew T. Ludwig

Table of Contents

Page

List of Figures

Page

List of Tables

Page

UHF ANTENNA DESIGN FOR AFIT RANDOM NOISE RADAR

I. Introduction

1.1 Chapter Overview

This chapter begins the discussion of the AFIT NoNET noise radar system, including current difficulties and future objectives. The current AFIT NoNET system is based on RNR technology and has become a highly accurate for target range estimation. Recently, the capability of simultaneous range and velocity computation has been developed, which allows the operator to estimate the target's relative position and speed. But the computation requirements for this operation are far too large to make it feasible for real-time use. In addition, the individual multistatic nodes are too large for ease of mobility and remain dependent on a local power source. The new objectives for the NoNET research efforts are to make the system smaller, faster, and more versatile.

Electromagnetic remote sensing systems can be divided into two major groups: active and passive. Active sensors transmit radiation and analyze the reflected returns from the environment, whereas passive sensors continuously receive radiation from their surroundings in order to monitor changes in the environment. Passive sensors possess an inherent advantage in terms of LPI capabilities. Because passive sensors do not transmit any radiation, there is no electromagnetic signature to be intercepted by an opponent. Infrared sensors are typically passive in nature. Radar, on the other hand, by design is as an active sensor. There are many other inherent advantages of the radar waveform, such as greater transmission through the atmosphere or resonances for wavelengths of similar size to targets of interest. The difficulty then is to develop a radar system that approaches the capability to “see without being seen” that is inherent with a passive sensor, while still maintaining all of the inherent advantages of radar operation.

1.2 Problem Description

To allow for future development and application of the system, the current bandwidth concerns must be addressed. The NoNET system bandwidth is both much smaller in reality than intended and possesses an inconsistent power spectral density. These issues arise primarily from the operating antenna for the current system setup. Ideally, an UWB system should have a uniform spectral response with high gain and minimal dispersion. The current AFIT RNR system uses a LPA designed to operate from 400MHz to 1000 MHz, as shown in Figure 1. Because it is built with a printed circuit board configuration, this antenna is easy to manufacture and fairly durable. The system performs well, but could be greatly improved by a good redesign of the antenna subsystem. This antenna design has been cause for concern since its initial implementation. The generic LPA design is convenient in that its operating bandwidth is scalable by merely lengthening or shortening the antenna support and adding or subtracting active elements along the length. This functionality permits a simple design for many different applications of varied band requirements, from narrowband to UWB. Also, the LPA is a proven design that has been used in a wide array of applications for many years.

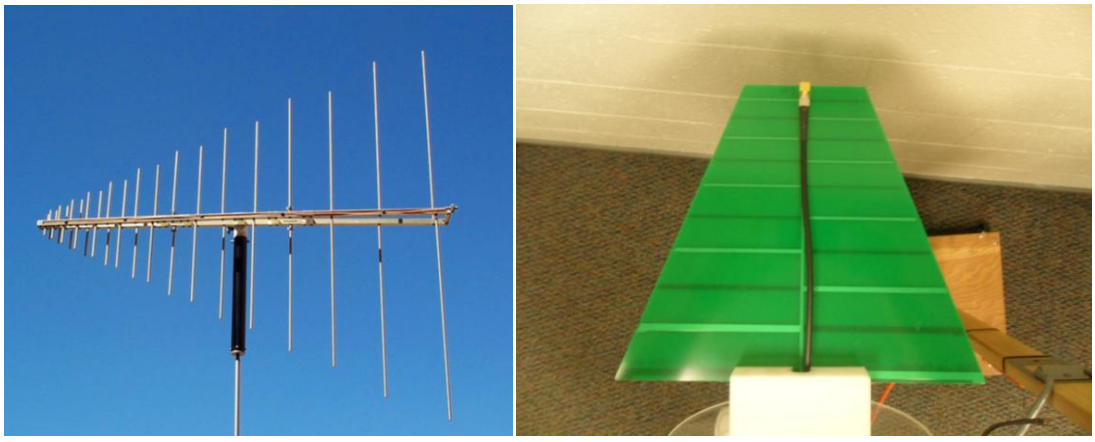

Figure 1 – Generic log-periodic antenna design [1] (left) and current AFIT NoNET log-periodic, printed circuit board antenna (right)

LPAs are commonly used for television antennas because they can be easily scaled to receive channels from both VHF (30 MHz – 300 MHz) and UHF (300 MHz – 1000 MHz) range. But the problem with any LPA is that, despite its performance across a wide band of frequencies, the full antenna bandwidth will be composed of many smaller adjacent bands, each dictated by the size and separation of the individual active element pairs along the length of the full LPA, as displayed in Figure 2. Such performance is satisfactory for television station applications, where each station is a different sub-band and steady spectral response across the entire bandwidth would only increase noise received between the channel bandwidths. But when noise is the information signal, the LPA attenuates the radar return unevenly across the operational bandwidth. The lack of a uniform spectral response of the radar return can lead to inaccuracies in the radar computation.

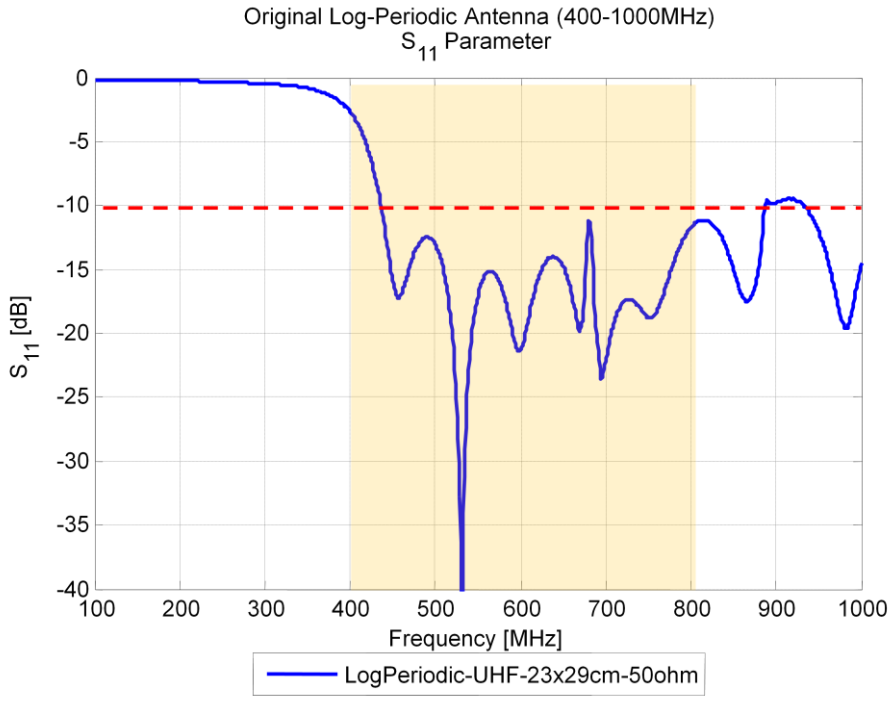

Figure 2 – CST Simulated S_{11} parameter of the LPA currently used on NoNET

Figure 3 displays the sub-band effect of the LPA on the AFIT NoNET radar return. Within the 3 dB bandwidth, there is an oscillation in the frequency response, which induces slight frequency dependence on the noise transmission. Also, the overall bandwidth of the system has been decreased from the desired range. The discontinuities of the NoNET response have become a problem in correlation processing because the sampled transmit signal has not passed through the transmit antenna.

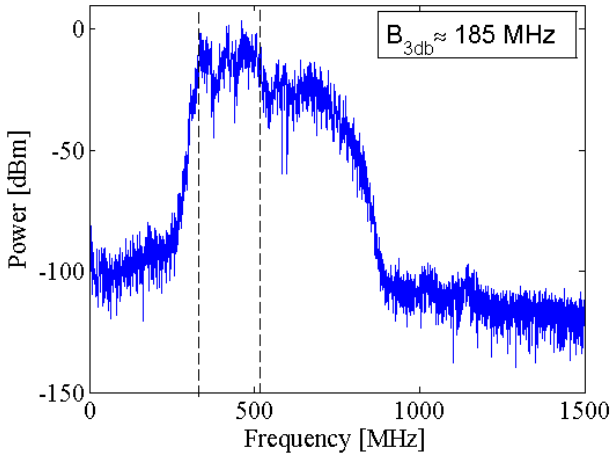

Figure 3 – Current AFIT NoNET antenna spectrum response [2]

Noise could be modeled theoretically as white Gaussian noise with an amplitude distribution mean of zero and a constant power spectral density. But when the return is spectrally dependent, the data are more difficult to characterize. Transmitting and receiving with a near frequency independent antenna across the full bandwidth reduces spectral coloring, which will allow for increased fidelity of the radar return.

Currently, the AFIT NoNET system claims an operational bandwidth from 400 MHz to 800 MHz, which corresponds to a fractional bandwidth of about 70%. As seen in Figure 3, the realized bandwidth is approximately 185 MHz, which is a significant reduction from the UWB design. First, sampling of the analog to digital converter (ADC) determines the high end of the

operational bandwidth. The A/D converter in the AFIT NoNET can sample at 3 G-samples/sec for one channel or 1.5 Gs/s in two channel mode [2]. The reason that the ADC is operated in two channel mode is that it must sample both the delayed transmitted signal and the received signal simultaneously in order to allow for correlation processing of the radar returns. To avoid aliasing with the ADC, the higher cutoff frequency of the AFIT NoNET system must be 750 MHz. Antenna performance reduces the actual 3 dB bandwidth to about one-half of the bandwidth of the band-pass filter. Fractional bandwidth assesses the breadth of a wideband system relative to its center frequency. A radio transmission system is considered to be UWB if it has a fractional bandwidth over 20%, according to the Federal Communications Commission, or 25% by the US Defense Advanced Research Project Agency [2]. If we were able to design an antenna subsystem that had a smooth spectral response and low reflectivity across the bandwidth from 400MHz to 750MHz, the fractional bandwidth would increase to about 61%, shown in (**1**), well over either requirement for an UWB system.

$$B_f = 2\left(\frac{f_h - f_l}{f_h + f_l}\right) \times 100\% = 2\left(\frac{750\ MHz - 400\ MHz}{750\ MHz + 400\ MHz_l}\right) \times 100\% = 60.9\% \qquad (1)$$

Antenna designs must begin from more than just a researched understanding of antenna parameters and basic resonant shapes by drawing from previously demonstrated successful designs. Luckily, there has been a surge of UWB antenna design for a variety of applications in the past few years, though not necessarily in the UHF bandwidth. Since the Federal Communications Commission (FCC) opened the frequency band from 3.1 GHz – 10.6 GHz for unlicensed UWB applications in 2002 [3], there have been many new developments in UWB antenna literature, ranging from new antenna designs to inspired recreations of old proven designs. The plethora of new and innovative designs being tested is definitely useful for research,

but a few challenges come from the differences between the noise radar application and UWB communications across this band. Most importantly, these antennas are developed for much higher frequencies than those employed in the AFIT NoNET. Though noise radars can be designed to work at these frequency bands, the AFIT NoNET operates at the UHF band in order to sample the return waveform directly as opposed to using a local oscillator, thus improving post-processing response time and reducing hardware size, which is one of the major drawbacks of noise radar. The primary factor in scaling one of these antennas down to the UHF is the size consideration. The largest dimension for the antennas based on a dipole construct is generally approximately $0.5\,\lambda_l$, where λ_l is the longest wavelength, or lowest frequency, in the desired bandwidth. For a lower bound of 300 MHz, this dimension would be about 0.5 meters. To reduce the size of the antenna further, electrically small antenna principles should be considered.

Desired improvements in the AFIT NoNET system include a uniform response across the desired bandwidth, small size, and low required transmit power. Low transmit power will drive gain and efficiency needs, which must be balanced against minimization of antenna size which reduces directivity and radiation efficiency. A near-uniform response can be attained by gradually tapering the antenna geometry as opposed to the discrete elements of the LPA, but significant simulation and research will be needed to attain such results.

1.3 Research Goals

Before manufacturing and testing antennas, a foundation of simulated results must direct the candidate designs. First, a collection of published antennas from the 3.1 – 10.6 GHz bandwidth were simulated to verify the simulation software. Then by adapting these antennas to the UHF bandwidth of the AFIT RNR, simulations were used to build an understanding of the behavior of

the antenna surface currents and the relationship between the spectral response and the antenna radiating geometry.

There are a wide variety of antennas to choose from when looking for an UWB design. A printed circuit board (PCB) antenna construction was chosen to satisfy desires for an inexpensive, small, durable antenna. Many of the UWB antenna designs of this construction are spatially-expanded relatives of monopole, dipole, and slot antennas. One particularly interesting style amongst these is the Vivaldi antenna. There are two primary variations of the Vivaldi antenna, Vivaldi slot antennas and Vivaldi dipole antennas, both shown in Figure 4.

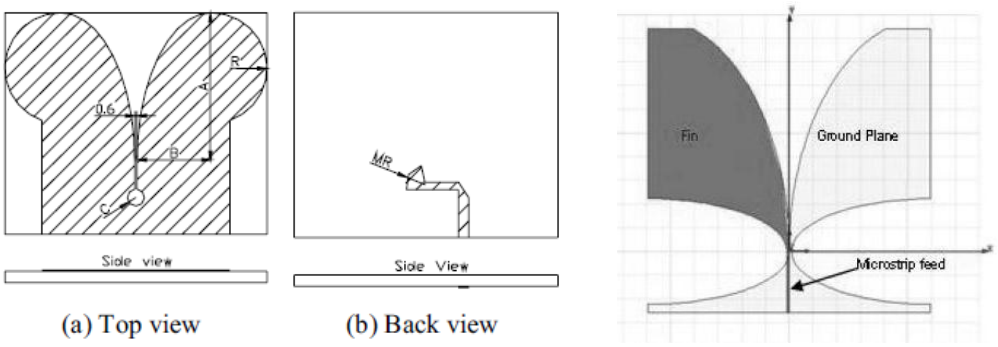

Figure 4 – Comparison of Vivaldi slot antenna (left) and Vivaldi dipole antenna (right) [4]

Vivaldi Slot antennas are essentially a planar ridged horn with an elliptical taper with the signal strip fed orthogonally across the base of the slot. Vivaldi Dipole antennas use a differential feed between the positive and negative signals to elliptically taper into an UWB dipole radiating structure. The other variable option of note is the antipodal versus balanced construction. The antipodal construction uses only two PCB layers to build the antenna, whereas the balanced construction repeats the negative sheet radiator on the opposite side of the positive sheet radiator to achieve a more stable polarization transmission. The balanced construction will be harder to construct, but would offer more stable co-polarization transmission, as well as minimized cross-polarization returns.

After drawing on the research of UWB antenna performance and how it relates to noise radar specifically, the priorities for the AFIT NoNET system were to first design an antenna which is reduced in size from that of the commercial LPA while maintaining inexpensive construction costs. The antenna should also have a high, uniform gain across the UWB frequency range. The gain profile should be as near to uniform as possible to avoid inadvertent "coloring" of the radar measurements that is not associated with the target behavior. The typical industry standard for antenna transmission is a S_{11} below -10 dB for the operational bandwidth. The antenna should then attempt to maintain a low reflection coefficient for a high percentage of the UWB frequency range. A performance metric important for the radar application is the stability of the phase center. The antenna should have minimal phase center drift, especially in the broadside direction, and minimize dispersion effects on the radar waveform. Keeping with the commercial LPA performance, the desire is to maintain a consistent endfire pattern through the UWB frequency range. Though not as important as reducing the overall size of the antenna, the endfire behavior of the antenna should be retained where applicable. Finally, the antenna should attain a high level of total efficiency through low reflections and radiating the majority of the energy received into the antenna. Total efficiency is comprised of both reflection efficiency and radiation efficiency, where reflection efficiency is defined as the percentage of energy transmitted to the antenna from the transmission line and radiation efficiency is defined as the percentage of energy radiated to the farfield, through EM fields, from the energy internal to the antenna structure.

Several different antenna designs were built and simulated in CST Microwave Studio to determine the best option according to the design objectives as well as to optimize the specifications of that design to attain the lowest reflection coefficient and highest broadside gain. After choosing the best designs, the antennas were constructed using either a milling machine or

chemical etching. The resulting PCB antennas were then tested in the AFIT Advanced Compact Electromagnetic Range (ACER) using an AFIT RNR node to drive the antennas for S_{21} measurements and a network analyzer for S_{11} measurements.

1.4 Chapter Conclusion

The efforts of this thesis will continue the development of the AFIT NoNET system. Historically, noise radar applications have had very limited entrance into operational use. Noise radar has many inherent benefits that could prove significantly useful in operational system as long as several of the difficulties can be overcome. The development of a compact, real-time noise radar system could have many more applications than a purely academic context. Therein lays the central drive of the AFIT Noise Radar team.

II. Theory

2.1 Chapter Overview

In an attempt to develop the narrative of noise radar and UWB antenna design, this chapter outlines the historical development and the current state of technology related to the operation of noise radar systems. The most time consuming operation of a noise radar system is the digital cross-correlation computation. This bitwise comparison of transmit and receive signals must be accomplished many times in order to determine the range and velocity of the target. The random noise radar system is a specific application of the digital correlation receiver. The random noise radar has many inherent benefits that validate the struggle with the required computational complexity. The major defining characteristic of a noise radar system is the operational bandwidth used. As the bandwidth is widened, the range resolution becomes finer. In addition, the choice of the center frequency affects the interaction of the radar waveform with the target and surrounding environment. In general, lower frequencies, such as VHF and UHF, are better for through-the-wall radar applications than high bands because of their larger skin depth. For example, radar looking to operate in a rural setting can be operated in the foliage penetration band, 50-600 MHz [5]. But, higher frequency bands have smaller wavelengths which do not require the large aperture sizes of the lower frequencies. Thus, higher frequency band radars can reduce system size by using smaller antennas.

2.2 RNR Background and AFIT NoNET

The concept of random noise as a radar waveform has a surprisingly long history. As early as 1904, scientists used noise-like pulses in the first radar-like experiments [6]. But the actual concept of using coherent noise radar reception did not occur until the late 1950s. The first published papers in which noise signals were used in range-measuring were written by Richard

Bourret in 1957, who used a continuous wave (CW) noise waveform and an analog correlation receiver [7], and by B. M. Horton in 1959, who also used a CW noise signal, but for frequency modulation as opposed to the actual waveform itself [8]. Further studies concerning the use of noise waveforms for radar continued through the 1960s and 70s. Afterwards, the 1980s and 1990s witnessed little development in the field. In recent years, the growth of the digital signal processing field and maturity of computer processor technology has reinvigorated the research and development of noise radar [9].

The use of random noise as a radar waveform has many inherent advantages over classical radar waveforms. First, a pure random noise waveform is not correlated with any other signal but itself. As a result, the noise radar can achieve excellent LPI properties as the signal is indistinguishable from normal background noise to the common observer [10]. Also, the radar has excellent resistance to jamming and interference from other sources [10]. The resistance to jamming is due to the "thumbtack" radar ambiguity function, or near pinpoint accuracy as well as the UWB of the radar signal. Jammers are generally configured to transmit as much power as they can with a narrowband transmitter in a specific direction according to the target they wish to jam. An UWB RNR system can reduce the damage to operation caused by such a jammer as its radar return is drawn from a wide range of frequencies as opposed to a single narrowband transmission. The rest of the UWB will be unjammed.

This operating condition also means that the radar does not cause major interference with any other RF subsystems in the overall system on which the noise radar is mounted [10]. Since the noise radar will only raise the noise floor of the nearby systems relative to its operational power, the RF cost of adding the radar to the overall system is reduced. As more and more devices

utilize transmitters and receivers, radar that does not interfere with neighboring RF systems occupies a niche in the world of radar systems.

The noise waveform's properties allow for excellent range accuracy, which is controlled by the integration time of the correlation receiver and the bandwidth transmitted by the radar. According to Dr. Krzysztof Kulpa, "there is no theoretical limitation in the non-ambiguous working range of noise radar" [10]. The longer the sampled waveform input into the correlation receiver the longer the range gate, but the tradeoff is the computation time necessary for the longer correlation.

Several noise radar systems have been developed in recent years, each aimed at different objectives either in research or in application. Several years ago, after using a 1-4 GHz noise radar for low cost RCS measurements, Ohio State University (OSU) worked on a noise radar system designed for the VHF/UHF bandwidth, specifically 50-600 MHz, that was used to identify moving vehicle targets based on their detailed wideband signatures [5,11,12]. Also, Dr. Konstantin Lukin of National Academy of Sciences of Ukraine, who has done significant work in the signal processing side of noise radar, has recently been working on a noise radar with either stepped-frequency or a stepped-delay construction [13,14,15]. One of the more fully developed noise radar systems in research today is at Pennsylvania State University (PSU), led by Dr. Ram Narayanan. The PSU system uses a heterodyne receiver to inject coherence into the noise waveform returns and performs the correlation processing at baseband [16,17,18,19].

The AFIT NoNET system, shown in Figure 5 and detailed in Table 1, varies from the OSU and PSU noise radar systems primarily in that it uses direct ADC sampling of the transmit and receive channels without the use of a local oscillator. This requires a high speed ADC as well as significant computation resources, since a very large amount of data is recorded quickly at the

frequencies of the UWB used. The ADC runs in dual-channel mode, sampling at 1.5 GHz on each channel, in order to sample, post-filtering, both the original noise source after half-power splitter and the signal from the receive antenna after filtering and amplification.

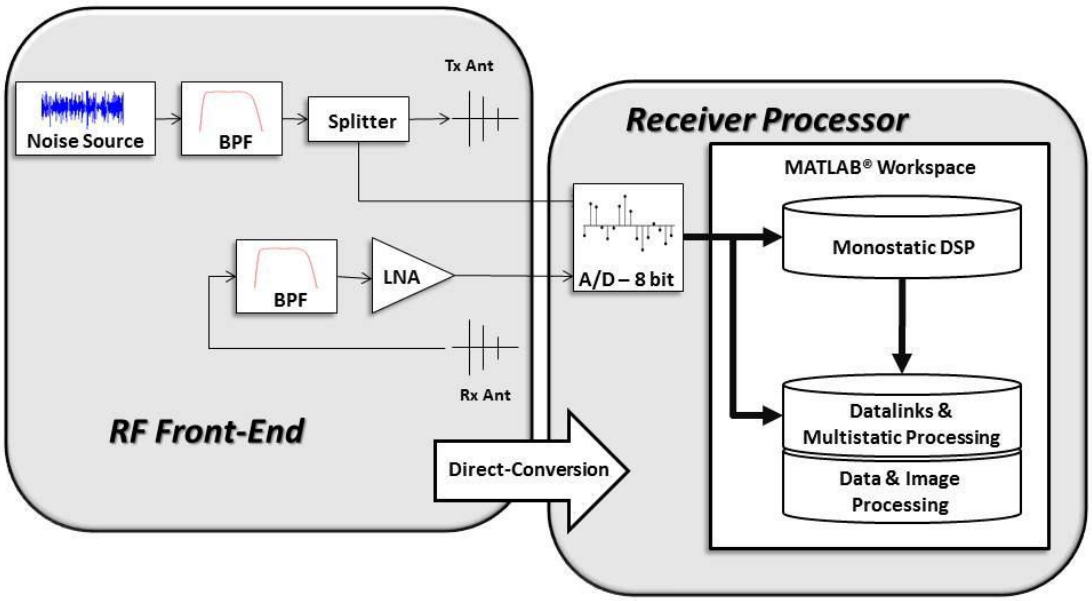

(a)

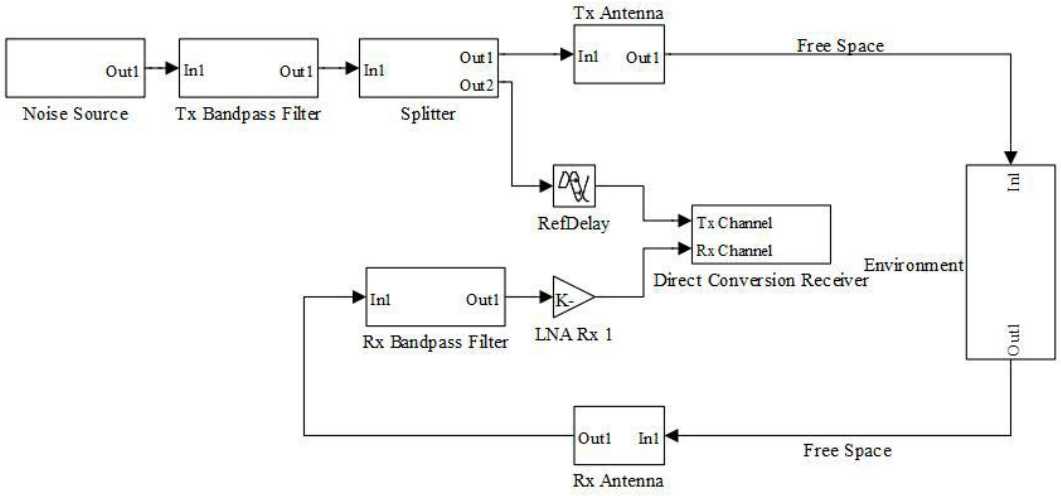

(b)

Figure 5 – Model of AFIT NoNET in (a) hardware and (b) software simulation [20]

Table 1 – AFIT NoNET specifications

Frequency Bandwidth	400 - 750 MHz
Noise Power	-80 dBm/Hz
LNA Gain	45 dB
LNA Noise Figure	0.8 dB
ADC Bits	8 bits/channel
ADC Rate	1.5 GS/s
ADC Channels	2 channels

The NoNET transmits the random noise signal at -83 dBm/Hz after the power splitter. The use of purely random noise is greatly advantageous from a LPI/LPD perspective, but it creates a few additional challenges from both radar and antenna design perspective. Because noise has no relative phase progression, a digital correlation receiver with a sampled version of the transmit waveform is necessary. The UWB waveform limits the options available for antenna system design. The use of a phased array antenna system to achieve a narrow, electrically-scanned, main beam is not available for noise waveform systems, as the array is based on the use of phase shifters between the multiple element feeds. UWB array theories can rely on the use of variable time delay differences between the elements for beam forming and steering.

The AFIT system was initially built and tested for human target detection in a through-the-wall configuration. Operating in a near-monostatic network orientation, the NoNET system was able to distinguish the human target from non-human in 8 of 10 test cases [21]. After the initial construction of the system, the AFIT NoNET underwent successive generations of software design to improve the digital correlation operation and signal processing. The development of a multistatic network allowed for high-fidelity imaging of a target scene through distributed computing of an UWB random noise radar [2]. An end-to-end Simulink model of the NoNET system has been built to evaluate the theoretical performance of the system without the need to alter or rebuild it in hardware, shown in Figure 5. The model demonstrated coarse accuracy of

range derived target velocity measurements, as an alternative to Doppler extraction. Evaluating the use of a pseudo-noise template as opposed to the purely random noise currently used from the thermal noise generator, the model showed the capability to reduce overall system signal processing time by 75% while still maintaining similar LPI properties [20]. As the AFIT noise radar system is primarily a time domain system, the target velocity problem needed to be confronted. Using the compression of the noise waveform due to the Doppler effect to generate matched filters, target velocity estimation could be accomplished simultaneously with range estimation using the time domain digital cross-correlation operation [22]. The greatest difficulty in the operation though became the lack of real-time processing of the target return. By simulating the operation of a binary ADC and parallel processing of multiple FFT operations, the computation time for the simultaneous range and velocity processing was able to be reduced from almost 40 min to less than 5 min [23].

2.3 Basic Resonant Antenna Theory, Measurement, and Calibration

Antenna functionality, just like any electromagnetic interaction, is grounded in Maxwell's equations, which relate electrostatic charges and alternating currents to electric and magnetic fields. Ampere's Law (2) declares that an electric current causes a circulating magnetic field. Faraday's Law (3) then states that a changing magnetic flux induces an orthogonally circulating electric field. Thus using the combination of these two of Maxwell's equations, one can evolve the surface currents on the structure of an antenna into the transverse electromagnetic (TEM) waves transmitted in the farfield region surrounding it.

$$\nabla \times H = J_i + J_c + \frac{\partial D}{\partial t} = J_{ic} + J_d \tag{2}$$

$$\nabla \times E = -\frac{\partial B}{\partial t} \tag{3}$$

where:

H = magnetic field intensity [A/m]

E = electric field intensity [V/m]

B = magnetic flux density [Wb/m^2]

D = electric fluxdensity [C/m^2]

J_i = impressed (source) electric current density [A/m^2]

J_c = conduction electric current density [A/m^2]

$J_{ic} = J_i + J_c$ = sum of impressed and conduction electric current densities [A/m^2]

$J_d = \frac{\partial D}{\partial t}$ = displacement electric current density [A/m^2]

The foundation of basic antenna theory is the Hertzian dipole, which is an infinitesimally small dipole antenna containing an ideal alternating current density of constant magnitude, J_{ic}. When the waves generated by the current density within the Hertzian dipole propagate to the farfield, the electric and magnetic fields for a TEM wave with field intensity vectors noted by (4) and (5).

$$\boldsymbol{E}(\boldsymbol{r}, f) = \hat{\theta}\, \eta\, \gamma \sin(\theta)\, J(f) \frac{e^{2\pi f\, \gamma\, r}}{4\pi r} \tag{4}$$

$$\boldsymbol{H}(\boldsymbol{r}, f) = \hat{\phi}\, \gamma \sin(\theta)\, J(f) \frac{e^{2\pi f\, \gamma\, r}}{4\pi r} \tag{5}$$

where:

r = range from the antenna [m]

η = equivalent impedance of free-space [Ω]

γ = propagation constant of wave medium

When expanding from a simplified Hertzian dipole to a full dipole antenna, the electric current density which generates the radiating fields becomes the spatially integrated sum of an infinite number of Hertzian dipole currents within the physical size limits of the full antenna. The accuracy of the final field intensity vectors from any antenna is primarily based on the accuracy with which the electric current density can be estimated.

To measure and compare the effectiveness of antennas, the primary group of metrics chosen is the scattering parameters, which compare the transmitted and received signal magnitudes between a pair of antennas. During an antenna measurement, the port 1 antenna is commonly used for the antenna under test (AUT) and port 2 for the source horn antenna, as shown in Figure 6. The input and output signals from the two port setup are related to the scattering parameter matrix, $\boldsymbol{S}$, according to (6).

Figure 6 – Two port antenna test setup

$$\begin{bmatrix} b_1 \\ b_2 \end{bmatrix} = \begin{bmatrix} S_{11} & S_{12} \\ S_{21} & S_{22} \end{bmatrix} \begin{bmatrix} a_1 \\ a_2 \end{bmatrix} \quad , \quad \boldsymbol{S} = \begin{bmatrix} S_{11} & S_{12} \\ S_{21} & S_{22} \end{bmatrix} \tag{6}$$

The direct antenna measurements can be calibrated through the use of a standard gain horn (SGH) antenna with a known gain spectral response. Calibrated antenna measurements use units of dBi, which is the power ratio relative to an ideal isotropic radiator, as opposed to simply dB. The SGH must have corresponding exact gain data in dBi before attempting calibration, which is accomplished through rigorous measurement. When all scattering parameter measurements are obtained for the AUT and SGH, the calibrated gain for the AUT can be obtained through (7).

$$G_{AUT} = \frac{S_{21-AUT}}{S_{21-SGH}} G_{SGH} \tag{7}$$

Calibrated gain plots offer that advantage of reducing many of the interference effects of the source horn and the test environment. Though the anechoic chamber tries very hard to reduce multiple bounces of radiation and external interference, significant contributions remain from the surroundings and isolating the AUT proves quite difficult.

2.4 UWB Antenna Theory

When using a wideband system, information is extracted from all frequency contents of the signal. For example, a radar target may have resonant structures that cause high energy returns at specific frequencies, forming a frequency dependent target fingerprint. This is one of the great

advantages of a wideband radar system. Because the band of frequencies used in the radar system has been expanded beyond the 10 percent of the carrier frequency common for narrowband radars, the information capacity of the signal is greatly increased [24].

Many inherent advantages have been identified for using UWB radar pulses over the classical narrowband configuration [24]:

- Improved target range measurement accuracy
- Increased target identification potential
- Reduced negative influence from passive interference sources (rain, aerosols, etc.)
- Improved immunity to narrowband RF interference effects
- Decreased radar "dead zone"
- LPI/LPD due to capability to use waveforms that are difficult to detect

When choosing a waveform for this wider bandwidth, it is important to emphasize distribution of the in-band power spectral density. Purely random noise then becomes a very convenient wideband signal because it theoretically has a uniform power spectral density. As a result, it is assumed that the noise waveform will return only the spectral response of the target. Since the AFIT RNR uses nearly pure random noise, it is important to avoid inadvertently "coloring" the radar signal through the frequency responses of the radar subsystems, such as the bandpass filters, low-noise amplifiers, or the antennas. The ideal UWB antenna would have a high, constant gain across the band of interest, high efficiency, consistent radiation pattern across all frequencies, and negligible phase dispersion in the broadside direction. This is the engineering challenge of building an UWB antenna.

Though UWB antennas have become increasingly popular in recent years due to a resurgence of wideband applications, the history of UWB antennas reaches back much farther than the past

10 years. The current drive in UWB technology development is primarily communications based in the 3.1 – 10.6 GHz bandwidth [25]. The FCC announced that the 3.1 – 10.6 GHz bandwidth could be used for unlicensed UWB transmission in an attempt to allow the research and production of UWB technology to develop naturally [3]. During the past decade, there has been an explosion of UWB antenna designs for the bandwidth designated by the FCC. These antennas can be used in the UHF bandwidth by scaling the size of the radiating geometry by the ratio of the bandwidth difference, while maintaining the impedance of the feed. Many of these designs are derived from narrowband designs, but some are accidental rediscoveries of historical wideband antennas from the early days of RF communications [26]. Therefore, it is important to establish an understanding of the historical development of RF antennas before attempting to conjure up new designs for modern applications.

In the early days of telecommunications, there was less emphasis on bandwidth and more concern on radiated power. But, as the telecommunications industry grew and necessary technologies matured, the drive toward narrowband communications over limited channel bandwidths pushed the design of antennas to radiate over smaller bands. Despite the drive toward narrowband communications, UWB antenna designs grew in parallel to their narrowband counterparts throughout the growth of the RF industry, though not always on purpose.

Many early designs of antennas were inherently wideband, albeit primarily by accident. Though the aim was actually tuned, narrowband transmissions through the use of resonant circuitry, the initial antenna designs were actually radiating UWB damped impulse signals [26]. For instance, when Oliver Lodge, in his 1898 patent, detailed his narrowband radio system, he also described some of the first UWB antenna designs [26].

> As charged surfaces or capacity areas, spheres or square plates or any other metal surfaces may be employed; but I prefer, for the purpose of combining low resistance with great electrostatic capacity, cones or triangles or other such diverging surfaces with the vertices adjoining and their larger areas spreading out into space; or a single insulated surface may be in conjunction with the earth, the earth or conductors embedded in the earth constituting the other oppositely-charged surface.
>
> - Oliver Lodge

Lodge quickly identified most of the basic antenna structures, which are still widely used to this day, including spherical dipoles, square plate dipoles, biconical dipoles, bow-tie dipoles, and their respective monopole versions using Earth's surface as a ground plane [26]. Antenna design and construction caught up with these early innovations over the next 50 years as the RF communications world grew and manufacturing methods allowed for greater precision. Many designs drew from these basic shapes, expanding them through surface revolutions, and coupled them to the transmission lines through coaxial extension transitions.

A major development came during the 1950s, as Victor Rumsey described how an antenna's impedance and pattern properties will be frequency independent if the structure is described in terms of angles. This led to the development of log-periodic antennas (LPA), spiral antennas, conical spiral antennas, and eventually helical antennas [26].

In recent years, the field of UWB technology has experienced resurgence due, in large part, to the greater information capacity in wideband signals over that of a narrowband signal. Such capacity allows for finer range resolution in radar applications or higher quality speech coding in

voice communications. In order to allow commercial markets to develop this technology and take advantage of its benefits, several countries have allowed unlicensed transmissions up to certain power restrictions below 900 MHz and from 3.1 – 10.6 GHz [27]. Also, existing spread spectrum techniques can possibly be improved by expanding them from wideband to UWB use.

Current broadband antennas can be gathered into six categories:

- Frequency independent antennas
- Electric antennas (e.g. dipoles and monopoles)
- Magnetic antennas (e.g. loops)
- Electrically small antennas
- Horn antennas
- Reflector antennas

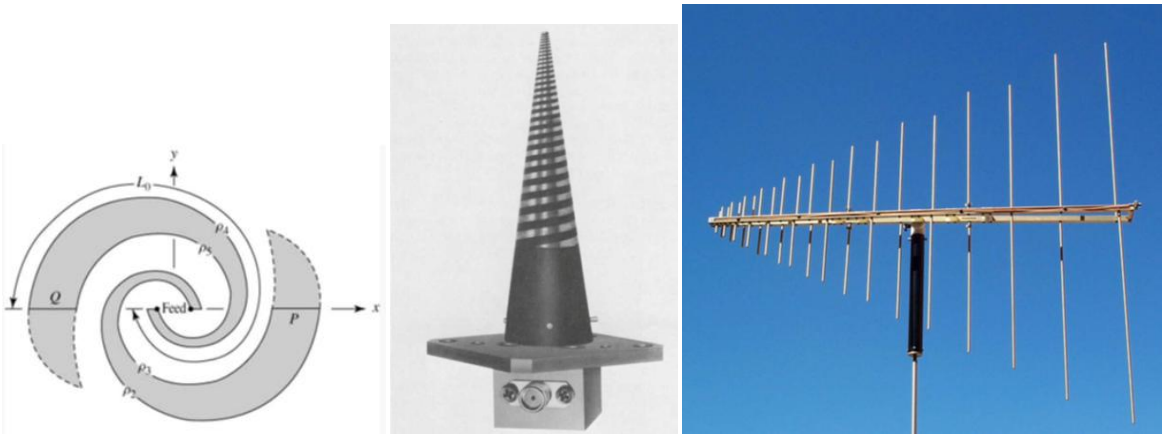

Figure 7 – Frequency independent antennas [1]

The general characteristics of frequency-independent antennas are that their impedance and radiation patterns are ideally uniform across the full bandwidth of operation. The antenna structure is defined by angular scaling from the smallest component to the largest component. The largest component defines the high end of the bandwidth and the small component sets the

lower end of the bandwidth. The basic types of frequency-independent antennas are spirals, conical spirals, log-periodics, and fractals. The far left antenna in Figure 7 shows is a planar spiral with both its spacing and strip width defined angularly. The middle antenna is a conical spiral antenna and on the right is a typical roof-mounted LPA used for TV reception. The difficulty of the spatially distributed structure of the antenna is that it causes dispersion [26]. Dispersion is a problem for radar applications, because the range measurement depends on the stability of the phase center and dispersion causes that point to move with frequency and sometimes be less stable even at a single frequency.

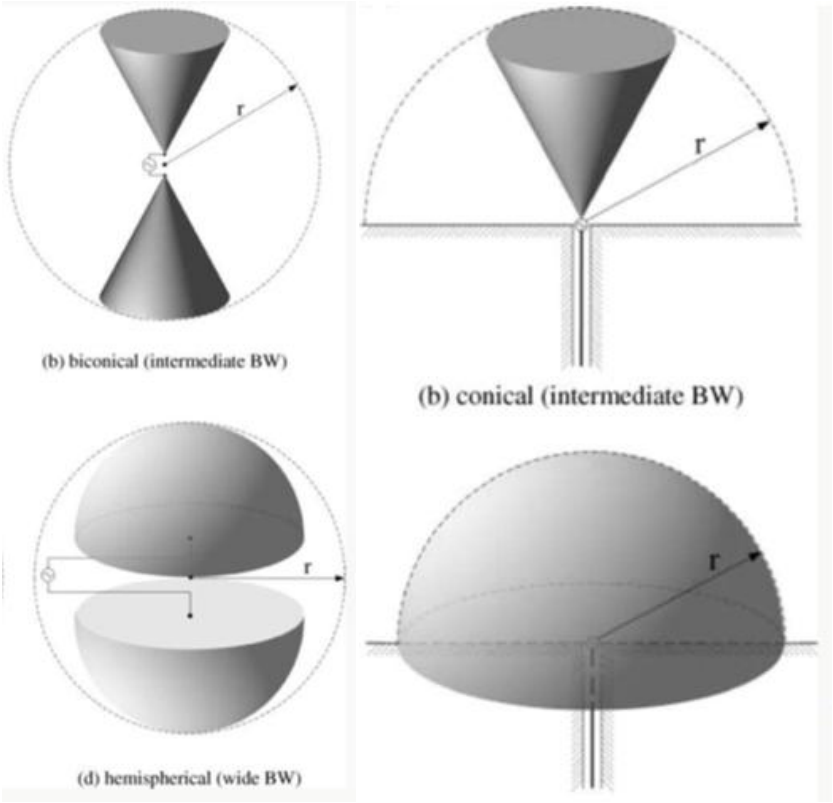

Figure 8 – Electrical antennas [1]

Electrical antennas are derived from the ideal Hertzian dipole antenna configuration and can be thought of as voltage driven [26]. They have omnidirectional radiation patterns in azimuth, or

similar to a donut sitting level in the H-plane. In terms of UWB antennas, this class includes dipoles and monopoles of various geometric shapes, such as cones, cylinders, diamonds, and spheroids, as well as their planar varieties: triangles, rectangles, and ellipses and circles. Figure 8 shows UWB dipoles and monopoles constructed with tapered cones and half spheres. The spherical dipole is theoretically the most efficient electrically small antenna.

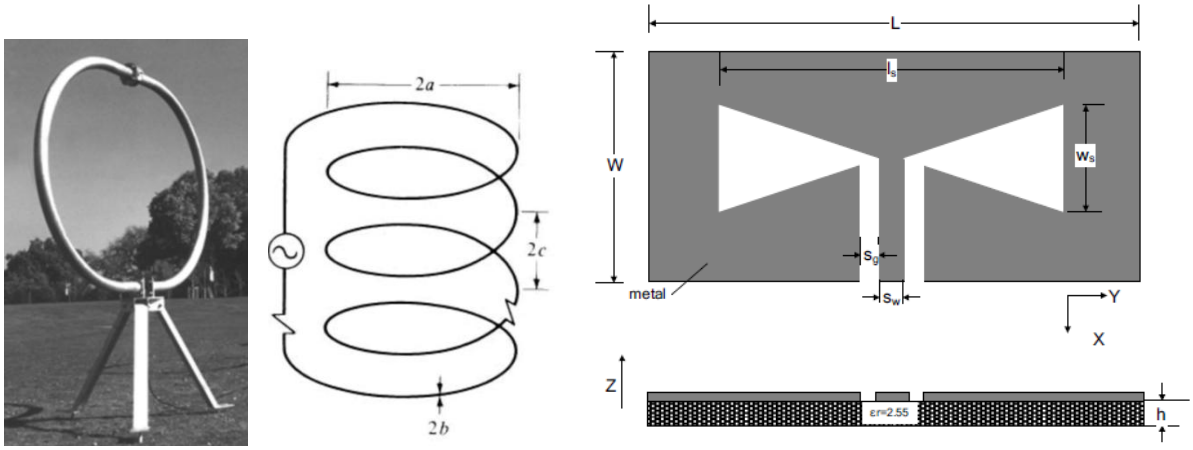

Figure 9 – Antennas: loops (left and center) [1] and slot (right) [28]

On the other hand, magnetic antennas are derived from a Hertzian magnetic dipole configuration, which is an infinitesimally small current-carrying loop, and can be thought or a current driven [26]. These antennas will have omnidirectional radiation patterns in the E-plane as different from their electrical counterparts. UWB designs in this family of antennas include large current radiators (LCRs), monoloops, loops, and slot antennas [26]. From left to right, Figure 9 displays a large monoloop antenna, a theoretical multi-loop design, and a bow-tie slot antenna fed with a coplanar waveguide. Similar to the slot antenna in Figure 9, most slot antennas use resonant geometries derived from electrical antennas but invert the construction. The resonant structures become empty slots and the substrate regions of the electrical antenna are replaced by conductive sheets.

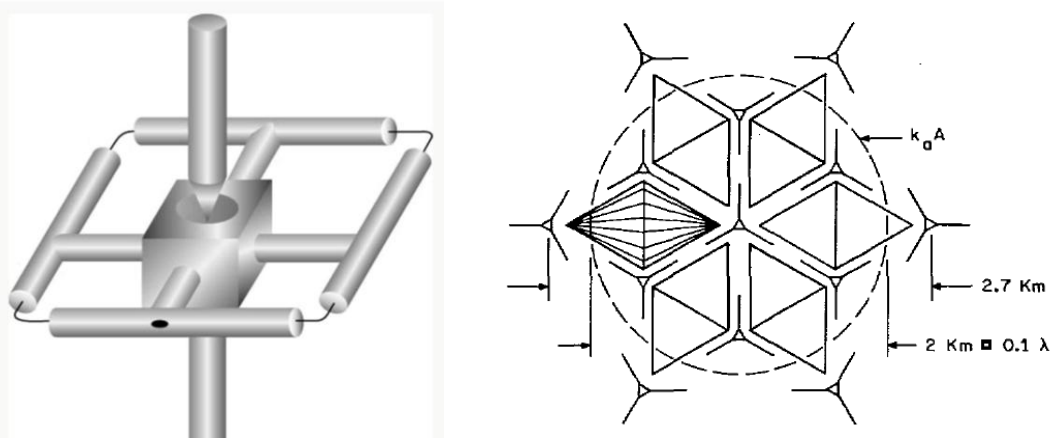

Figure 10 – Electrically small antennas: electric-magnetic dipole (left) [1] and VLF antenna based on Goubau antenna design (right) [29]

An antenna is typically considered electrically small if its greatest dimension measures less than a quarter wavelength of the designated operating frequency [29]. The left antenna of Figure 10 is the theoretical electrically small antenna, built from a combination of a dipole and loop antenna, which ideally radiates isotropically. The antenna on the right is an electrically small antenna that is over 2km in diameter. The US Navy uses it for submarine communications at 15.5 kHz, $\lambda = 19.3$ km. For an UWB antenna to be electrically small, the largest dimension of the antenna structure must be smaller than 25 percent of the largest wavelength of the UWB, or lower end of the frequency band, detailed in (**8**).

$$L_{max} < \frac{\lambda_{low}}{4} = \frac{c}{4\, f_{low}} \tag{8}$$

Because electrically small antennas do not maintain resonance, the antenna radiation pattern will be nearly isotropic in shape. Though electrically small antennas are extremely useful in terms of space use, the problem becomes that as the sphere containing the antenna becomes

smaller, fewer modes are transmitted from the antenna and the bandwidth of the antenna decreases [30].

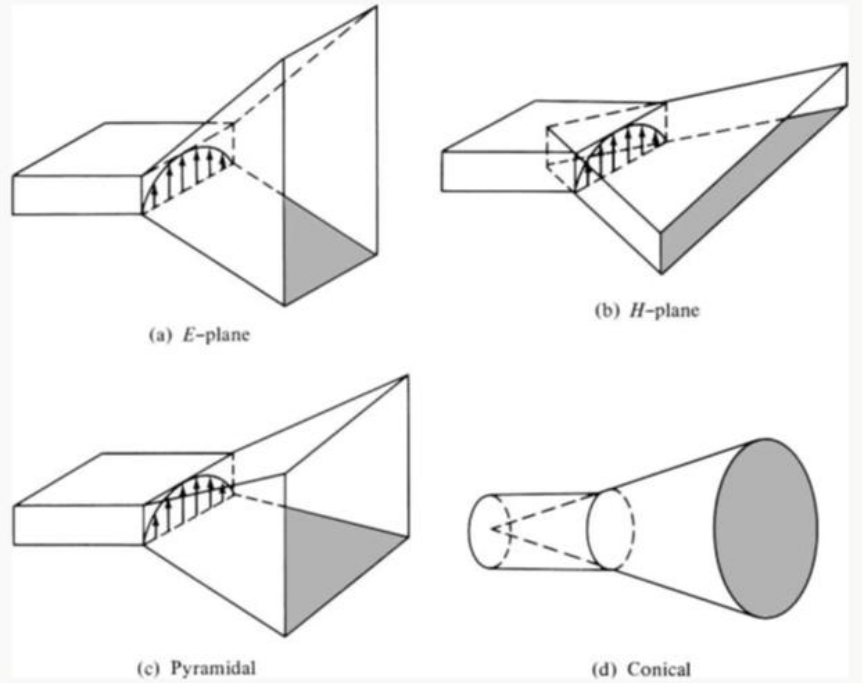

Figure 11 – Various types of horn antennas [1]

Horn antennas, first introduced by Jagadis Chandra Bose in the 1890s, are basically a transmission line that terminates in a tapered (flared) opening [26]. There are many types of horn antennas, as shown in Figure 11, but nearly all horn antennas are designed to radiate mostly in a particular direction. The basic types of horns are sectoral horns (E-plane or H-plane), pyramidal horns, and conical horns [1]. Sectoral and pyramidal horns are typically coupled to rectangular waveguide transmission lines, while conical horns are coupled to circular waveguides. Horn antennas are very efficient radiators with high gain, but remain on the order of a half wavelength, meaning that it is difficult to scale the size of a horn antenna.

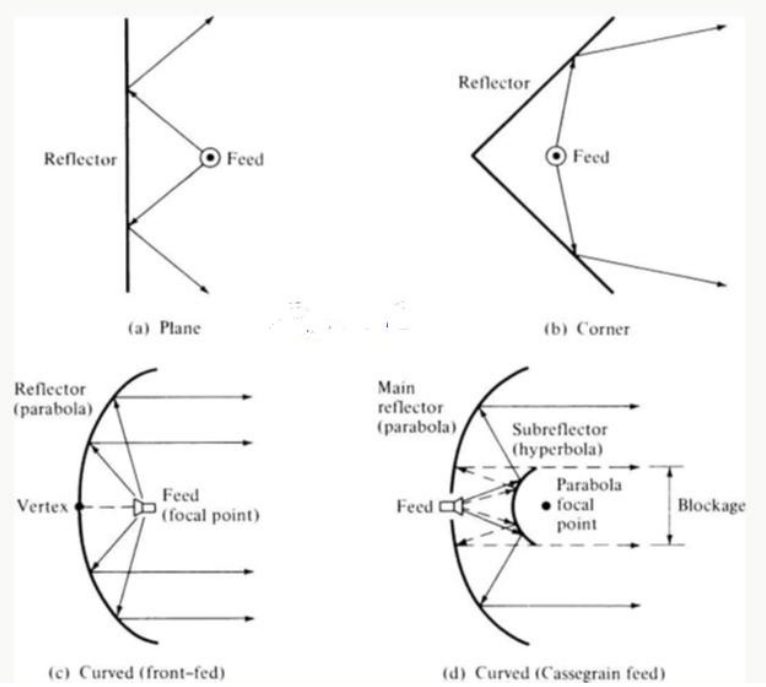

Figure 12 – Various types of antenna reflectors [1]

Reflector antennas rely on a physical optics reflection of the electromagnetic waves from the feed to the area of illumination. There are three primary types of reflectors: plane, corner, and curved (including the highly popular parabaloid) [1]. Figure 12 shows these reflector types and how multiple reflectors can be used to increase focusing or reduce interference. All reflectors function to concentrate the transmissions from the feed antenna into a particular direction. Plane and corner reflectors are simpler and cheaper to construct, but cannot concentrate fields as well as a parabolic reflector. Complex systems of reflectors can be assembled to achieve greater directivity and minimize diffraction and side lobes. Horns are typically large, directive, and high gain antennas [26].

The innovations over the past decade of UWB antenna design have drawn from these basic antenna families and meshed a wide variety of characteristics to achieve an innovative design for

a specific application [27]. Most of these recent antennas can still be classified according to these divisions despite exhibiting traits of multiple.

2.5 UWB Antenna Design

Designing antennas is considered a difficult art form by some, but history and experience can offer some simple rules of thumb for an initial approach [26]. Dr. Hans Schantz, after many years spent in the study and design of antennas, has discussed a few quantitative rules for matching an antenna to an application [26].

> "First, one needs some idea of the bandwidth and frequency response of the antenna under analysis. This allows one to select a tentative time domain response that should be characteristic of what the design can generate. Second is the observation that RF currents tend to concentrate on the edges of planar structures. Third is understanding that radiation occurs roughly orthogonally to the direction in which the current is changing. Fourth is the idea that the current distribution on an antenna is roughly sinusoidal with a periodicity dependent on the center frequency. The final topic is tracking the differences in path length from sources distributed on an extended object."

The final point mentioned by Schantz is particularly important for an antenna applied to UWB radar. One of the primary advantages of UWB radar is the increased range resolution of the target returns. The accuracy of these radar measurements rely on the stability of the phase center of the antenna [5]. The phase center moves with respect to the center of the antenna the primary concentration of the surface currents changes with frequency. In order to maintain a

consistent phase center location, an antenna designer should attempt to keep the surface current locations stable across the bandwidth.

The stability of the phase center relates back to Schantz's second point as the placement of the sharp edges of the planar antenna structure will determine the locations of the primary surface current concentrations. By strategically placing the edges of the antenna structure, the designer can shape the radiation pattern and attempt to stabilize the phase center. When attempting so, the designer must also keep in mind that surface currents concentrate on the structural edges more as frequency increases [26].

An approach to antenna design must be founded on an understanding of the measures by which they are compared and evaluated. Traditionally, an antenna would be considered broadband if the impedance and radiation pattern did not change significantly over an octave of frequencies [31]. In recent years the DARPA and the FCC, have defined UWB systems in greater detail due to the increased potential that the technology possesses. According to the US Defense Advanced Research Project Agency (DARPA), an UWB system must have a fractional bandwidth of 25% or more [2]. The FCC defines an UWB RF system to have either a bandwidth greater than 500 MHz or a fractional bandwidth of greater than 20% [3]. Since an octave bandwidth corresponds to an upper frequency that is double that of the lower frequency, $f_H = 2\,f_L$, (**9**) shows that the traditional definition of broadband easily classifies as UWB according to the new standards.

$$BW_{f-octave} = 2\frac{2\,f_L - f_L}{2\,f_L + f_L} = \frac{2}{3} = 66.67\% \tag{9}$$

In any radar application, the antenna selection can have a great impact on the results of the system, as shown by the radar range equation (RRE) in (**10**) [32]. This fact becomes especially

true for UWB applications, because the effects of the antennas influence the radar return over the full bandwidth and may or may not be constant with respect to frequency.

$$SNR(f) = \frac{P_t(f)\, G_t(f)\, G_r(f)\, c^2\, \sigma(f)}{(4\pi)^3\, k\, T_0\, B\, F(f) L_S(f)\, f^2\, R^4} \tag{10}$$

Classic narrowband approaches to antenna parameters treat most of these characteristics as constants, which is acceptable because most experience little or no change over the small frequency bands involved. But, when using UWB radar, these assumptions fall apart. Frequency-independent antennas might be considered a great alternative because they have nearly constant gain and radiation pattern across the frequency band, but they emit dispersed signals as the phase center moves with frequency [26]. Dispersion was never a concern in the narrowband antenna application, but the engineering problem becomes much more complicated when UWB antennas are considered.

While narrowband antenna metrics can be assumed to be constant and measured only at the operating frequency, broadband antenna metrics must be measured across a range of frequencies. Traditional antenna measurements begin with scattering parameters, or S-parameters, shown in (**11**) and (**13**). S-parameters are defined according to the input port, Port 1 as connected to the AUT, and the output port, Port 2 as connected to the source horn antenna, of a network analyzer used to measure the complex voltage of the signals into and out of each port. The S-parameters are defined for a particular polarization orientation of the antenna link, either co-polarization or cross-polarization. An additional way to consider the reflection coefficient is the voltage standing wave ratio (VSWR), shown in (**12**), which is ratio of the steady state input and reflected voltage signals in the transmission line feeding the antenna.

$$\mathbf{S_{11}}(f) = \boldsymbol{\Gamma}(f) = \frac{\mathbf{V_{Rx\,1}}(f)}{\mathbf{V_{Tx\,1}}(f)} \tag{11}$$

$$\mathrm{VSWR}(f) = \frac{1 + |\boldsymbol{\Gamma}(f)|}{1 - |\boldsymbol{\Gamma}(f)|} \tag{12}$$

$$\mathbf{S_{21}}(f) = \frac{\mathbf{V_{Rx\,2}}(f)}{\mathbf{V_{Tx\,1}}(f)} \tag{13}$$

where:

$\boldsymbol{\Gamma}(f)$ = AUT reflection coefficient [unitless]

$\mathrm{VSWR}(f)$ = voltage standing wave ratio [unitless]

$\mathbf{V_{Rx\,1}}(f)$ = received voltage signal at AUT [V]

$\mathbf{V_{Tx\,1}}(f)$ = transmitted voltage signal at AUT [V]

$\mathbf{V_{Rx\,2}}(f)$ = received voltage signal at the standard gain horn (SGH) [V]

S-parameters are excellent for relating antenna test results, but it is also important to understand how the antenna is physically operating. An antenna generates electric and magnetic fields by moving currents through its structure. Maxwell's equations relate a changing electric current to the generation of magnetic and electric fields, which transmit into the far-field region as electromagnetic waves. As shown in (14), the average power carried by these waves is derived from the relationship between the electric and magnetic field strengths [1].

$$P_{rad}(f) = \oiint_{\mathbf{s}} \mathbf{W_{rad}}(f) \cdot d\mathbf{s} = \frac{1}{2} \oiint_{\mathbf{s}} \mathrm{Re}\{\mathbf{E}(f) \times \mathbf{H}^*(f)\} \cdot d\mathbf{s} \tag{14}$$

where

$P_{rad}(f)$ = average radiated power to surface **s** [W]

$\mathbf{W_{rad}}(f)$ = complex radiation density [W/m^2]

$\mathbf{E}(f)$ = time-varying complex electric field [V/m]

$\mathbf{H}(f)$ = time-varying complex magnetic field [A/m]

When discussing antennas, it is useful to relate this radiated power to the radiation intensity, which is the power radiated from an antenna per solid angle [30]. Radiation intensity is related to power density by the square of the radius as in (15).

$$U(f) = r^2 W_{rad}(f) \tag{15}$$

where

$U(f)$ = radiation intensity [W/unit solid angle]

$W_{rad}(f)$ = radiation density [W/m^2]

The average radiated power can then be related to the radiation intensity through the integration over a specific solid angle [1], as shown in (16).

$$P_{rad}(f) = \oiint_{\Omega} U(f, \theta, \phi)\, d\Omega = \int_{\phi_0}^{\phi_1} \int_{\theta_0}^{\theta_1} U(f, \theta, \phi) \sin(\theta)\, d\theta\, d\phi \tag{16}$$

Using this relationship for radiated power and radiation intensity, an expression for antenna directivity can be derived. Directivity, (17), of a non-isotropic antenna is defined as the ratio of

its radiation intensity in a particular direction to that of an isotropic source with the same radiated power [1]. Since an isotropic source emits radiation in all directions equally, its radiation intensity evaluated to $U\_0 = P\_rad \ / \ 4\pi$.

$$D(f,\theta,\phi) = \frac{U(f,\theta,\phi)}{U_0(f)} = \frac{4\pi\, U(f,\theta,\phi)}{P_{rad}(f)} \tag{17}$$

Antenna directivity is useful in understanding how well an antenna shapes its radiation pattern into a main beam. This measurement of directivity can be expanded by incorporating the antenna's efficiency to derive the antenna gain, (18), measurement, which is defined as the ratio of the radiation intensity in a particular direction to the radiation intensity that would be obtained if all power sent to the antenna were emitted isotropically [1].

$$G(f,\theta,\phi) = \frac{4\pi\, U(f,\theta,\phi)}{P_{in}(f)} = \eta_{rad}(f)\ \frac{4\pi\, U(f,\theta,\phi)}{P_{rad}(f)} \tag{18}$$

where

$\eta_{rad}(f)$ = antenna radiation efficiency [dimensionless]

Antenna gain includes radiation losses, but assumes a perfectly matched transmission line, or $|\boldsymbol{\Gamma}(f)| = 0$. If one is to understand the absolute gain of the system, (19), the reflection efficiency, $\eta_r(f) = (1 - |\boldsymbol{\Gamma}(f)|^{\mathbf{2}})$, must be included [1].

$$G_{abs}(f,\theta,\phi) = \eta_r(f)\ \eta_{rad}(f)\ \frac{4\pi\, U(f,\theta,\phi)}{P_{rad}(f)} = \eta_{total}(f) D(f,\theta,\phi) \tag{19}$$

Similar to narrowband antennas, higher gain and a lower reflection coefficient are generally better, but in UWB applications the goal of higher performance at one frequency must be

balanced with stability across all operating frequencies. While attempting to maximize gain and efficiency and minimize the voltage standing wave ratio (VSWR) of the antenna, the designer must aim to keep these properties frequency independent, or constant across the band of interest [33]. Also, the antenna should maintain a constant phase center with respect to frequency in order to avoid dispersion [34]. Dispersion is primary cause of phase distortions in the received signals [33].

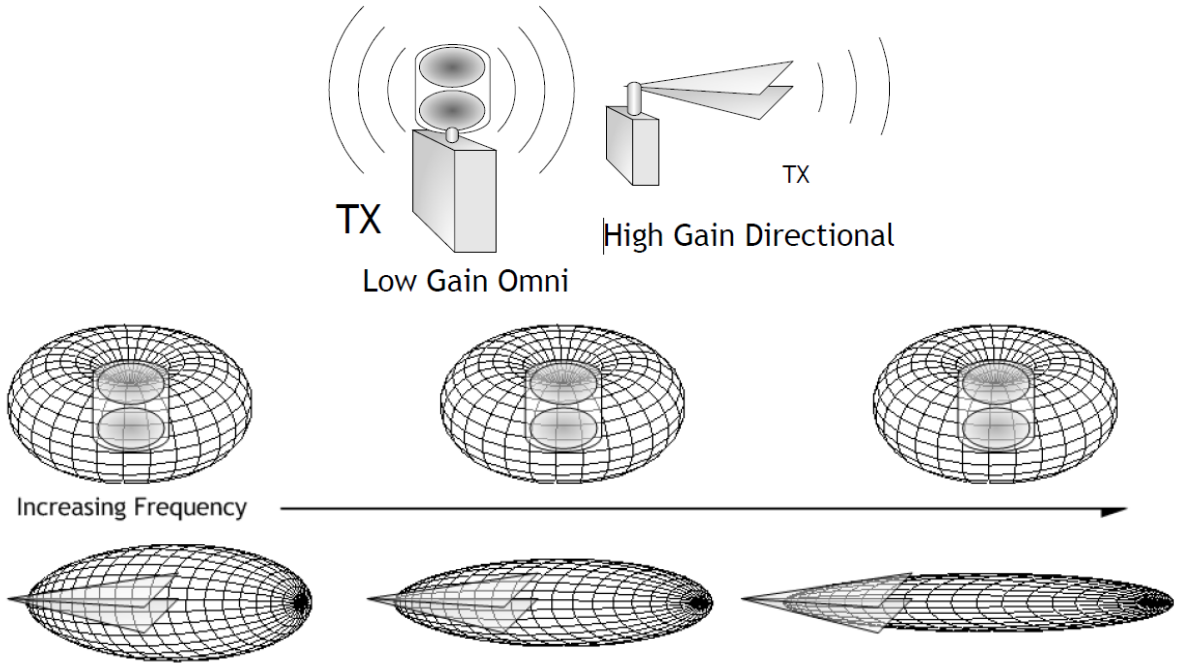

Figure 13 – Comparison of constant gain antenna to constant aperture antenna [35]

The fundamental engineering problem emerges as non-dispersive, frequency-independent antennas do not exist aside from the theoretically ideal, isotropic, point-source radiator. In addition to the trade-off between frequency independence and low dispersion, there also exists a dichotomy between pattern stability and constant gain. While the antenna pattern of a constant gain, omnidirectional antenna will remain constant with respect to frequency, the antenna pattern of a constant aperture antenna will narrow as frequency increases, as shown in Figure 13 [26].

Though aperture antennas generally have higher gain than the omnidirectional antennas, the aperture antennas must also be larger in order to maintain the greater directional pattern. But, the drawback of an omnidirectional to omnidirectional antenna link is that the overall received power rolls off at a rate of $1 / f^2$ with respect to frequency, as opposed to remaining constant across the frequency band [26].

Because the AFIT NoNET system uses direct sampling of WUB noise, a phased array, in the traditional sense, is not an option for gaining a narrower, steerable main beam. Noise inherently has no phase; therefore, unless the noise signal is modulated by a carrier signal, the radar waveform cannot form the interference pattern that is necessary to generate an array pattern. Instead, an UWB theory based on relative time delays between array elements would have to be applied. The objective of this thesis is to design an antenna that will replace the current LPA with a smaller antenna, with similar radiation properties but more stable bandwidth properties. The antenna design priorities for the AFIT NoNET system are as follows.

1. Compact structure that is cheap to construct
2. High, uniform gain in the UWB frequency range $\mathrm{G}(400\text{:}\,750\ \mathrm{MHz}) \approx 5\mathrm{dB}$
3. Low reflection coefficient in the UWB frequency range $\mathrm{S}_{11}(400\text{:}\,750\ \mathrm{MHz}) \leq -10\mathrm{dB}$
4. Minimize dispersion and stabilize phase center location throughout the UWB frequency range
5. Consistent endfire pattern throughout the UWB frequency range
6. High total efficiency

To accomplish these design objectives, favorable antenna geometry must be chosen that will radiate efficiently in an endfire pattern. This will require a review of many modern and historical

designs and their performance. After choosing the proper design, a well matched feed from an SMA connection must be designed and gradually tapered to meet the radiating structure.

2.6 Chapter Conclusion

There is great diversity in the field of noise radar, just as with any type of radar. This thesis will attempt to design an antenna that will maximize the performance of the current AFIT NoNET system, but also leave room for future developments and alterations to the system within the realm of noise radar operation. Though the current system does not take into account the polarization of the target return, an antenna that reduces the cross-polar component of the received signal could be useful if target identification becomes a future task for the system. Also, an antenna that can be used a phased array will be useful if the use of a pseudo-random code modulated on a carrier signal is tested in trails in the future. Though, flexibility in the antenna performance is an excellent goal, it must still come secondary to the primary design goals of the antenna, as outlined in the previous section.

III. Antenna Design, Simulation, and Construction

3.1 Chapter Overview

The design of UWB antennas is greatly assisted by the use of computational software [27]. Since the geometry of UWB antennas generally involves expanded conductive surfaces in contrast with the many resonant antennas of classic antenna theory, the rigorous solutions for the spherical radiated electromagnetic fields in the far-field region are practically impossible. Therefore, the use of computer-aided design (CAD) software to construct antenna designs and electromagnetic solver programs to compute approximations to the antenna performance are very useful in approximating the performance of an antenna without having to build and test it in an anechoic chamber. By developing good simulated antenna results, a designer can make more informed decisions about which antennas to construct and measure.

3.2 Review of Current Designs

To minimize the cost of the antennas to be constructed, the research is primarily directed towards planar antenna designs. This is beneficial for a couple reasons. First, AFIT already has copper clad boards that can be quickly cut for either milling or etching. Second, this will keep the final antenna design compact, as minimization is one of the primary design goals. Also, to maintain easy compatibility to the current system, the antenna will be mounted with an SMA connector to mate to the coaxial cable for the noise radar.

Beginning with the current LPA antenna on the AFIT NoNET system, the difficulty for an UWB radar system comes from the construction of the full bandwidth from adjacent sub-bands, as evident from the S_{11} measurement [36]. Not only is the instability in the reflection coefficient a problem in the RNR application, but the phase center moves along the axis of the antenna as frequency increases. Since the LPA is built with a series of dipole antennas matched to

alternating feeds, it uses each pair of linear elements to radiate a narrowband channel within the full bandwidth of the antenna, as illustrated in Figure 14.

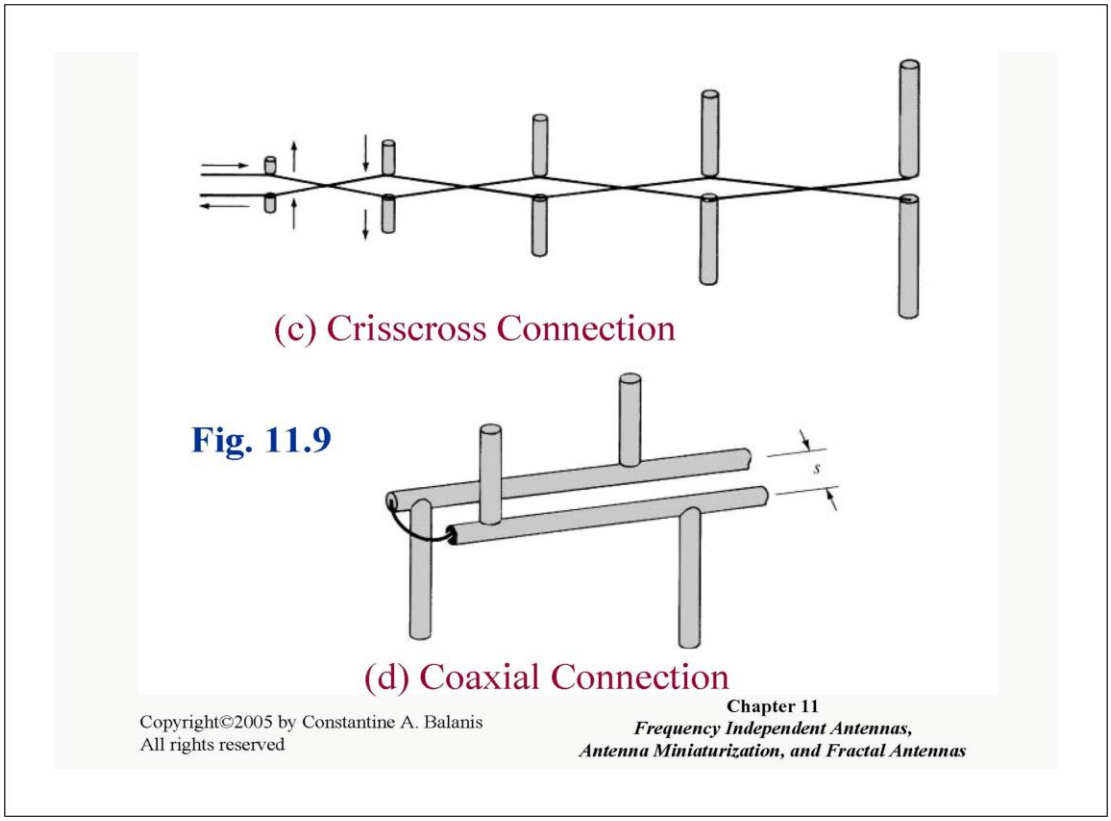

Figure 14 – Log-periodic antenna configuration [1]

As the frequency radiated through the LPA increases the pair of dipole elements with the greatest current density steps forward on the overall antenna structure to smaller and smaller elements. This movement of the surface current distribution is what causes the phase center of the LPA to shift location with frequency.

Though the LPA is not a good choice for the RNR system due to lack of bandwidth uniformity and phase center movements, not all frequency-independent antennas are disqualified from use. Spiral, spiral-cone, and helical antennas are other examples of frequency-independent antennas that have gradual tapers in their structure, which would improve the bandwidth

continuity. The helical and spiral-cone antennas will still have the phase center movement problem. The planar spiral, on the other hand, maintains a stable frequency response and has a stable phase center as the surface currents gradually rotate around the central point of the spiral in a single plane, which could cause new problems as the resulting polarization rotates around the central axis. The phase center is well maintained at the center point of the antenna. Though these antennas offer stable patterns and frequency responses, the antenna size must be one the order of a wavelength. For example, a UHF spiral antenna has difficulty transmitting between 300 and 400 MHz even when it has an outer radius of 1.25m [37]. Since size is a major factor in the design, these antennas will most likely not satisfy the needs of the AFIT system.

The next class of antennas under consideration is the set of electrical antennas, such as dipoles and monopoles. Since a monopole ground plane is difficult to incorporate in a planar design, the dipoles will be better suited for the design. Some shapes seem to be better suited to the UWB application than others. Diamond dipoles have great bandwidth responses, but they do not have good pattern stability [38,39]. Bow-tie antennas operate similar to the diamond dipoles, as the geometry is nearly mirrored. Circles and ellipses seem to have geometries more conducive to UWB radiation with more stable pattern behavior [40,41,42]. Rectangular geometry is another possibility, but the bandwidth response is slightly less consistent as the side dimensions determine resonances [43]. The circular and elliptical dipoles are elegant UWB antennas with stable frequency responses and fairly consistent radiation patterns. The main drawback is the omnidirectional radiation pattern. The current LPA has a slight endfire pattern, which would be preferred in the final design.

Magnetic antennas are similar in performance to their electronic counterparts. Loop antennas radiate very similarly to dipole antennas, with the only difference being in the orientation of the

antenna. Dipole antennas radiate orthogonal to the plane of the antenna geometry, whereas loop antennas radiate orthogonally in the plane of the antenna structure [26]. But, in addition to the lack of directivity with the loop antenna, the loop antennas generally must be built on the order of a wavelength, similar to the spiral antenna, and thus do not satisfy the desire to reduce the overall size of the antenna subsystem. Slot antennas are another form of magnetic antenna that offers great flexibility. Basically a slot antenna is a conductive metal sheet with a differential feed that forms a loop with a geometrical cutout in the center. The combination of the antenna feed and loading with the geometry of the slot cutout determines the unique properties of each antenna [28,44,45,46]. Slot antennas seem capable of better efficiency than loop antennas when sized to smaller fractions of wavelength. Similar to the drawbacks of dipole antennas, the slot antennas radiate omnidirectionally, leaving the endfire design requirement unsatisfied. Though, the unique geometry of many of the slot antennas designed could be useful in considering design tweaks to a final antenna design.

A group of antennas called Vivaldi antennas looks to have potential for a very strong fit with an UWB radar application. The Vivaldi antenna adapts dipole and slot antennas by drawing elements from planar horn antennas. The primary distinguishing feature of a Vivaldi antenna is the exponential taper of the central gap in the radiating geometry [47]. There are two basic divisions in style of Vivaldi antennas [4]. Though antenna engineers use several different names for these antennas, the author will classify Vivaldi antennas into two basic groups, the Vivaldi Slot antenna [47,48,49,50] and the Vivaldi Dipole antenna [51,52,53,54,55,56].

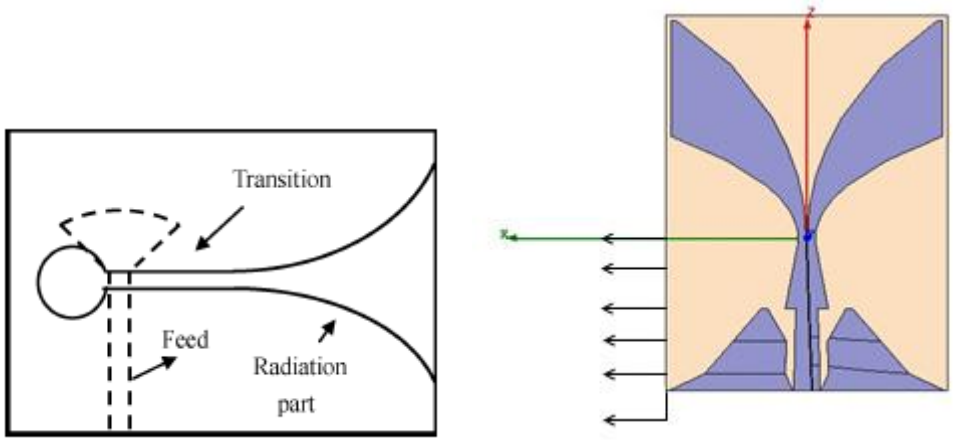

Figure 15 – Vivaldi slot antennas: classic design (left) [49], novel (right) [47]

The Vivaldi slot antenna is very similar to a ridged horn antenna without the outer walls. It has a ground plane with an exponentially tapered slot opening toward the endfire direction. The left antenna in Figure 15 is the classic Vivaldi slot antenna. By shaping the slot geometry or even the feed structure, an antenna designer can affect the antenna radiation properties. This tapered slot is either terminated in an open or short geometry [26]. The signal feed is then routed orthogonally across the base of the tapered slot similar to the differential pole feed at the base of a ridged horn, as shown in Figure 16.

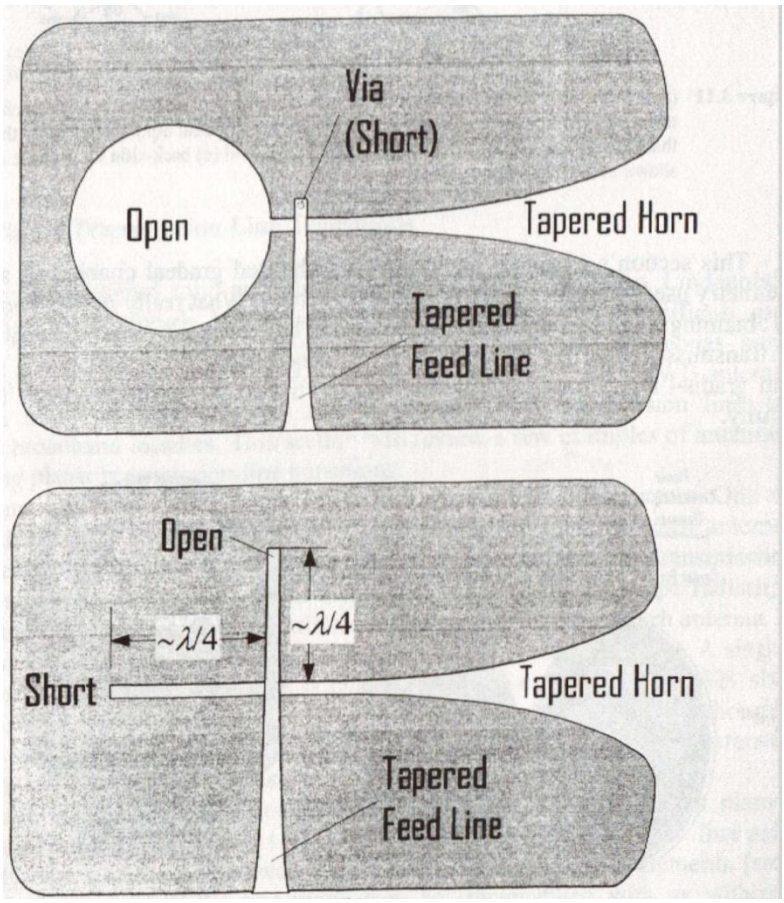

Figure 16 – Vivaldi slot antenna feed options [26]

Vivaldi Slot antennas offer good flexibility in design of frequency response and impedance matching [48,50] and high, stable gain within the bandwidth of interest [47,49], but the antenna structure must be sized to approximately $\lambda/2$ at the lower end of the bandwidth.

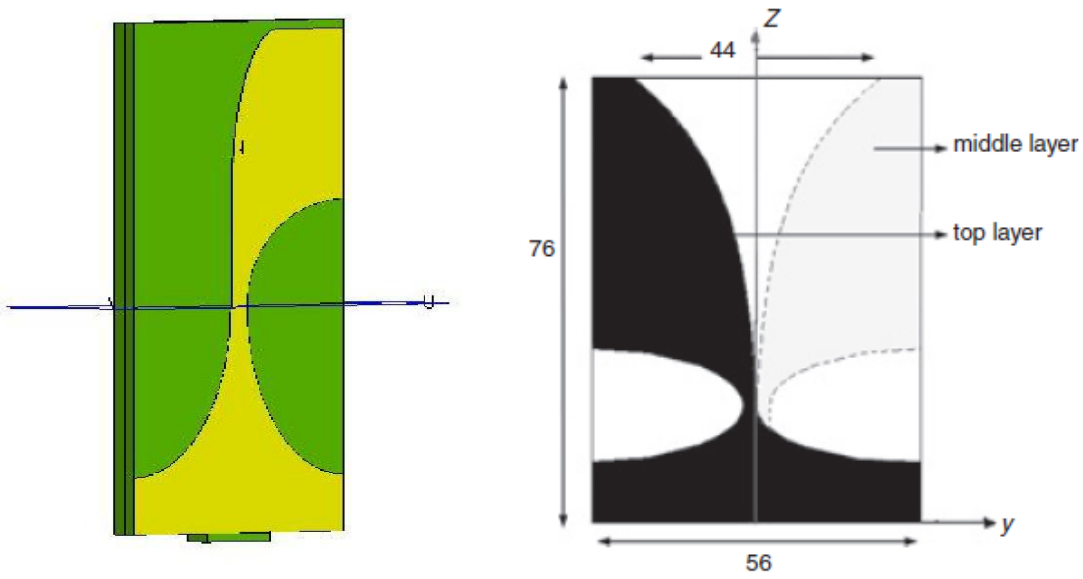

Figure 17 – Balanced Vivaldi dipole antennas from (left) [54] and (right) [56]

Vivaldi dipole antennas appear to have greater size flexibility as they seem capable of radiating when scaled to smaller fractions of a wavelength. Instead of connecting both sides of the slot, the Vivaldi dipole antenna treats each side as a separate arm of an UWB dipole antenna. The Vivaldi dipole antenna is also generally fed with a microstrip feed. Though there can be various shapes, the general construction is shown for a couple antennas in Figure 17. From the microstrip feed, the signal expands out into one arm of the antenna dipole while the ground plane narrows into the throat of the antenna structure before expanding again into the opposite arm of the dipole.

The Vivaldi dipole antenna's polarization distinction decreases as the arms of the dipole are offset slightly by the substrate material that separates them. This effect can be reduced by the addition of another ground plane arm in order to generate a linear polarization with greater control of the electric field exiting the antenna [55].

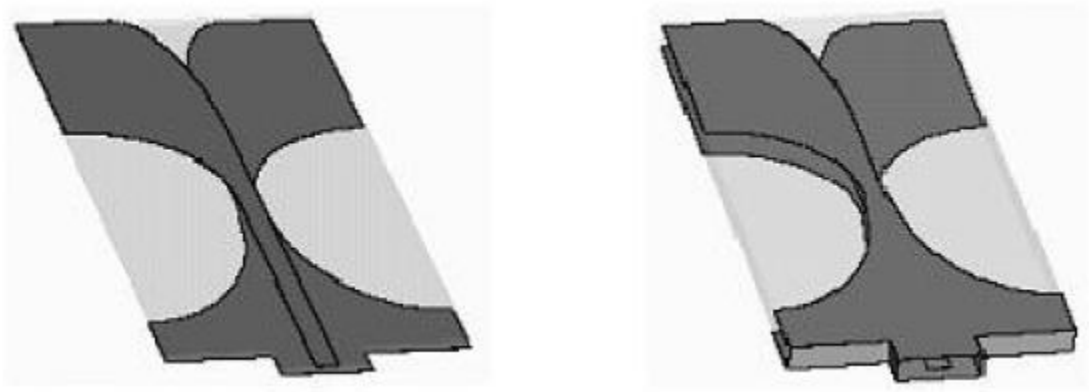

(a)

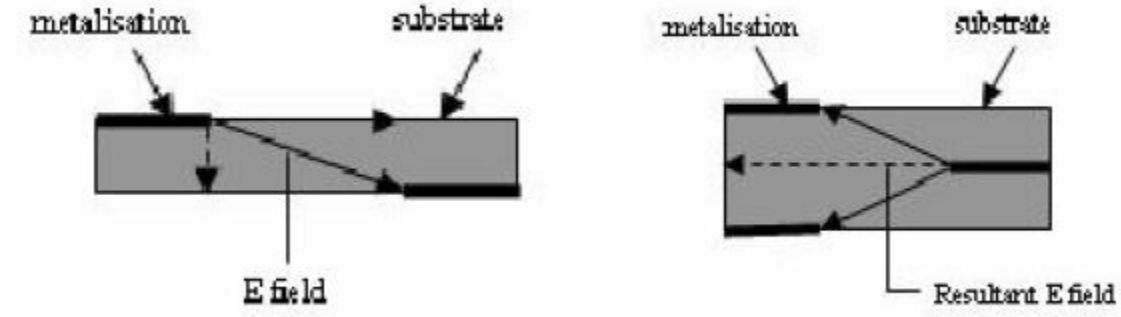

(b)

Figure 18 – Antipodal (left) vs. balanced (right) Vivaldi dipole antenna (a) construction and corresponding (b) E-field transmissions [55]

The standard Vivaldi dipole with two radiators is called antipodal as they are offset from one another, as seen on the left side of Figure 18. When the ground plane radiator is duplicated across the signal radiator for a total of three radiators, as seen on the right side of Figure 18, it is named a balanced Vivaldi dipole. Aside from the classic Vivaldi dipole design [51,54,55,56], there is room for geometry adaptation in order to affect directivity and gain [52,53].

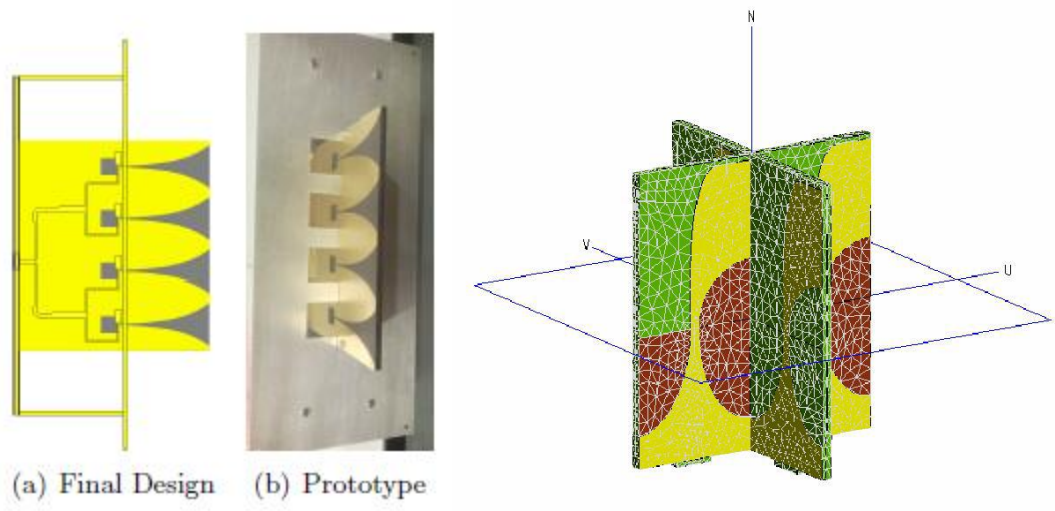

Figure 19 – Single polarization, 1x4, Vivaldi slot antenna array (left) [48] and dual polarization, 2x2, Vivaldi dipole antenna array (right) [54]

Both Vivaldi antenna types, slot and dipole, will array well, as seen in Figure 19, and have the possibility to keep polarization distinction [55]. There are similarly high gain and frequency response stability for both antenna styles. The phase center will move more than a standard UWB dipole antenna will, but balancing that movement against the directivity of the antenna will be controlled in the design process. In the end, the design process will move forward best with the Vivaldi dipole antenna, due to its capacity to radiate at smaller fractions of a wavelength than the Vivaldi slot antenna.

3.3 Antenna Geometries for Computational Analysis

Beginning with a few published results to calibrate simulation software use, various Vivaldi dipole antenna variations were built using the CST Microwave studio software suite. The first antenna simulated was the classic configuration of the Antipodal Vivaldi Dipole from Yang et. al. [51]. The shaping of the antenna geometry is shown in Figure 20 and the measurements from

Yang et. al. are shown in Table 2, as corresponding to the variable names shown from the structural drawing.

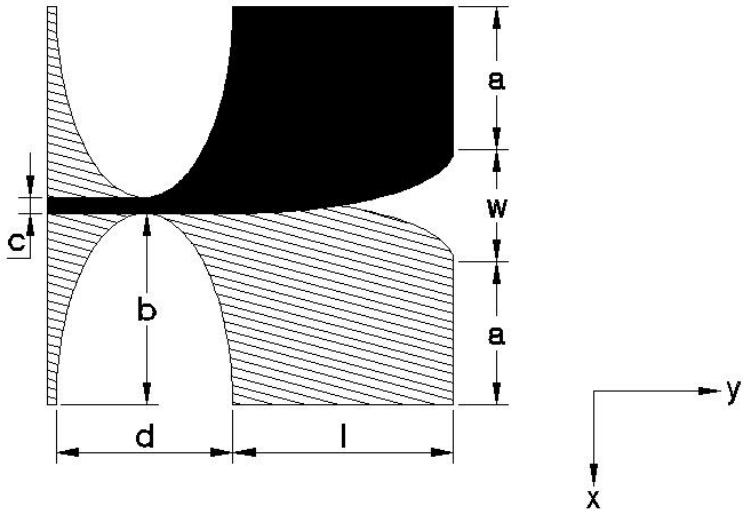

Figure 20 – Classic antipodal chopped Vivaldi dipole antenna [51]

Table 2 – Geometry for classic antipodal chopped Vivaldi dipole antenna [51]

Variable Name	Dimension Size [cm]
a	1.615
b	2.160
c	0.180
d	1.000
l	2.500
w	1.270
PCB thickness	0.080

Both antipodal and balanced versions were simulated despite the article only building and testing the antipodal version. This was attempted in order to demonstrate the cross-polar reduction of the balanced configuration of the Vivaldi antenna. The results of this comparison are shown in Section 4.2, Figure 55 and Figure 57.

The second antenna simulated was an Antipodal Vivaldi Dipole with elliptical tips on at the ends of the radiator branches as drawn from Wang et. al. [52]. This geometry was intriguing, because it maintained curvature continuity completely around the entire structure of the radiators. Since the surface current would concentrate at the sharp edges of the classic setup, a design with smooth curvature should offer a more distributed surface current response, which could reduce steep resonances in the spectral response leading to a more uniformity. The antenna geometry is shown in Figure 21 and the geometry measurements, as interpreted from the information in Wang et. al., is shown in Table 3. Both balanced and antipodal versions were simulated for this design as well.

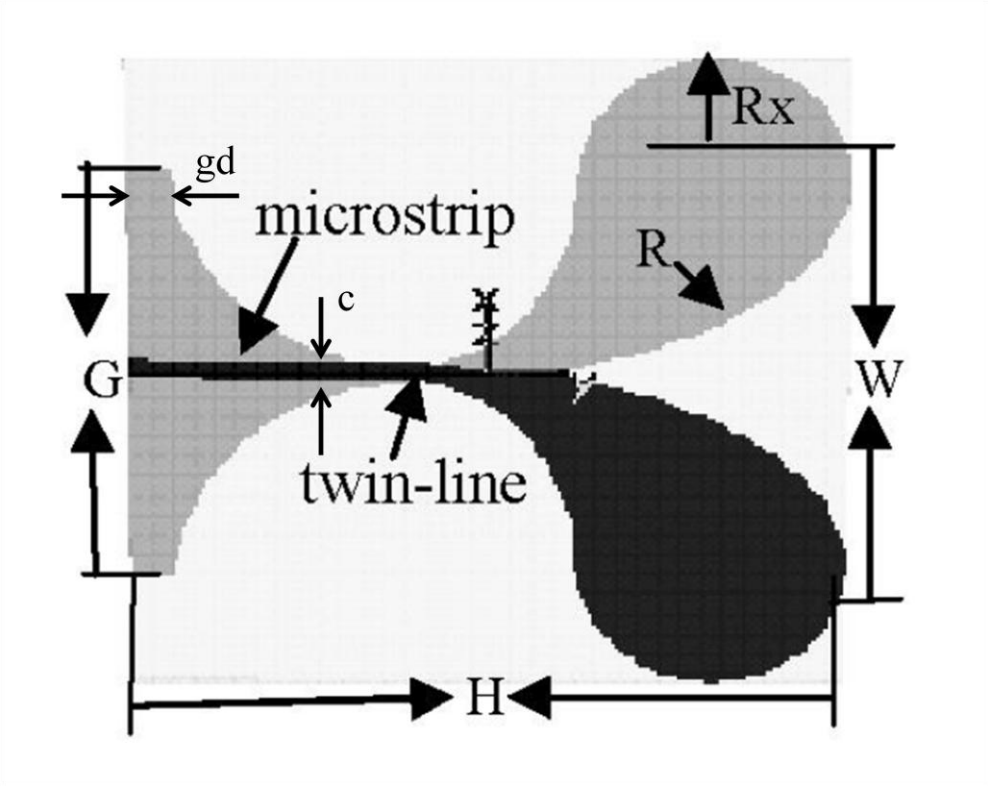

Figure 21 – Antipodal elliptically-tipped Vivaldi dipole antenna [52]

Table 3 – Geometry for antipodal elliptically-tipped Vivaldi dipole antenna [52]

Variable Name	Dimension Size [cm]
H	5.000
G	1.600
W	4.000
Rx	1.000
c	0.203
gt	0.500
PCB thickness	0.080

Though the exact dimensions cannot be determined merely from the information given in the article, care should be taken in their estimation because minor changes in their measure will make large changes in the frequency response of the antenna, as shown in Figure 22.

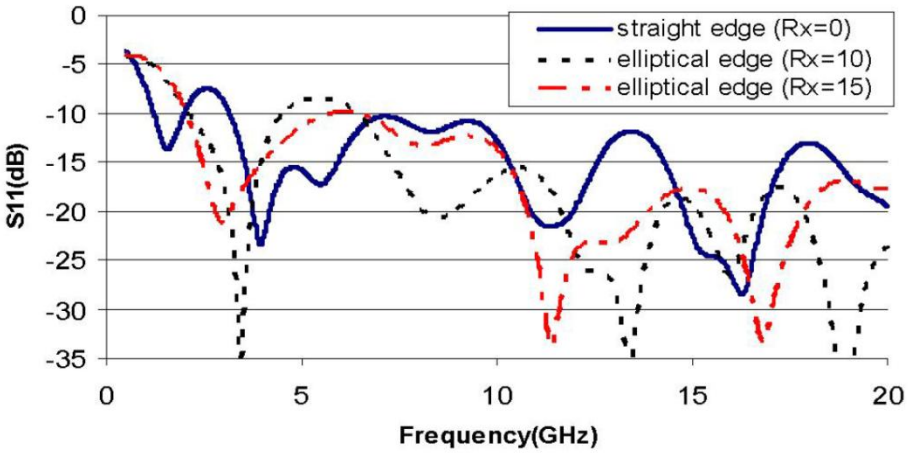

Figure 22 – S_{11} for Antipodal Elliptically-Tipped Vivaldi Dipole Antenna [52]

Mueller et. al. was the third article to be drawn from for simulation purposes. This antenna was interesting to test because it uses a very unique shape for its radiators, is built to operate down to 300 MHz, and produces what appears to be a very directive pattern which achieves nearly a 25 dB front-to-back ratio at 600 MHz [53]. The interesting features of the antennas geometry, as shown in Figure 23, are the flares at the rear of the radiating arms and the use of

only two discontinuity points in the shaping. The prime difficulty in reconstructing this antenna arises as the authors did not provide any detailed shaping data aside from the overall length and width of the antenna. A balanced version of this design will be simulated in addition to the antipodal.

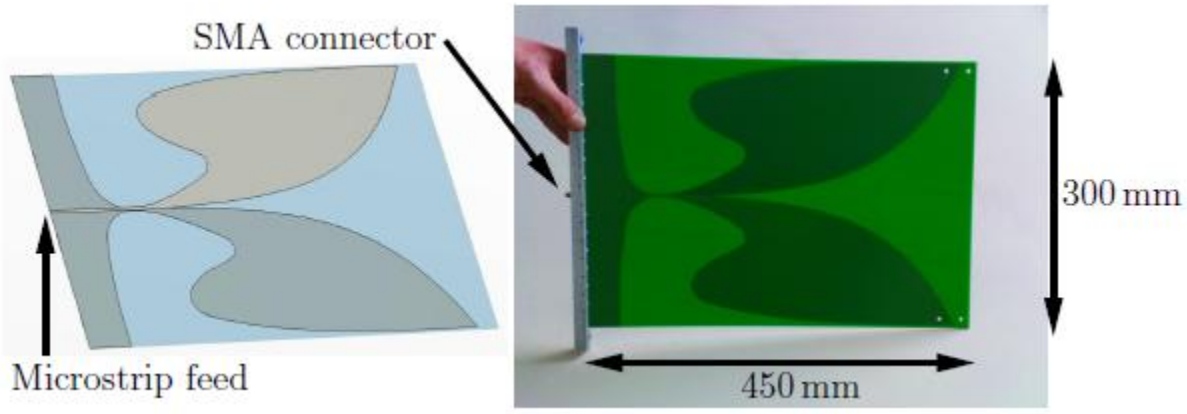

Figure 23 – Flared antipodal Vivaldi dipole antenna [53]

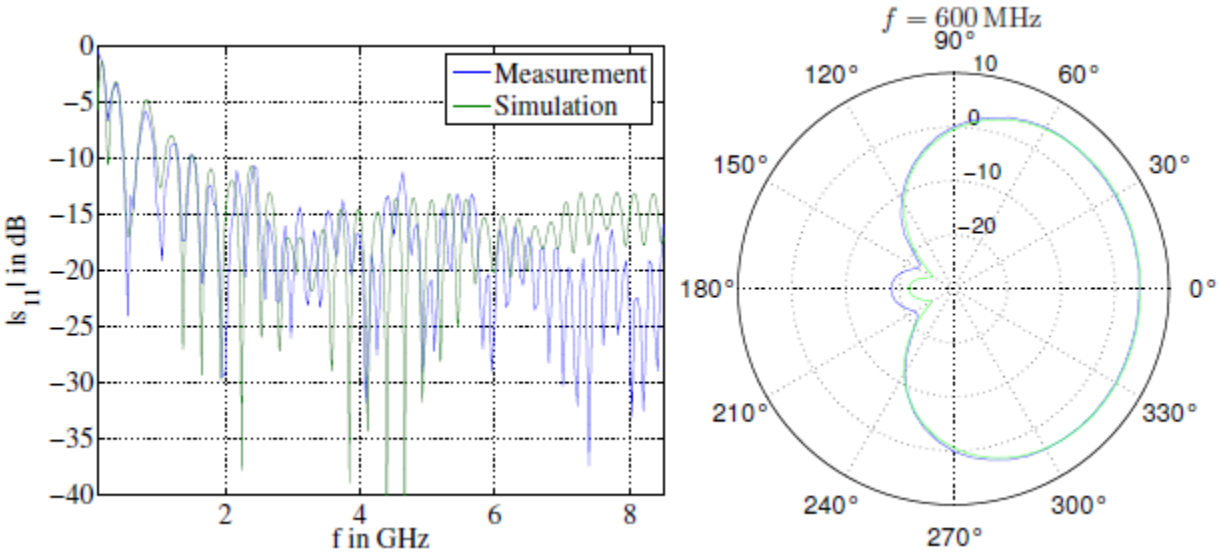

Figure 24 – S_{11} (left) and H-plane gain pattern [dBi] (right) for antipodal flared Vivaldi dipole antenna [53]

The next antenna design approach began as a deviation from the planar horn traits of the Vivaldi antenna. The elliptical dipole offered excellent frequency response and low reflections [26]. The hope is that the use of elliptically shaped radiating arms on the Vivaldi antenna might offer similar properties with minimal loss in directivity. Two versions of this antenna were designed, both with ellipses for radiating arms. The first, the Antipodal Ellipse Vivaldi Dipole, runs the elliptical taper directly into the forward end of radiating arms, as shown in Figure 25. This leaves a sharp edge in the geometry of the antenna. The second antenna, the Antipodal Bunny-Ears Vivaldi Dipole, removes this sharp corner by curving the feed section into the ellipse radiator, as shown in Figure 26.

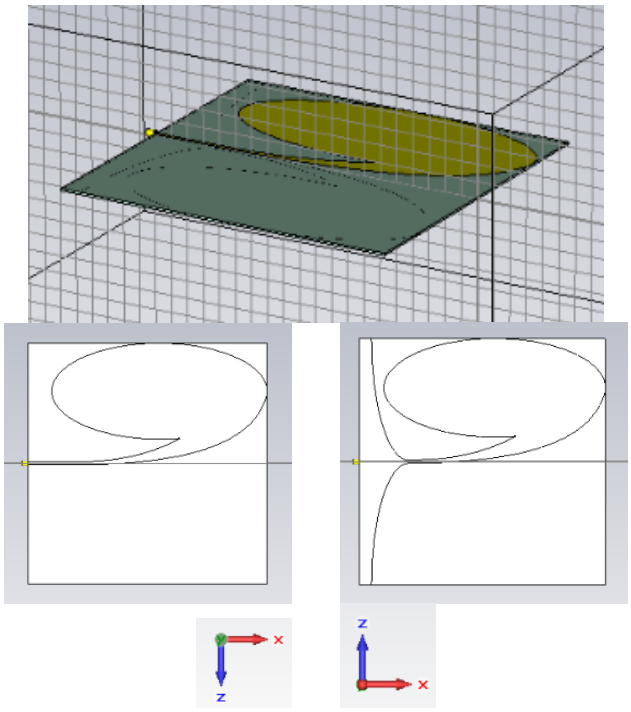

Figure 25 – Antipodal ellipse Vivaldi dipole antenna construction

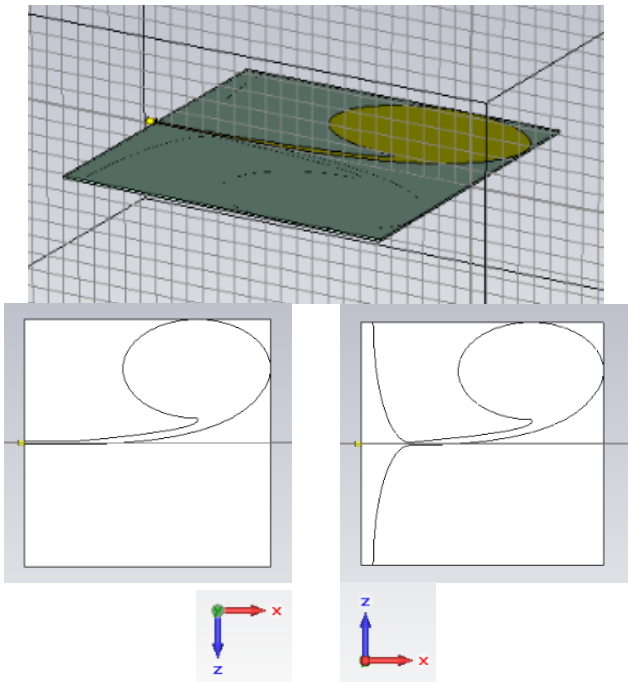

Figure 26 – Antipodal bunny-ears Vivaldi dipole antenna construction

After simulation, surface currents were found to concentrate on the sharp turns at the back end of the feed section in both antennas. An idea to reduce this surface current concentration was to continue the feed around the ellipse in a spiral pattern. This Antipodal Spiral Ellipse Vivaldi Dipole antenna is shown in Figure 27.

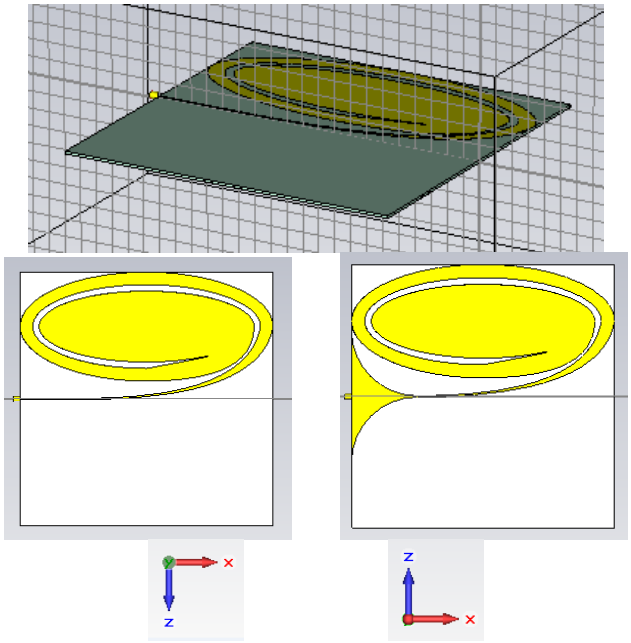

Figure 27 – Antipodal spiral ellipse Vivaldi dipole antenna construction

Also, after initial analysis of the Bunny-Ear Vivaldi, two improvements were made. First, the elements were extended to the full length of the antenna, as shown in Figure 28, to bring the lower frequency cutoff down. In addition, the central half of either radiating ellipse appeared to be the most important part in terms of the dipole functionality. Therefore, by chopping off the outer half, seen in Figure 29, the overall antenna size is reduced. When this reduction is accomplished, the final antenna, in Figure 35, resembles a planar design of a historical biconical antenna designed by P.S. Carter in 1939 [57].

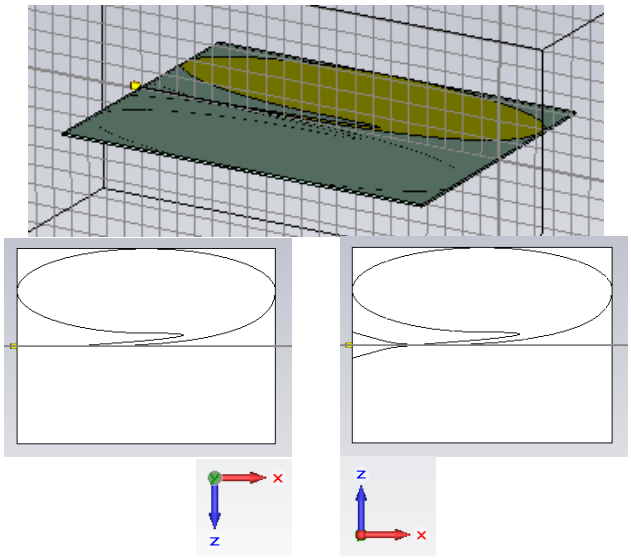

Figure 28 – Antipodal full bunny-ears Vivaldi dipole antenna

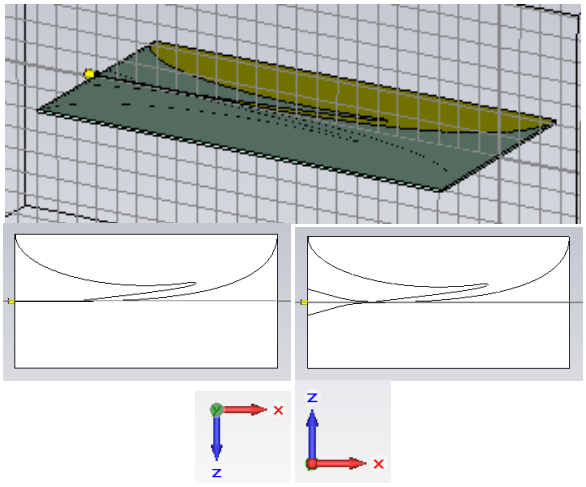

Figure 29 – Antipodal chopped bunny-ears Vivaldi dipole antenna

These various antenna designs were built and simulated in CST Microwave Studio and analyzed using the Frequency Domain Solver to attain the S_{11} parameter, port impedance, electric fields, magnetic fields, surface currents, and radiation patterns of each antenna design. Wide sweeps of structural measurements are attempted in order to find a good operating range, from which to fine tune and optimize the antenna.

Table 4 – Number of antennas constructed by design style

Antenna Name	Simulated Designs
Antipodal Chopped Vivaldi Dipole	17
Antipodal Elliptically-Tipped Vivaldi Dipole	6
Antipodal Flared Vivaldi Dipole	6
Antipodal Ellipse Vivaldi Dipole	6
Antipodal Spiral Ellipse Vivaldi Dipole	8
Antipodal Bunny-Ears Vivaldi Dipole	18
Log-Periodic Antenna	1

In total, 61 antennas were simulated in addition to the simulated model of the original LPA, as listed according to design category in Table 4. Finally, three designs were chosen for construction based on their performance with respect to the objectives.

3.4 Design Decisions

After simulation of this assortment of antenna designs, the best of the best were gathered and compared according to their size, reflection coefficient, and gain performance, as shown in Table 5. The best antenna is obviously the chopped Vivaldi dipole when extended to a full half-meter construction size, but one of the primary objectives is to reduce the size of the antenna used from that of the LPA. Therefore, by focusing on keeping the size of the antenna under 20x20 cm, or 400 cm2, to accomplish a reasonable reduction in size, the best small antennas were chosen primarily according to the percentage of the operational UWB for which the S_{11} was less than -10 dB and the maximum gain achieved within the UWB. All of the antennas possessed primarily omnidirectional radiation patterns due to their size with respect to the wavelengths of the bandwidth of interest. The spiral ellipse Vivaldi design ended up more resonant than desired and did not achieve low reflections between 400 and 750 MHz, which its designs did not emerge in the highest ranking antennas. The bunny-ears Vivaldi dipole (BEVD) performed better than the ellipse Vivaldi dipole because the smooth transition from the elliptical feed to the radiating

geometry allowed for lower reflections, and was thus able to be reduced in size without significant loss in performance. The chopped Vivaldi dipole (CVD) did the best job of keeping pace with the LPA in performance while still reducing the antenna size. With less than half the size of the LPA, the CVD maintained a low reflection coefficient for a high percentage of the bandwidth and, though it did not achieve as high of a maximum gain, its broadside gain was much closer to uniform than the LPA. The next best unique design that achieved a size reduction from the LPA is the chopped bunny-ears Vivaldi dipole (CBEVD), which had low reflections for much less of the bandwidth but still attained similar uniformity characteristics. The full BEVD also performed well in these regards and was included in the list of constructed antennas.

Table 5 – Simulated antenna performance and comparison

	S_{11}: % < -10dB	Max S_{11} Diff [dB]	Size [cm^2]	Max Gain in-Band	Min Gain in-Band	Gain Diff
Chopped Vivaldi (100Ω) FULL HALF WAVE SIZE	100.00%	32.244	1250	6.365	0.500	5.865
Original Log-Periodic (50Ω)	69.80%	43.296	667	6.840	3.461	3.379
Chopped Vivaldi (100Ω) - BUILT	49.80%	12.569	200	1.849	0.618	1.231
Ellipse Radiators (100Ω)	31.20%	16.979	400	2.916	0.302	2.614
Bunny-Ears (100Ω) FULL HALF WAVE SIZE	29.40%	37.239	1250	5.511	-1.215	6.726
Chopped Vivaldi (50Ω)	25.80%	11.608	400	3.848	-2.114	5.962
Flared Vivaldi from Mueller et.al. (50Ω)	22.60%	15.400	1350	5.246	-2.060	7.306
Chopped Vivaldi (50Ω)	20.20%	16.652	225	1.112	-0.749	1.861
Chopped Vivaldi (100Ω) 20cm Gnd	18.40%	17.841	200	1.666	-7.517	9.183
Chopped Bunny-Ears Vivaldi (100Ω) - BUILT	18.20%	10.844	200	1.840	-1.065	2.905
Flared Vivaldi (50Ω)	18.00%	10.404	225	0.851	-0.354	1.205
Bunny-Ears Vivaldi (100Ω) - BUILT	17.00%	15.265	300	0.105	-9.821	9.926
Chopped Vivaldi (100Ω)	16.80%	26.212	400	3.217	-2.923	6.140
Flared Vivaldi (100Ω)	16.40%	22.675	400	4.330	-2.501	6.831

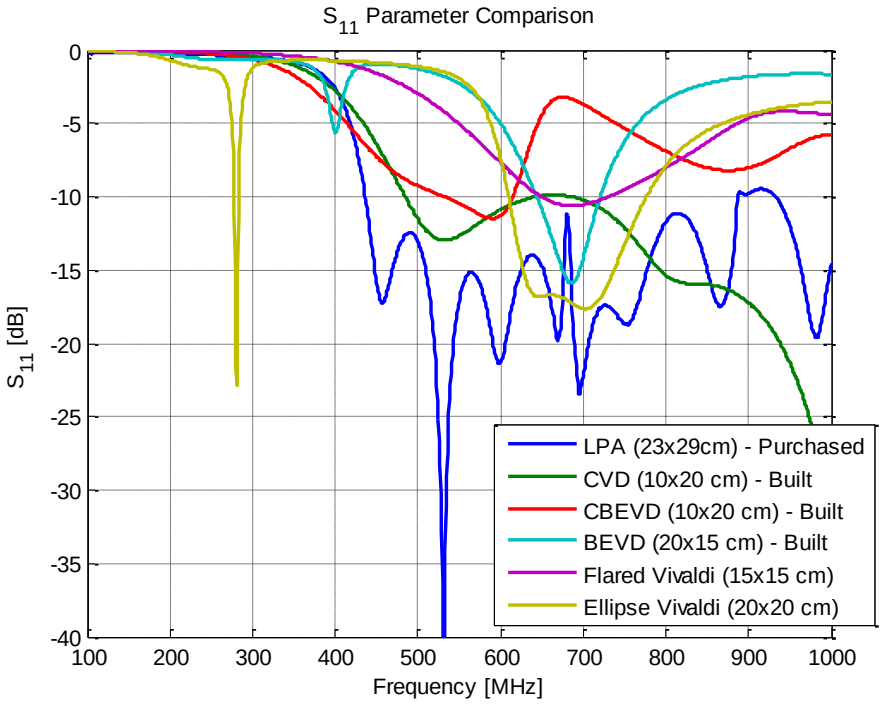

Figure 30 – S_{11} Comparison of most promising simulated antenna designs

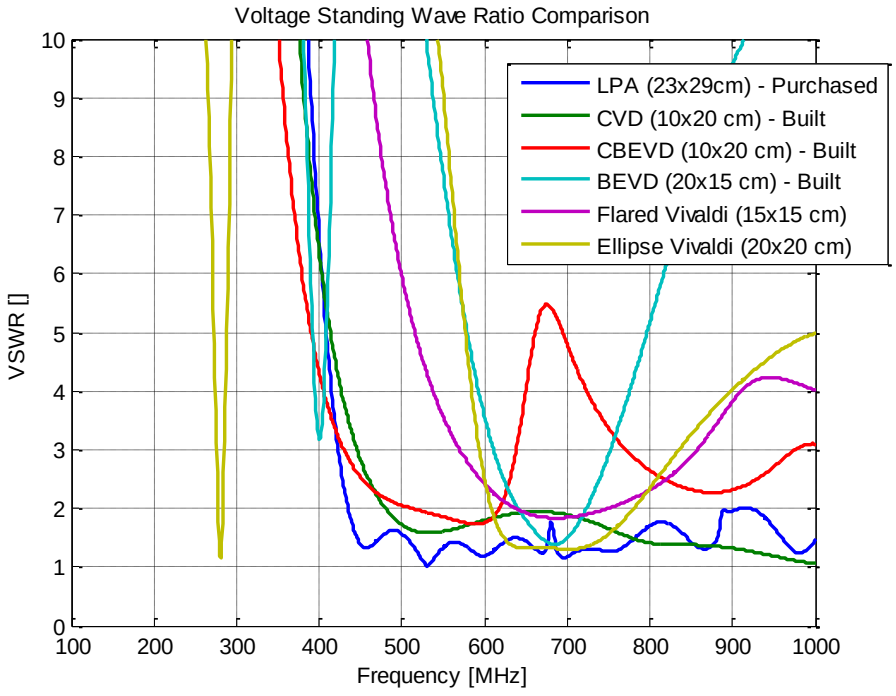

Figure 31 – VSWR comparison of most promising simulated antenna designs

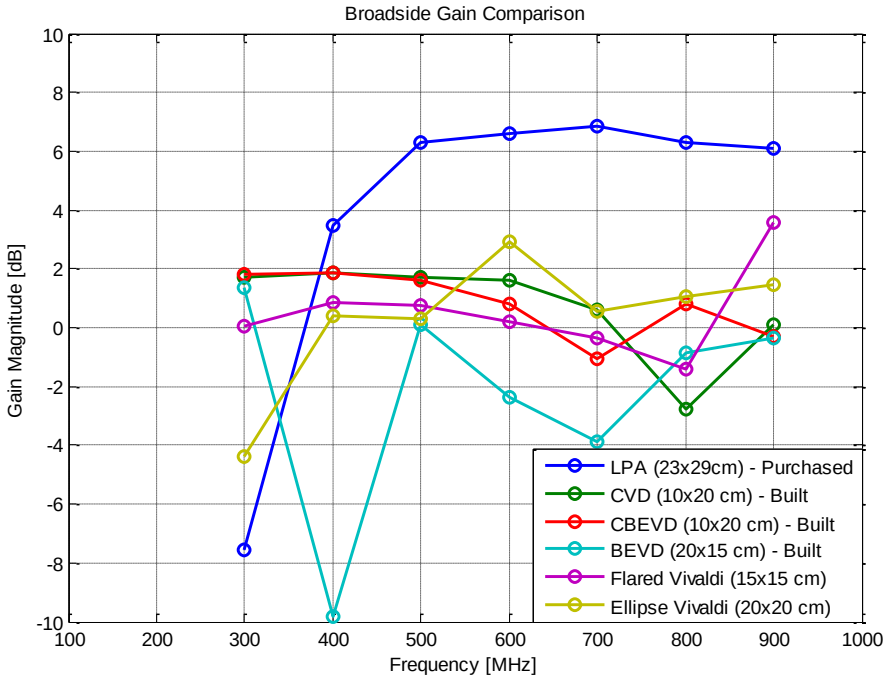

Figure 32 – Broadside gain comparison of most promising simulated antenna designs

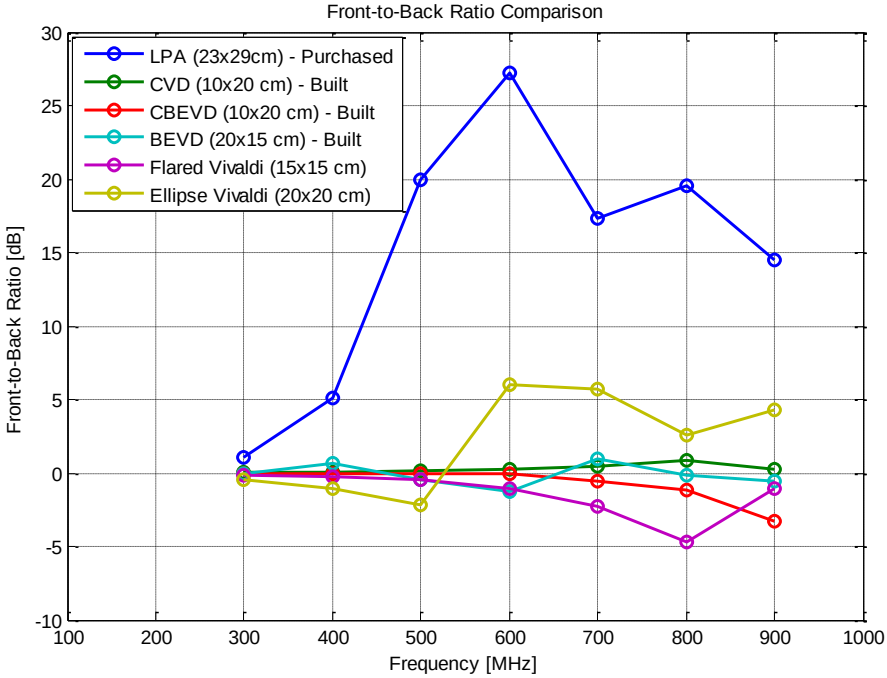

Figure 33 – Front-to-Back ratio comparison of most promising simulated antenna designs

The lowest S_{11} and highest gain across the bandwidth from 400 to 750 MHz were attained by the Chopped Vivaldi Dipole, Chopped Bunny-Ears Vivaldi Dipole, and Bunny-Ears Vivaldi Dipole antennas. These antennas were then chosen to be optimized through CST Microwave Studio's frequency solver optimization feature, which computes performance changes for minor adjustments in geometry measurements, specifically the feed diameter, the ground plane diameter and the radiating shape width.

The final antennas chosen to be built and tested maintained low reflection coefficients, high efficiencies and gains, and general directivity. The three antennas chosen for construction are:

- Antipodal Chopped Vivaldi Dipole Antenna (CVD) [10cm x 20cm]
    - 87.18 Ω Microstrip feed, shown in Figure 34
- Antipodal Chopped Bunny-Ears Vivaldi Dipole Antenna (CBEVD) [10cm x 20cm]
    - 87.18 Ω Microstrip feed, shown in Figure 35
- Antipodal Bunny-Ears Vivaldi Dipole Antenna (BEVD) [20cm x 15cm]
    - 87.18 Ω Microstrip feed, shown in Figure 36

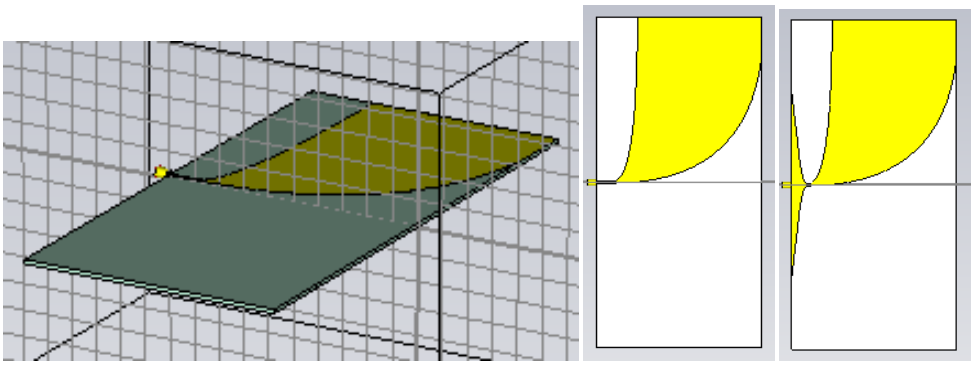

Figure 34 – Antipodal chopped Vivaldi dipole antenna, as built

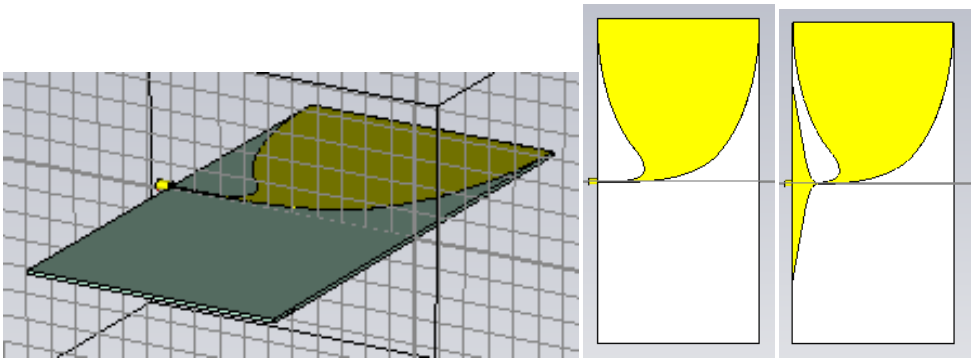

Figure 35 – Antipodal chopped bunny-ears Vivaldi dipole antenna, as built

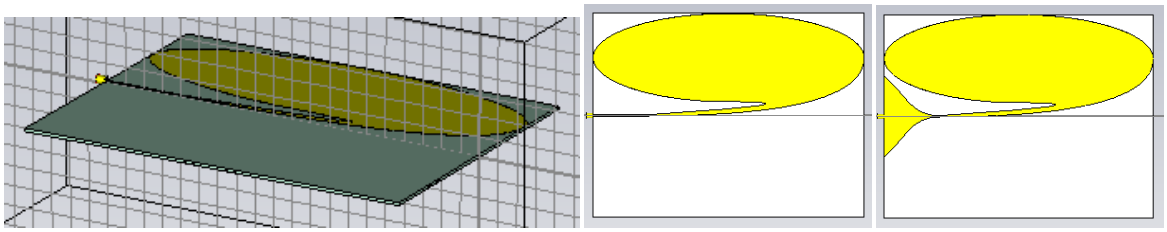

Figure 36 – Antipodal bunny-ears Vivaldi dipole antenna, as built

The completed PCB antenna designs were then exported to structural GERBER (*.gbr) files, which could be easily imported into the AFIT milling machine or printed using a laser printer for use in the etching process.

3.5 Antenna Manufacturing Methodology

There are two printed circuit board (PCB) antenna manufacturing techniques available for use, precision milling and etchant solution. AFIT has a milling machine that is used for removing unwanted copper from copper-clad boards ready to be turned into PCBs. In addition, home PCB etching can be accomplished with the use of a few store-bought chemicals. Three antenna designs need to be constructed and the etchant solution method will be the fastest. But, in order to test both manufacturing techniques, the most optimistic of the three designs, the CVD, will be constructed using both methods as a control case.

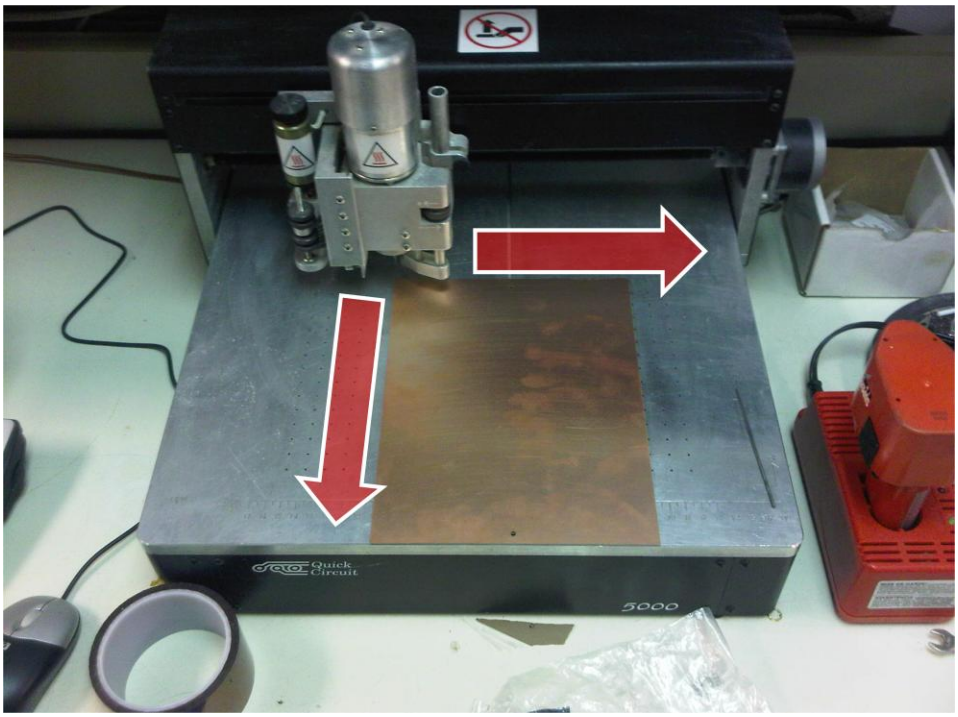

Figure 37 – AFIT milling machine with copper-clad board for PCB construction

The milling machine uses a small drill bit attached to a press mounted on a pair of tracks, shown in Figure 37. When mated to a computer, the structures of the PCB to be cut can be uploaded and traced. Though the process is fairly simple, the antenna is a dual sided structure and requires care to ensure that both sides match as well as possible. The accuracy of the milling machine is very good and cuts the antenna with only very minor nicks or frays. The result of milling the antenna is excellent, aside from a few drawbacks. The milling takes off not only the copper, but some of the substrate material beneath it. This causes the thickness of the substrate to be inconsistent and thinner than the simulated thickness. Also, the two radiating arms ended up being offset just slightly as seen in Figure 38. Though this does not make a big difference in terms of the large radiating arms, the feed section could cause an impedance mismatch and increase the reflection coefficient as a result.

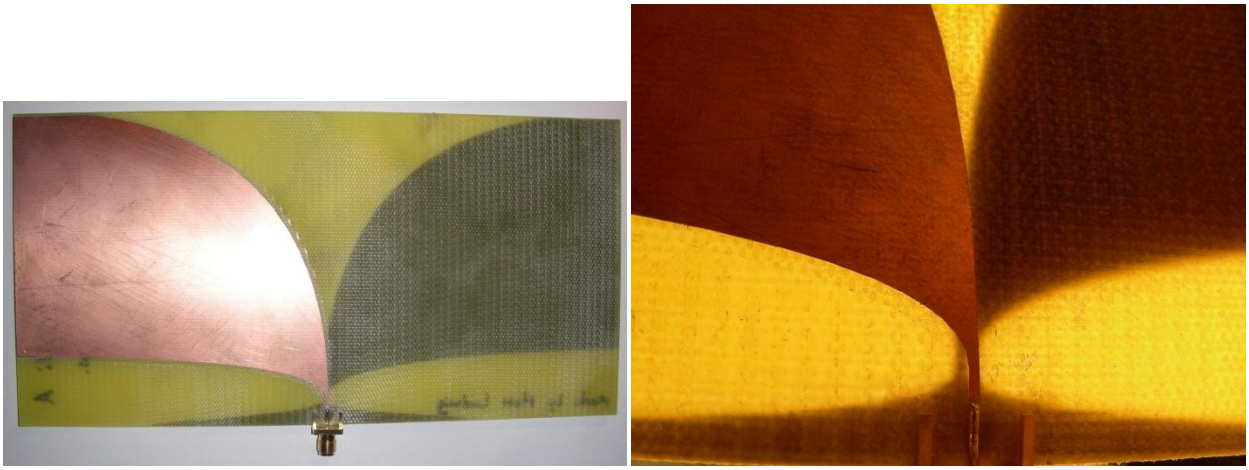

Figure 38 – Milled antenna and offset feed section

The process of PCB etching is slightly more complex, though runs quickly once started. A PCB etching solution removes any copper that it comes into contact with. In order to etch a specific pattern, one must treat the copper board beforehand in order to ensure that only the undesirable copper is removed. In this case, printer ink toner was transferred using a special sugar paper, which when treated was able to transfer the toner from the paper to the copper board. This process is fragile as even the slightest misalignment could offset one side of the antenna from the other. After transferring the toner ink, the board is ready for the etchant solution.

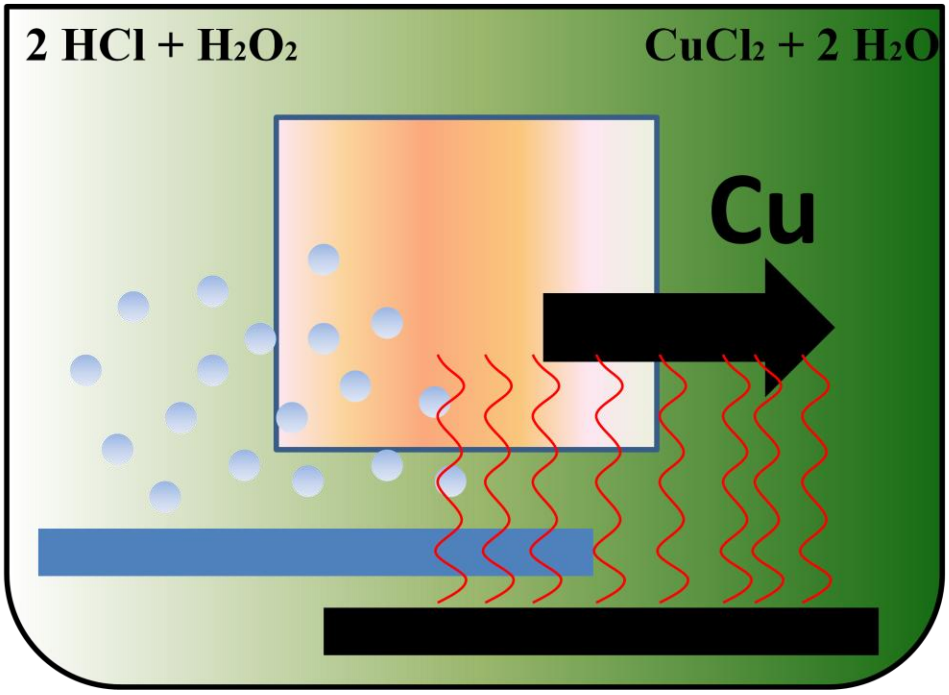

Figure 39 – PCB etching process

Using a combination of hydrochloric acid, HCl, and hydrogen peroxide, H_2O_2, the copper clad board will etch very fast. Figure 39 shows the chemical process in the presence of oxygenating bubble bar and heat source, both of which increase the reaction speed. Hydrochloric acid is easily found in hardware stores, supplied as a strong acid used for pool pH control. Hydrogen peroxide can be picked up at just about any grocery or health store. Combining the two compounds in solution according to a 2:1 ratio by mass according to (20), creates the reaction when the copper board is dipped into the solution.

$$\mathrm{Cu} + 2\,\mathrm{HCl} + \mathrm{H_2O_2} \rightarrow \mathrm{CuCl_2} + 2\mathrm{H_2O} \tag{20}$$

As more of the copper is etched away from the board, copper (II) chloride, $CuCl_2$, becomes the dominant compound in the solution as the solution turns green. The convenient part is that $CuCl_2$ will continue to etch the copper boards, according to (21), just not as fast as the solution of

HCl and H_2O_2. The speed of the etching can be improved by adding heat and oxygen to the solution.

$$CuCl_2 + Cu \rightarrow 2\ CuCl \tag{21}$$

Copper chloride, CuCl, is a dark brown color and is the end product as it does not dissolve copper. CuCl can be revived as an etchant solution by adding more HCl and oxygenating the solution, according to (22).

$$4\ CuCl + 4\ HCl + O_2 \rightarrow 4\ CuCl_2 + 2H_2O \tag{22}$$

After the unwanted copper had been etched away, the toner could be cleaned away easily using the powerful cleaning power of acetone. The results of the etching process were of lesser quality than the milling machine. Though the substrate material was unharmed and maintained a uniform thickness, the copper of the antenna's radiating arms suffered due to the toner depositing process. Since thicker boards were used, the heat press had difficulty transferring the toner ink from the paper to the copper board. Many gaps were left in the structure of the antenna. Most gaps were small and probably wouldn't affect the results significantly. But, the gaps in the copper in and around the feed section of the antenna offer significant difficulties, as shown in Figure 40. These small gaps are quite large relative to the narrow feed sections of the antennas and will disturb the surface current immensely.

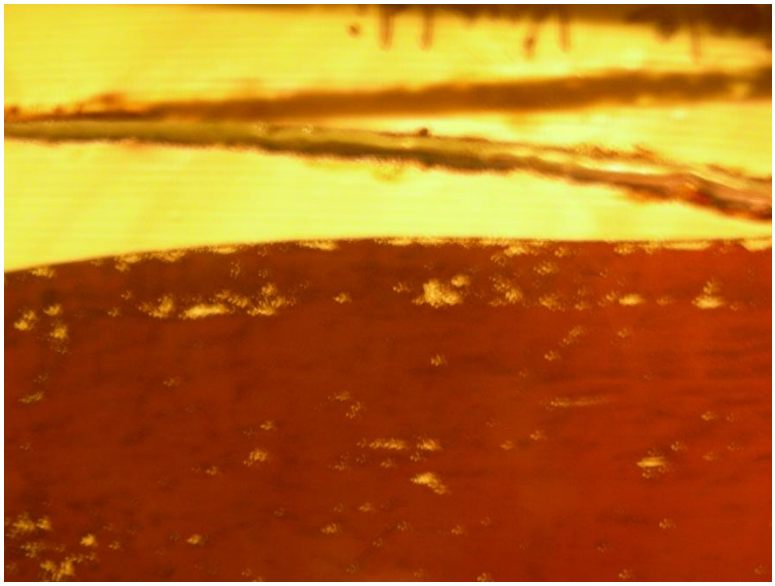

Figure 40 – Gaps left by PCB etching process

Figure 41 – Soldering fix to gaps left by PCB etching process

In order to attempt a fix for the gaps in the feed section, a solder gun was used to lay solder over the gaps, as seen in Figure 41. Though this would alter the thickness of the metal and possibly the radiating properties, it would be a better result than leaving the gaps alone.

3.6 Antenna Test Setup

Using the AFIT network analyzer and calibration kit in the microwave lab, calibrated S_{11} measurements can be recorded for each antenna. The microwave lab has an Agilent Technologies E8362B PNA Network Analyzer operating from 10 MHz to 20 GHz and calibrated with a Maury Microwave Corporation calibration kit, model number 8050Y-07. In order to gather S_{21} measurements, an antenna link must be setup, such as in an anechoic chamber to reduce multipath and sources of outside interference.

The AFIT anechoic chamber is setup with a 2 – 18 GHz radar to perform primarily RCS measurements. For this reason, the anechoic chamber needed to be reconfigured to perform UHF antenna measurements. The AFIT NoNET noise radar would satisfy the radar system requirement. For use as standard gain horns, AFIT was able to borrow a pair of 200 MHz – 2 GHz ridged horn antennas with corresponding exact broadside wideband gain data, shown in Figure 42.

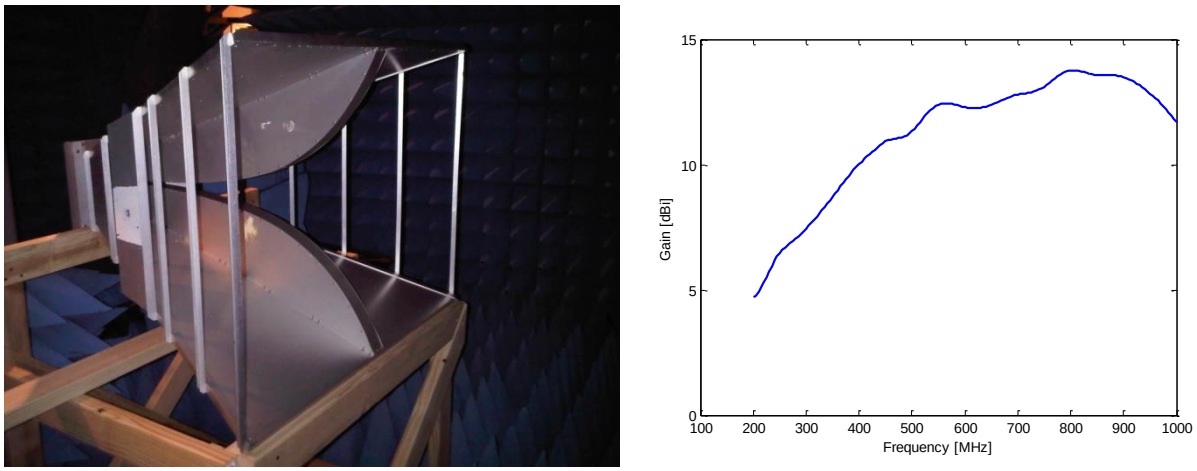

Figure 42 – EMCO ridged horn antenna (200 MHz – 2 GHz) (left) and corresponding exact gain profile according to AFRL records (right)

Figure 43 – Noise radar desk setup

A wooden frame is built to hold the transmit horn steadily near the work station. Because of the proximity to many other items, as Figure 43 displays the transmit environment, the addition of the wooden frame is not a significant source of scattering. The frame elevates the radiating element of the large horn antenna 49 1/8" off the ground, in order to mitigate interference with the floor of the chamber, but not so high as to interfere with the large parabolic reflector above, which has a lower end 73" above the floor. The immediate area surrounding the transmit antenna contains many scattering objects, as seen in Figure 44, but the use of the noise radar's fine range resolution correlation receiver can be used with post-processing windows to reduce the effects of that interference. The target stand is placed in the center of the anechoic chamber in order to reduce interference with the walls or the radar test stand. The antenna under test (AUT) is

mounted on a foam pylon which can then be moved through a full rotation in azimuth, as shown in Figure 45.

Figure 44 – Full anechoic chamber setup

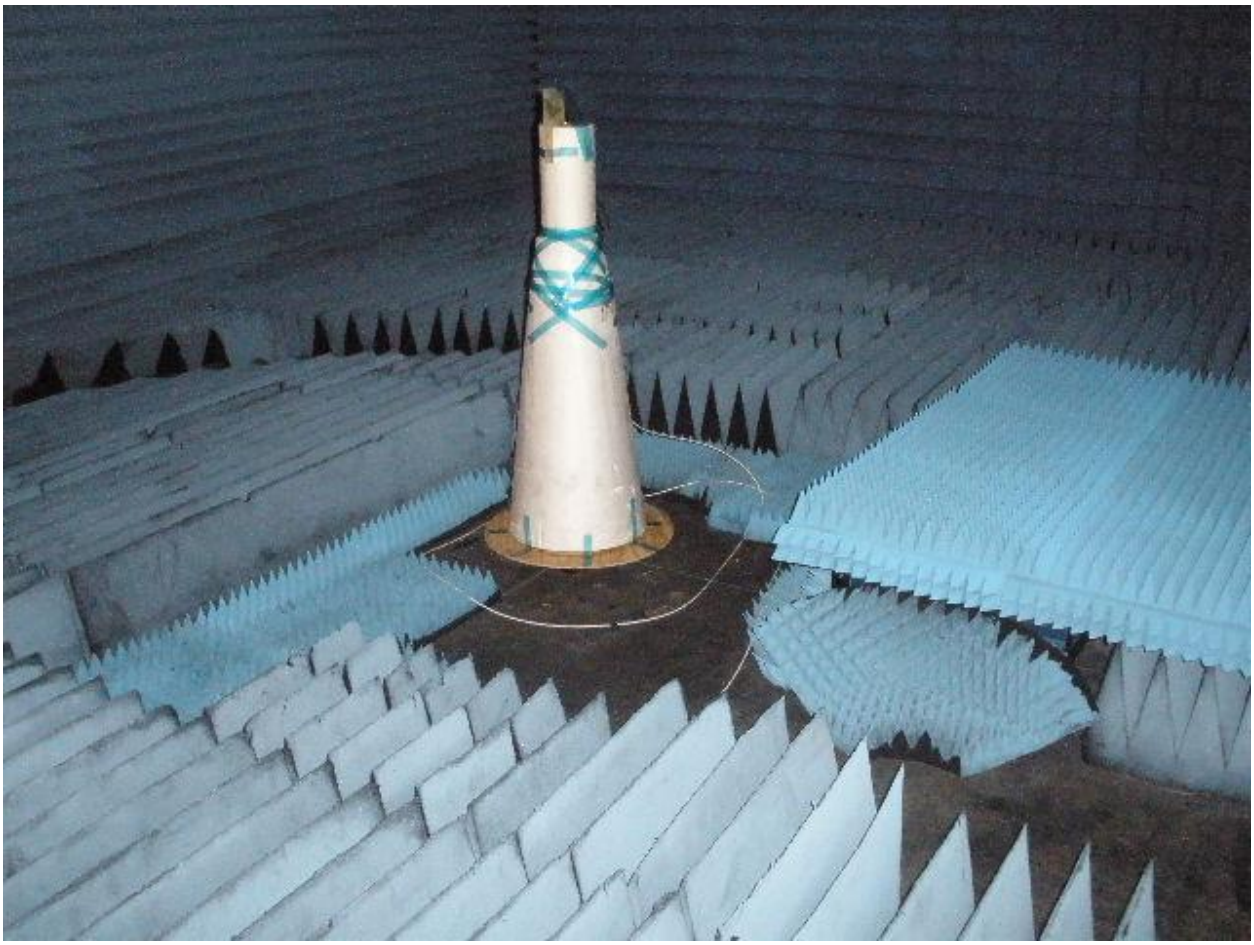

Figure 45 – AUT pylon setup on stepper motor rotating platform

The noise radar is programmed specially to record both transmit and receive waveforms at a specific rate to correspond to the stepper motor rotation of the AUT pylon. The antenna pattern is oversampled in azimuth to prepare for post processing. The motor controlling the pylon is set to rotate at 1°/sec and the radar records every 0.5 sec in order to sample at half degree intervals. The measurements start at -20° and continue through a full rotation and to +20°. The 40° overlap will identify system drift during a particular S_{21} measurement in azimuth.

3.7 Chapter Conclusion

The analysis of current UWB antennas was detailed and the eventual Vivaldi antenna design approach was presented. Through the simulation of several different Vivaldi Dipole antenna designs, an understanding of the behavior of the surface currents on the radiating arms was developed, which led to three final designs ready for production. These three designs were constructed using PCB etchant copper chloride in aqueous hydrochloric acid solution. In addition, one of the three designs was built using the milling machine at AFIT as a control case to determine the impact of the manufacturing method. The antennas were then tested for radiation patterns in the anechoic chamber using the large UHF horns.

IV. Experimental Results and Analysis

4.1 Chapter Overview

After designing, simulating, building, and testing the antennas, the designs must be compared and evaluated for performance relative to the design objectives. The CST computer simulations established an understanding of the behavior of the UWB antenna surface currents and radiation properties as geometries and parameters were adjusted. Using the knowledge gained from the variety of simulations, the best performing antennas were improved and then optimized for the highest gain and lowest S_{11}. After optimization, the antennas were constructed using both the AFIT milling machine and the PCB etchant solution. The constructed antennas were then placed in the anechoic chamber to attain E-plane and H-plane S_{21} measurements. In addition, S_{11} measurements were gained from the network analyzer in the AFIT microwave lab. In the end, the best antenna built was the chopped Vivaldi dipole (CVD) constructed with the milling machine.

4.2 Simulation Results

The first task in simulating the antennas was to verify CST model accuracy and ensure process repeatability for new designs. The antenna from Yang et al was used for verification due to the well published results for S_{11}, Gain, and radiation patterns [51]. The S_{11} results were similar, though not exact, as seen in Figure 47. The difference in the S_{11} parameters is most likely due to the difference in simulation solver and minor differences in simulated feed construction. Figure 46 shows how minor changes in simulated construction parameters can easily shift the resonant behaviors of simulated antennas. As displayed in Figure 46, three antennas with coaxial feeds and two with differential feeds were simulated. The only parameter changed between these simulated antennas was the choice of the substrate material between

Teflon and FR4. The choice of lossy Teflon performed closest to the published S_{11} results. The results for broadside Gain, as well as co-polar and cross-polar gain, were very promising, as seen in Figure 49 - Figure 50. The radiation patterns of the CST simulated and published article antennas track well with each other, as seen in Figure 51 - Figure 54.

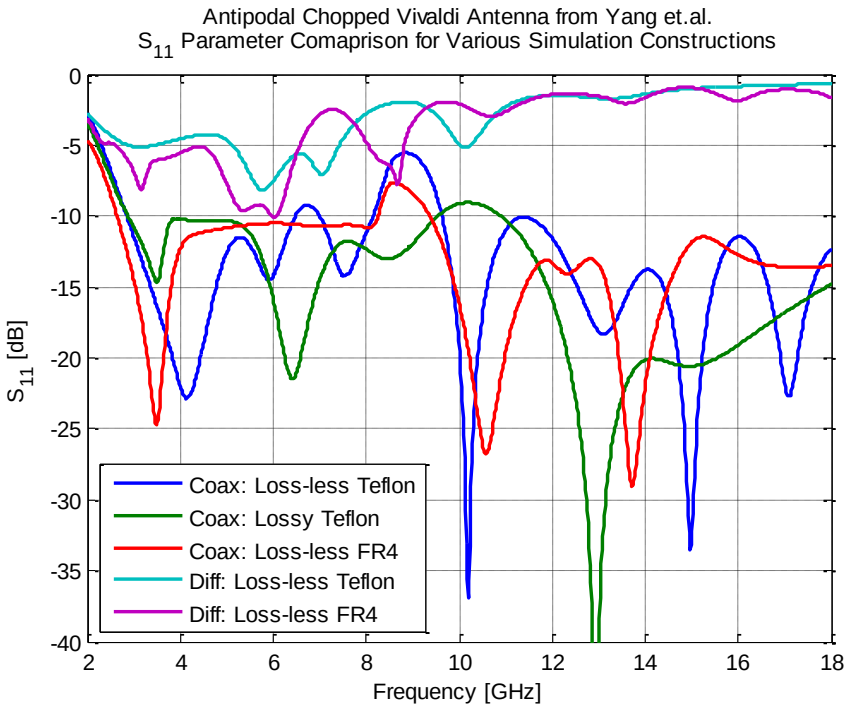

Figure 46 – Vivaldi antenna from Yang et al simulated in CST

The CST simulation calculates a very detailed electromagnetic solution for the antenna operation at specific frequencies. The initial set of frequencies for analysis can be declared by the user, but the software will declare new frequency sample points as needed. The software tries to approach convergence as it fits a spline curve to the simulated parameters, among which is the reflection coefficient. Figure 47 shows the calculated points as well as the curve fitted to them for the CST simulation results in blue.

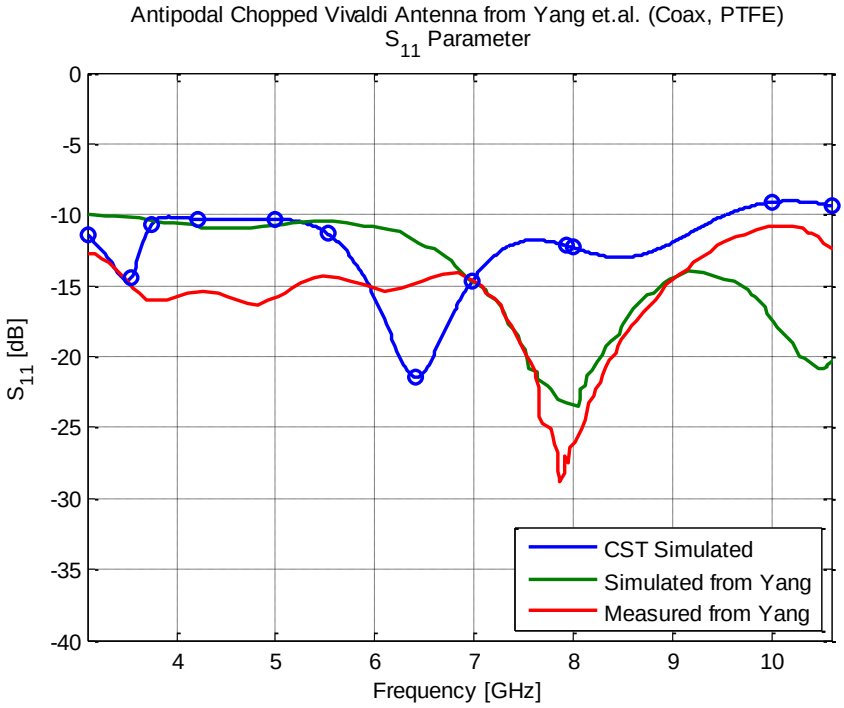

Figure 47 – CST simulated S_{11} vs. results extracted from Yang et al [51]

In order to quantify the accuracy of the CST simulation software in comparison to published measured results, error metrics were developed for both null locations in frequency and reflection coefficient magnitude. The error in frequency measures the percent error as a result of the shift in antenna resonance regions, or nulls, in the S_{11} measurement.

$$e_f = \frac{|f_{null-sim} - f_{null-meas}|}{f_{null-meas}} \times 100\% \tag{23}$$

$$\delta(f) = S_{11-sim}(f) - S_{11-meas}(f) \tag{24}$$

The error in S11 magnitude measures the difference across the full bandwidth between the simulated and measured values. The CST simulated antenna had a resonant frequency of 6.42 GHz while the Yang antenna resonated at 7.87 GHz. This resulted in a $e_f = 18.50\%$ according

to (23). Figure 48 displays the S_{11} magnitude difference results, according to (24), both before and after a frequency shift according to the resonant error was taken into account. After accounting for the resonance shift, the error of the CST simulation decreased dramatically and followed Yang's own simulation error.

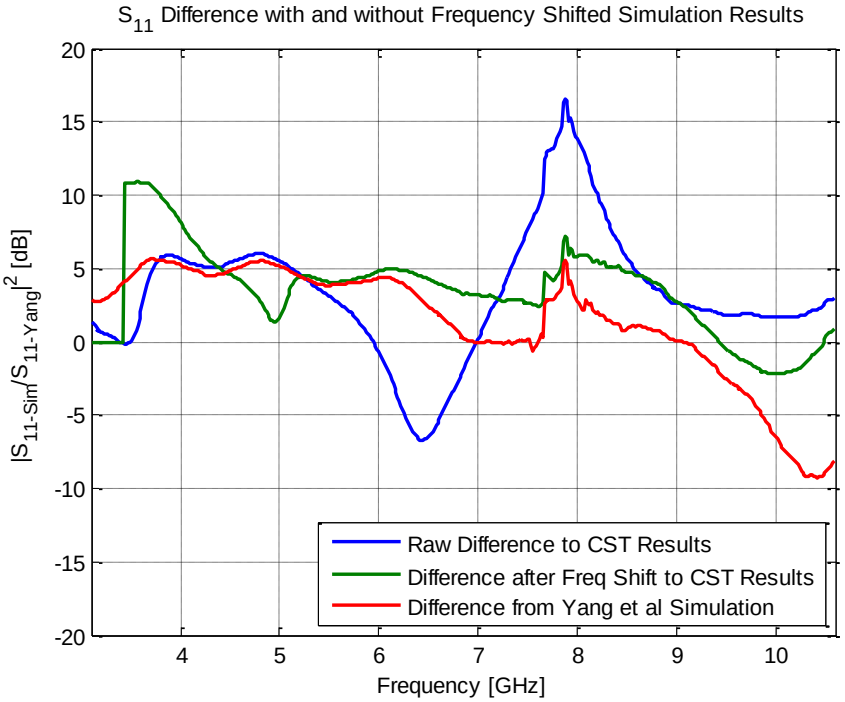

Figure 48 – S_{11} difference error analysis of CST simulation results

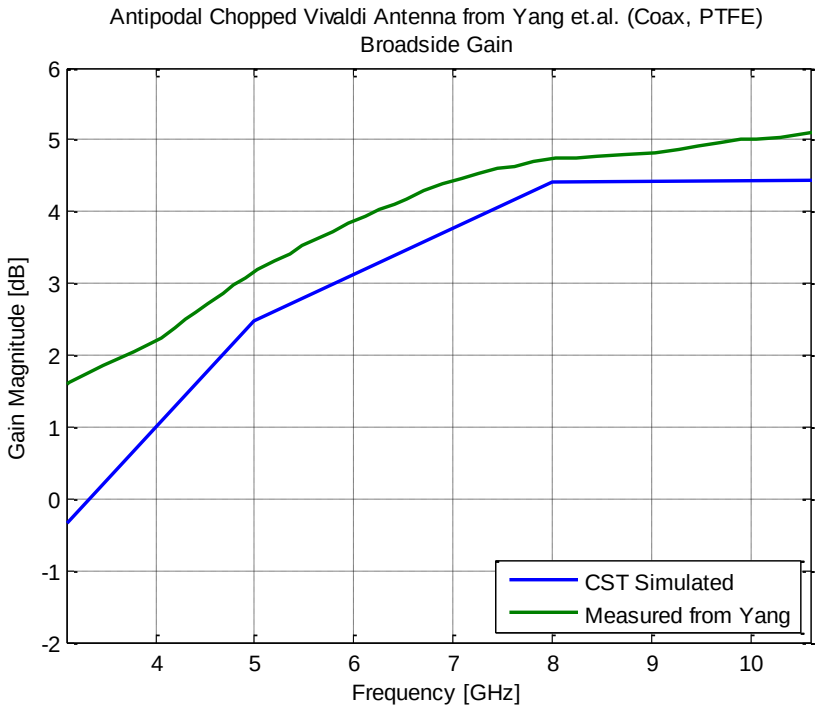

Figure 49 – CST simulated total broadside gain vs. results extracted from Yang et al [51]

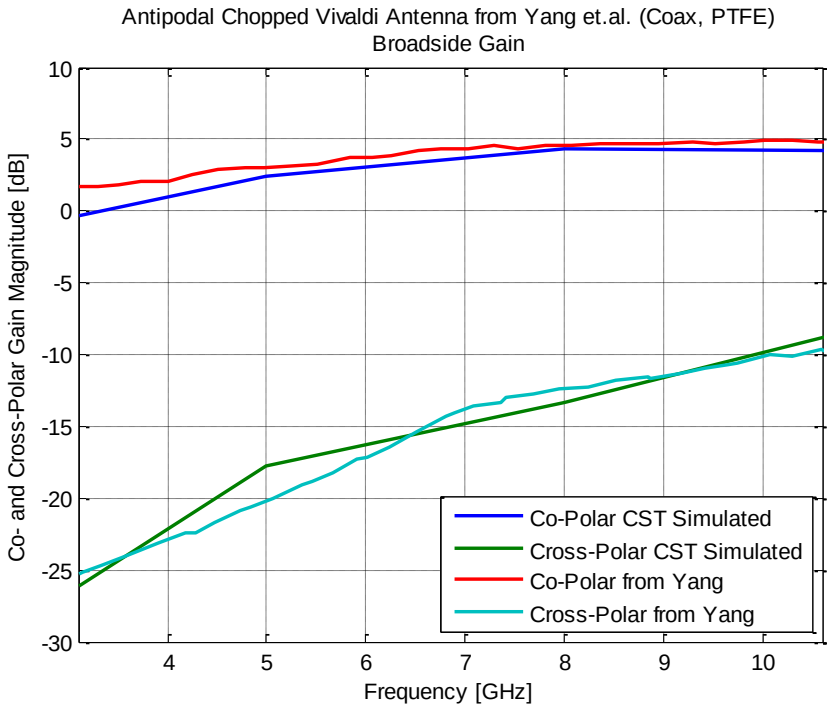

Figure 50 – CST simulated component gains vs. results extracted from Yang et al [51]

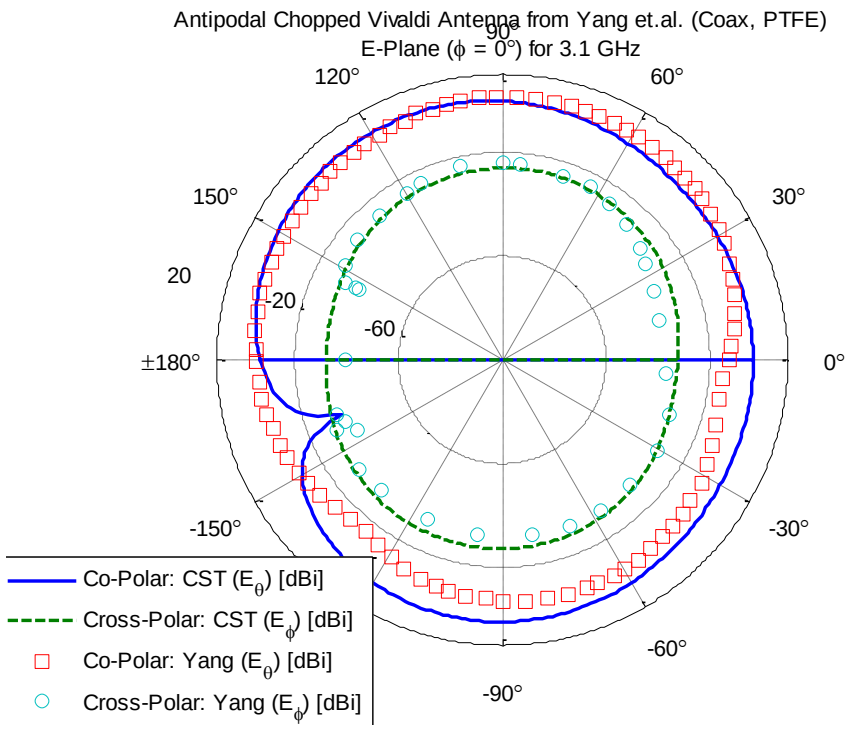

Figure 51 – CST simulated E-plane vs. Yang et al for 3.1 GHz [51]

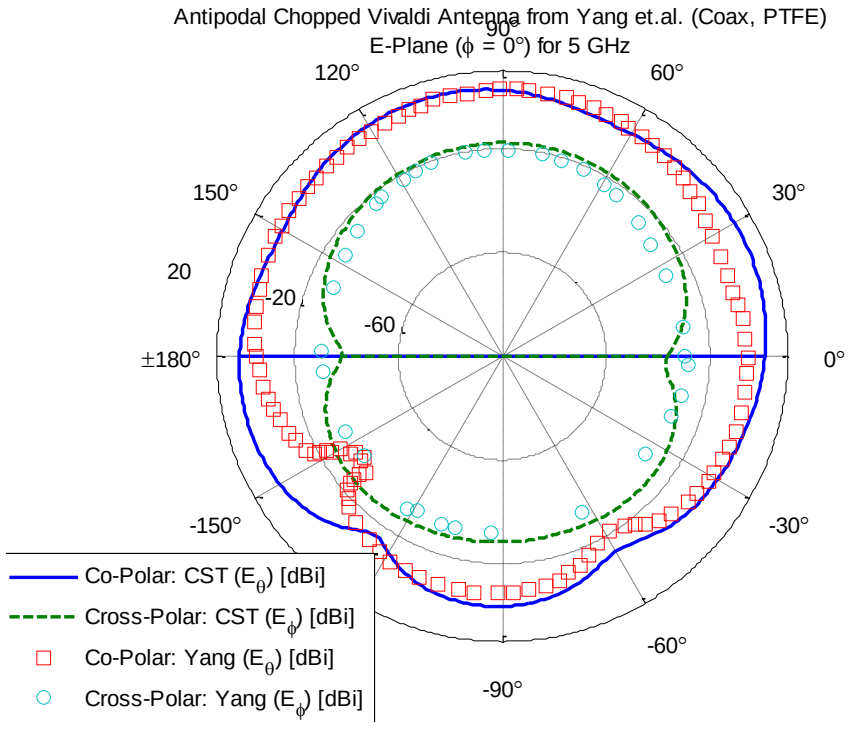

Figure 52 – CST simulated E-plane vs. Yang et al for 5 GHz [51]

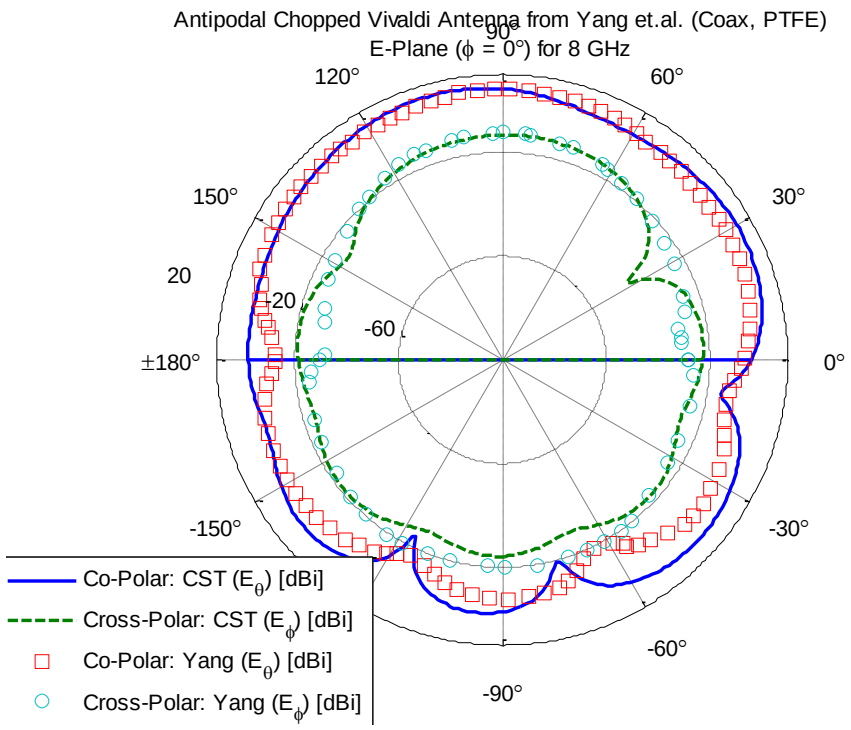

Figure 53 – CST simulated E-plane vs. Yang et al for 8 GHz [51]

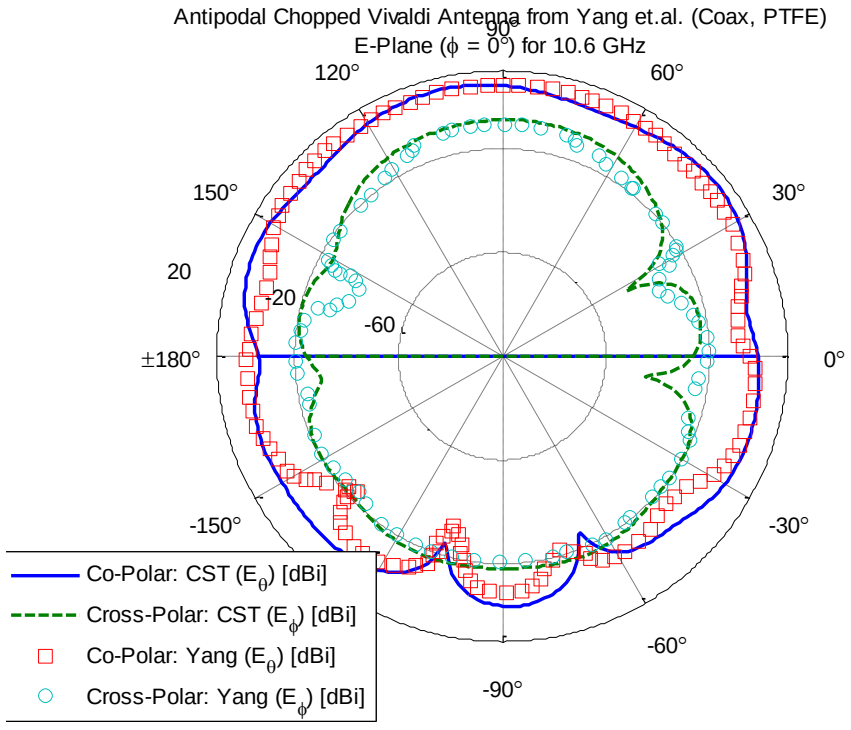

Figure 54 – CST simulated E-plane vs. Yang et al for 10.6 GHz [51]

When the chopped Vivaldi antenna was constructed in CAD software as a balanced design, as opposed to the simpler antipodal configuration, the E-plane cross-polar radiation component experienced drastic reduction of greater 20 dB, as seen in Figure 55, with little cost to VSWR, Gain, or efficiency, Figure 56 - Figure 59. Similar results were observed in the comparison of antipodal and balanced design simulations for each of the Elliptically-Tipped Vivaldi Dipole and the Flared Vivaldi Dipole antenna pairs. While the use of the balanced design does reduce the cross-polar component at little cost to performance, it does increase manufacturing complexity. Since the polarization is not utilized in the current AFIT system, the balanced design will not be constructed, but its demonstration in simulated results could be useful in future antenna generations.

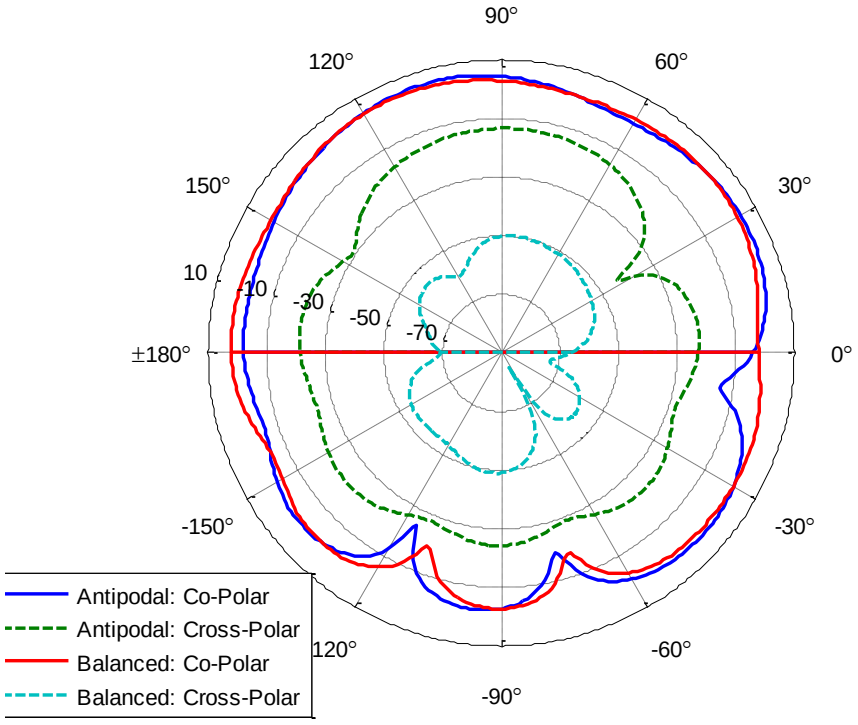

Figure 55 – 8GHz radiation patterns of antipodal vs. balanced CVD

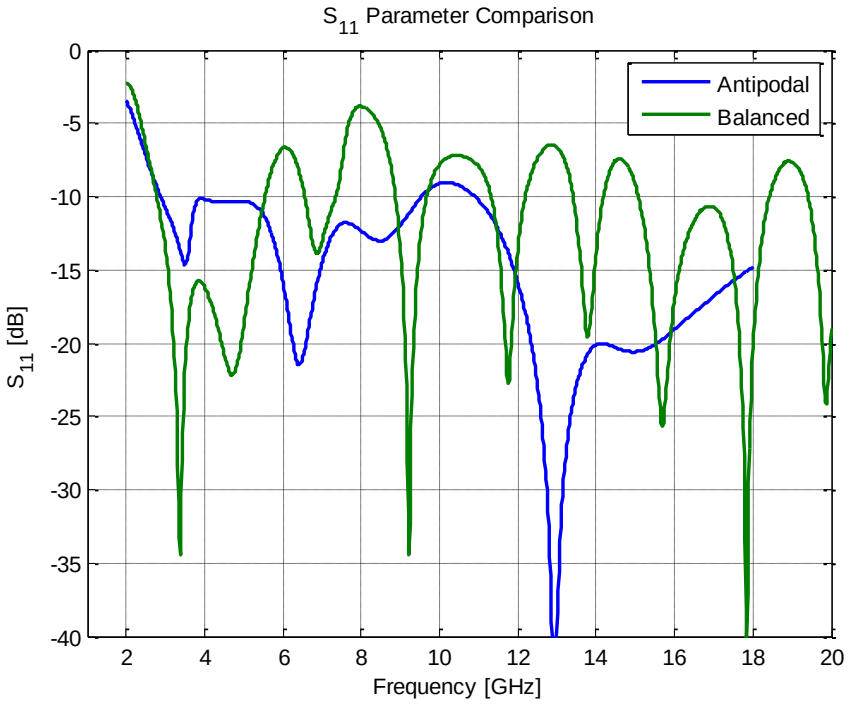

Figure 56 – S_{11} parameter of antipodal vs. balanced CVD

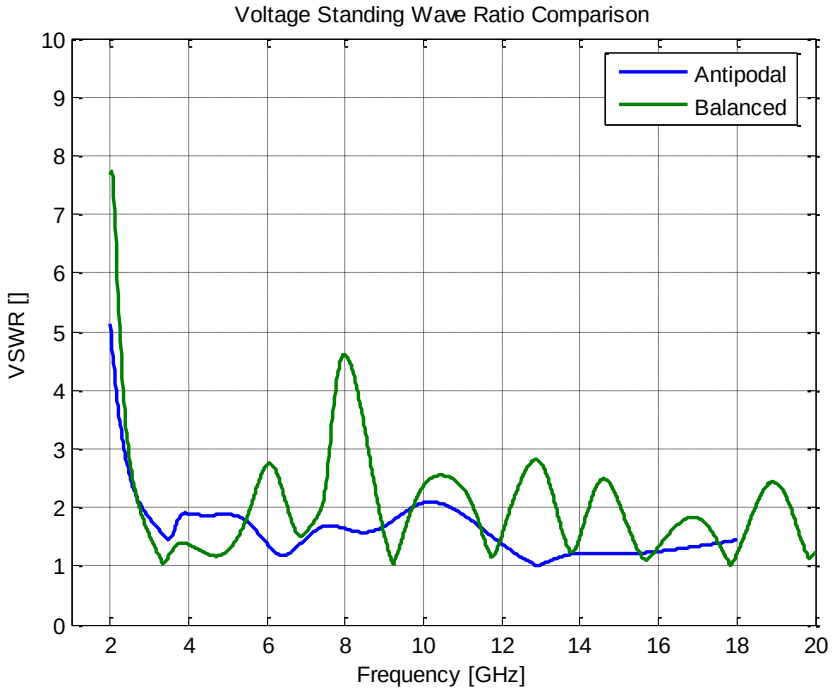

Figure 57 – VSWR of antipodal vs. balanced CVD

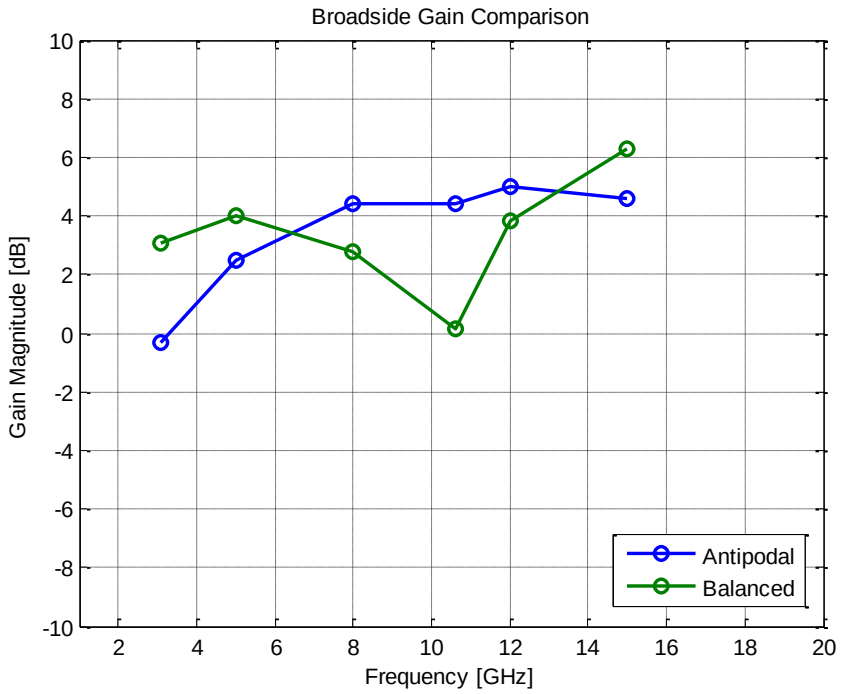

Figure 58 – Broadside gain of antipodal vs. balanced CVD

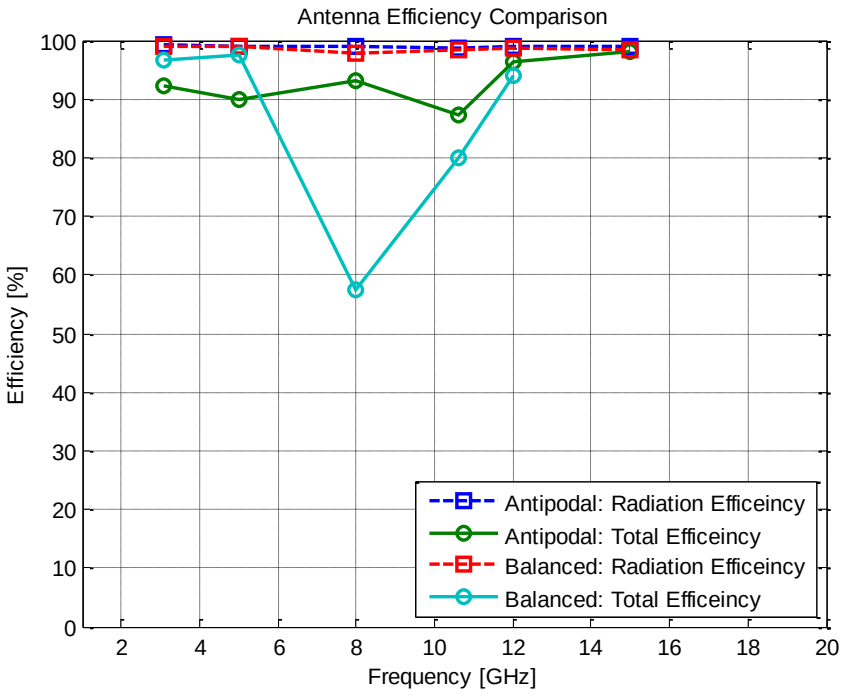

Figure 59 – Efficiency of antipodal vs. balanced CVD

In the process of simulating a variety of antenna designs in an array of scaled sizes, several behaviors were observed, some unique to a specific style of antenna and others fairly consistent amongst all of the UWB antenna designs. Possibly the most important behavior is the surface current resonances. There were two ways in which the surface currents displayed resonant behavior, on the structural edges of the antenna and broadly through the full area of the planar radiating arms. First, the surface current concentrations on the edges are fairly easy to observe and understand, as seen in Figure 60 - Figure 61.

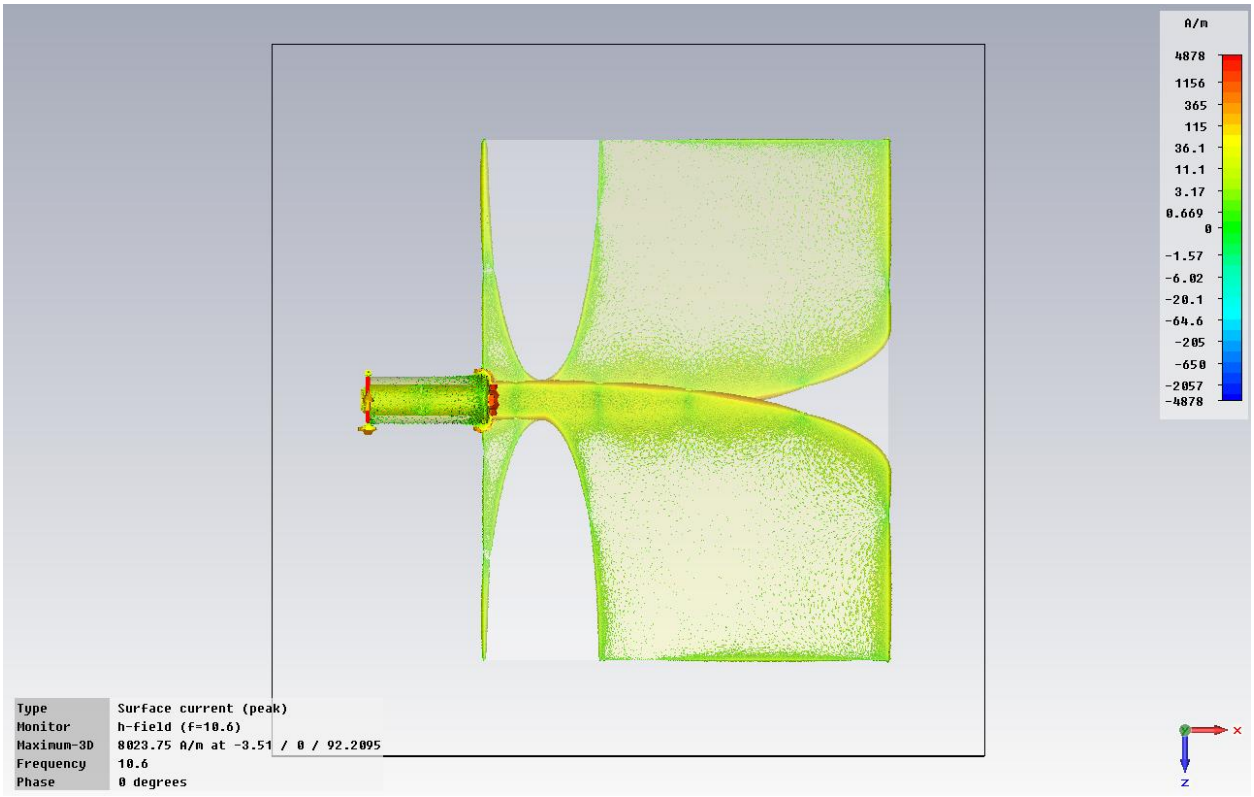

Figure 60 – Surface current (10.6 GHz) of antipodal CVD antenna from Yang et al [1] (4.5cm x 4.6cm, 50Ω microstrip feed)

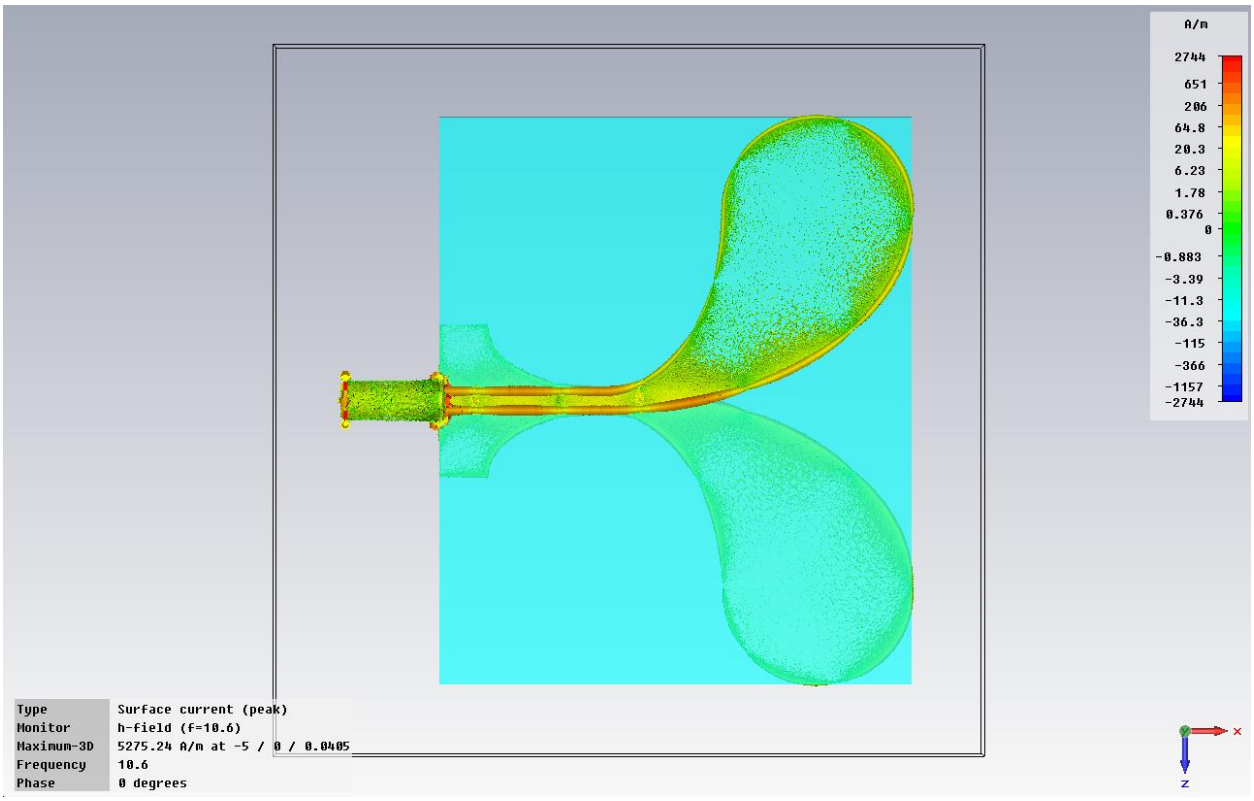

Figure 61 – Surface current (10.6 GHz) of antipodal elliptically-tipped Vivaldi dipole antenna (5cm x 4cm, 50Ω microstrip feed)

The second type of surface current periodicity observed appears as a full planar wave across the broad surface of the radiating strips. It is most easily viewed in the lines of the nodes it creates which emerge generally orthogonal to the greatest geometry dimension from the feed out into the radiating arm. The behavior of this surface current resonance is shown in Figure 61.

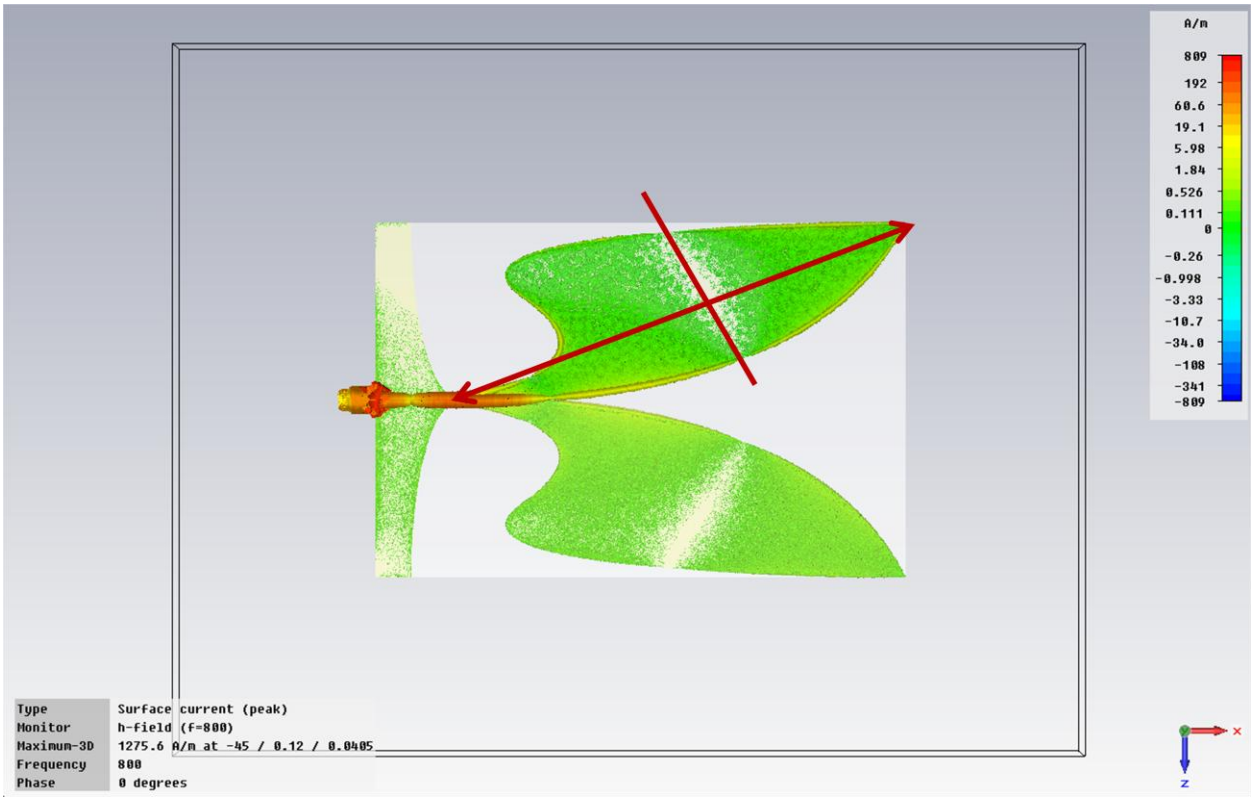

Figure 62 – Surface current (800 MHz) of antipodal flared Vivaldi dipole antenna (45cm x 30cm, 50Ω microstrip feed)

As evident from the difference between Figure 60 and Figure 61, the edge currents will wrap around the curvature of the radiating arms, but discontinuities in the shaping of the antenna geometry artificially disrupt this behavior. The discontinuities force resonance at specific frequencies relative to the length of the edge they create. These resonances cause high gain at the specific frequency relative to the rest of the bandwidth. The flared Vivaldi, as shown in Figure 62, has only one point of discontinuity placed at the farthest possible point in the antenna structure from the feed source.

The resonances disperse as the length of the edges and major dimensions fall below $\lambda / 2$, as the edges behave similar to a wire monopole antenna. The objective in shaping the antenna is

then to keep edges short enough to avoid resonance regions in the UWB, but still maintain high levels of radiation across the bandwidth. Ideally this would result in high, but uniform gain across the UWB. The overall length of the major dimension of each radiating shape should also be reduced as much as possible to trade the resonant radiation behavior for uniform radiation. Figure 63 - Figure 65 show the constructed antennas displaying limited resonant behavior with highly distributed surface currents.

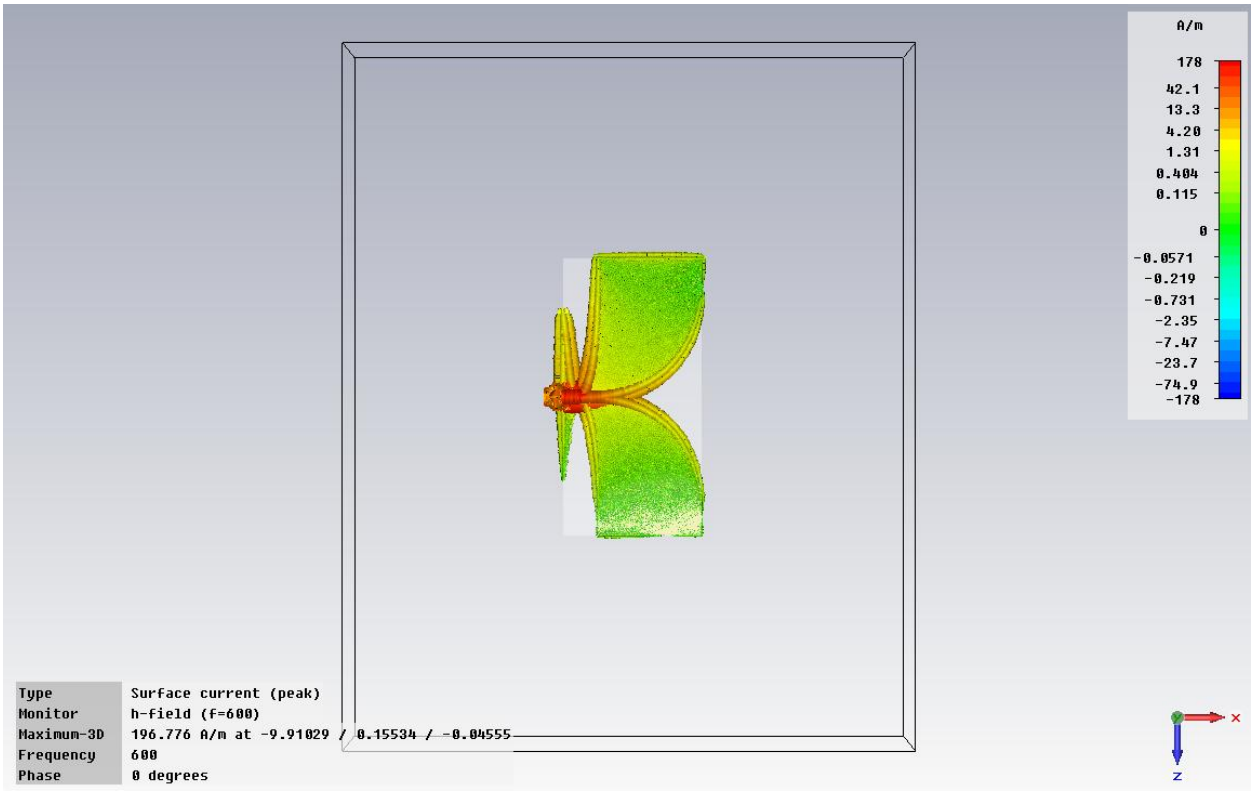

Figure 63 – Surface current (600 MHz) for antipodal CVD (10cm x 20cm, 100Ω microstrip feed)

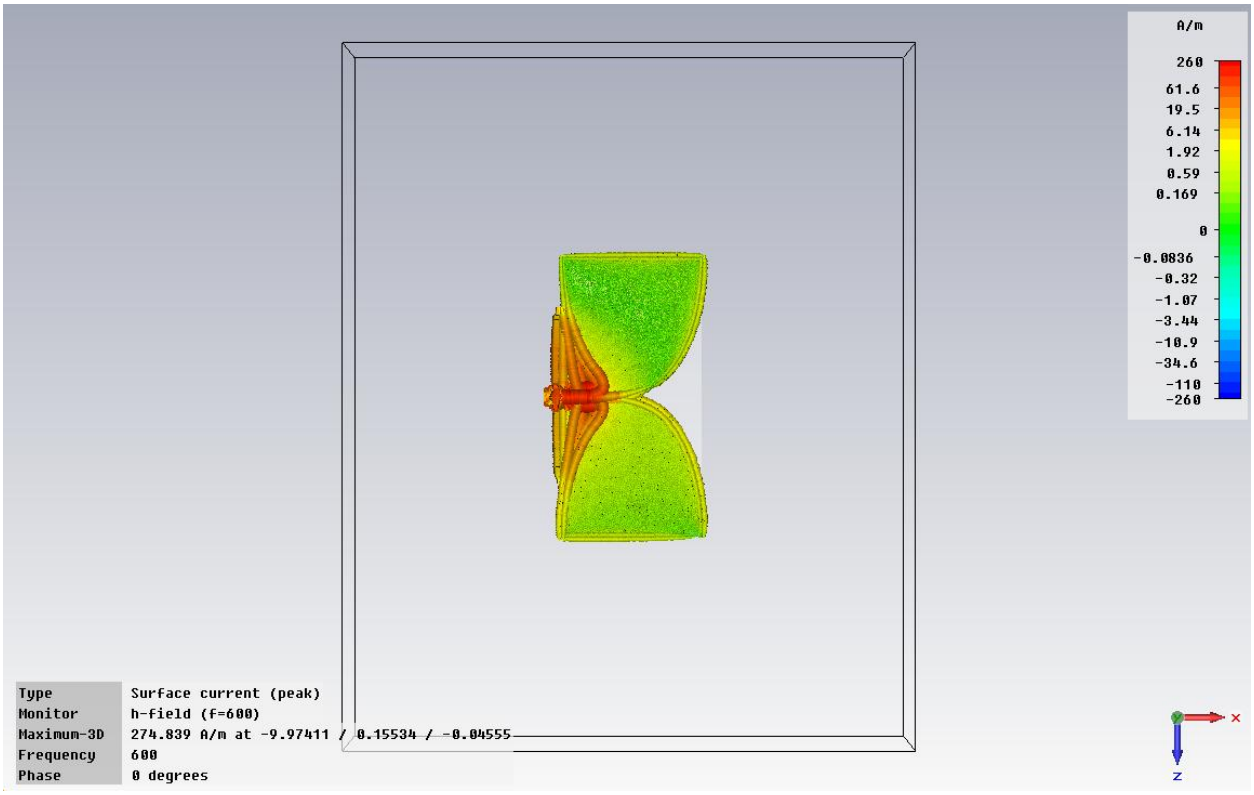

Figure 64 – Surface current (600 MHz) for antipodal CBEVD (10cm x 20cm, 100Ω microstrip feed)

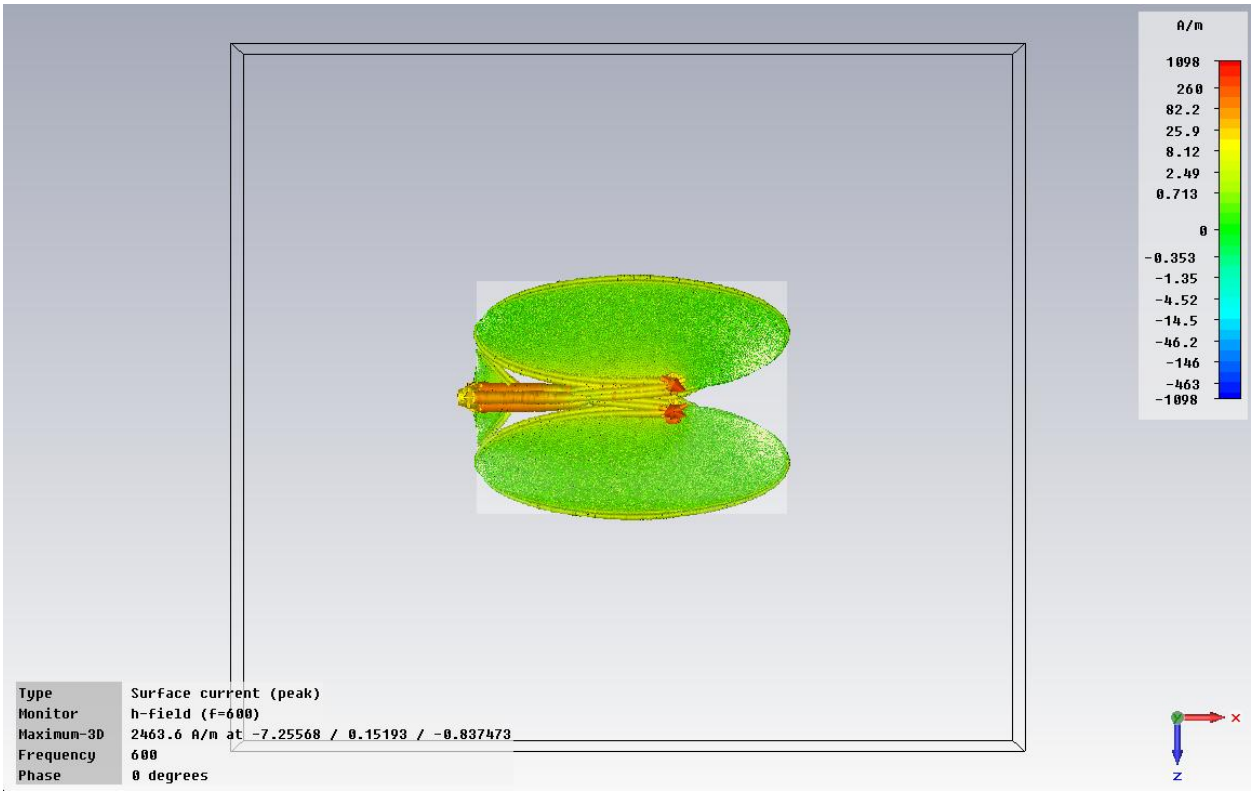

Figure 65 – Surface current (600 MHz) of antipodal BEVD antenna (20cm x 15cm, 100Ω microstrip feed)

The next important behavior observation of the UWB antennas concerns what happens when the antenna size is scaled too small for it to radiate effectively at the lower frequencies of the bandwidth. The result appears to be that the surface currents have difficulty emerging from the feed section due to the small size of the radiating geometry. Therefore, the feed section alone is illuminated and ends up operating as a very poor monopole without a ground plane. This behavior is shown for two 10 cm^2 antennas and the original Log-Periodic antenna at 300 MHz in Figure 66 - Figure 68.

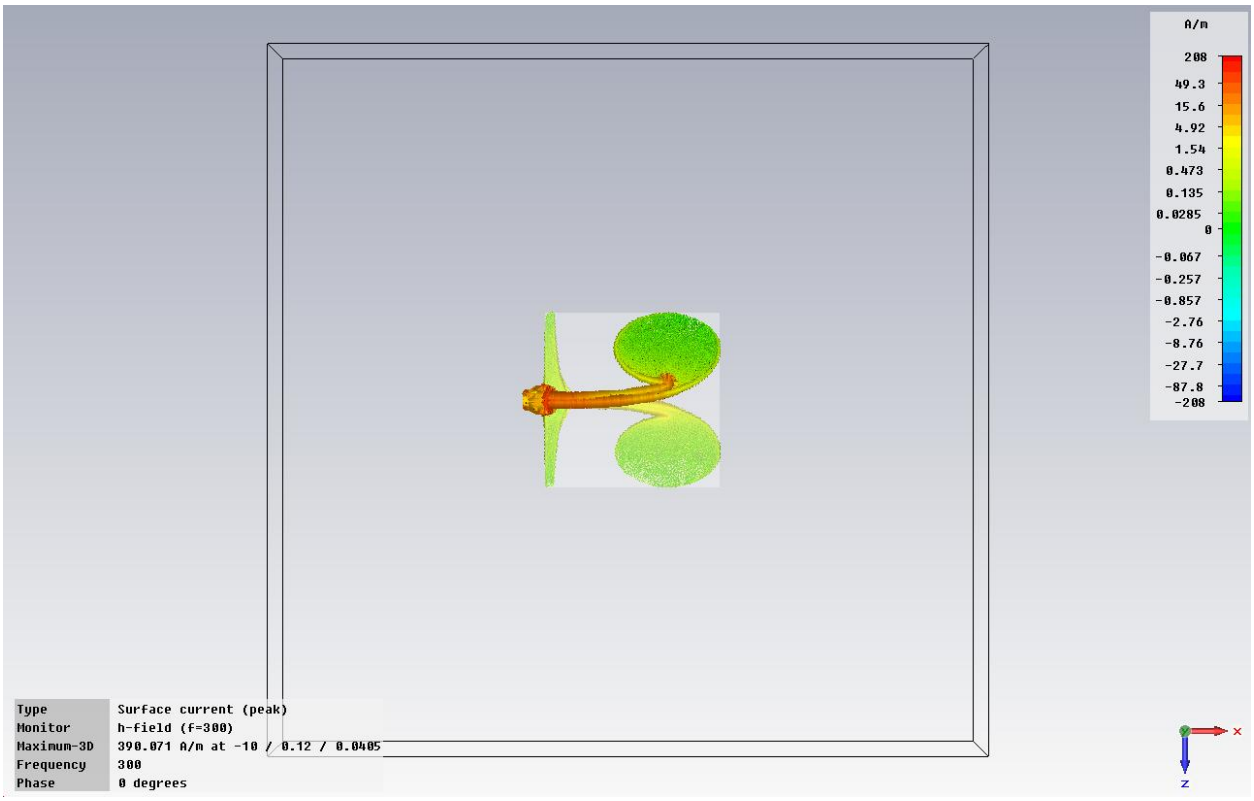

Figure 66 – Surface current (300 MHz) of antipodal BEVD antenna (10cm x 10cm, 50Ω microstrip feed) operating with total efficiency of 0.534%

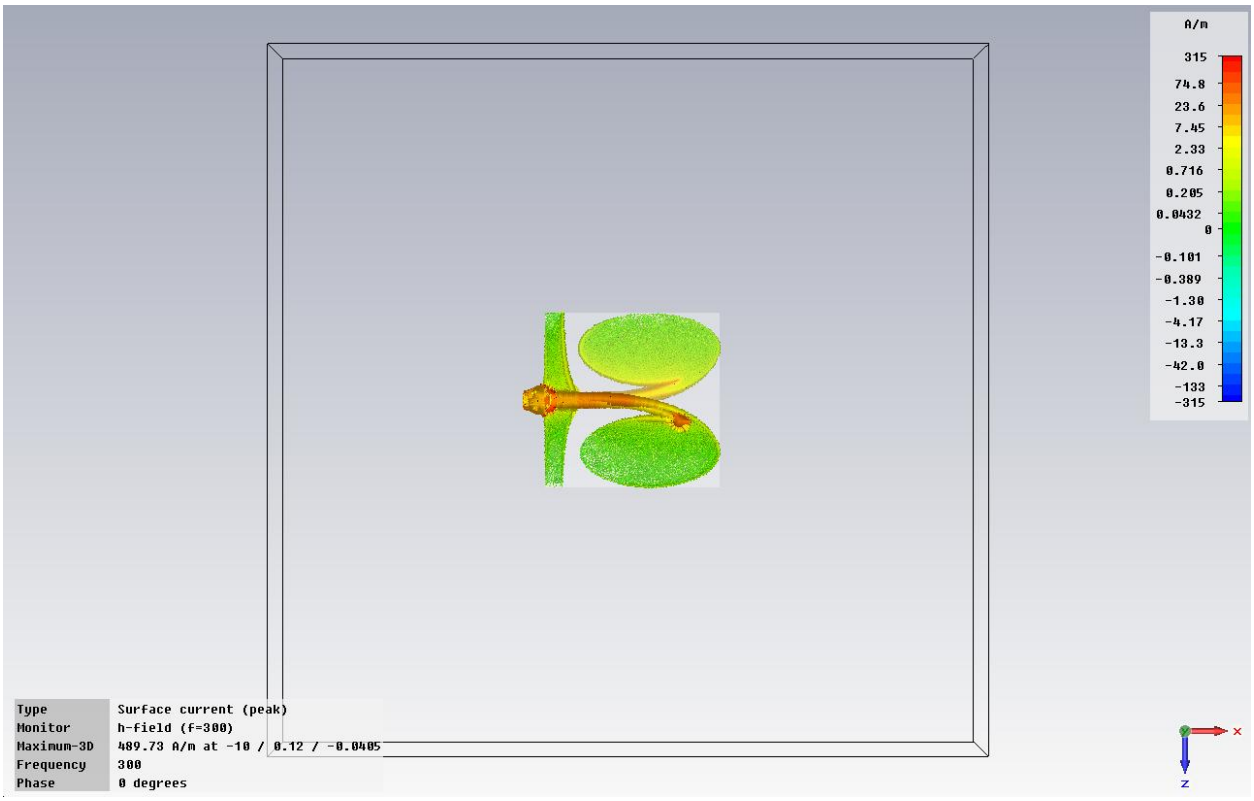

Figure 67 – Surface current (300 MHz) of antipodal ellipse Vivaldi dipole antenna (10cm x 10cm, 50Ω microstrip feed) operating at total efficiency of 0.782%

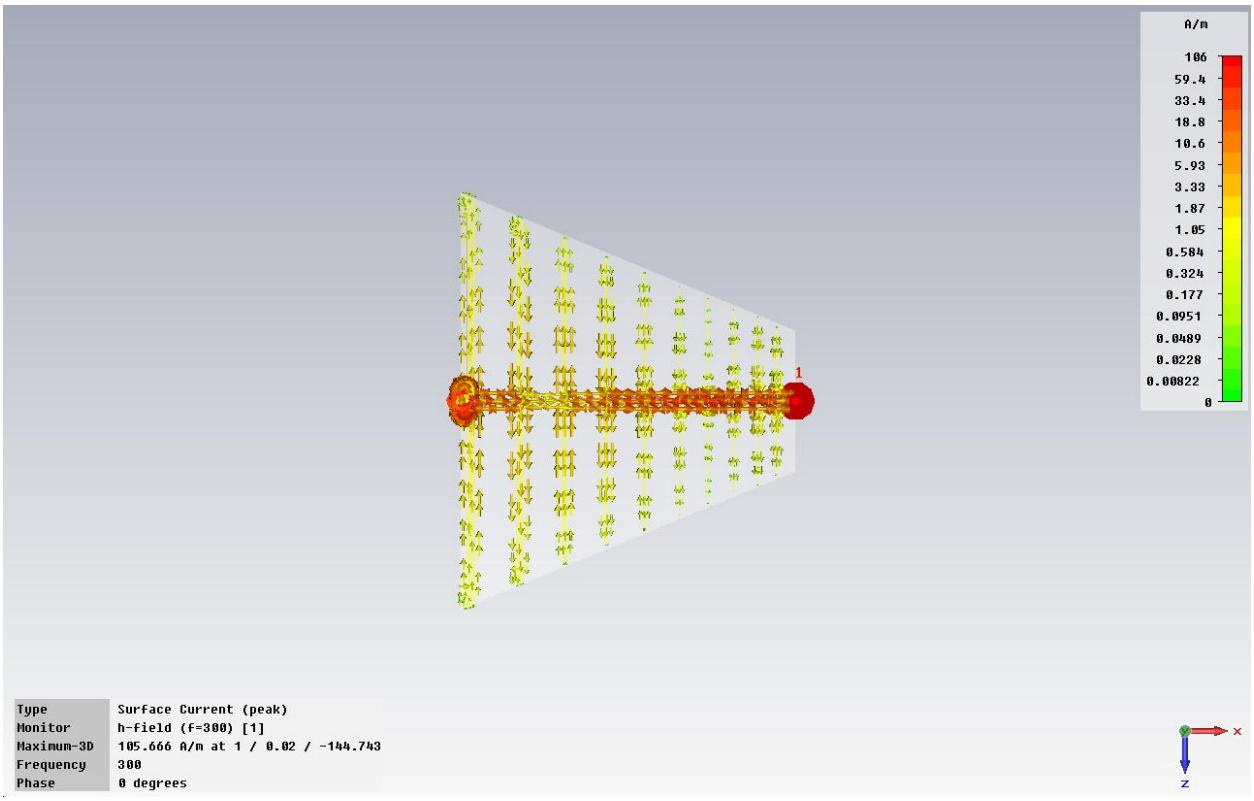

Figure 68 – Log-periodic antenna (23cm x 29cm, 50Ω microstrip feed) operating at total efficiency of 1.101%

The final observation was discovered on accident. When an improperly constructed coaxial feed line was fully simulated through CST and yielded a lower VSWR and higher surface currents, the matching to a 50Ω came into question. The actual impedance of the coaxial feed was about 35Ω due to an improperly selected dielectric material. When this resulted in lower reflections back to the source port, it was evident that there was a major issue present at the matching of the coaxial cable to the microstrip feed of the antenna.

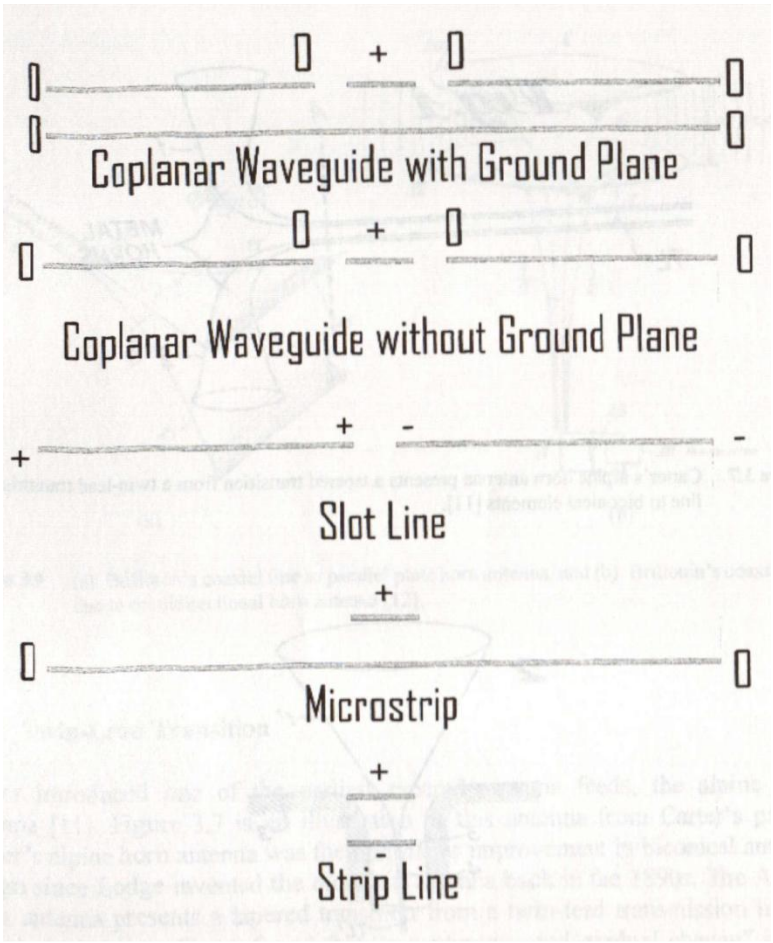

Figure 69 – Variety of PCB transmission lines [26]

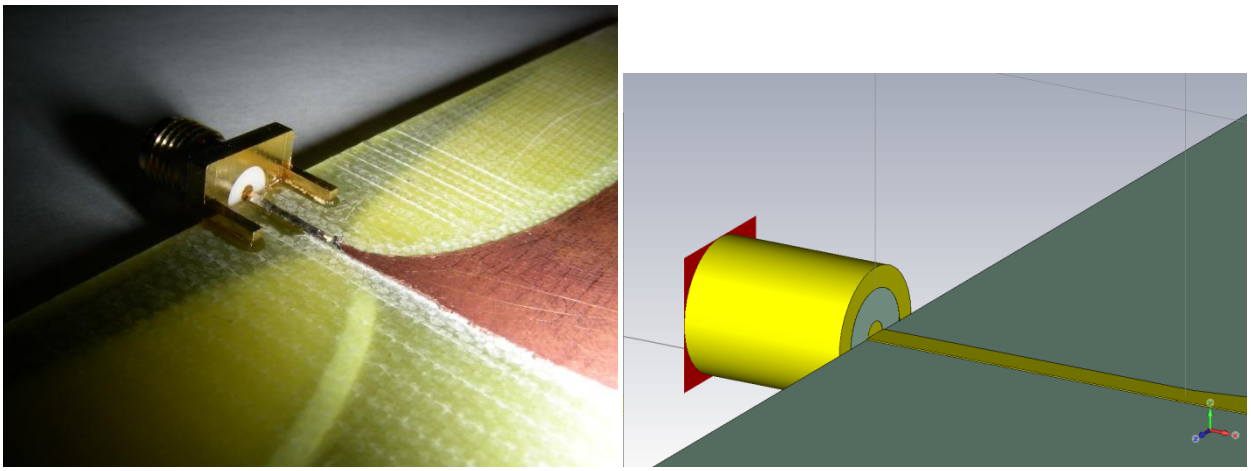

Figure 70 – Antenna matching to coaxial cable through SMA connection

The coaxial cable is rated to 50Ω with high fidelity. And the microstrip feed of the antenna is calculated to be 50Ω according to its dimensions. Therefore, the problem must lie in the connection of the two. The fields in a coaxial cable travel along the cable within the dielectric material, while the fields in a microstrip feed are linear between the signal strip and the ground plane. Figure 70, shows how about half of the coaxial waveguide does not match to the antenna. This is thought to be the cause of the mismatch. Because the microstrip only matches to half of the coaxial waveguide, the impedance of the microstrip should be higher in order to compensate, similar to the way in which microstrip feeds break a single strip into multiple element feeds of a microstrip antenna array [3]. Figure 71 shows the geometry of a microstrip antenna array feed.

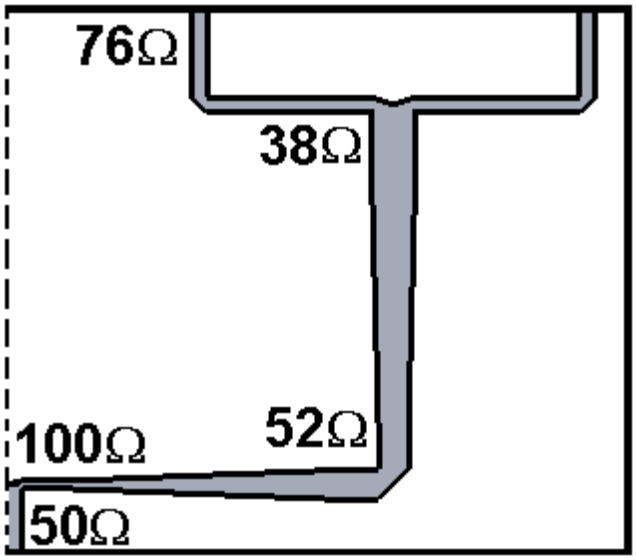

Figure 71 – Microstrip array feed network [48]

When adjusting the impedance of the antenna's microstrip feed, the simulation results can show how well the match was improved. The Ellipse Vivaldi Dipole was simulated at three different microstrip impedance values and a 100Ω match performed the best, as shown in Figure 73.

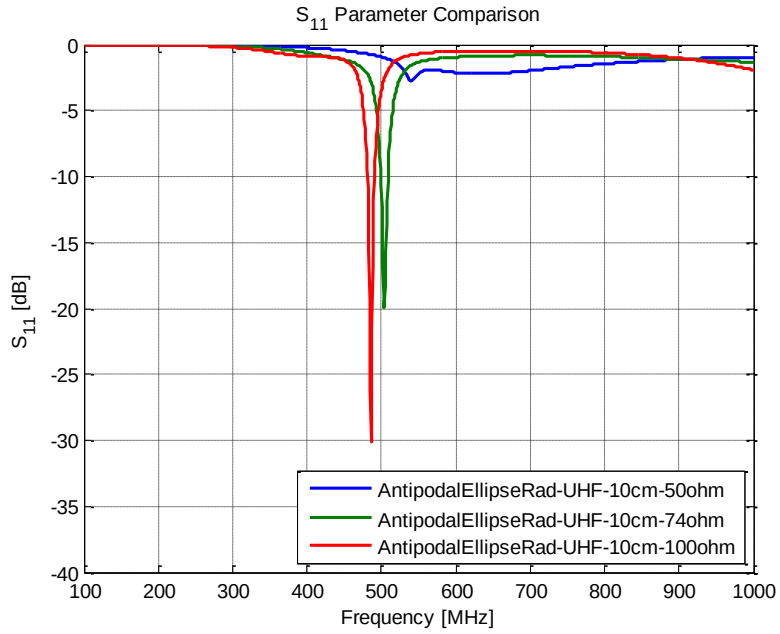

Figure 72 – Reflection coefficient magnitudes of antipodal ellipse Vivaldi dipole antenna measuring (10cm x 10cm) for 50Ω, 74Ω, and 100Ω microstrip feeds

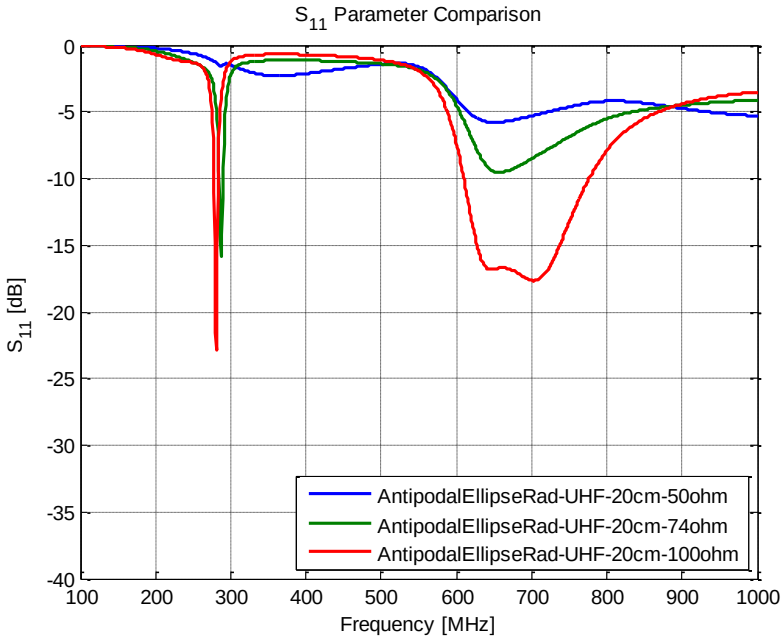

Figure 73 – Reflection coefficient magnitudes of antipodal ellipse Vivaldi dipole antenna measuring (20cm x 20cm) for 50Ω, 74Ω, and 100Ω microstrip feeds

The change in the microstrip feed impedance may slightly change the location of the resonance regions of the antenna, but the new lower reflection coefficient allows for significantly improved designs through refined shaping.

Finally, after applying these lessons learned from extensive design and simulation to the antenna designs, the best designs small in size and have low reflection coefficients. The final designs may be less directive than the LPA, but they are smaller and maintain as good or better efficiency. The phase centers of the three antennas are also very stable. See the Appendix for radiation pattern, surface current, and phase center plots. Figure 74 - Figure 79 detail the constructed antennas' performance.

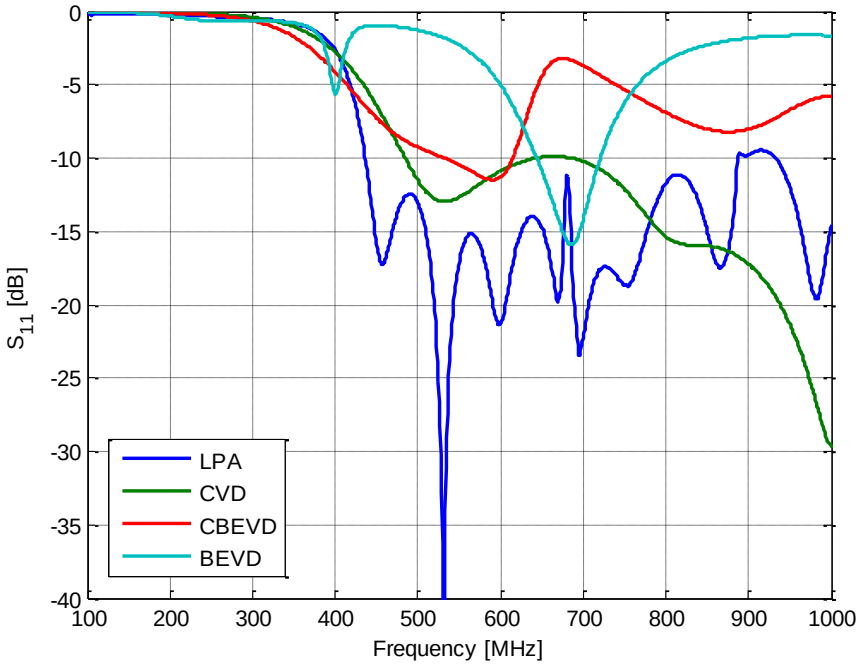

Figure 74 – S_{11} parameters of constructed antennas

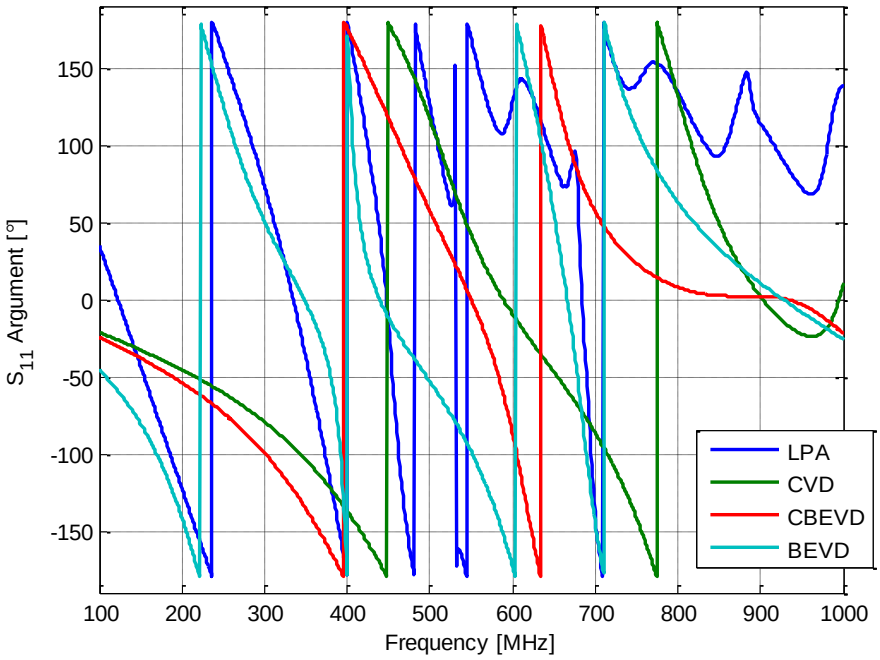

Figure 75 – S_{11} phase of constructed antennas

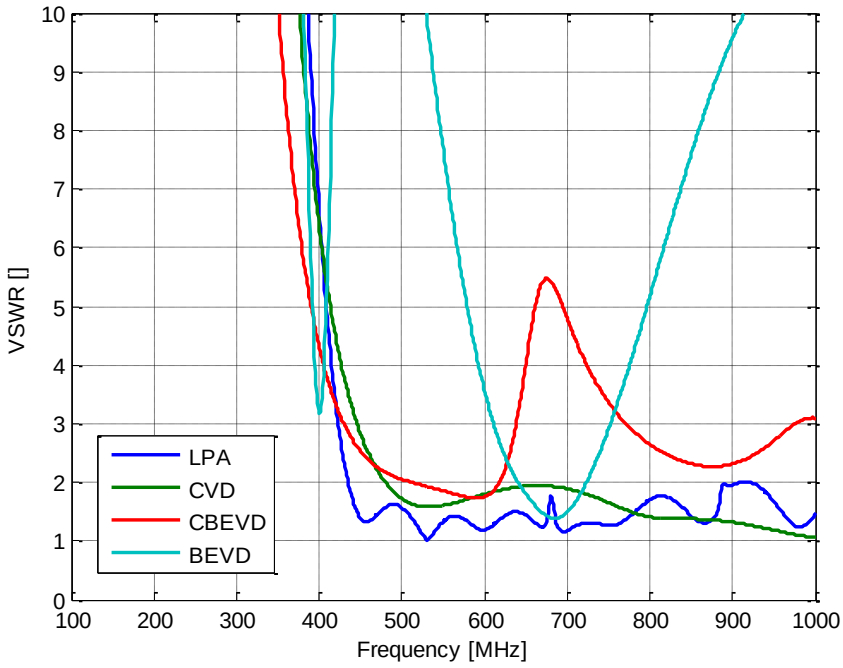

Figure 76 – VSWR of constructed antennas

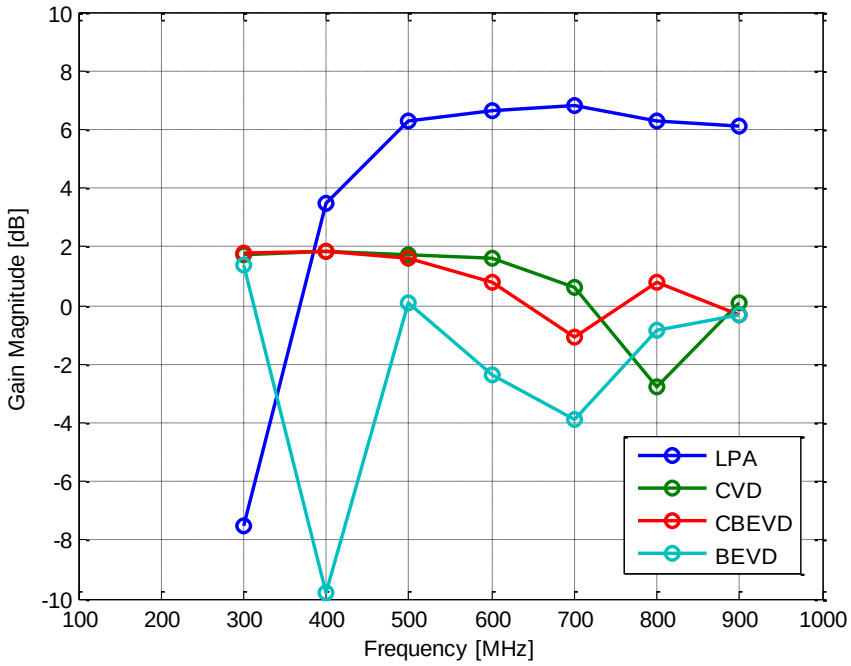

Figure 77 – Gain of constructed antennas

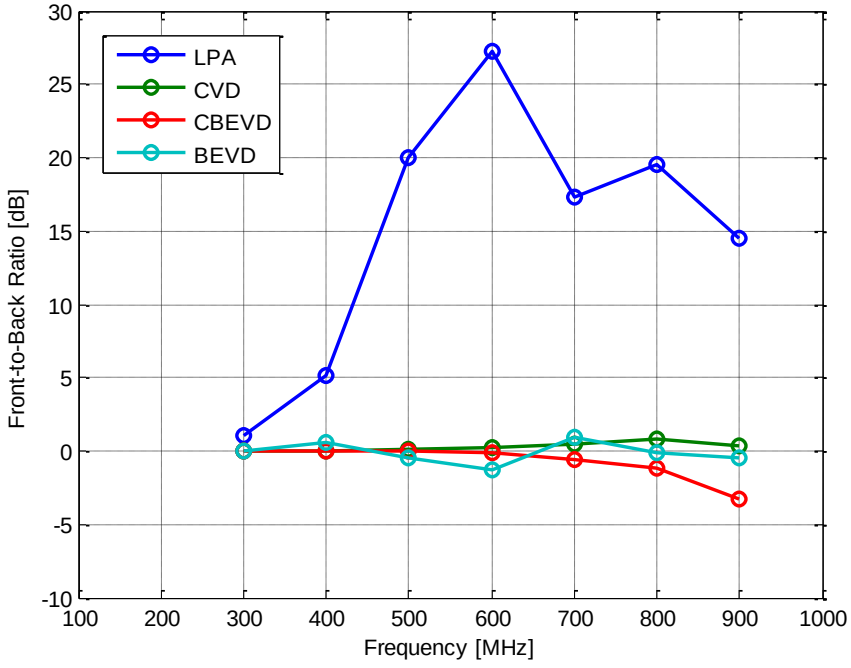

Figure 78 – Front-to-back ratio of constructed antennas

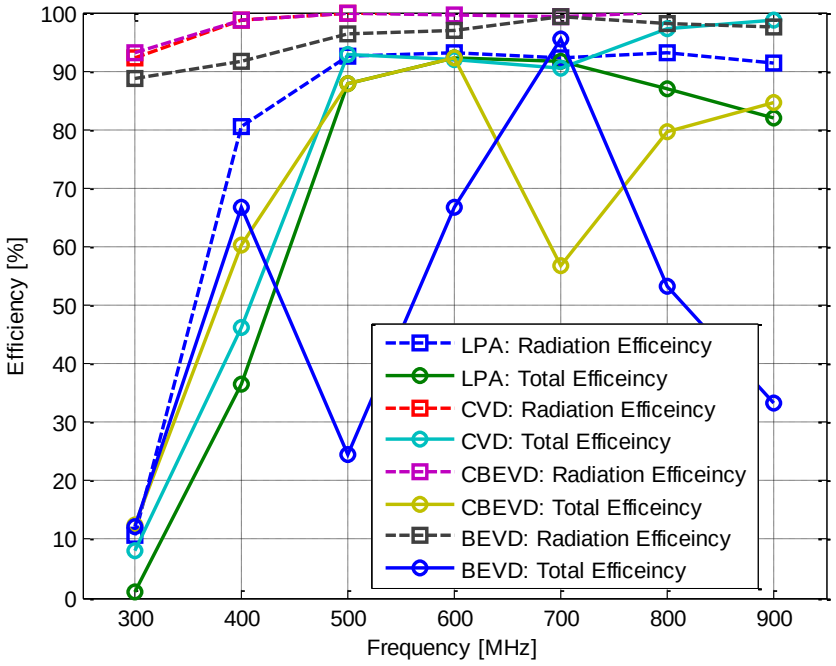

Figure 79 – Efficiency of constructed antennas

In addition to typical antenna performance metrics, the designer should also monitor the stability of the antenna phase center across the bandwidth as a measure of the additional dispersion added to the waveform by antenna. CST uses the phase variation of the radiated E-fields within a defined angular region of the broadside direction to compute the antenna phase center. By using the relative phases of the farfield radiated electric fields for a particular frequency solution, the software can statistically extrapolate the location of the phase center as well as the uncertainty of that location. Figure 80 - Figure 83 graphically display the simulated phase center movements for each of the constructed antennas relative to the antenna's physical profile as well as the corresponding uncertainty with respect to frequency. The most concerning movement of the phase center is in the broadside direction as it directly results in radar measurement inaccuracies in front of the system.

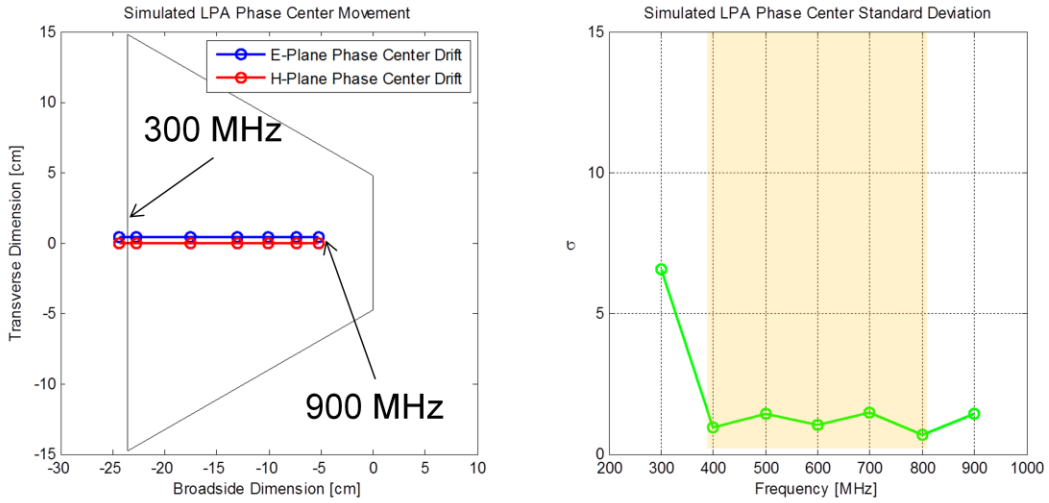

Figure 80 – Simulated phase center movement relative to antenna profile and corresponding uncertainty vs. frequency for LPA

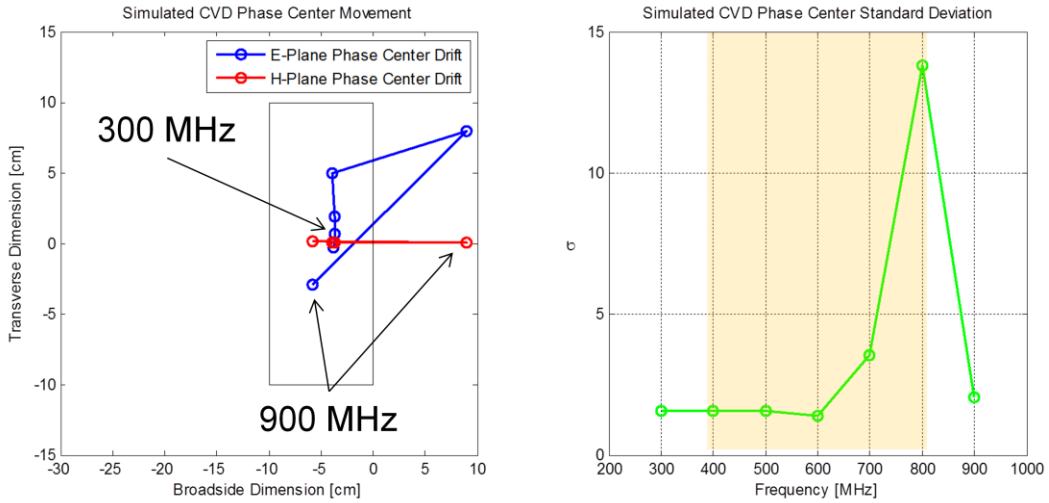

Figure 81 – Simulated phase center movement relative to antenna profile and corresponding uncertainty vs. frequency for CVD

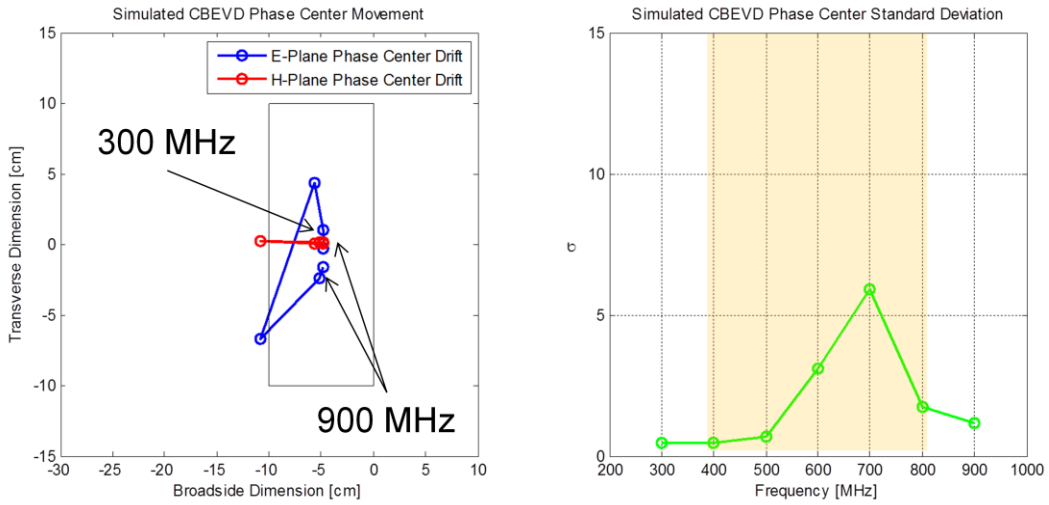

Figure 82 – Simulated phase center movement relative to antenna profile and corresponding uncertainty vs. frequency for CBEVD

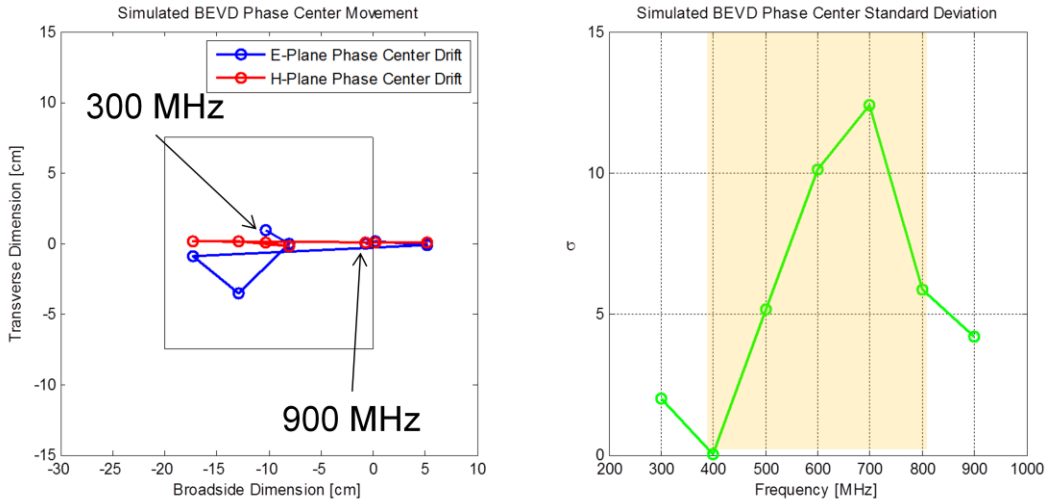

Figure 83 – Simulated phase center movement relative to antenna profile and corresponding uncertainty vs. frequency for BEVD

The LPA, shown in Figure 80, has phase center drift purely in the broadside direction and moves 12.58 cm from 400 MHz to 700 MHz, which is half of a range cell in the current radar setup. Of the Vivaldi antennas, the BEVD, in Figure 83, definitely performed the worst with

22.49 cm of movement, especially if considered in conjunction with the high uncertainties in its phase center location measurements. Shown in Figure 82, the CBEVD performs fairly well with only 6.06 cm of drift in the broadside direction. The best performing simulated antenna is the CVD, as in Figure 81, with only 0.26 cm of phase center drift from 400 MHz to 700 MHz.

4.3 Constructed Antennas

The three antenna designs built are the Antipodal Chopped Vivaldi Dipole, the Antipodal Chopped Bunny-Ears Vivaldi Dipole, and the full Antipodal Bunny-Ears Vivaldi Dipole. Two versions of the Chopped Vivaldi Dipole were built using each manufacturing method. Version A was built using the milling machine, while Version B was built using the PCB etchant.

Figure 84 – Milling machine constructed CVD antenna

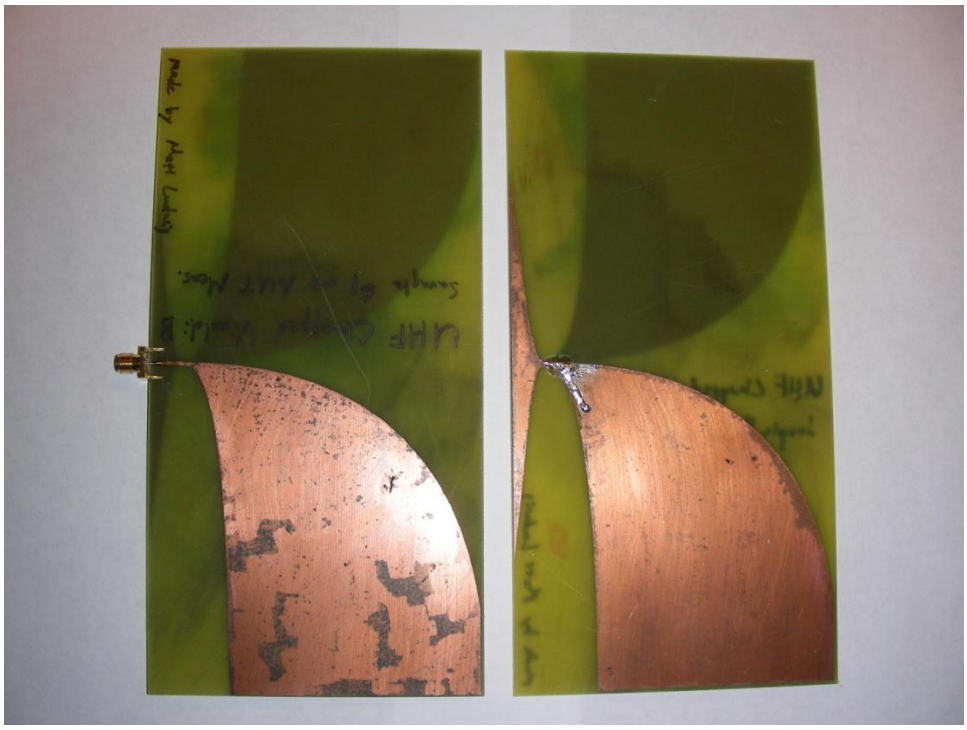

Figure 85 – Etching constructed CVD antenna

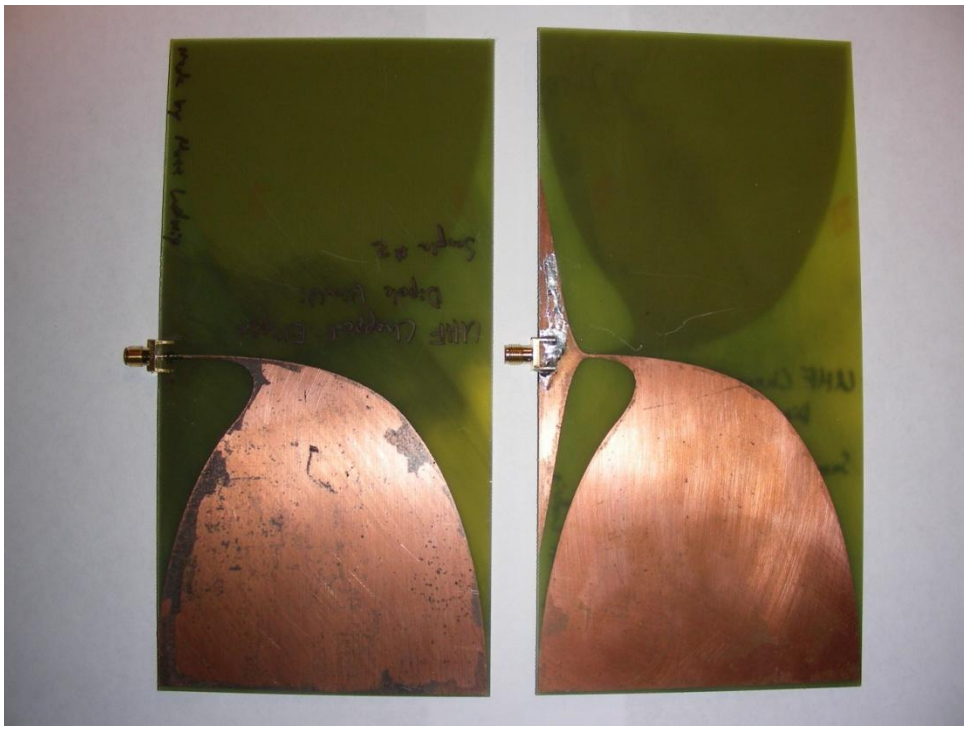

Figure 86 – Etching constructed CBEVD antenna

Figure 87 – Etching constructed full BEVD antenna

The remaining ink was removed from the surface of the etched antennas using acetone cleaner. This allowed the gaps in the copper conductor to be easily observed with the naked eye. Finally, the antennas were chopped down to size by removing the excess substrate material and SMA connectors were mounted at the feed ends.

4.4 Measurement Results

Calibrated S_{11} and S_{21}, for all four primary polarization setups, measurements were recorded for each antenna according to the test Matrix in Table 6. Antenna polarization configurations correspond to pattern measurement great circle cuts according to Table 7.

Table 6 – Antenna test matrix for anechoic chamber

Measurement	Antenna Name	Size	Tx Antenna Orientation	Frequencies	Azimuth	Polarization
AM01	Standard UHF Horn Antenna	36"x29"	Vertical	300:800	0°	VV,HV
AM02	Chopped Vivaldi	10x20 cm	Vertical	300:800	0:1:360°	VV,HV
AM03	Bunny Ears Vivaldi (Chopped Ellipse)	20x15cm	Vertical	300:800	0:1:360°	VV,HV
AM04	Bunny Ears Vivaldi (Full Ellipse)	20x15cm	Vertical	300:800	0:1:360°	VV,HV
AM05	Log-Periodic Antenna	23x29cm	Vertical	300:800	0:1:360°	VV,HV
AM06	Standard UHF Horn Antenna	36"x29"	Horizontal	300:800	0°	VH,HH
AM07	Chopped Vivaldi	10x20 cm	Horizontal	300:800	0:1:360°	VH,HH
AM08	Bunny Ears Vivaldi (Chopped Ellipse)	20x15cm	Horizontal	300:800	0:1:360°	VH,HH
AM09	Bunny Ears Vivaldi (Full Ellipse)	20x15cm	Horizontal	300:800	0:1:360°	VH,HH
AM10	Log-Periodic Antenna	23x29cm	Horizontal	300:800	0:1:360°	VH,HH

Table 7 – Antenna polarization conversion

Polarization	Rx Antenna	Tx Antenna	Planar Measurement
HH	Horizontal	Horizontal	E-Plane Co-Polar
HV	Horizontal	Vertical	E-Plane Cross Polar
VV	Vertical	Horizontal	H-Plane Co-Polar
VH	Vertical	Vertical	H-Plane Cross-Polar

After the antenna S_{21} measurements were recorded with the random noise radar, the results needed to be run through the digital correlation operation and then post processed in order to remove significant noise from the measurement results. By filtering the correlation results, the post processing methods could isolate the AUT in range and remove major sources of noise caused by the interactions with the anechoic chamber. The filtering of the correlation receiver result is accomplished by a signal processing window placed over the peak of the cross-

correlation return. In effect, this removes the major effects outside of a small radius surrounding the antenna, determined by the size of the window, as shown by the orange circle surrounding the Antenna test stand in Figure 88 below.

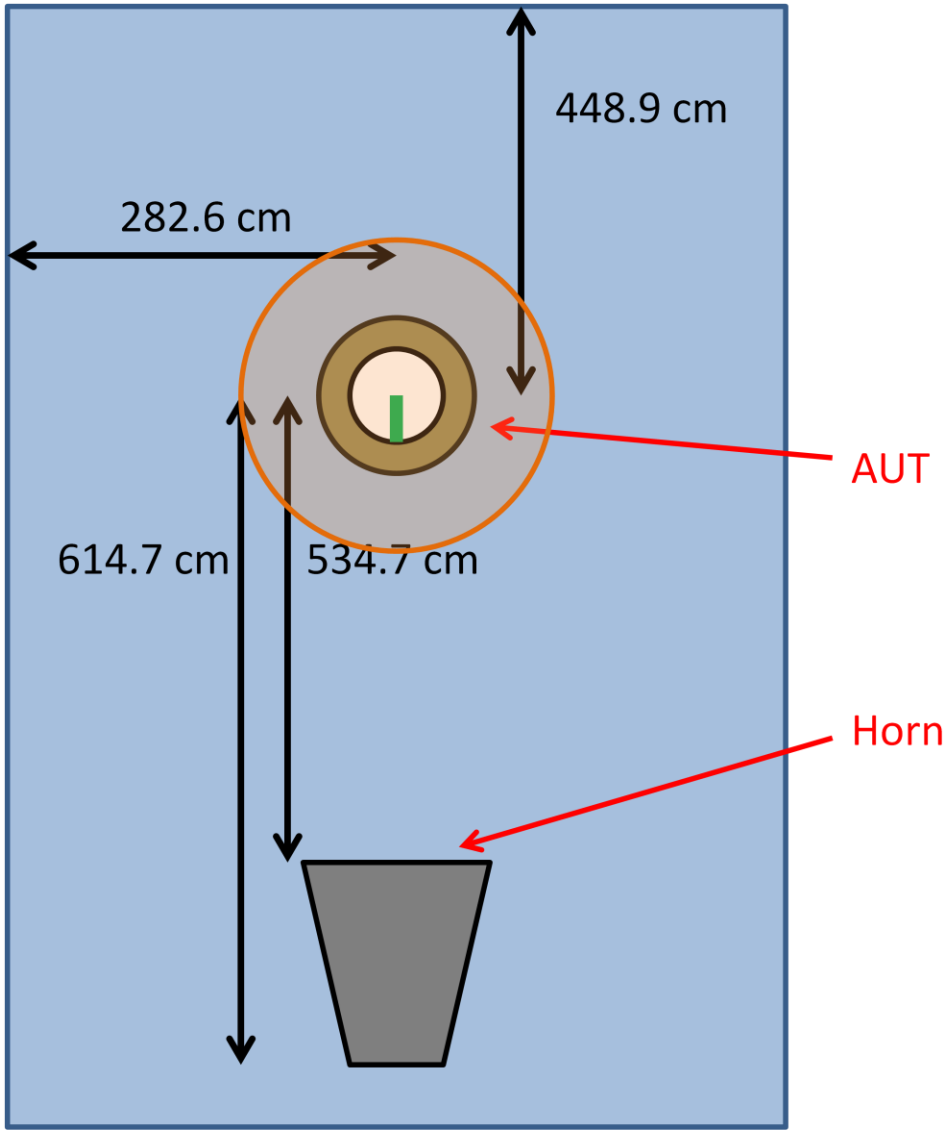

Figure 88 – Anechoic chamber setup for antenna measurements

A Kaiser window of size $n = 300$ range cells was used surrounding the AUT correlation result, which is sufficiently large to account for all effects of the antenna. In choosing the window type and size, a balance had to be struck between the resolution in the frequency domain

and the amount of noise allowed within the measurement. Though the cross correlation operation results in a very narrow peak return for the target, the conversion of this signal into a wideband frequency measurement requires a Fourier transform. As the resolution for the time-domain window used on the correlation result narrows, the frequency domain measurement will become significantly blurred. But when the window is widened, more uncorrelated noise is carried through the Fourier transform operation resulting in cluttered results. After extensive trials of various window types and lengths, the Kaiser window of length $n = 300$ was chosen as the best balance of noise reduction without significant loss of frequency domain resolution.

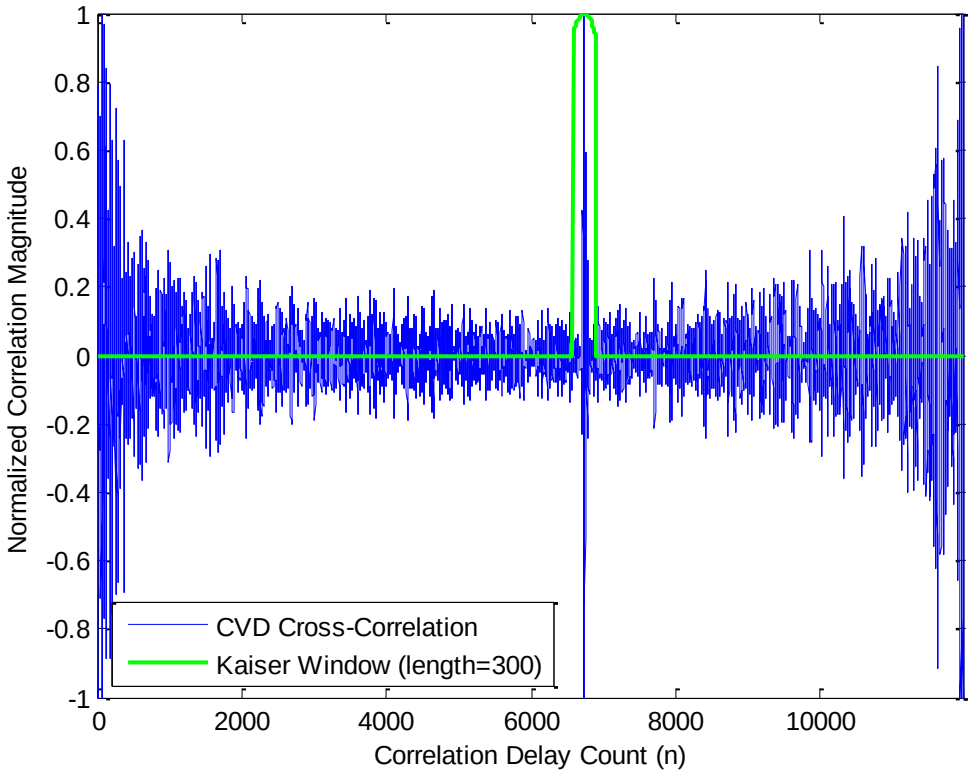

Figure 89 – AUT measurement from correlation receiver and post-processing window (recorded from CVD at broadside incidence and magnitude normalized to central peak)

After choosing the window type and size, the process of calibrating the measured S_{21} results began. Each antenna was measured over a full rotation in azimuth, but the exact gain horn data from AFRL is only available for the broadside direction. The standard gain horn was measured for the broadside antennas link to establish the calibration ratio, $SGH_{exact}(\phi = 0°)/SGH_{meas}(\phi = 0°)$, which is applied to the AUT measurements at all azimuth orientations according to (25). The final outcome of the $S_{21-calibrated}$ calculation results in gain measurements in units of dBi, which is the antenna gain referenced to that of an ideal isotropic radiator.

$$S_{21-calibrated} = AUT_{meas-cal}(\phi) = AUT_{meas}(\phi)\,\frac{SGH_{exact}(\phi = 0°)}{SGH_{meas}(\phi = 0°)} \tag{25}$$

S_{11}, calibrated gain, and front-to-back ratio plots compare the measured results to the CST simulated results for each antenna: LPA (Figure 90 - Figure 93), CVD ver-A (Figure 94 - Figure 97), CVD ver-B (Figure 98 - Figure 101), CBEVD (Figure 102 - Figure 105), and the BEVD (Figure 106 - Figure 109). The errors observed between the measured and simulated antennas were detailed in Figure 114 and Table 8. As shown in Figure 90, the LPA experienced several resonance changes from the simulated to the measured S_{11} parameters, but they were not consistent enough to indicate a BW shift due to the feed or construction. Each antenna had much faster phase changes in the reflection coefficient that predicted, as seen in Figure 91, Figure 95, Figure 99, Figure 103, and Figure 107. The CVD antennas, both versions, seemed to have been affected by the inaccurate feed constructions more than the bunny-ears antennas, as the reflections were according to the S11 measurements in Figure 94 and Figure 98.

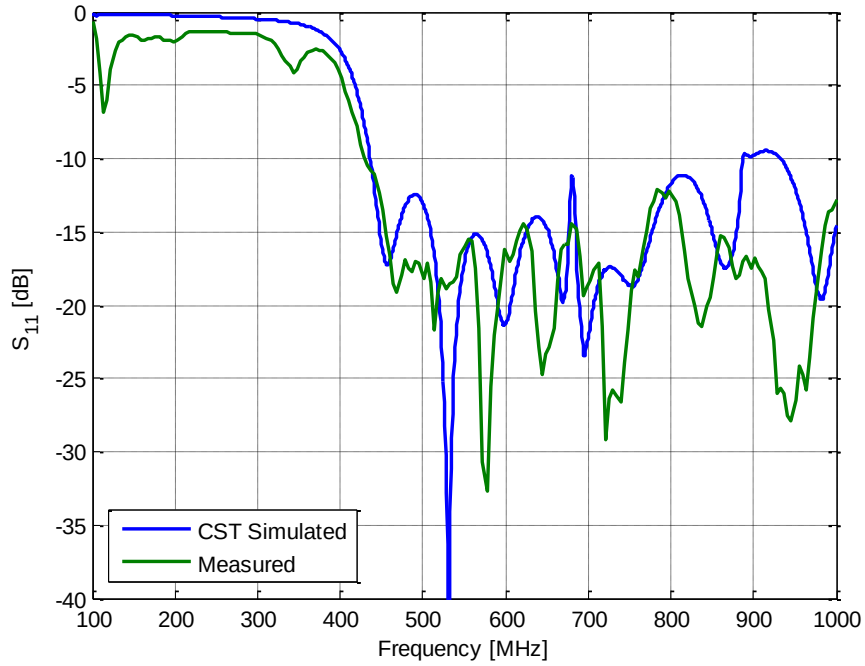

Figure 90 – Measured vs. simulated results for the original LPA: S_{11} magnitude

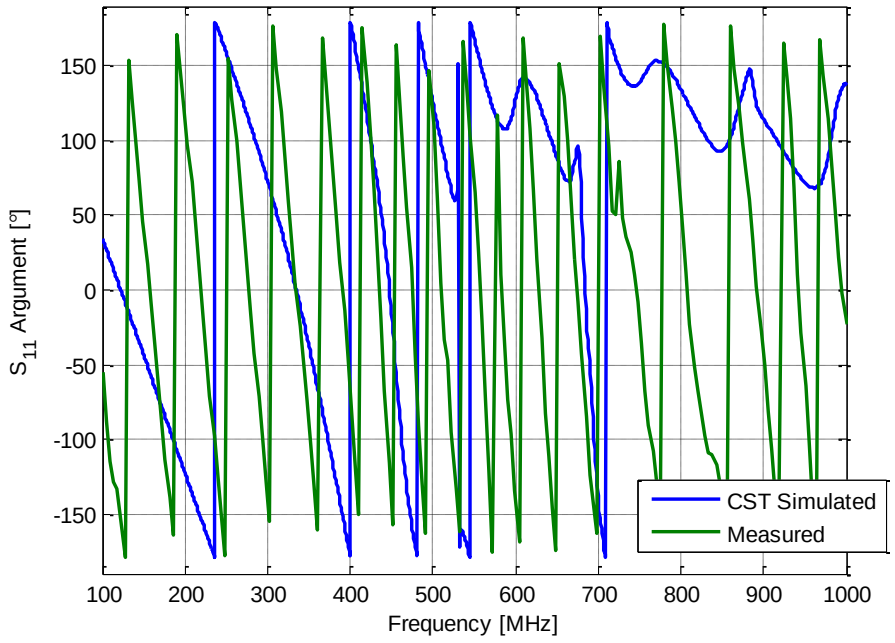

Figure 91 – Measured vs. simulated results for the original LPA: S_{11} phase

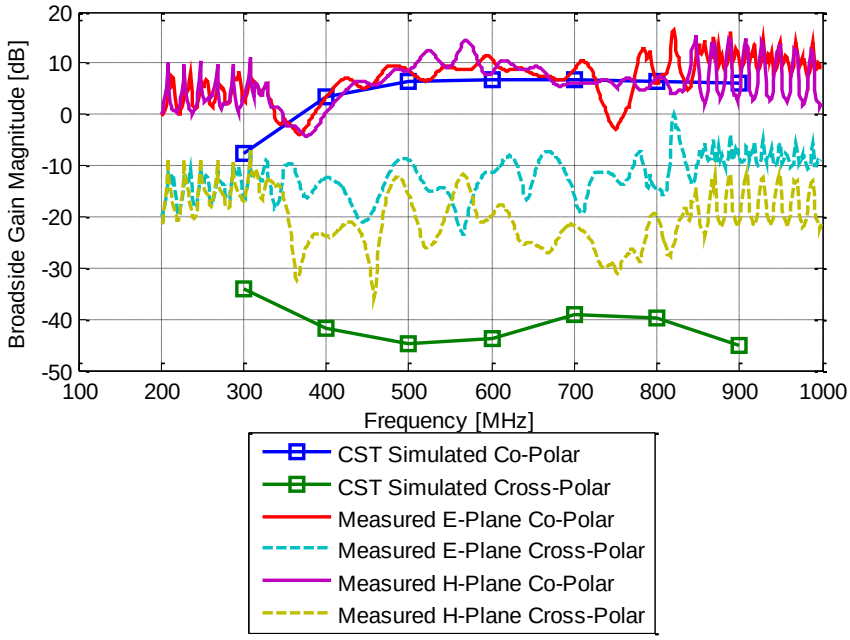

Figure 92 – Measured vs. simulated results for the original LPA: broadside gain

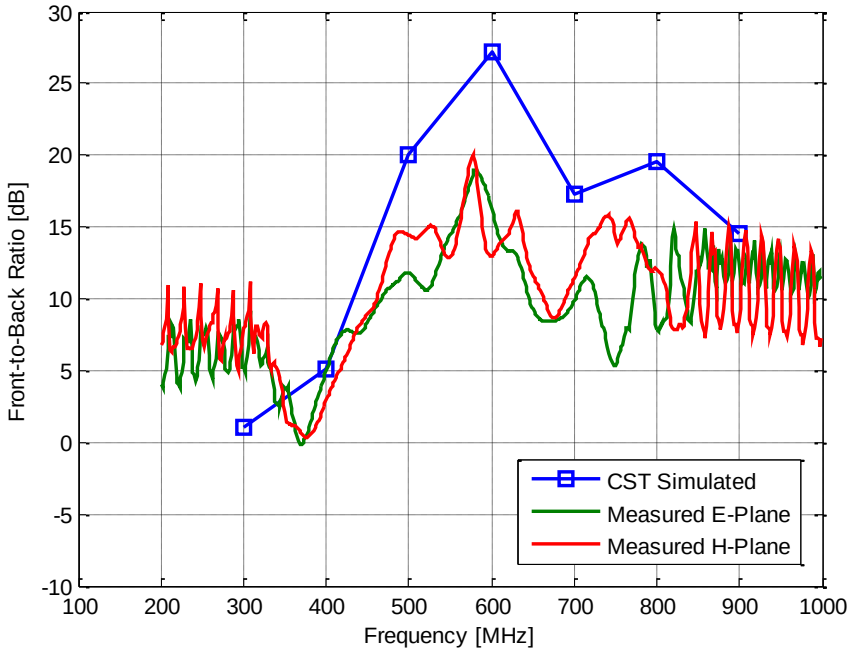

Figure 93 – Measured vs. simulated results for the original LPA: front-to-back ratio

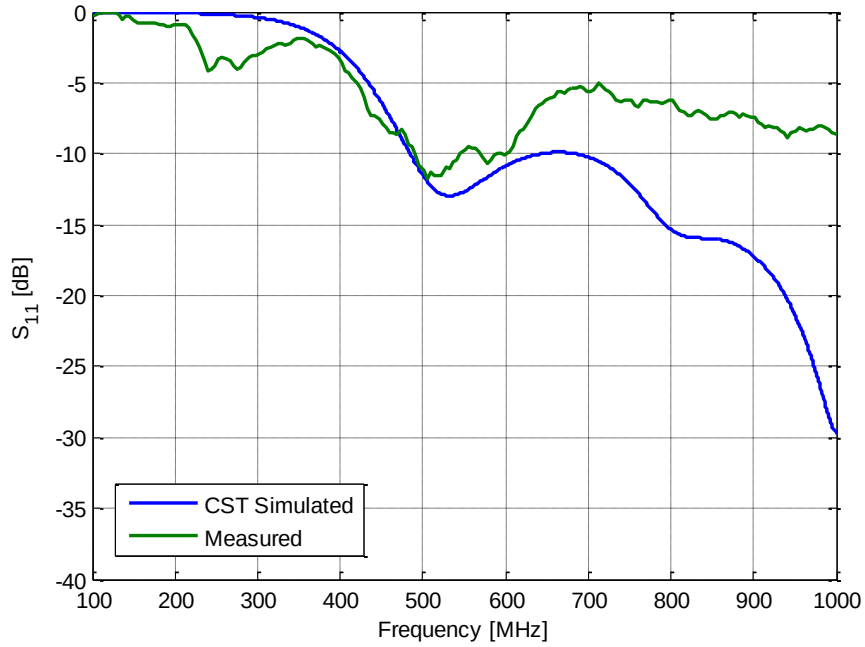

Figure 94 – Measured vs. simulated results for CVD antenna ver-A: S_{11} magnitude

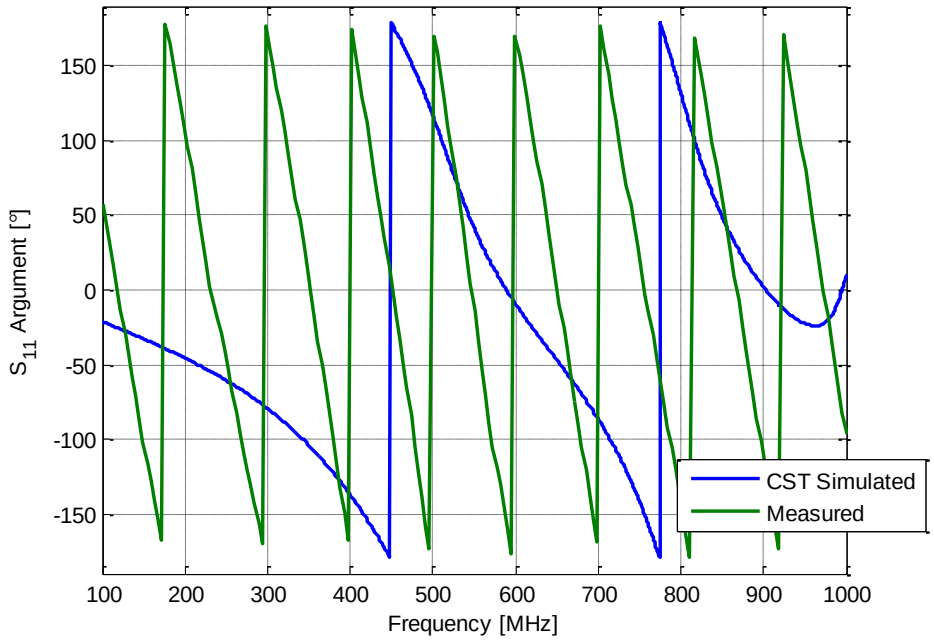

Figure 95 – Measured vs. simulated results for CVD antenna ver-A: S_{11} phase

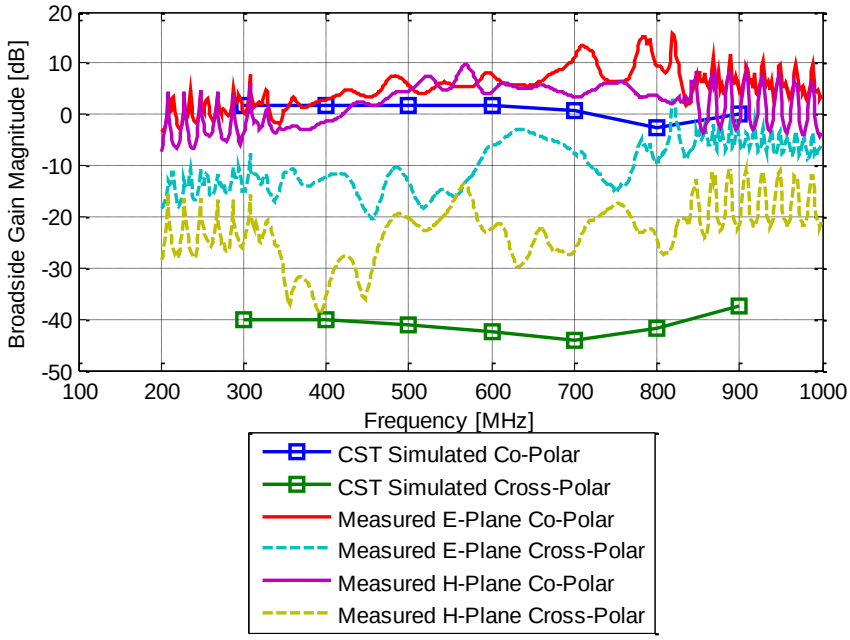

Figure 96 – Measured vs. simulated results for CVD antenna ver-A: broadside gain

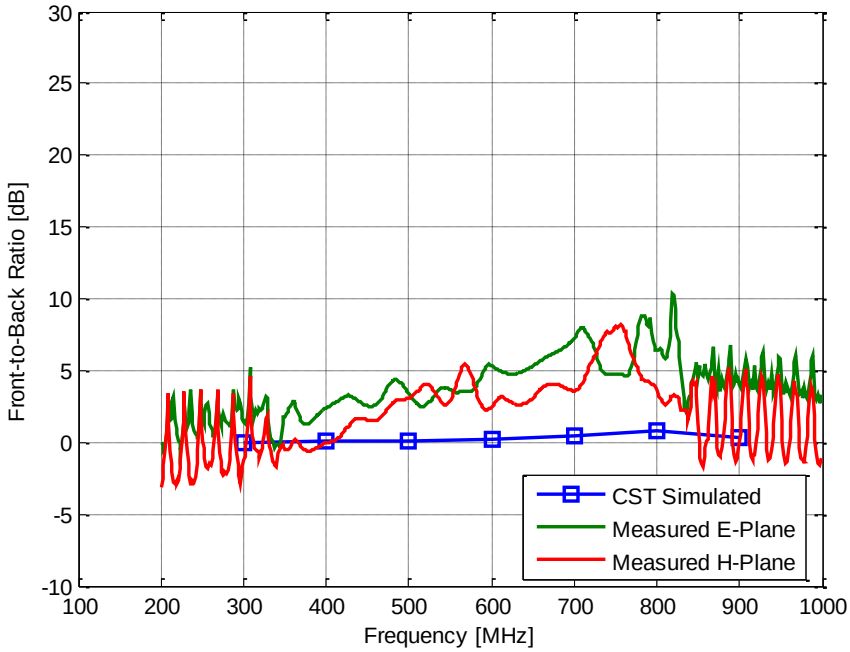

Figure 97 – Measured vs. simulated results for CVD antenna ver-A: front-to-back ratio

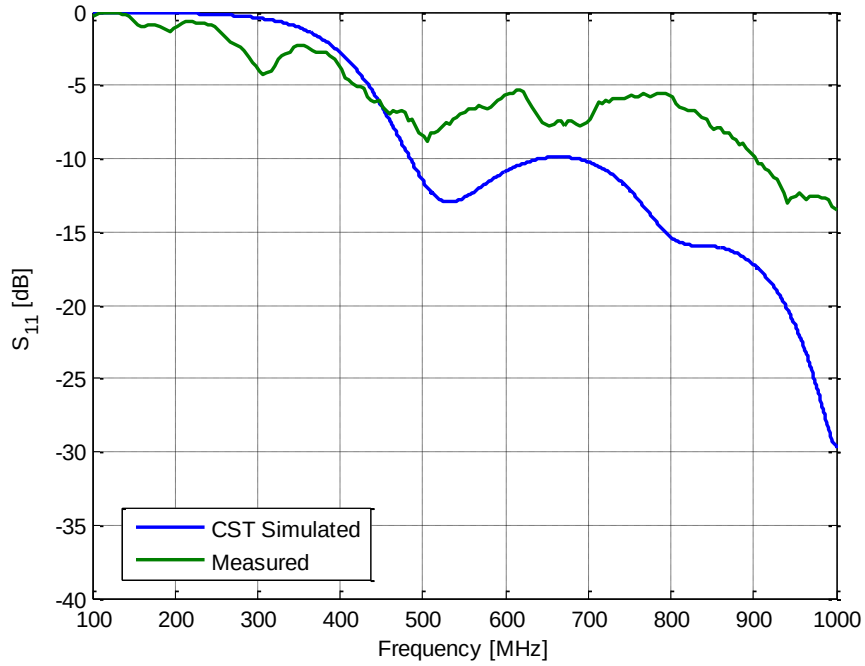

Figure 98 – Measured vs. simulated results for CVD antenna ver-B: S_{11} magnitude

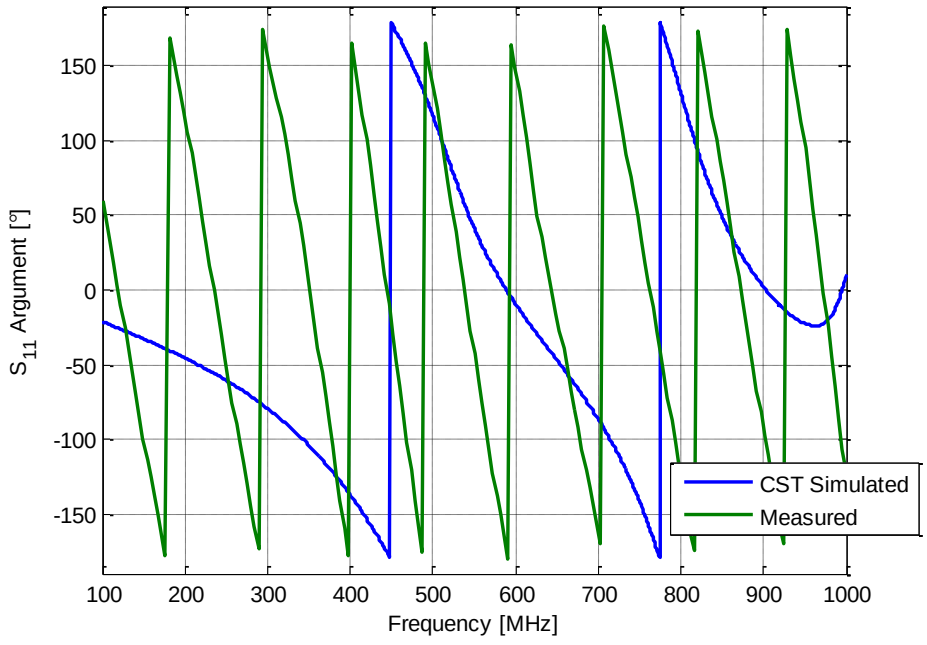

Figure 99 – Measured vs. simulated results for CVD antenna ver-B: S_{11} phase

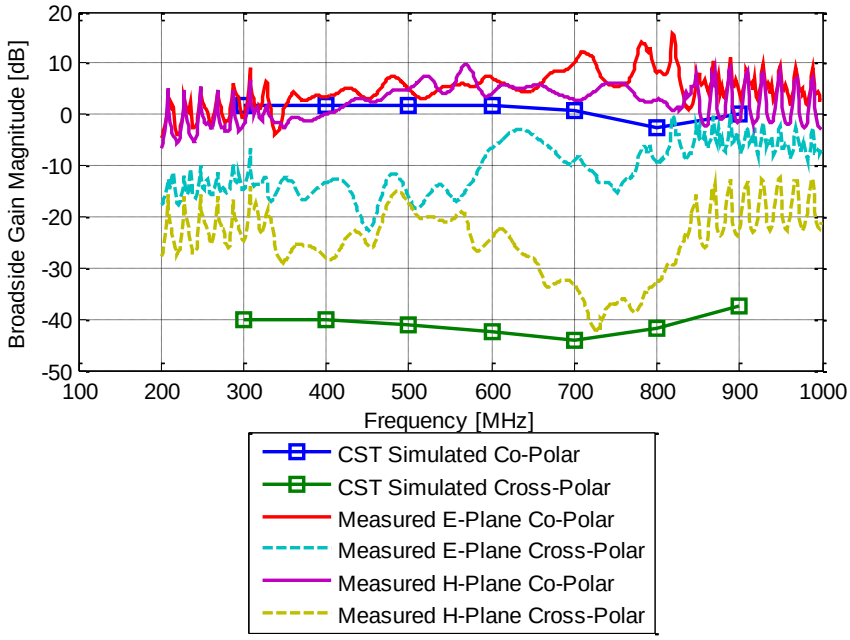

Figure 100 – Measured vs. simulated results for CVD antenna ver-B: broadside gain

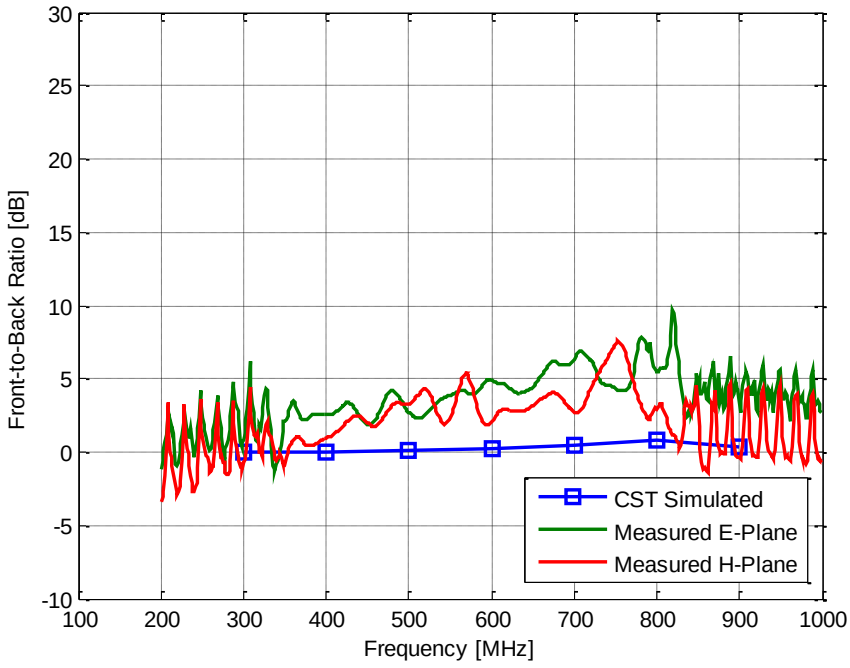

Figure 101 – Measured vs. simulated results for CVD antenna ver-B: front-to-back ratio

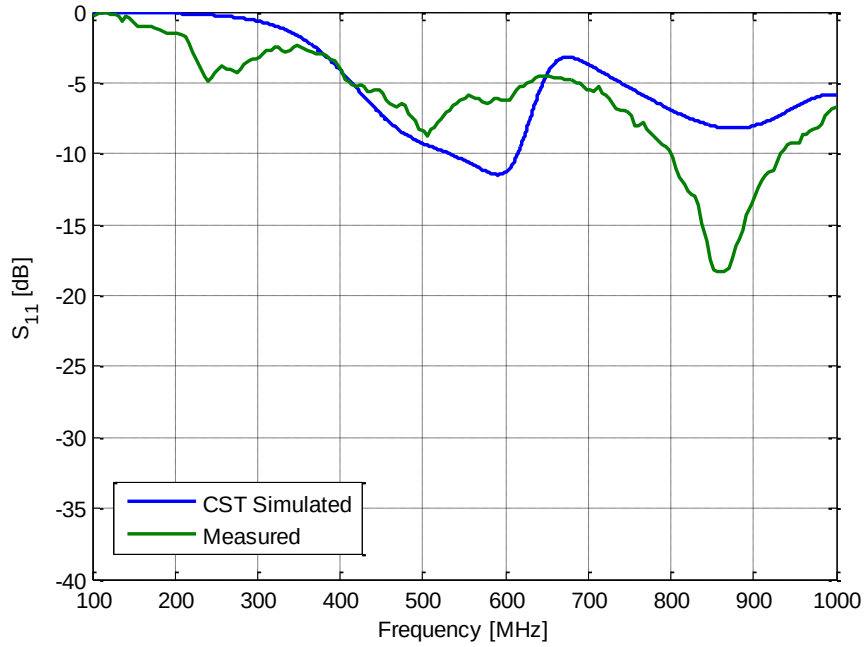

Figure 102 – Measured vs. simulated results for CBEVD antenna: S_{11} magnitude

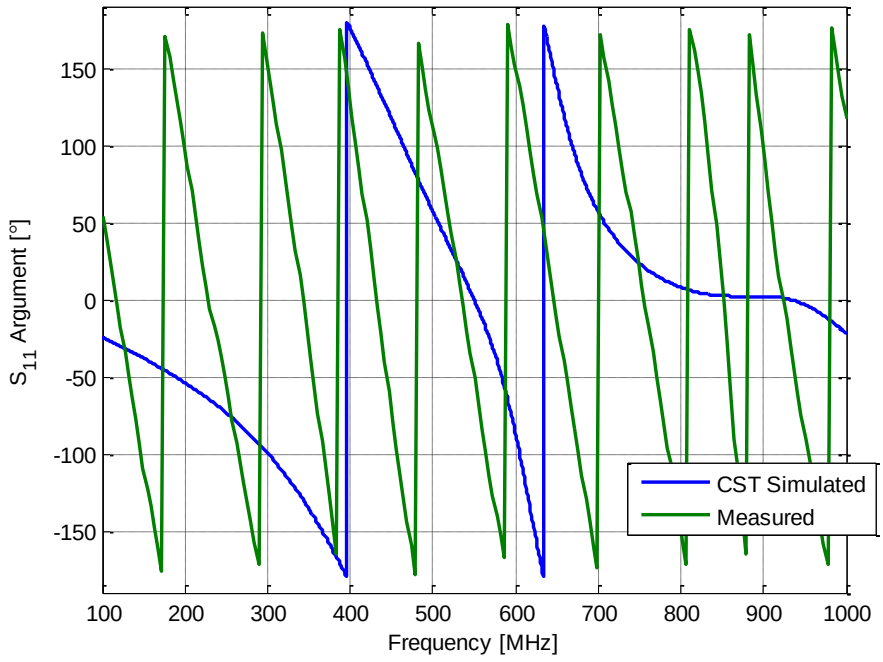

Figure 103 – Measured vs. simulated results for CBEVD antenna: S_{11} phase

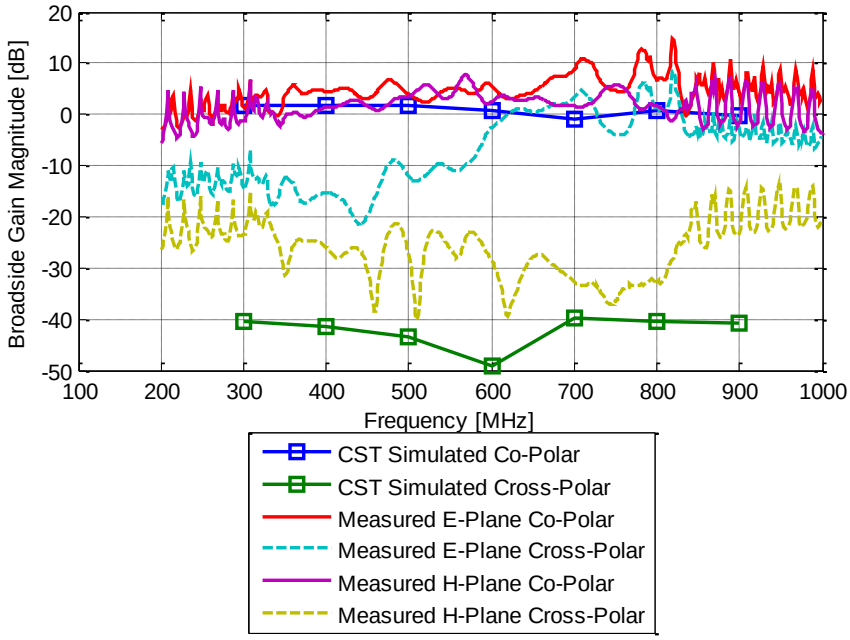

Figure 104 – Measured vs. simulated results for CBEVD antenna: broadside gain

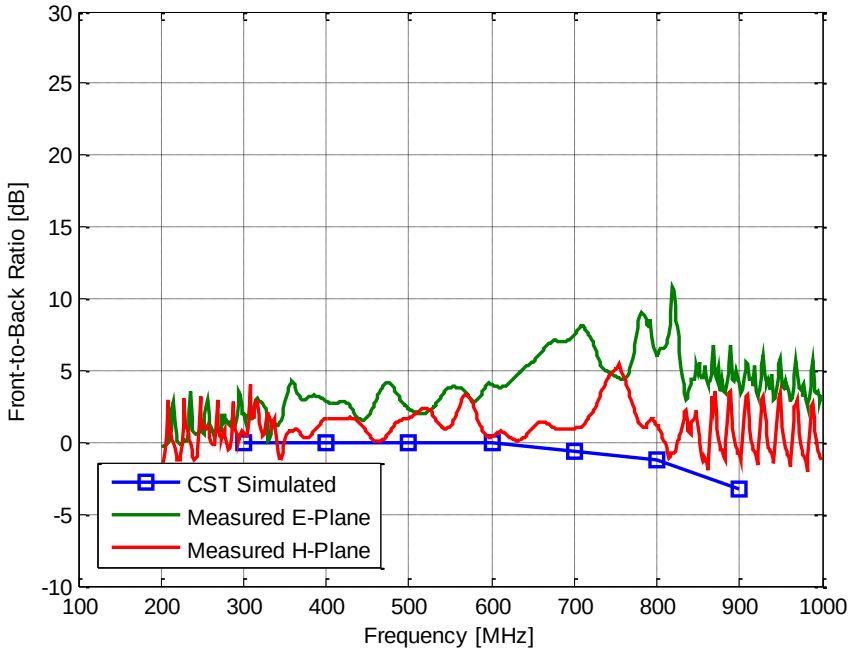

Figure 105 – Measured vs. simulated results for CBEVD antenna: front-to-back ratio

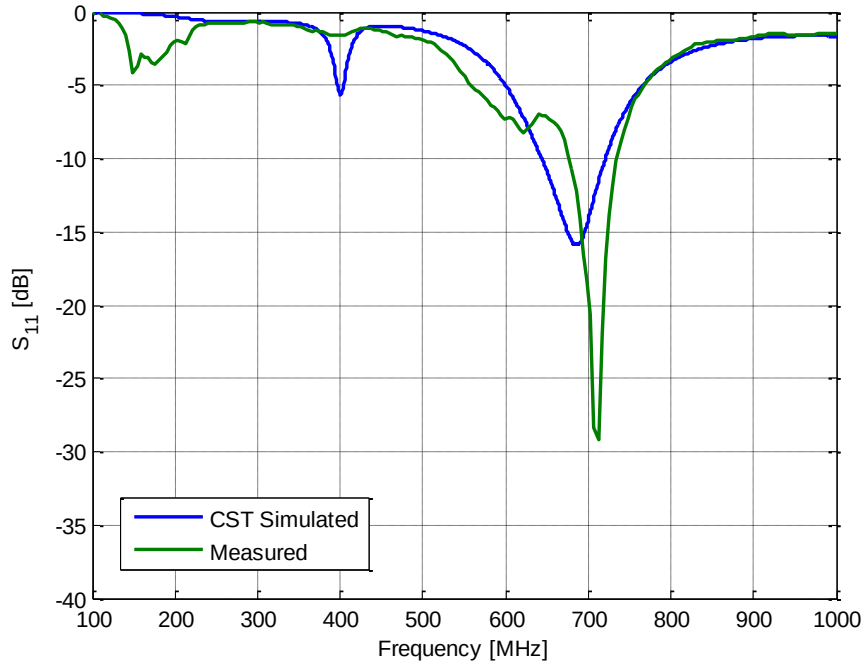

Figure 106 – Measured vs. simulated results for BEVD antenna: S_{11} magnitude

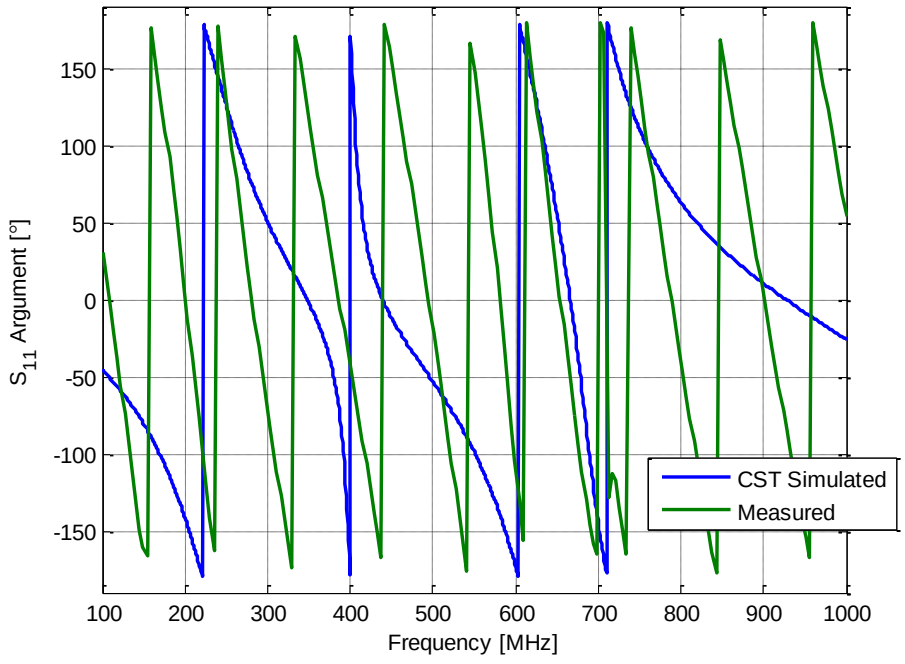

Figure 107 – Measured vs. simulated results for BEVD antenna: S_{11} phase

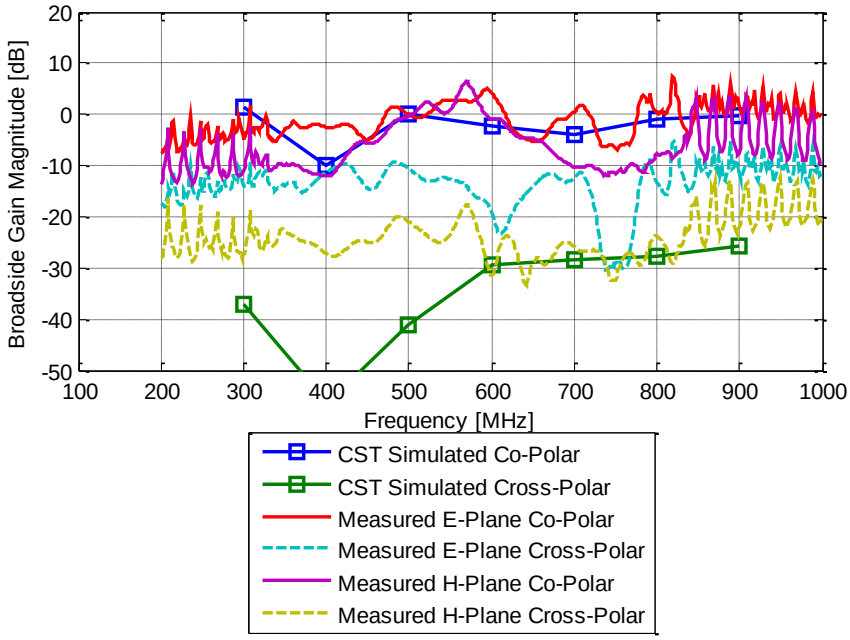

Figure 108 – Measured vs. simulated results for BEVD antenna: broadside gain

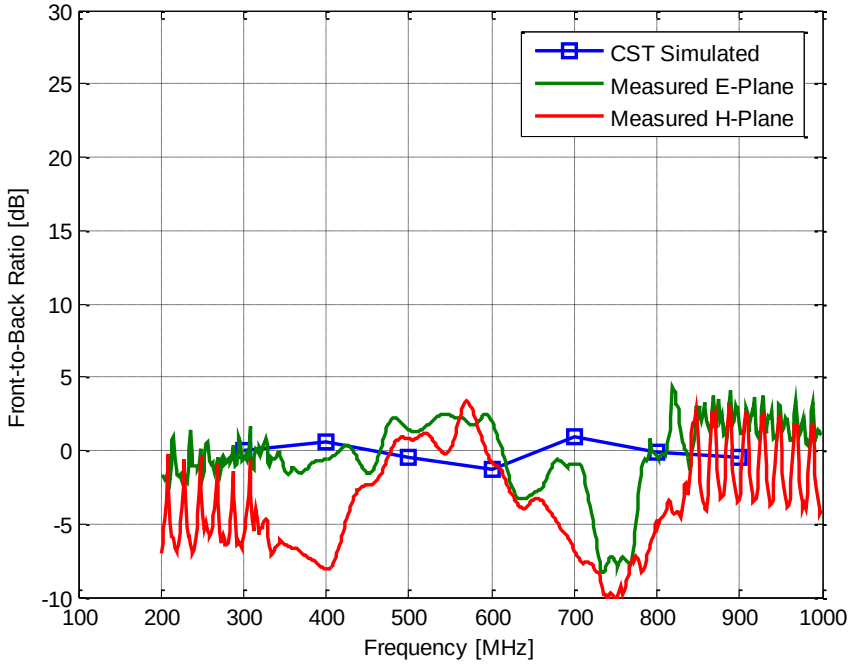

Figure 109 – Measured vs. simulated results for BEVD antenna: front-to-back ratio

The CVD displayed the best cross-polar component reduction of the Vivaldi antennas, though not quite as much as the LPA, as seen in comparison of Figure 92, Figure 96, Figure 100, Figure 104, and Figure 108. Finally, by comparing the antennas primarily in terms of reflection coefficient, S11, broadside gain, and front-to-back ratio, we can determine which constructed antenna performed best and how closely it came to beating the original LPA.

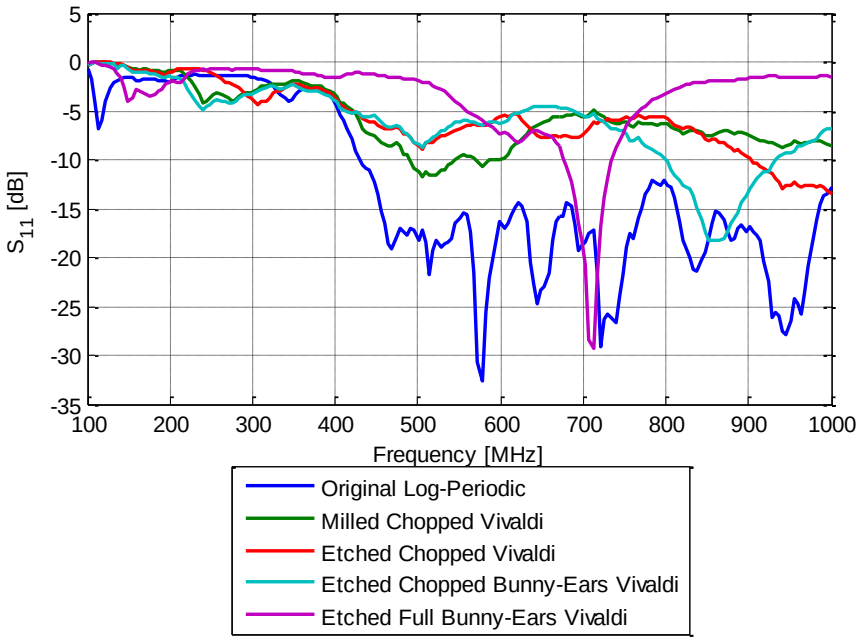

Figure 110 – Measured S_{11} of constructed antennas

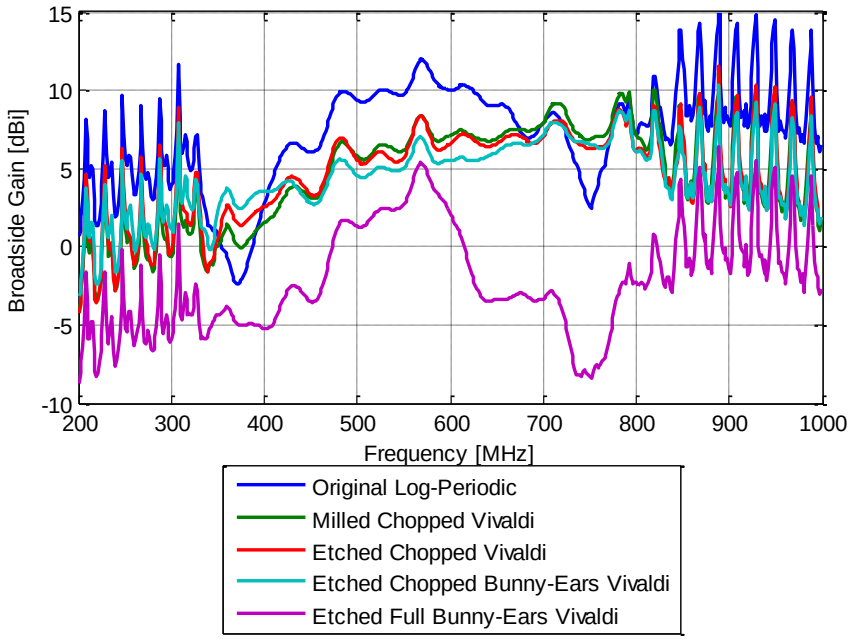

Figure 111 – Measured broadside gain of constructed antennas

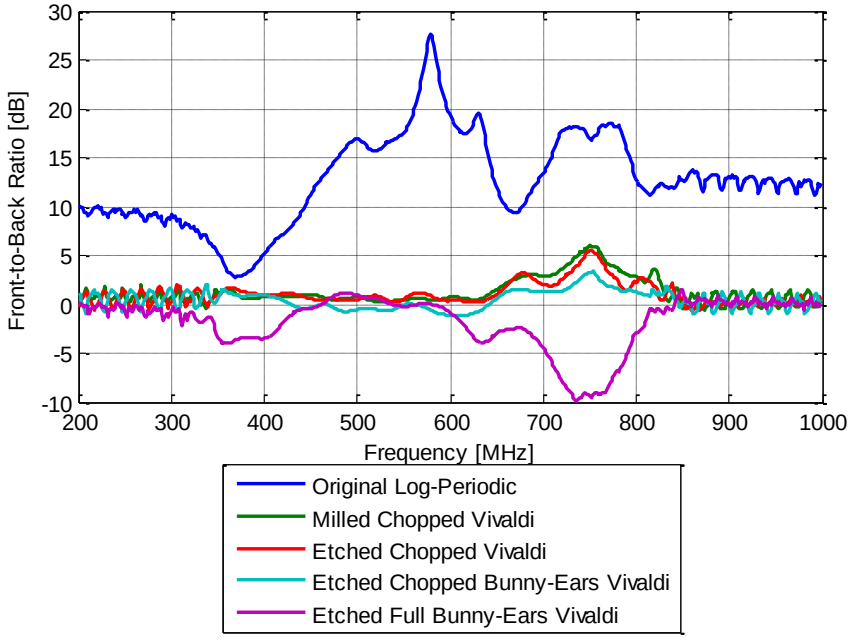

Figure 112 – Measured front-to-back ratio of constructed antennas

After inspecting Figure 110 - Figure 112, the chopped antennas are all very close in gain performance, but the CVD antenna achieved the lowest reflection coefficient within the bandwidth of interest. Comparing the two construction methods in Figure 113 shows that the milled antenna caused less of an impedance mismatch in the feed section of the antenna causing less of a detriment to the total efficiency. Therefore, the best antenna designed and built was the CVD from the milling machine.

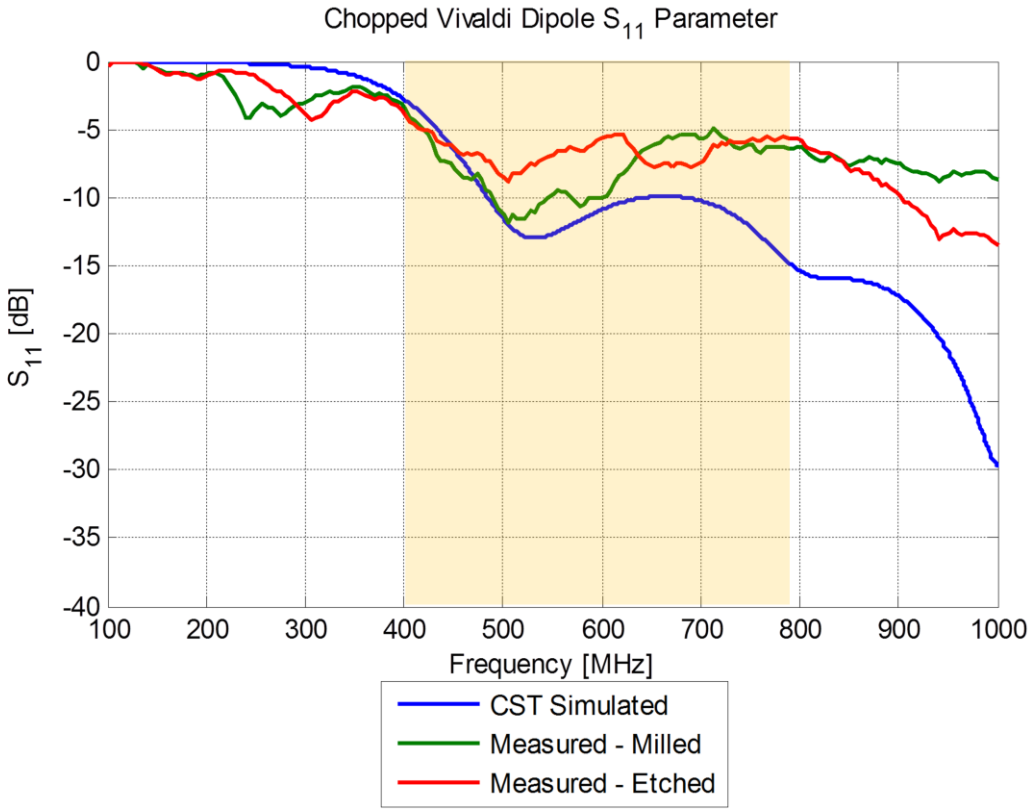

Figure 113 – Comparison of construction method results using S_{11} parameters of CVD

In overall error analysis in Figure 114, there is a general increase in error as frequency increases, which is most likely due to the construction methods. As the frequency increases, small deviations in construction impact the antenna results more. The LPA shows the greatest

error because of the resonance differences. The LPA is a difficult antenna to simulate correctly as small changes in the details of each dipole element in the antenna will affect the placement and behavior of each resonance region. In general, the Vivaldi antennas were simulated with high accuracy including resonance prediction greater than accomplished for the article validation case before, as seen in Table 8.

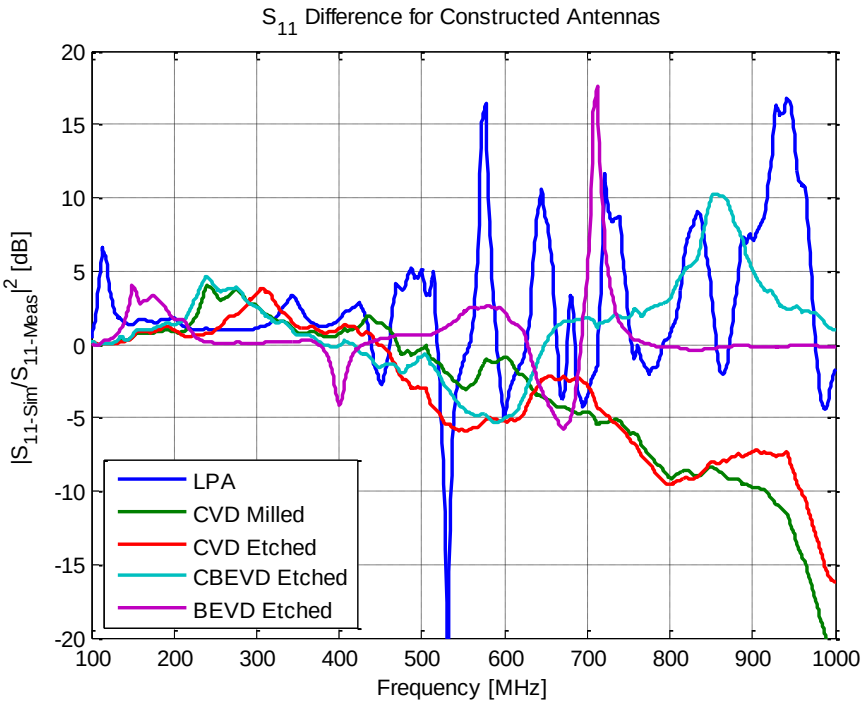

Figure 114 –S_{11} magnitude error for constructed antennas according to (24)

Table 8 – Resonance % error of constructed antennas extracted from S_{11} according to (23)

Constructed Antenna	Primary Resonance % Error
Log-Periodic Antenna	7.9549%
Milled Chopped Vivaldi Dipole	5.5248%
Etched Chopped Vivaldi Dipole	5.5248%
Etched Chopped Bunny-Ears Vivaldi Dipole	16.9307%
Etched Bunny-Ears Vivaldi Dipole	3.6657%

4.5 Chapter Conclusion

The major lessons learned through the use of varied simulations were applied to the design process in order to attain the final three designs for production. The constructed designs were displayed and their measured results were described and compared to the simulation expectations. After analysis of the final measured results, the milling machine constructed chopped Vivaldi dipole (CVD) antenna was the best performing of the antennas tested.

V. Conclusions

5.1 Chapter Overview

Antenna aperture reduction is essential to system size reduction. For example, cell phone antennas are generally one of the largest physical components within the structure of such a compact micro-electronic device. Yet these antennas remain inefficient and measure only very small fractions of wavelengths across. Many performance sacrifices result from down-scaling an antenna's size, but a firm understanding of antenna current behavior can lead the designer to maximize the potential within such size constraints. Understanding of UWB antenna behavior combined with computational analysis software supports the designer in finding capable antenna geometry for the specific application needed.

5.2 Review of Objectives and Methodology

The primary design objective for the antenna construction was to shrink the overall size of the subsystem in order to pave the way for future size reduction work on the AFIT RNR. In addition, the antenna should perform as well or better than the current commercial LPA used on the Noise Network (NoNET). In prioritized order the design objectives of this thesis were:

1. Compact structure that is cheap to construct
2. High, uniform gain in the UWB frequency range $\mathrm{G}(400\text{:}\,750\ \mathrm{MHz}) \approx 5\mathrm{dB}$
3. Low reflection coefficient in the UWB frequency range $\mathrm{S}_{11}(400\text{:}\,750\ \mathrm{MHz}) \leq -10\mathrm{dB}$
4. Minimize dispersion and stabilize phase center location throughout the UWB frequency range
5. Consistent endfire pattern throughout the UWB frequency range
6. High total efficiency

The measurement methods used in this thesis consisted of S_{11} parameters attained through a network analyzer after calibration and S_{21} measurements through the AFIT RNR and calibrated with standard gain horns borrowed from AFRL. The network analyzer use is a standard measurement approach, but the RNR and correlation receiver approach to the S_{21} measurements is less conventional. The antenna pattern and gain plots were fairly cluttered, but produced valid results after post-processing. It could be beneficial to have pattern and gain measurements acquired through a larger, more standardized anechoic chamber, but for a first level design validation, the RNR measurements are effective and inexpensive to obtain.

5.3 Results and Contributions

Overall, the new CVD antenna design is promising. It may not achieve as high of a front-to-back ratio or as low of a reflection coefficient as the commercial LPA did, but this is a trade-off for the reduction in size. As the antenna becomes smaller with respect to wavelength, the feed reflects more radiation back into the transmission line and the radiation pattern becomes more omnidirectional than directive. The constructed CVD and CBEVD antennas were able to attain nearly as high broadside gain as the LPA antenna, which will be necessary in maintaining the multistatic system operation. The CVD gain profiles were also more uniform than the commercial LPA, despite the noisy measurements.

Though the time and equipment were not available to measure the phase center, the simulated results show that the phase center of the new CVD antenna designs moves less than the current LPA design. A more precise UHF radar system and a larger anechoic chamber would be necessary to accurately measure the phase center of each antenna type.

5.4 Future Work

The AFIT RNR has incredible potential, both in research and operationally. The baseline system could be expanded in a variety of ways to satisfy a wide array of applications; it is hard to fully describe the future of the program. Some possible future directions for the AFIT NoNET improvement, and as well as specifically the antenna subsystem, could include:

- Build more antennas with higher manufacturing fidelity in order to satisfy current system needs
- Acquire high-gain horn antennas for use with the NoNET system when used in a stationary capacity, such as measurement of target RCS
- Incorporate the antenna subsystem into a controllable UWB array for scenarios when the NoNET size is less important than searching capability
- Investigate antenna parameter improvements that could result from different choices of substrate material, over that of FR4, which could increase the compression of EM waves within the antenna structure and increase radiation efficiency at lower frequencies
- Consider substrate extensions that could improve pattern shaping and directivity, such as identified by [56]
- Reduce losses in the feed section of the antenna by changing the SMA connection for a smoother tapered option and if a new integrated circuit is constructed for the minimized NoNET possibly consider incorporating the antenna into the same PCB
- Investigate the target identification capabilities of the AFIT NoNET by leveraging the full system bandwidth
- Integrate system software and filtering onto a compact software based radar unit

- Reduce the radar signal processing time with the incorporation of a "real-time" FPGA
- Incorporate GPS into the multistatic configuration to allow for target GPS location computation

Appendix

CST Simulation Results for Constructed Antennas

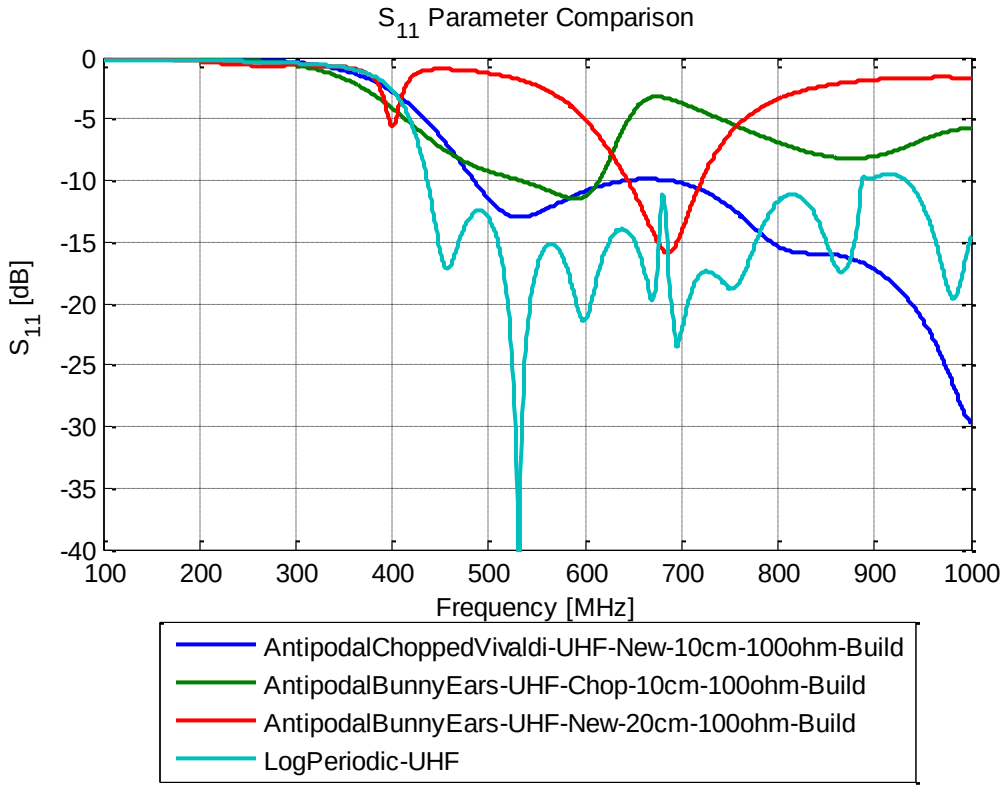

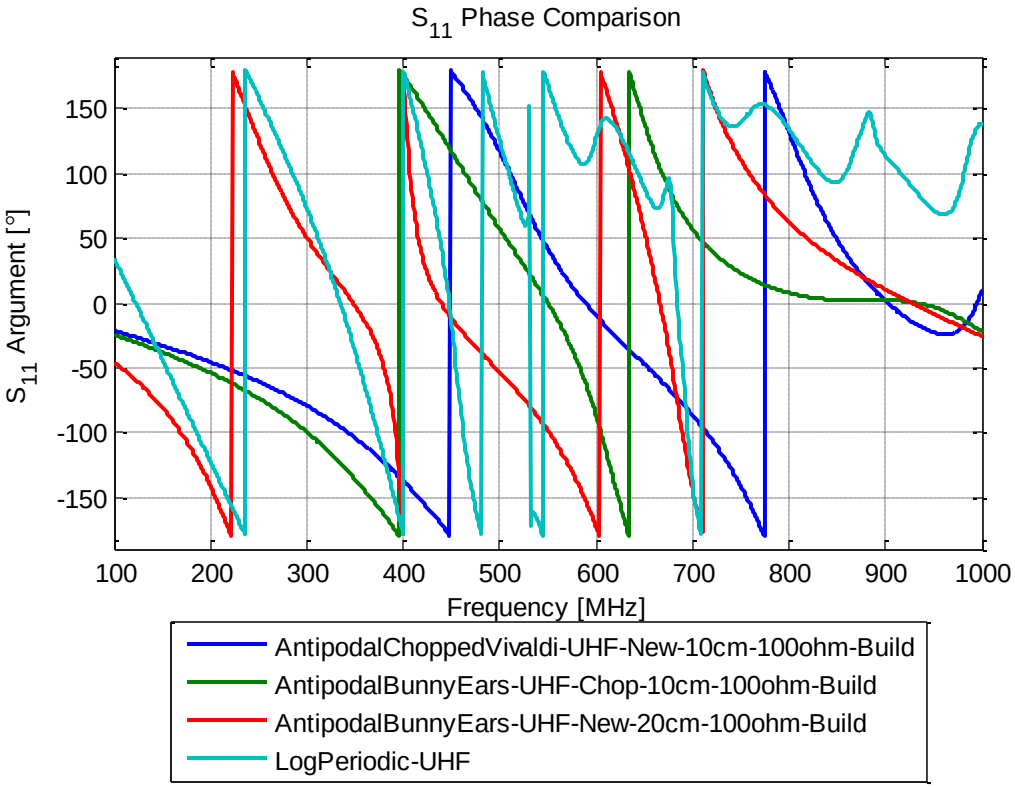
S11 Phase Comparison
S11 Argument [°]
150
100
50
0
-50
-100
-150
100
200
300
400
500
600
700
800
900
1000
Frequency [MHz]
AntipodalChoppedVivaldi-UHF-New-10cm-100ohm-Build
AntipodalBunnyEars-UHF-Chop-10cm-100ohm-Build
AntipodalBunnyEars-UHF-New-20cm-100ohm-Build
LogPeriodic-UHF

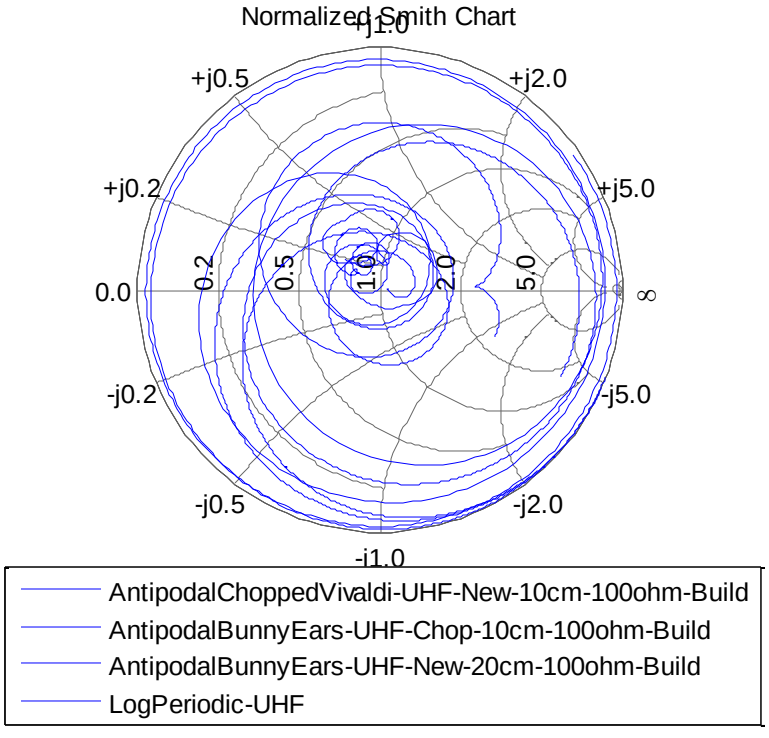
Normalized Smith Chart
+j1.0
+j0.5
+j2.0
+j0.2
+j5.0
0.0
0.2
0.5
1.0
2.0
5.0
∞
-j0.2
-j5.0
-j0.5
-j2.0
-j1.0
AntipodalChoppedVivaldi-UHF-New-10cm-100ohm-Build
AntipodalBunnyEars-UHF-Chop-10cm-100ohm-Build
AntipodalBunnyEars-UHF-New-20cm-100ohm-Build
LogPeriodic-UHF

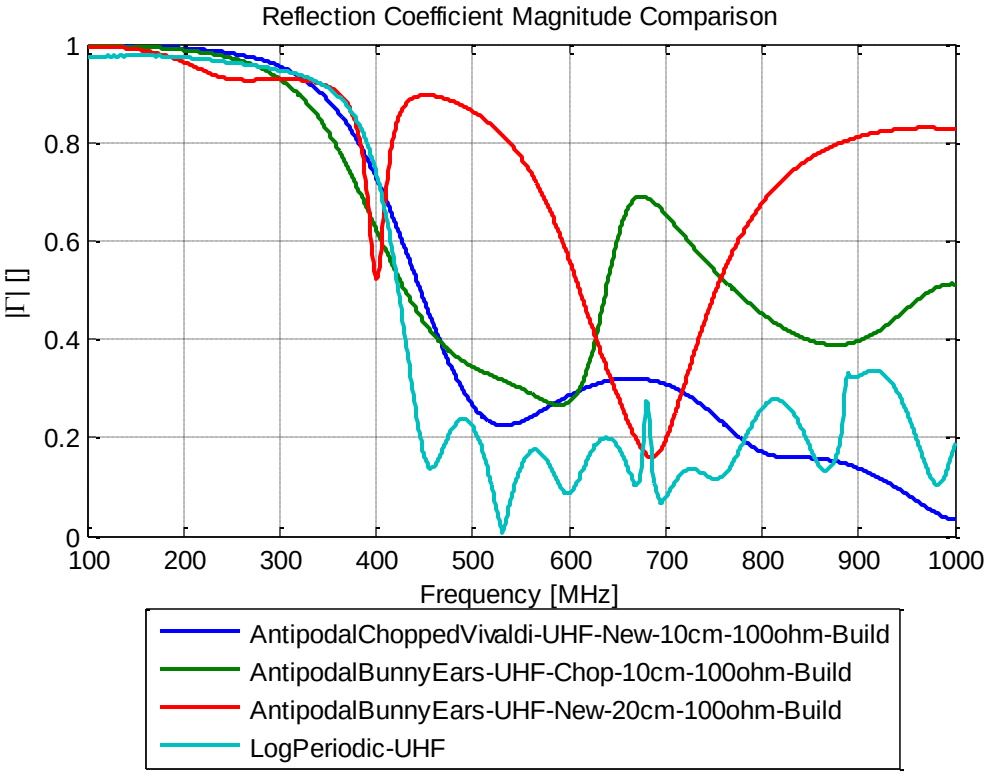
Reflection Coefficient Magnitude Comparison
|Γ| []
Frequency [MHz]
AntipodalChoppedVivaldi-UHF-New-10cm-100ohm-Build
AntipodalBunnyEars-UHF-Chop-10cm-100ohm-Build
AntipodalBunnyEars-UHF-New-20cm-100ohm-Build
LogPeriodic-UHF

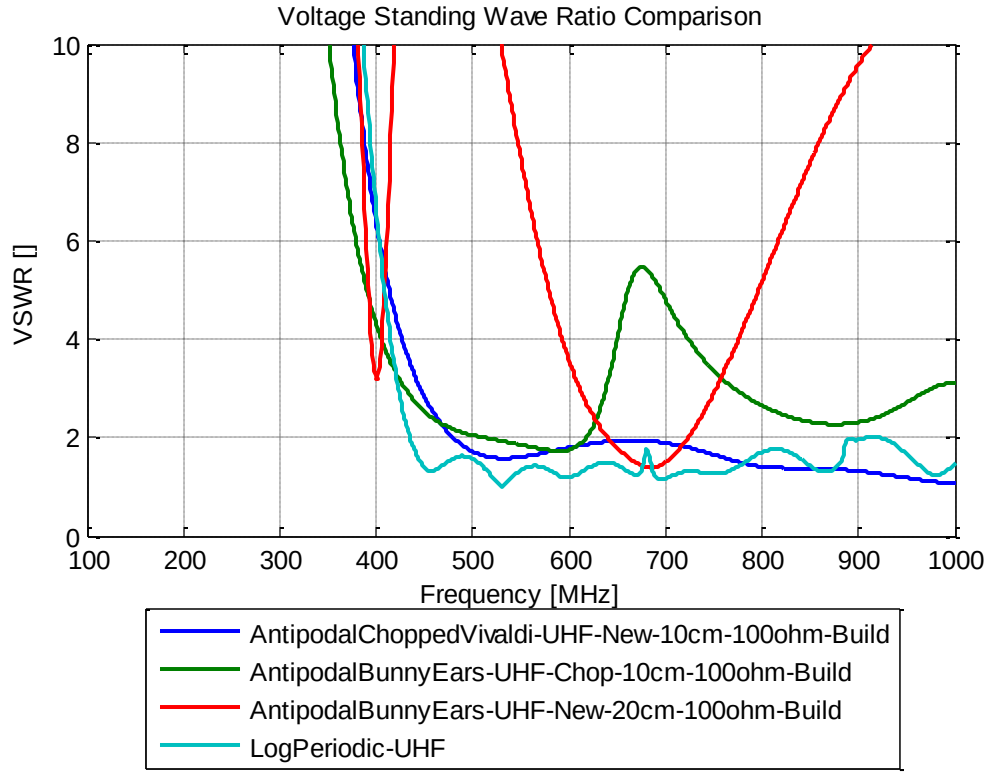
Voltage Standing Wave Ratio Comparison
VSWR []
Frequency [MHz]
AntipodalChoppedVivaldi-UHF-New-10cm-100ohm-Build
AntipodalBunnyEars-UHF-Chop-10cm-100ohm-Build
AntipodalBunnyEars-UHF-New-20cm-100ohm-Build
LogPeriodic-UHF

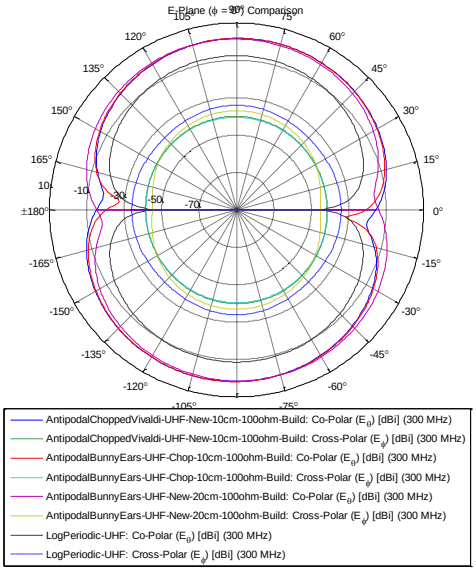
E-Plane (ϕ = 90°) Comparison
90°
75°
60°
45°
30°
15°
0°
-15°
-30°
-45°
-60°
-75°
-90°
-105°
-120°
-135°
-150°
-165°
±180°
165°
150°
135°
120°
105°
-10
-30
-50
-70
AntipodalChoppedVivaldi-UHF-New-10cm-100ohm-Build: Co-Polar (Eθ) [dBi] (300 MHz)
AntipodalChoppedVivaldi-UHF-New-10cm-100ohm-Build: Cross-Polar (Eφ) [dBi] (300 MHz)
AntipodalBunnyEars-UHF-Chop-10cm-100ohm-Build: Co-Polar (Eθ) [dBi] (300 MHz)
AntipodalBunnyEars-UHF-Chop-10cm-100ohm-Build: Cross-Polar (Eφ) [dBi] (300 MHz)
AntipodalBunnyEars-UHF-New-20cm-100ohm-Build: Co-Polar (Eθ) [dBi] (300 MHz)
AntipodalBunnyEars-UHF-New-20cm-100ohm-Build: Cross-Polar (Eφ) [dBi] (300 MHz)
LogPeriodic-UHF: Co-Polar (Eθ) [dBi] (300 MHz)
LogPeriodic-UHF: Cross-Polar (Eφ) [dBi] (300 MHz)

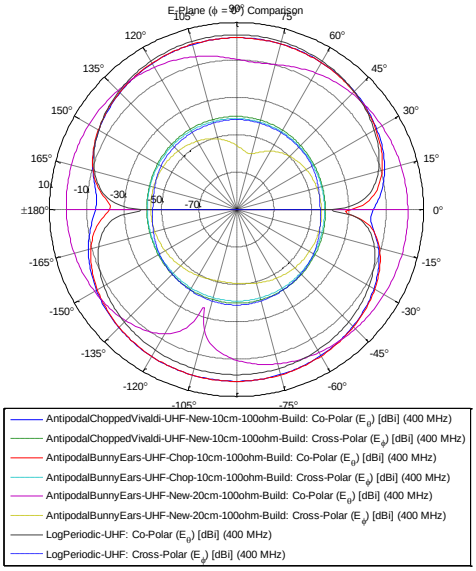
E-Plane (ϕ = 90°) Comparison
90°
75°
60°
45°
30°
15°
0°
-15°
-30°
-45°
-60°
-75°
-90°
-105°
-120°
-135°
-150°
-165°
±180°
165°
150°
135°
120°
105°
-10
-30
-50
-70
AntipodalChoppedVivaldi-UHF-New-10cm-100ohm-Build: Co-Polar (Eθ) [dBi] (400 MHz)
AntipodalChoppedVivaldi-UHF-New-10cm-100ohm-Build: Cross-Polar (Eφ) [dBi] (400 MHz)
AntipodalBunnyEars-UHF-Chop-10cm-100ohm-Build: Co-Polar (Eθ) [dBi] (400 MHz)
AntipodalBunnyEars-UHF-Chop-10cm-100ohm-Build: Cross-Polar (Eφ) [dBi] (400 MHz)
AntipodalBunnyEars-UHF-New-20cm-100ohm-Build: Co-Polar (Eθ) [dBi] (400 MHz)
AntipodalBunnyEars-UHF-New-20cm-100ohm-Build: Cross-Polar (Eφ) [dBi] (400 MHz)
LogPeriodic-UHF: Co-Polar (Eθ) [dBi] (400 MHz)
LogPeriodic-UHF: Cross-Polar (Eφ) [dBi] (400 MHz)

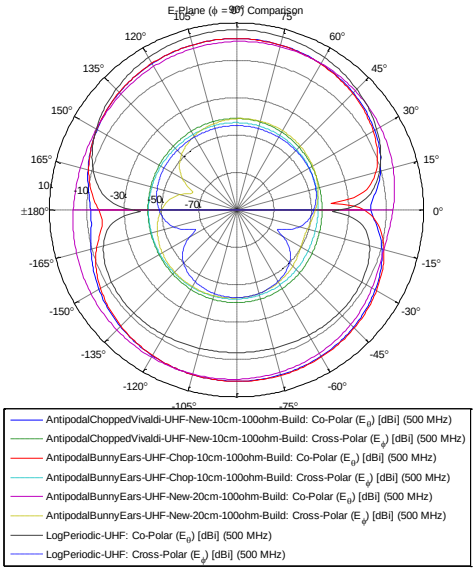
E-Plane (ϕ = 90°) Comparison
90°
75°
60°
45°
30°
15°
0°
-15°
-30°
-45°
-60°
-75°
-90°
-105°
-120°
-135°
-150°
-165°
±180°
165°
150°
135°
120°
105°
10
-10
-30
-50
-70
AntipodalChoppedVivaldi-UHF-New-10cm-100ohm-Build: Co-Polar (Eθ) [dBi] (500 MHz)
AntipodalChoppedVivaldi-UHF-New-10cm-100ohm-Build: Cross-Polar (Eφ) [dBi] (500 MHz)
AntipodalBunnyEars-UHF-Chop-10cm-100ohm-Build: Co-Polar (Eθ) [dBi] (500 MHz)
AntipodalBunnyEars-UHF-Chop-10cm-100ohm-Build: Cross-Polar (Eφ) [dBi] (500 MHz)
AntipodalBunnyEars-UHF-New-20cm-100ohm-Build: Co-Polar (Eθ) [dBi] (500 MHz)
AntipodalBunnyEars-UHF-New-20cm-100ohm-Build: Cross-Polar (Eφ) [dBi] (500 MHz)
LogPeriodic-UHF: Co-Polar (Eθ) [dBi] (500 MHz)
LogPeriodic-UHF: Cross-Polar (Eφ) [dBi] (500 MHz)

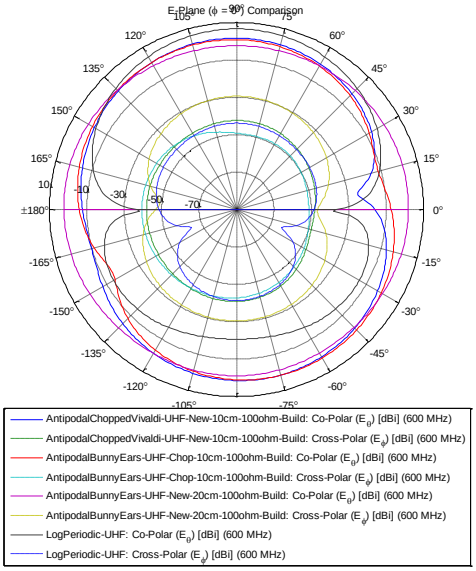
E-Plane (ϕ = 90°) Comparison
90°
75°
60°
45°
30°
15°
0°
-15°
-30°
-45°
-60°
-75°
-90°
-105°
-120°
-135°
-150°
-165°
±180°
165°
150°
135°
120°
105°
10
-10
-30
-50
-70
AntipodalChoppedVivaldi-UHF-New-10cm-100ohm-Build: Co-Polar (Eθ) [dBi] (600 MHz)
AntipodalChoppedVivaldi-UHF-New-10cm-100ohm-Build: Cross-Polar (Eφ) [dBi] (600 MHz)
AntipodalBunnyEars-UHF-Chop-10cm-100ohm-Build: Co-Polar (Eθ) [dBi] (600 MHz)
AntipodalBunnyEars-UHF-Chop-10cm-100ohm-Build: Cross-Polar (Eφ) [dBi] (600 MHz)
AntipodalBunnyEars-UHF-New-20cm-100ohm-Build: Co-Polar (Eθ) [dBi] (600 MHz)
AntipodalBunnyEars-UHF-New-20cm-100ohm-Build: Cross-Polar (Eφ) [dBi] (600 MHz)
LogPeriodic-UHF: Co-Polar (Eθ) [dBi] (600 MHz)
LogPeriodic-UHF: Cross-Polar (Eφ) [dBi] (600 MHz)

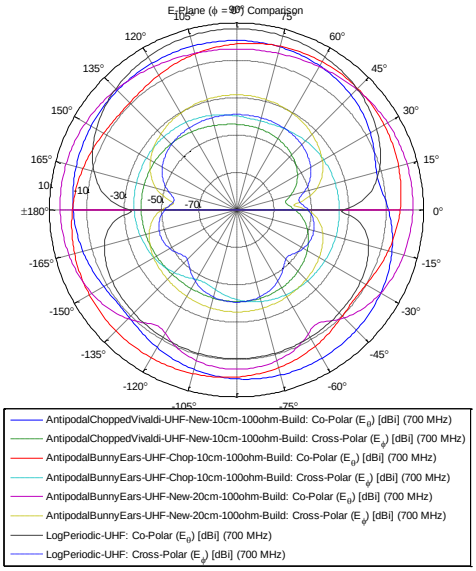
E-Plane (ϕ = 90°) Comparison
90°
75°
60°
45°
30°
15°
0°
-15°
-30°
-45°
-60°
-75°
-90°
-105°
-120°
-135°
-150°
-165°
±180°
-10
-30
-50
-70
AntipodalChoppedVivaldi-UHF-New-10cm-100ohm-Build: Co-Polar (Eθ) [dBi] (700 MHz)
AntipodalChoppedVivaldi-UHF-New-10cm-100ohm-Build: Cross-Polar (Eϕ) [dBi] (700 MHz)
AntipodalBunnyEars-UHF-Chop-10cm-100ohm-Build: Co-Polar (Eθ) [dBi] (700 MHz)
AntipodalBunnyEars-UHF-Chop-10cm-100ohm-Build: Cross-Polar (Eϕ) [dBi] (700 MHz)
AntipodalBunnyEars-UHF-New-20cm-100ohm-Build: Co-Polar (Eθ) [dBi] (700 MHz)
AntipodalBunnyEars-UHF-New-20cm-100ohm-Build: Cross-Polar (Eϕ) [dBi] (700 MHz)
LogPeriodic-UHF: Co-Polar (Eθ) [dBi] (700 MHz)
LogPeriodic-UHF: Cross-Polar (Eϕ) [dBi] (700 MHz)

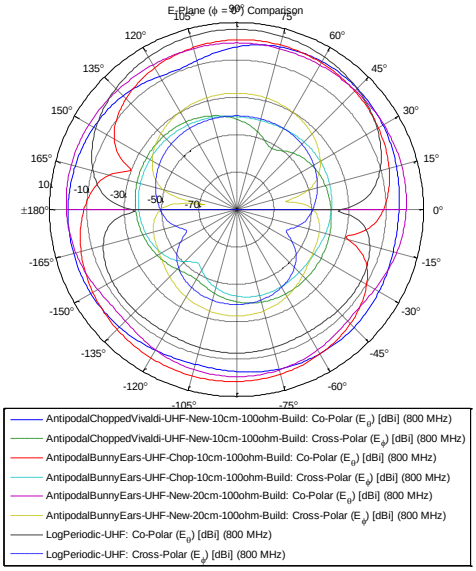
E-Plane (ϕ = 90°) Comparison
90°
75°
60°
45°
30°
15°
0°
-15°
-30°
-45°
-60°
-75°
-90°
-105°
-120°
-135°
-150°
-165°
±180°
-10
-30
-50
-70
AntipodalChoppedVivaldi-UHF-New-10cm-100ohm-Build: Co-Polar (Eθ) [dBi] (800 MHz)
AntipodalChoppedVivaldi-UHF-New-10cm-100ohm-Build: Cross-Polar (Eϕ) [dBi] (800 MHz)
AntipodalBunnyEars-UHF-Chop-10cm-100ohm-Build: Co-Polar (Eθ) [dBi] (800 MHz)
AntipodalBunnyEars-UHF-Chop-10cm-100ohm-Build: Cross-Polar (Eϕ) [dBi] (800 MHz)
AntipodalBunnyEars-UHF-New-20cm-100ohm-Build: Co-Polar (Eθ) [dBi] (800 MHz)
AntipodalBunnyEars-UHF-New-20cm-100ohm-Build: Cross-Polar (Eϕ) [dBi] (800 MHz)
LogPeriodic-UHF: Co-Polar (Eθ) [dBi] (800 MHz)
LogPeriodic-UHF: Cross-Polar (Eϕ) [dBi] (800 MHz)

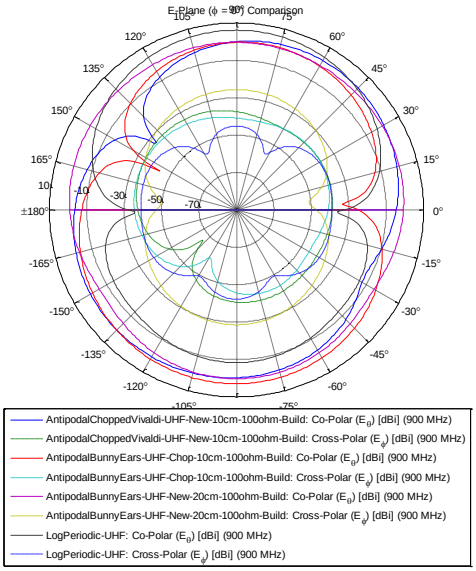
E-Plane (ϕ = 90°) Comparison
90°
105°
75°
120°
60°
135°
45°
150°
30°
165°
15°
±180°
0°
-165°
-15°
-150°
-30°
-135°
-45°
-120°
-60°
-105°
-75°
-10
-30
-50
-70
AntipodalChoppedVivaldi-UHF-New-10cm-100ohm-Build: Co-Polar (Eθ) [dBi] (900 MHz)
AntipodalChoppedVivaldi-UHF-New-10cm-100ohm-Build: Cross-Polar (Eϕ) [dBi] (900 MHz)
AntipodalBunnyEars-UHF-Chop-10cm-100ohm-Build: Co-Polar (Eθ) [dBi] (900 MHz)
AntipodalBunnyEars-UHF-Chop-10cm-100ohm-Build: Cross-Polar (Eϕ) [dBi] (900 MHz)
AntipodalBunnyEars-UHF-New-20cm-100ohm-Build: Co-Polar (Eθ) [dBi] (900 MHz)
AntipodalBunnyEars-UHF-New-20cm-100ohm-Build: Cross-Polar (Eϕ) [dBi] (900 MHz)
LogPeriodic-UHF: Co-Polar (Eθ) [dBi] (900 MHz)
LogPeriodic-UHF: Cross-Polar (Eϕ) [dBi] (900 MHz)

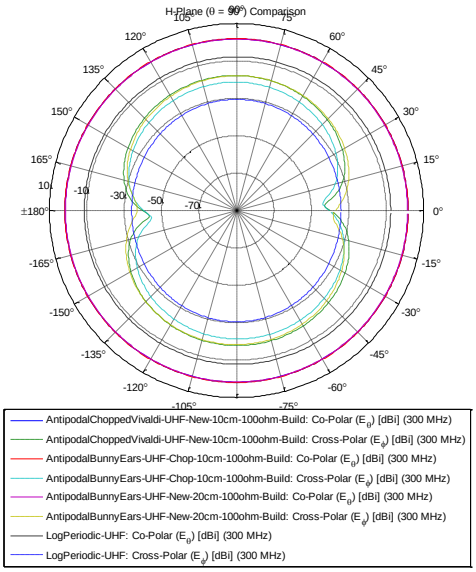
H-Plane (θ = 90°) Comparison
90°
105°
75°
120°
60°
135°
45°
150°
30°
165°
15°
±180°
0°
-165°
-15°
-150°
-30°
-135°
-45°
-120°
-60°
-105°
-75°
-10
-30
-50
-70
AntipodalChoppedVivaldi-UHF-New-10cm-100ohm-Build: Co-Polar (Eθ) [dBi] (300 MHz)
AntipodalChoppedVivaldi-UHF-New-10cm-100ohm-Build: Cross-Polar (Eϕ) [dBi] (300 MHz)
AntipodalBunnyEars-UHF-Chop-10cm-100ohm-Build: Co-Polar (Eθ) [dBi] (300 MHz)
AntipodalBunnyEars-UHF-Chop-10cm-100ohm-Build: Cross-Polar (Eϕ) [dBi] (300 MHz)
AntipodalBunnyEars-UHF-New-20cm-100ohm-Build: Co-Polar (Eθ) [dBi] (300 MHz)
AntipodalBunnyEars-UHF-New-20cm-100ohm-Build: Cross-Polar (Eϕ) [dBi] (300 MHz)
LogPeriodic-UHF: Co-Polar (Eθ) [dBi] (300 MHz)
LogPeriodic-UHF: Cross-Polar (Eϕ) [dBi] (300 MHz)

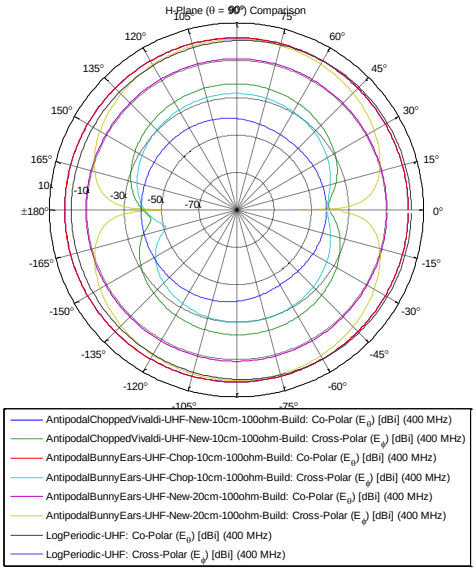
H-Plane (θ = 90°) Comparison
105°
75°
120°
60°
135°
45°
150°
30°
165°
15°
±180°
0°
-165°
-15°
-150°
-30°
-135°
-45°
-120°
-60°
-105°
-75°
-10
-30
-50
-70
AntipodalChoppedVivaldi-UHF-New-10cm-100ohm-Build: Co-Polar (Eθ) [dBi] (400 MHz)
AntipodalChoppedVivaldi-UHF-New-10cm-100ohm-Build: Cross-Polar (Eφ) [dBi] (400 MHz)
AntipodalBunnyEars-UHF-Chop-10cm-100ohm-Build: Co-Polar (Eθ) [dBi] (400 MHz)
AntipodalBunnyEars-UHF-Chop-10cm-100ohm-Build: Cross-Polar (Eφ) [dBi] (400 MHz)
AntipodalBunnyEars-UHF-New-20cm-100ohm-Build: Co-Polar (Eθ) [dBi] (400 MHz)
AntipodalBunnyEars-UHF-New-20cm-100ohm-Build: Cross-Polar (Eφ) [dBi] (400 MHz)
LogPeriodic-UHF: Co-Polar (Eθ) [dBi] (400 MHz)
LogPeriodic-UHF: Cross-Polar (Eφ) [dBi] (400 MHz)

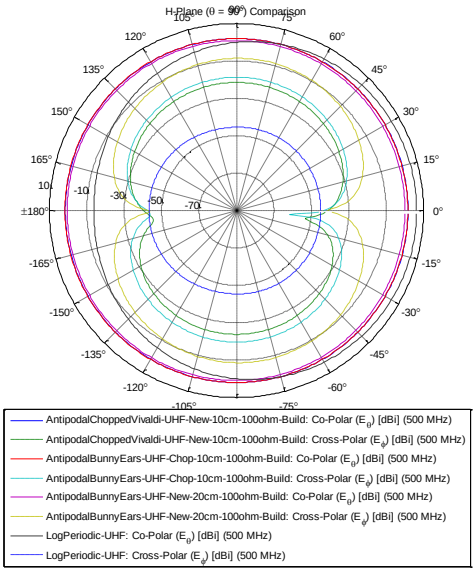
H-Plane (θ = 90°) Comparison
105°
75°
120°
60°
135°
45°
150°
30°
165°
15°
±180°
0°
-165°
-15°
-150°
-30°
-135°
-45°
-120°
-60°
-105°
-75°
-10
-30
-50
-70
AntipodalChoppedVivaldi-UHF-New-10cm-100ohm-Build: Co-Polar (Eθ) [dBi] (500 MHz)
AntipodalChoppedVivaldi-UHF-New-10cm-100ohm-Build: Cross-Polar (Eφ) [dBi] (500 MHz)
AntipodalBunnyEars-UHF-Chop-10cm-100ohm-Build: Co-Polar (Eθ) [dBi] (500 MHz)
AntipodalBunnyEars-UHF-Chop-10cm-100ohm-Build: Cross-Polar (Eφ) [dBi] (500 MHz)
AntipodalBunnyEars-UHF-New-20cm-100ohm-Build: Co-Polar (Eθ) [dBi] (500 MHz)
AntipodalBunnyEars-UHF-New-20cm-100ohm-Build: Cross-Polar (Eφ) [dBi] (500 MHz)
LogPeriodic-UHF: Co-Polar (Eθ) [dBi] (500 MHz)
LogPeriodic-UHF: Cross-Polar (Eφ) [dBi] (500 MHz)

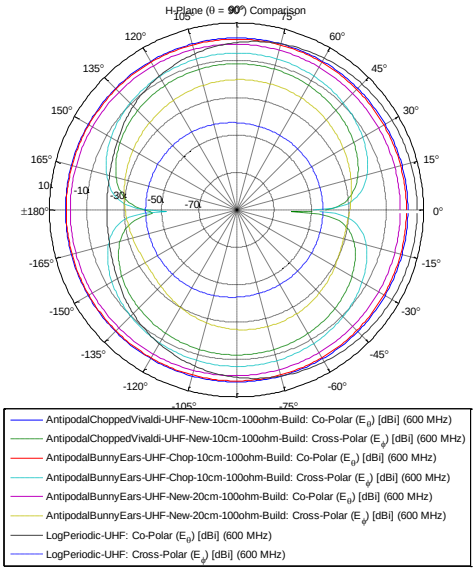
H-Plane (θ = 90°) Comparison
105°
75°
120°
60°
135°
45°
150°
30°
165°
15°
10
-10
-30
-50
-70
±180°
0°
-165°
-15°
-150°
-30°
-135°
-45°
-120°
-60°
-105°
-75°
AntipodalChoppedVivaldi-UHF-New-10cm-100ohm-Build: Co-Polar (Eθ) [dBi] (600 MHz)
AntipodalChoppedVivaldi-UHF-New-10cm-100ohm-Build: Cross-Polar (Eφ) [dBi] (600 MHz)
AntipodalBunnyEars-UHF-Chop-10cm-100ohm-Build: Co-Polar (Eθ) [dBi] (600 MHz)
AntipodalBunnyEars-UHF-Chop-10cm-100ohm-Build: Cross-Polar (Eφ) [dBi] (600 MHz)
AntipodalBunnyEars-UHF-New-20cm-100ohm-Build: Co-Polar (Eθ) [dBi] (600 MHz)
AntipodalBunnyEars-UHF-New-20cm-100ohm-Build: Cross-Polar (Eφ) [dBi] (600 MHz)
LogPeriodic-UHF: Co-Polar (Eθ) [dBi] (600 MHz)
LogPeriodic-UHF: Cross-Polar (Eφ) [dBi] (600 MHz)

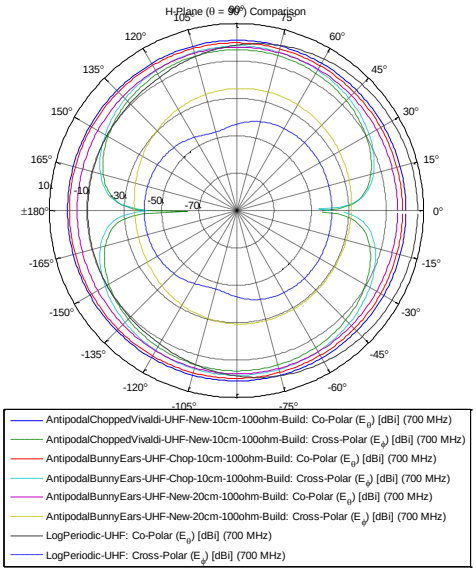
H-Plane (θ = 90°) Comparison
105°
75°
120°
60°
135°
45°
150°
30°
165°
15°
10
-10
-30
-50
-70
±180°
0°
-165°
-15°
-150°
-30°
-135°
-45°
-120°
-60°
-105°
-75°
AntipodalChoppedVivaldi-UHF-New-10cm-100ohm-Build: Co-Polar (Eθ) [dBi] (700 MHz)
AntipodalChoppedVivaldi-UHF-New-10cm-100ohm-Build: Cross-Polar (Eφ) [dBi] (700 MHz)
AntipodalBunnyEars-UHF-Chop-10cm-100ohm-Build: Co-Polar (Eθ) [dBi] (700 MHz)
AntipodalBunnyEars-UHF-Chop-10cm-100ohm-Build: Cross-Polar (Eφ) [dBi] (700 MHz)
AntipodalBunnyEars-UHF-New-20cm-100ohm-Build: Co-Polar (Eθ) [dBi] (700 MHz)
AntipodalBunnyEars-UHF-New-20cm-100ohm-Build: Cross-Polar (Eφ) [dBi] (700 MHz)
LogPeriodic-UHF: Co-Polar (Eθ) [dBi] (700 MHz)
LogPeriodic-UHF: Cross-Polar (Eφ) [dBi] (700 MHz)

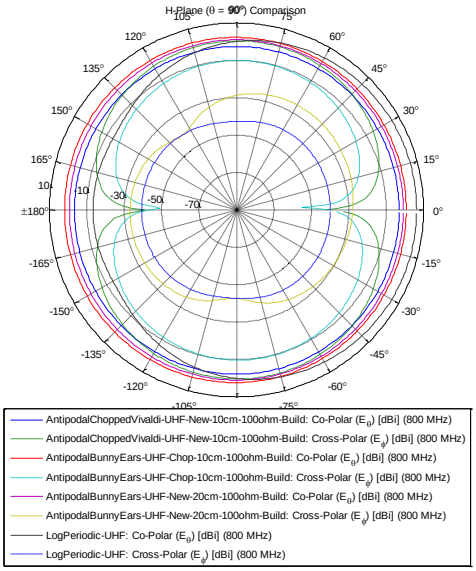
H-Plane (θ = 90°) Comparison
105°
75°
120°
60°
135°
45°
150°
30°
165°
15°
±180°
0°
-165°
-15°
-150°
-30°
-135°
-45°
-120°
-60°
-105°
-75°
-10
-30
-50
-70
AntipodalChoppedVivaldi-UHF-New-10cm-100ohm-Build: Co-Polar (Eθ) [dBi] (800 MHz)
AntipodalChoppedVivaldi-UHF-New-10cm-100ohm-Build: Cross-Polar (Eφ) [dBi] (800 MHz)
AntipodalBunnyEars-UHF-Chop-10cm-100ohm-Build: Co-Polar (Eθ) [dBi] (800 MHz)
AntipodalBunnyEars-UHF-Chop-10cm-100ohm-Build: Cross-Polar (Eφ) [dBi] (800 MHz)
AntipodalBunnyEars-UHF-New-20cm-100ohm-Build: Co-Polar (Eθ) [dBi] (800 MHz)
AntipodalBunnyEars-UHF-New-20cm-100ohm-Build: Cross-Polar (Eφ) [dBi] (800 MHz)
LogPeriodic-UHF: Co-Polar (Eθ) [dBi] (800 MHz)
LogPeriodic-UHF: Cross-Polar (Eφ) [dBi] (800 MHz)

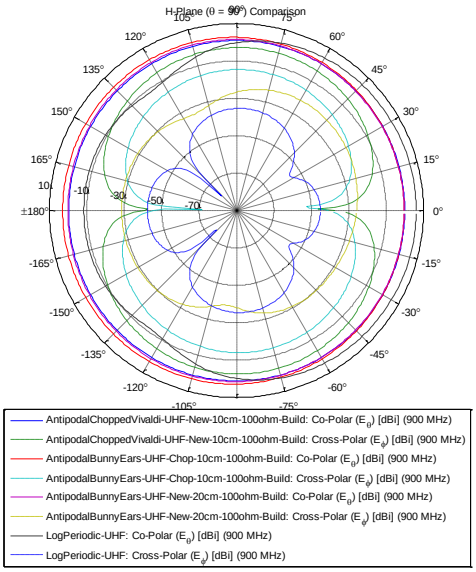
H-Plane (θ = 90°) Comparison
105°
75°
120°
60°
135°
45°
150°
30°
165°
15°
±180°
0°
-165°
-15°
-150°
-30°
-135°
-45°
-120°
-60°
-105°
-75°
-10
-30
-50
-70
AntipodalChoppedVivaldi-UHF-New-10cm-100ohm-Build: Co-Polar (Eθ) [dBi] (900 MHz)
AntipodalChoppedVivaldi-UHF-New-10cm-100ohm-Build: Cross-Polar (Eφ) [dBi] (900 MHz)
AntipodalBunnyEars-UHF-Chop-10cm-100ohm-Build: Co-Polar (Eθ) [dBi] (900 MHz)
AntipodalBunnyEars-UHF-Chop-10cm-100ohm-Build: Cross-Polar (Eφ) [dBi] (900 MHz)
AntipodalBunnyEars-UHF-New-20cm-100ohm-Build: Co-Polar (Eθ) [dBi] (900 MHz)
AntipodalBunnyEars-UHF-New-20cm-100ohm-Build: Cross-Polar (Eφ) [dBi] (900 MHz)
LogPeriodic-UHF: Co-Polar (Eθ) [dBi] (900 MHz)
LogPeriodic-UHF: Cross-Polar (Eφ) [dBi] (900 MHz)

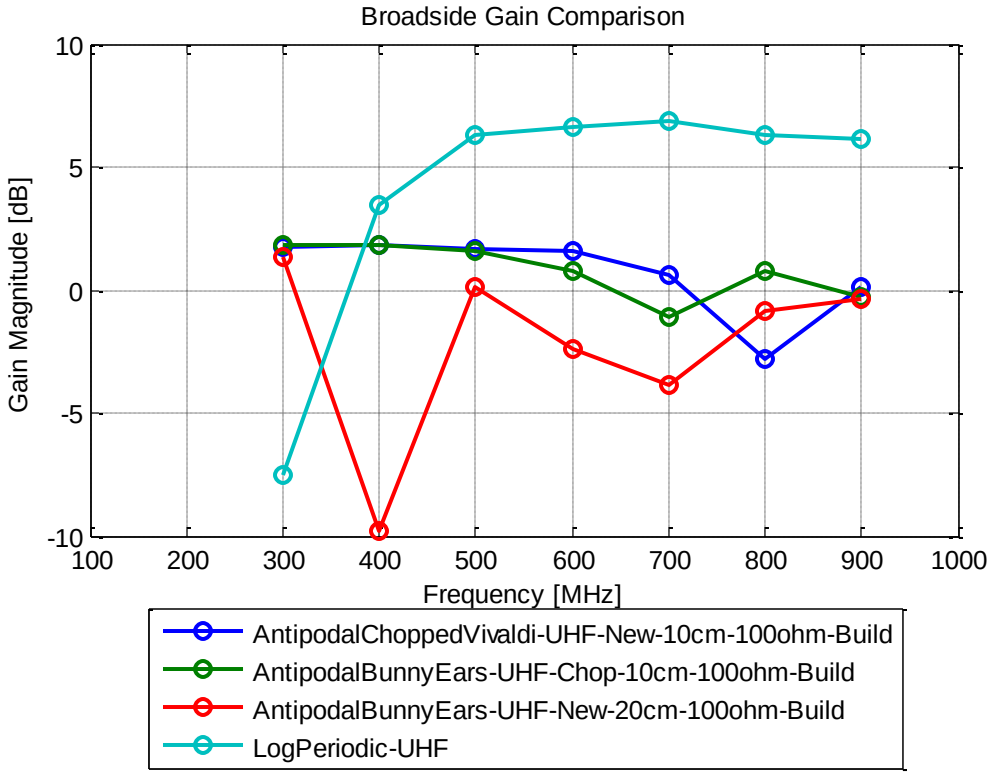
Broadside Gain Comparison
Gain Magnitude [dB]
10
5
0
-5
-10
100
200
300
400
500
600
700
800
900
1000
Frequency [MHz]
AntipodalChoppedVivaldi-UHF-New-10cm-100ohm-Build
AntipodalBunnyEars-UHF-Chop-10cm-100ohm-Build
AntipodalBunnyEars-UHF-New-20cm-100ohm-Build
LogPeriodic-UHF

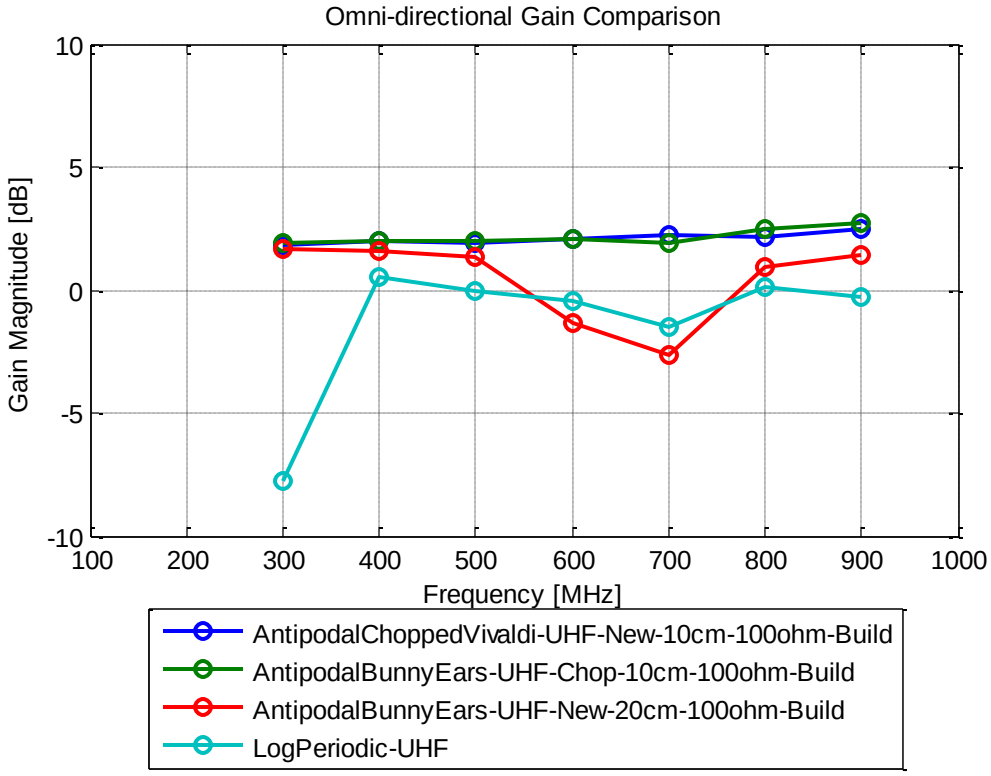
Omni-directional Gain Comparison
Gain Magnitude [dB]
10
5
0
-5
-10
100
200
300
400
500
600
700
800
900
1000
Frequency [MHz]
AntipodalChoppedVivaldi-UHF-New-10cm-100ohm-Build
AntipodalBunnyEars-UHF-Chop-10cm-100ohm-Build
AntipodalBunnyEars-UHF-New-20cm-100ohm-Build
LogPeriodic-UHF

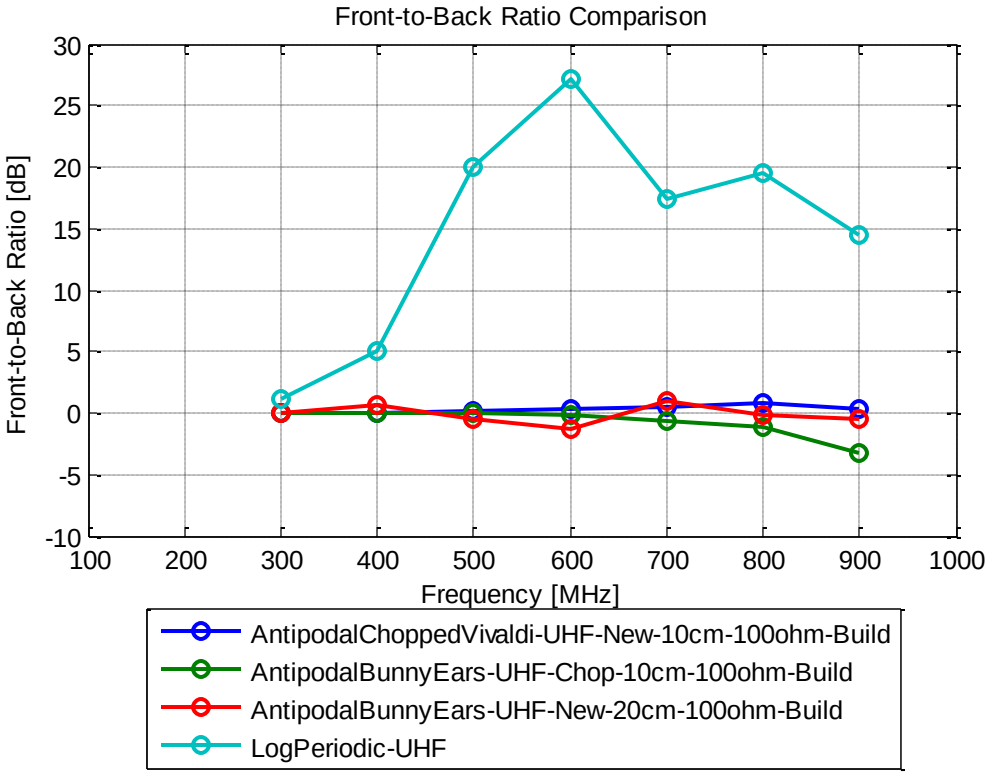
Front-to-Back Ratio Comparison
Front-to-Back Ratio [dB]
30
25
20
15
10
5
0
-5
-10
100
200
300
400
500
600
700
800
900
1000
Frequency [MHz]
AntipodalChoppedVivaldi-UHF-New-10cm-100ohm-Build
AntipodalBunnyEars-UHF-Chop-10cm-100ohm-Build
AntipodalBunnyEars-UHF-New-20cm-100ohm-Build
LogPeriodic-UHF

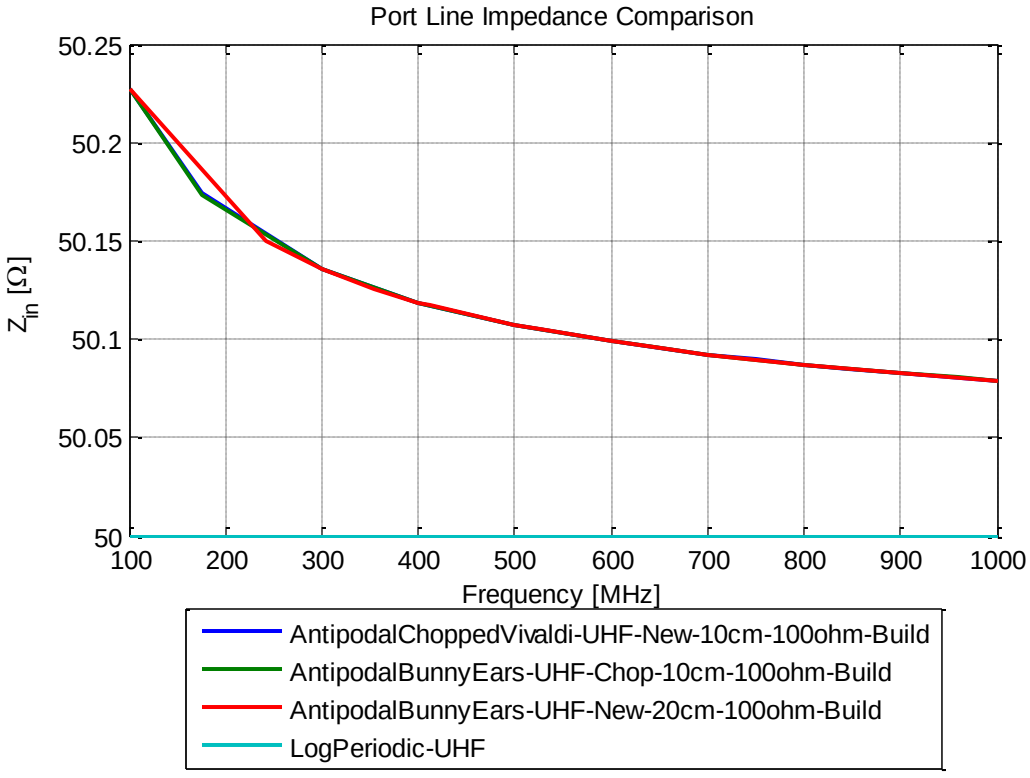
Port Line Impedance Comparison
Z_{in} [Ω]
50.25
50.2
50.15
50.1
50.05
50
100
200
300
400
500
600
700
800
900
1000
Frequency [MHz]
AntipodalChoppedVivaldi-UHF-New-10cm-100ohm-Build
AntipodalBunnyEars-UHF-Chop-10cm-100ohm-Build
AntipodalBunnyEars-UHF-New-20cm-100ohm-Build
LogPeriodic-UHF

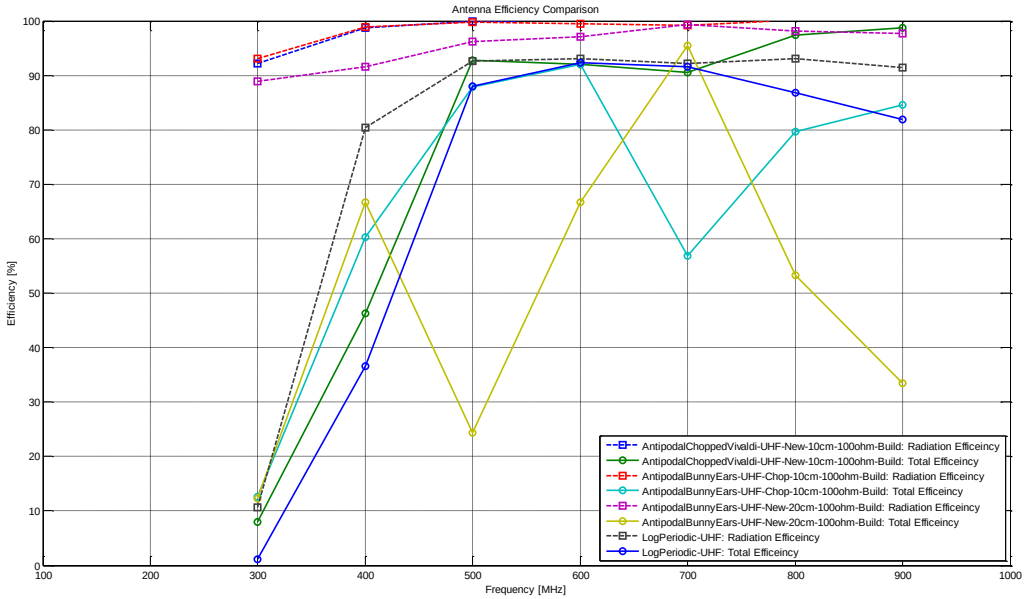
Antenna Efficiency Comparison
Efficiency [%]
Frequency [MHz]
AntipodalChoppedVivaldi-UHF-New-10cm-100ohm-Build: Radiation Efficeincy
AntipodalChoppedVivaldi-UHF-New-10cm-100ohm-Build: Total Efficeincy
AntipodalBunnyEars-UHF-Chop-10cm-100ohm-Build: Radiation Efficeincy
AntipodalBunnyEars-UHF-Chop-10cm-100ohm-Build: Total Efficeincy
AntipodalBunnyEars-UHF-New-20cm-100ohm-Build: Radiation Efficeincy
AntipodalBunnyEars-UHF-New-20cm-100ohm-Build: Total Efficeincy
LogPeriodic-UHF: Radiation Efficeincy
LogPeriodic-UHF: Total Efficeincy

Antipodal Chopped Vivaldi (10cm x 20cm, 100ohm)

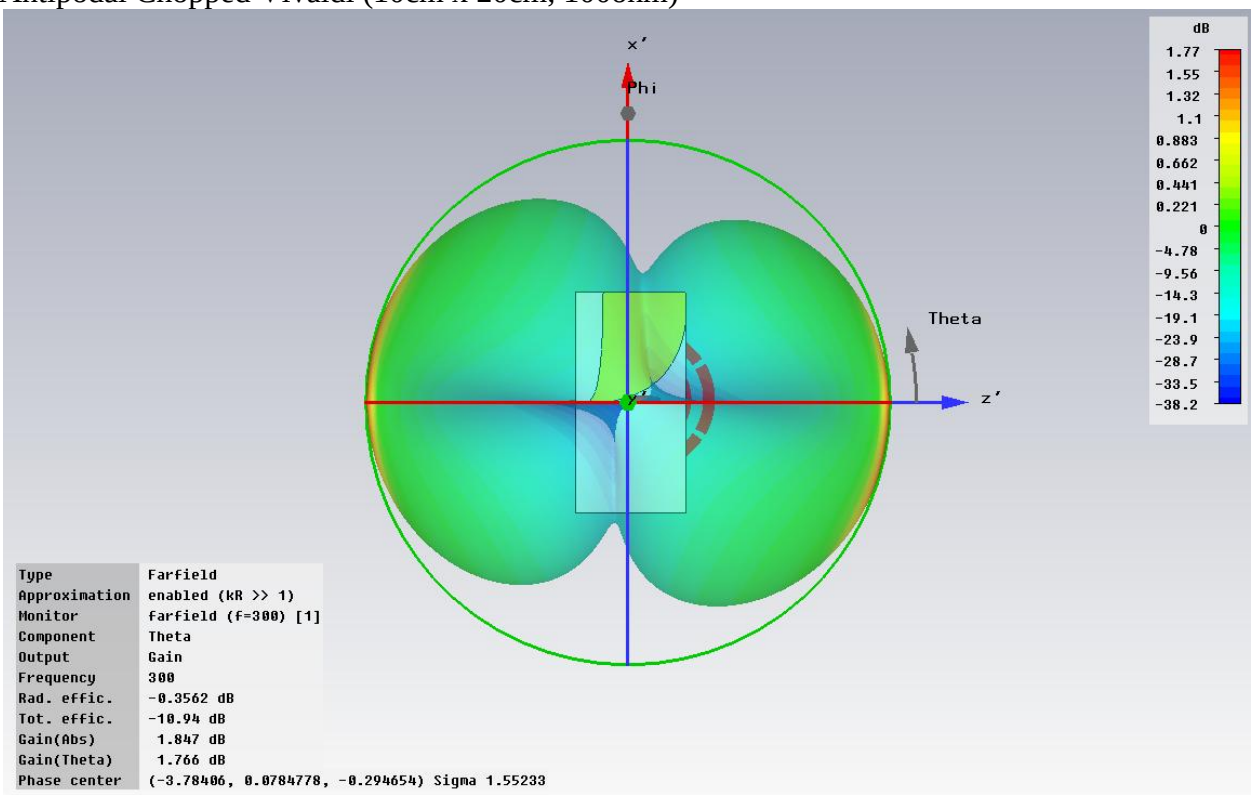

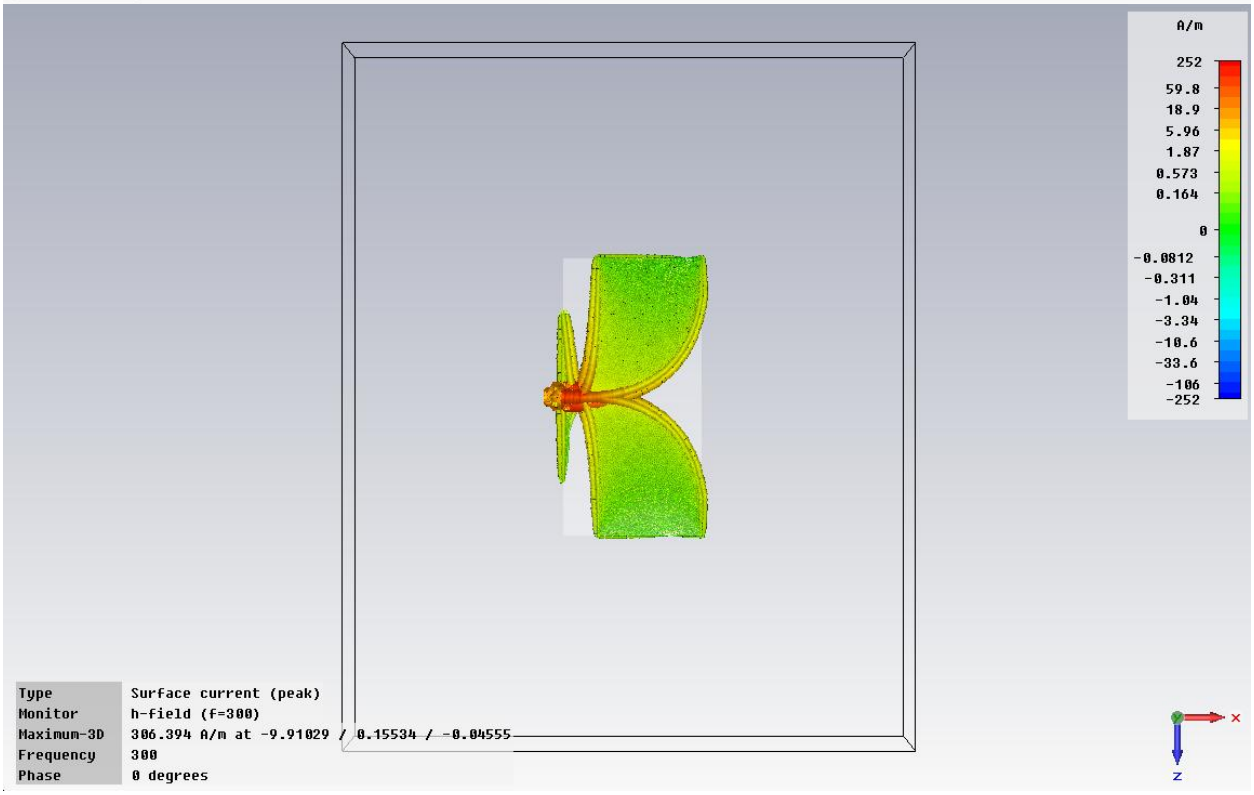

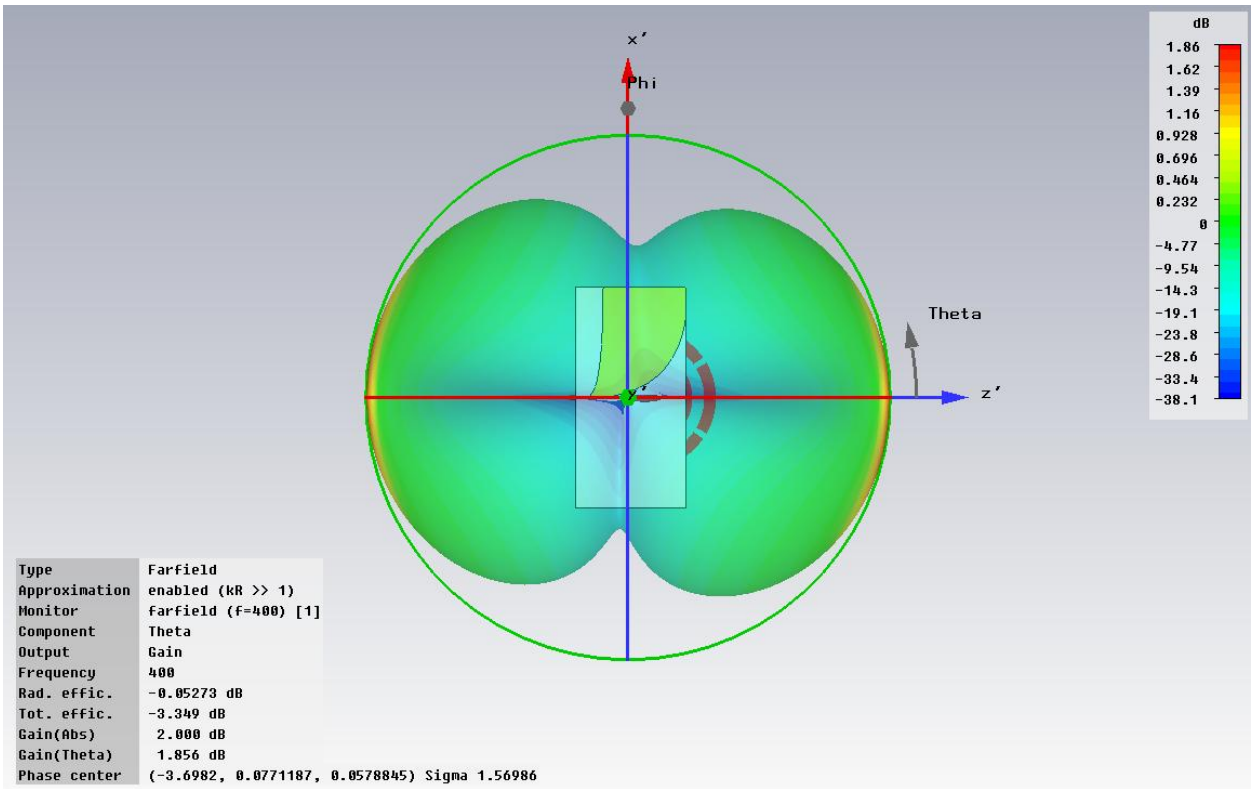

Type	Farfield
Approximation	enabled (kR >> 1)
Monitor	farfield (f=400) [1]
Component	Theta
Output	Gain
Frequency	400
Rad. effic.	-0.05273 dB
Tot. effic.	-3.349 dB
Gain(Abs)	2.000 dB
Gain(Theta)	1.856 dB
Phase center	(-3.6982, 0.0771187, 0.0578845) Sigma 1.56986

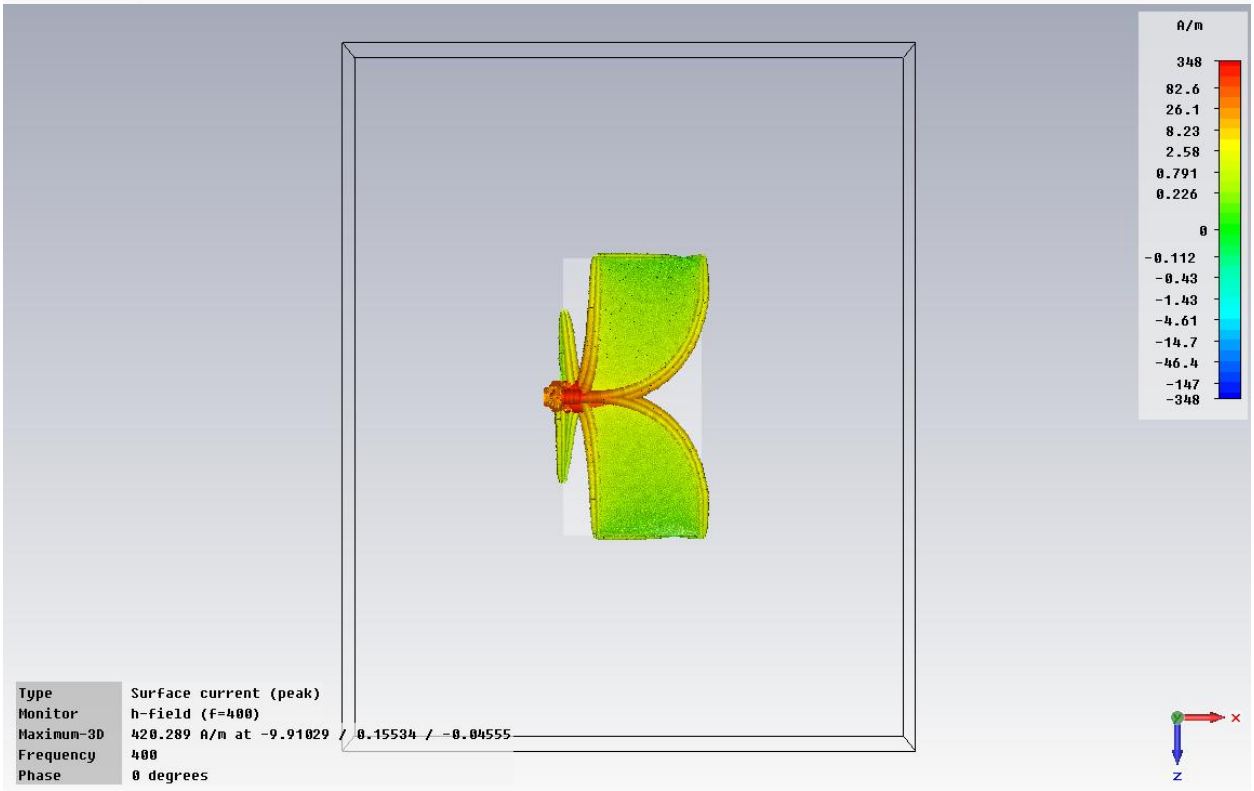

Type	Surface current (peak)
Monitor	h-field (f=400)
Maximum-3D	420.289 A/m at -9.91029 / 0.15534 / -0.04555
Frequency	400
Phase	0 degrees

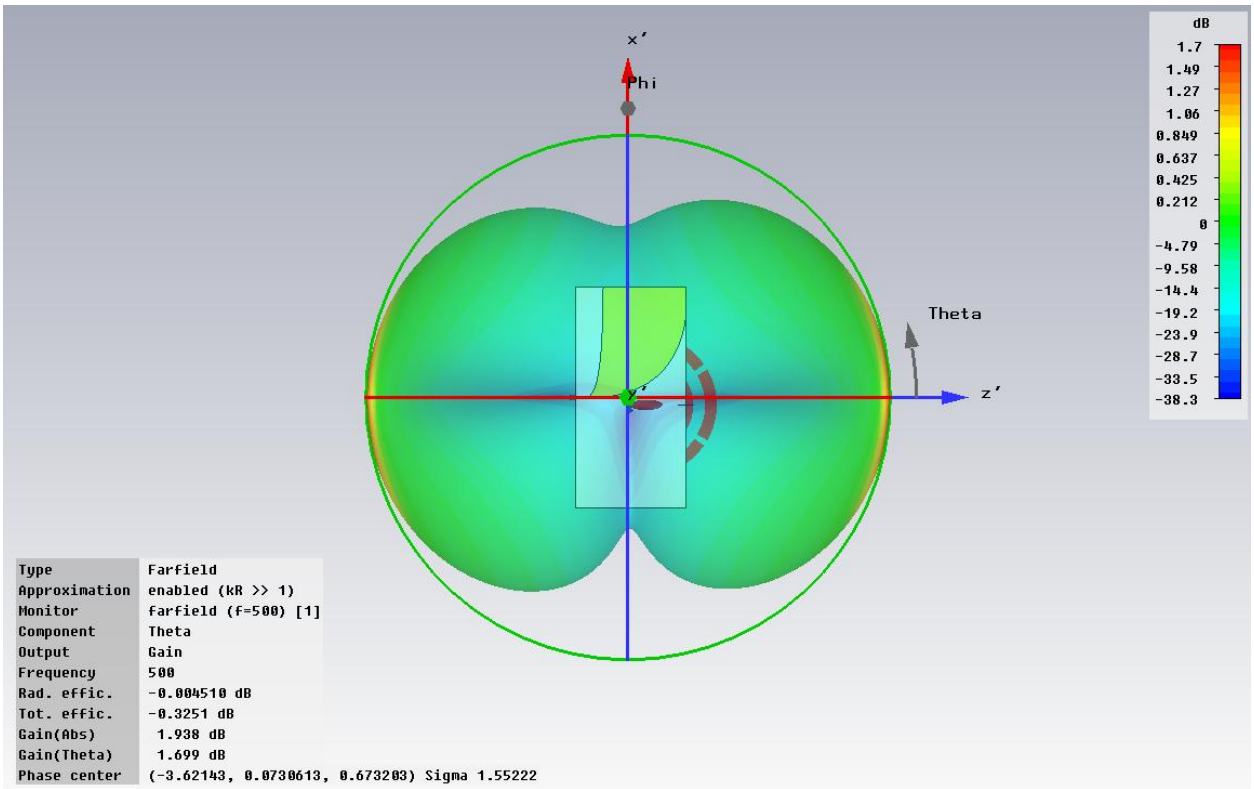
x'
Phi
Theta
z'
dB
1.7
1.49
1.27
1.06
0.849
0.637
0.425
0.212
0
-4.79
-9.58
-14.4
-19.2
-23.9
-28.7
-33.5
-38.3
Type Farfield
Approximation enabled (kR >> 1)
Monitor farfield (f=500) [1]
Component Theta
Output Gain
Frequency 500
Rad. effic. -0.004510 dB
Tot. effic. -0.3251 dB
Gain(Abs) 1.938 dB
Gain(Theta) 1.699 dB
Phase center (-3.62143, 0.0730613, 0.673203) Sigma 1.55222

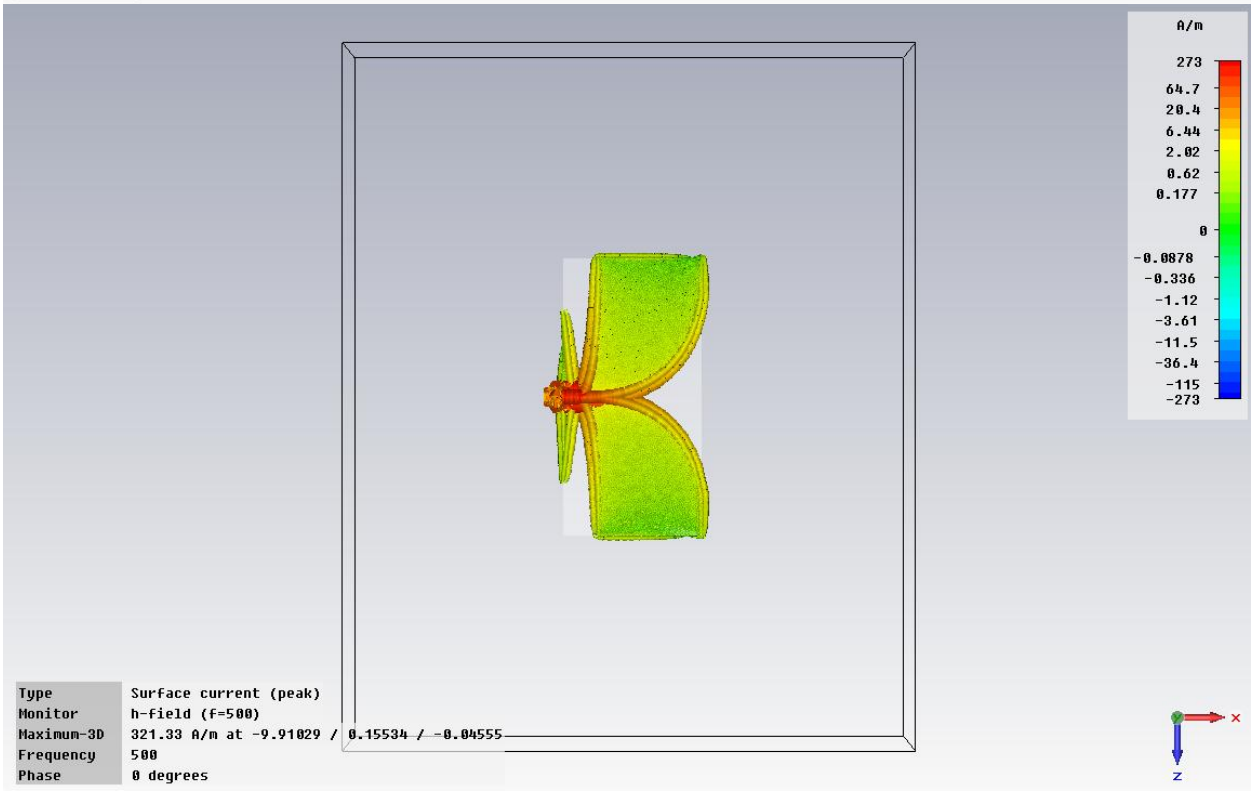
A/m
273
64.7
20.4
6.44
2.02
0.62
0.177
0
-0.0878
-0.336
-1.12
-3.61
-11.5
-36.4
-115
-273
Type Surface current (peak)
Monitor h-field (f=500)
Maximum-3D 321.33 A/m at -9.91029 / 0.15534 / -0.04555
Frequency 500
Phase 0 degrees
x
z

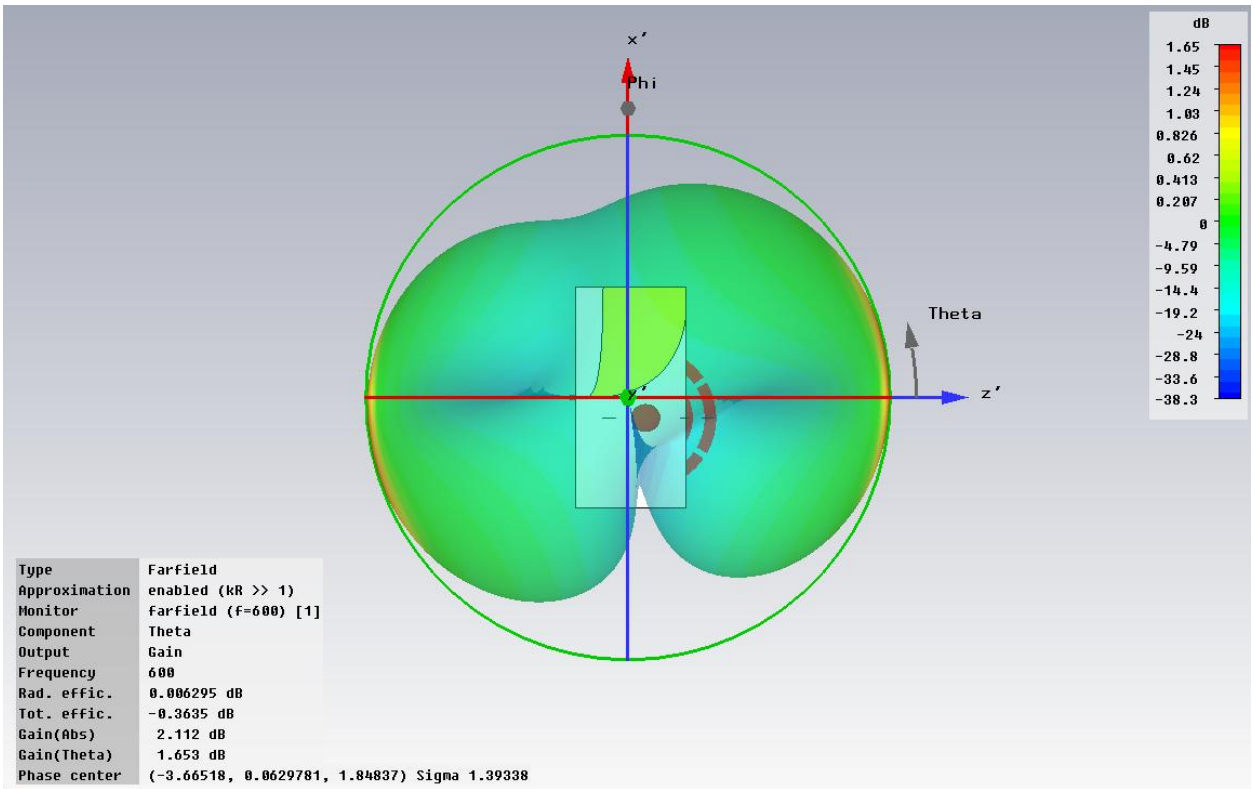

Type	Farfield
Approximation	enabled (kR >> 1)
Monitor	farfield (f=600) [1]
Component	Theta
Output	Gain
Frequency	600
Rad. effic.	0.006295 dB
Tot. effic.	-0.3635 dB
Gain(Abs)	2.112 dB
Gain(Theta)	1.653 dB
Phase center	(-3.66518, 0.0629781, 1.84837) Sigma 1.39338

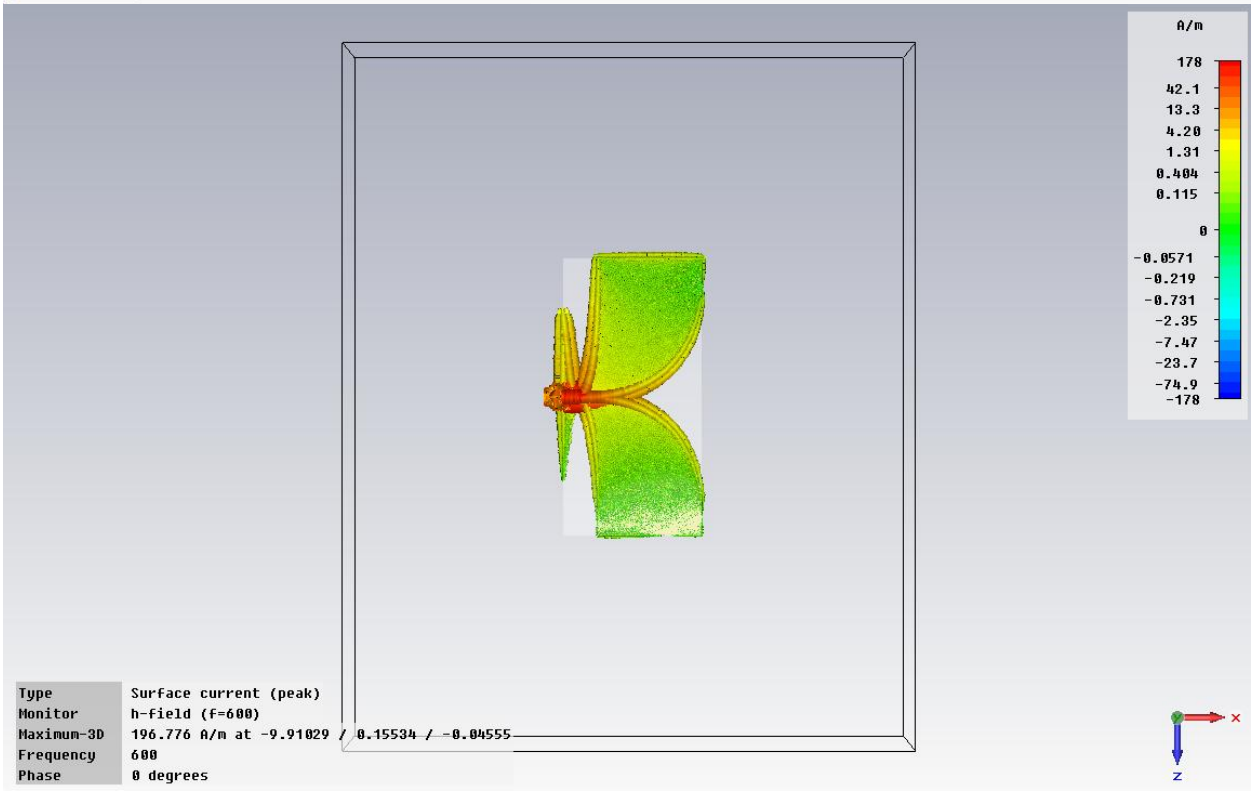

Type	Surface current (peak)
Monitor	h-field (f=600)
Maximum-3D	196.776 A/m at -9.91029 / 0.15534 / -0.04555
Frequency	600
Phase	0 degrees

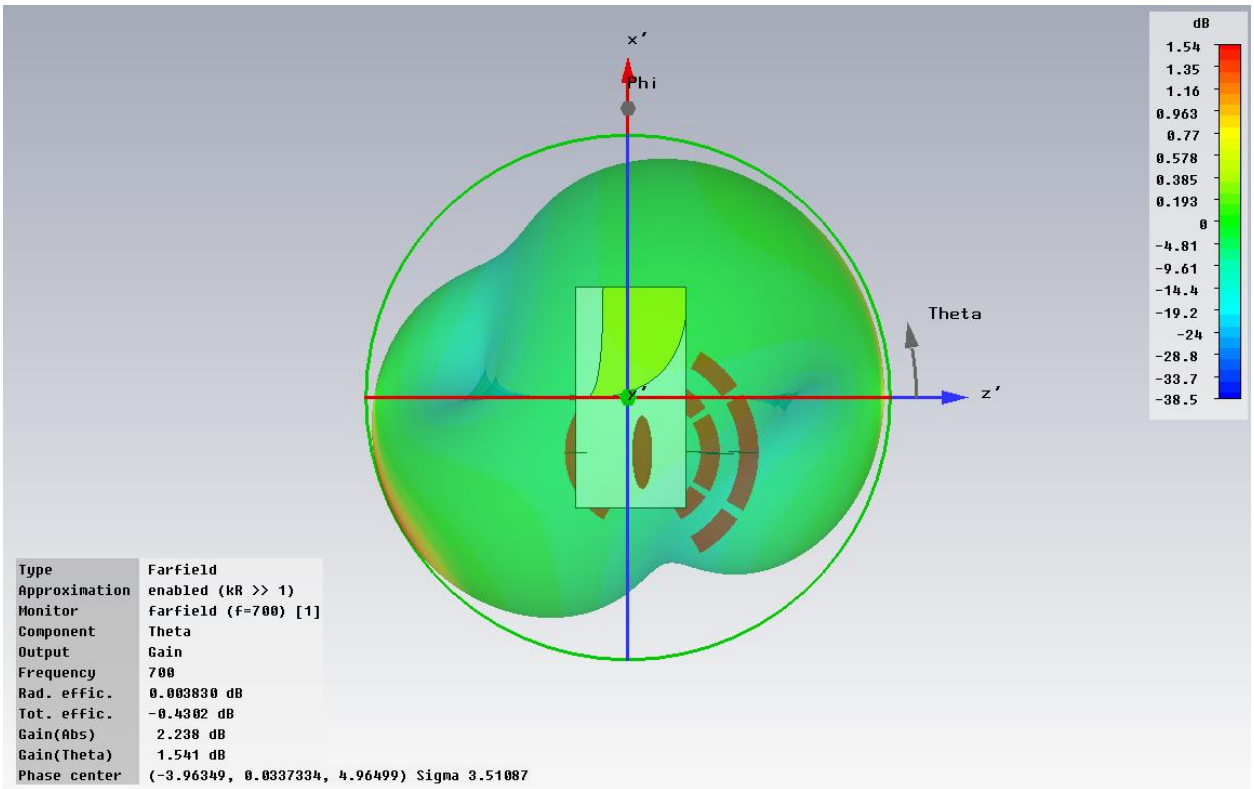

Type	Farfield
Approximation	enabled (kR >> 1)
Monitor	farfield (f=700) [1]
Component	Theta
Output	Gain
Frequency	700
Rad. effic.	0.003830 dB
Tot. effic.	-0.4302 dB
Gain(Abs)	2.238 dB
Gain(Theta)	1.541 dB
Phase center	(-3.96349, 0.0337334, 4.96499) Sigma 3.51087

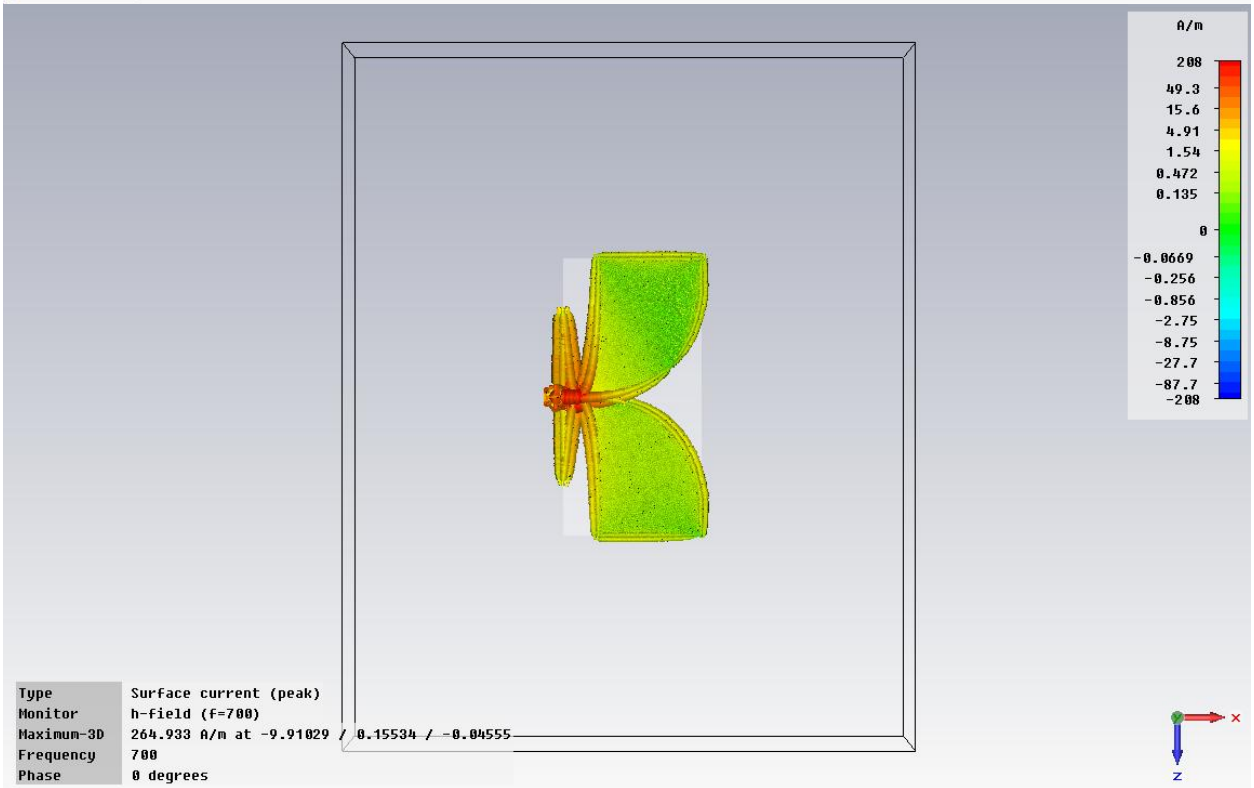

Type	Surface current (peak)
Monitor	h-field (f=700)
Maximum-3D	264.933 A/m at -9.91029 / 0.15534 / -0.04555
Frequency	700
Phase	0 degrees

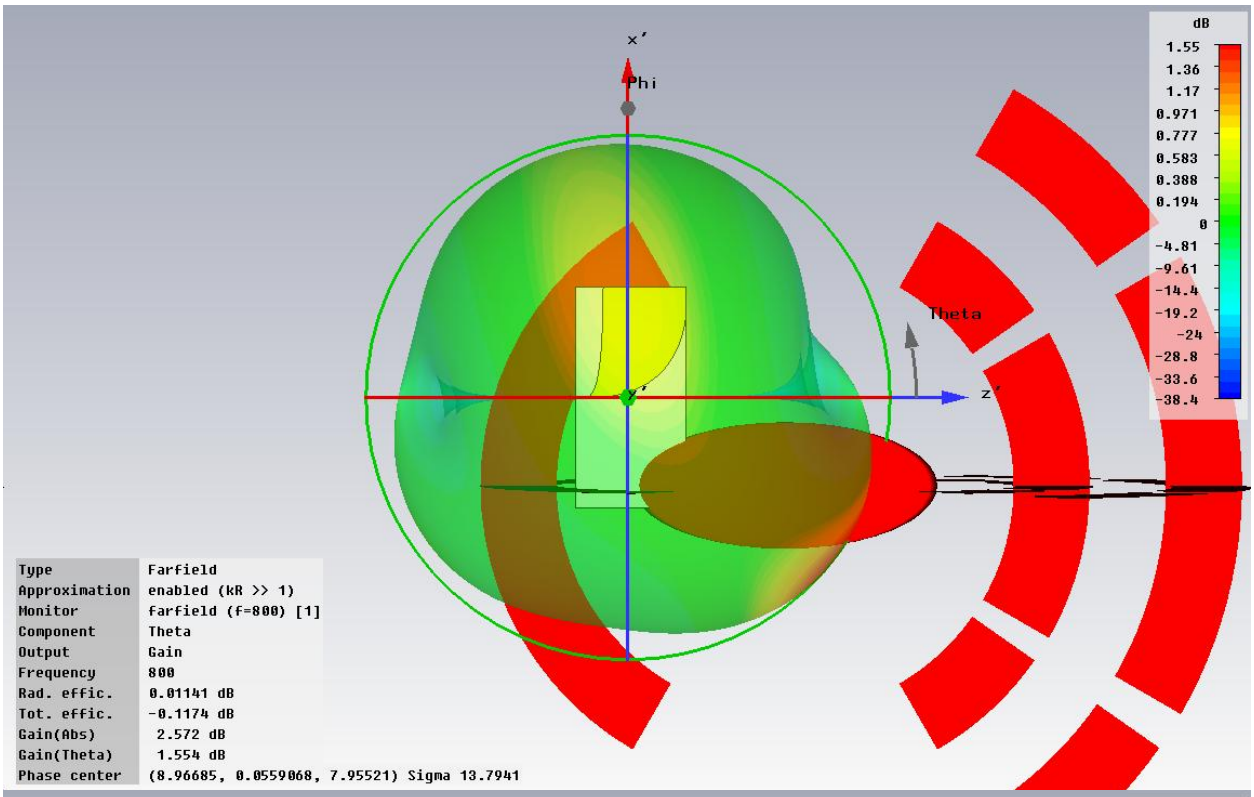
x'
Phi
Theta
z'
y'
dB
1.55
1.36
1.17
0.971
0.777
0.583
0.388
0.194
0
-4.81
-9.61
-14.4
-19.2
-24
-28.8
-33.6
-38.4
Type Farfield
Approximation enabled (kR >> 1)
Monitor farfield (f=800) [1]
Component Theta
Output Gain
Frequency 800
Rad. effic. 0.01141 dB
Tot. effic. -0.1174 dB
Gain(Abs) 2.572 dB
Gain(Theta) 1.554 dB
Phase center (8.96685, 0.0559068, 7.95521) Sigma 13.7941

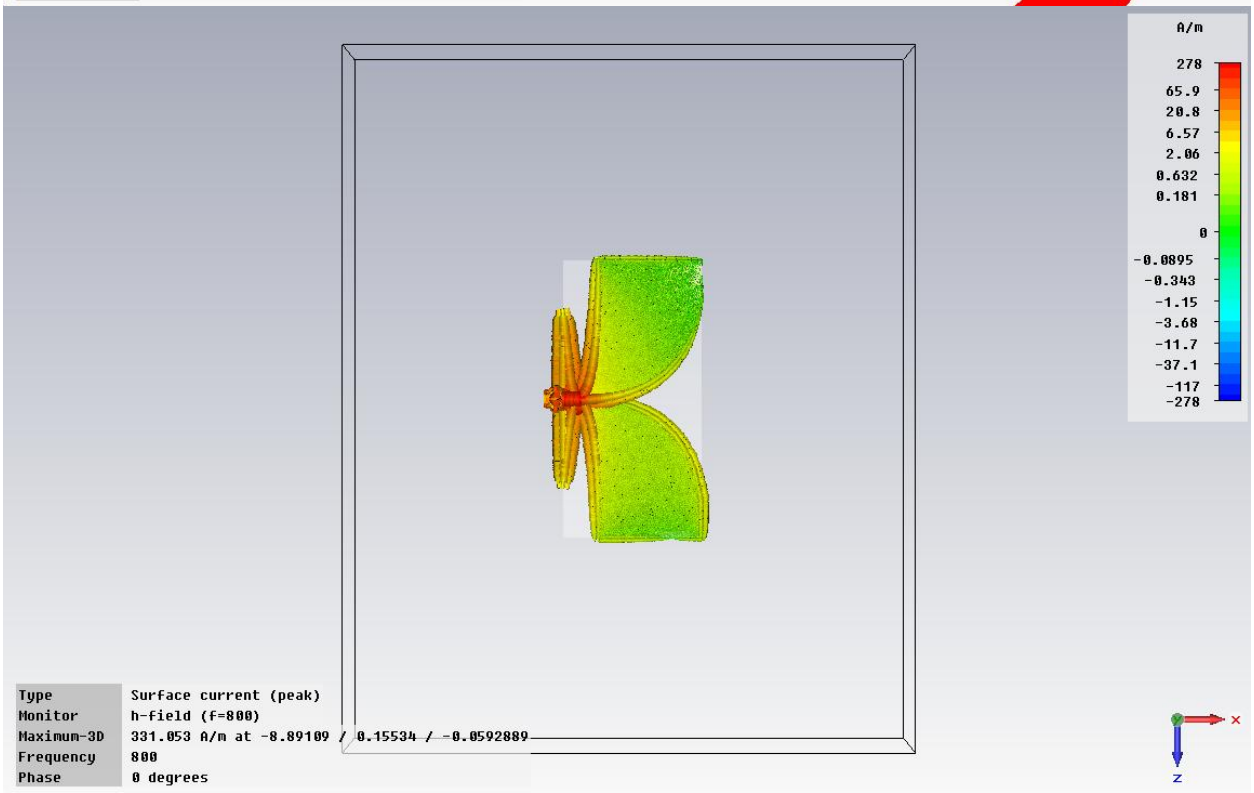
A/m
278
65.9
20.8
6.57
2.06
0.632
0.181
0
-0.0895
-0.343
-1.15
-3.68
-11.7
-37.1
-117
-278
Type Surface current (peak)
Monitor h-field (f=800)
Maximum-3D 331.053 A/m at -8.89109 / 0.15534 / -0.0592889
Frequency 800
Phase 0 degrees
x
z

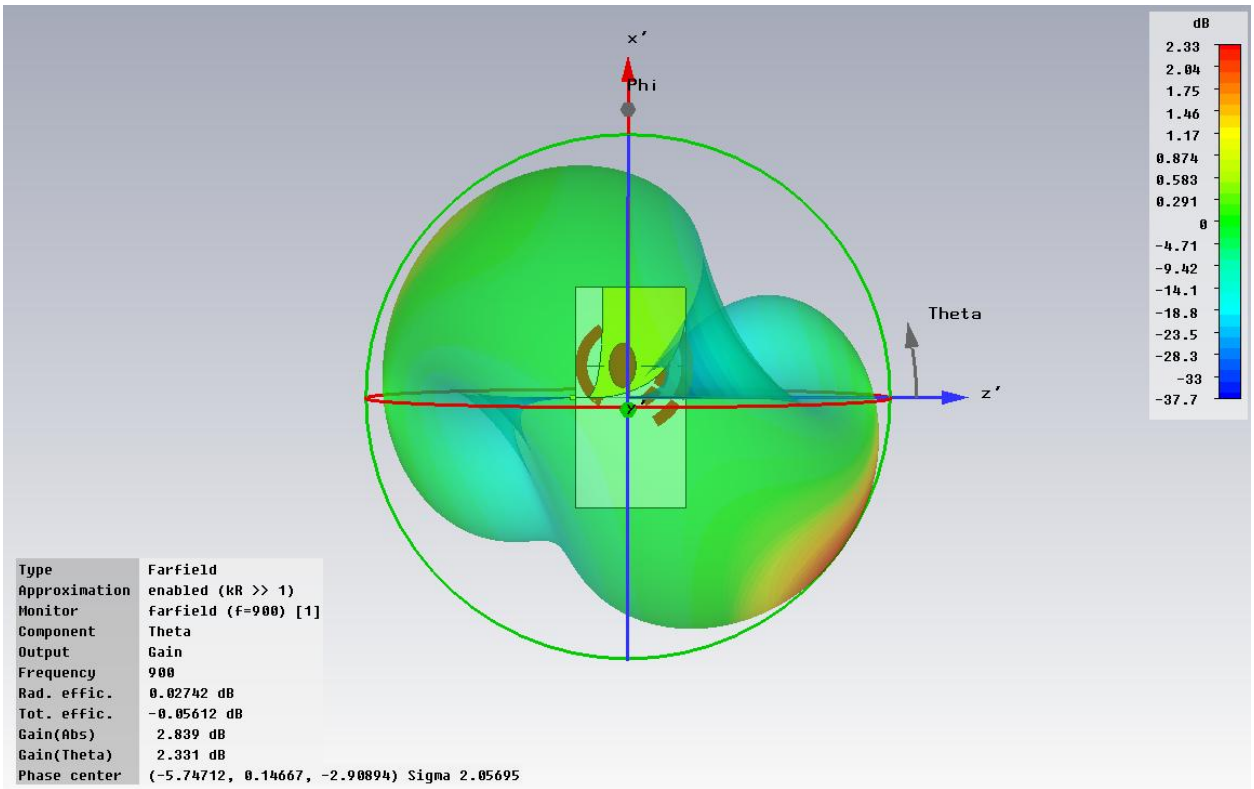
x'
Phi
Theta
z'
dB
2.33
2.04
1.75
1.46
1.17
0.874
0.583
0.291
0
-4.71
-9.42
-14.1
-18.8
-23.5
-28.3
-33
-37.7
Type Farfield
Approximation enabled (kR >> 1)
Monitor farfield (f=900) [1]
Component Theta
Output Gain
Frequency 900
Rad. effic. 0.02742 dB
Tot. effic. -0.05612 dB
Gain(Abs) 2.839 dB
Gain(Theta) 2.331 dB
Phase center (-5.74712, 0.14667, -2.90894) Sigma 2.05695

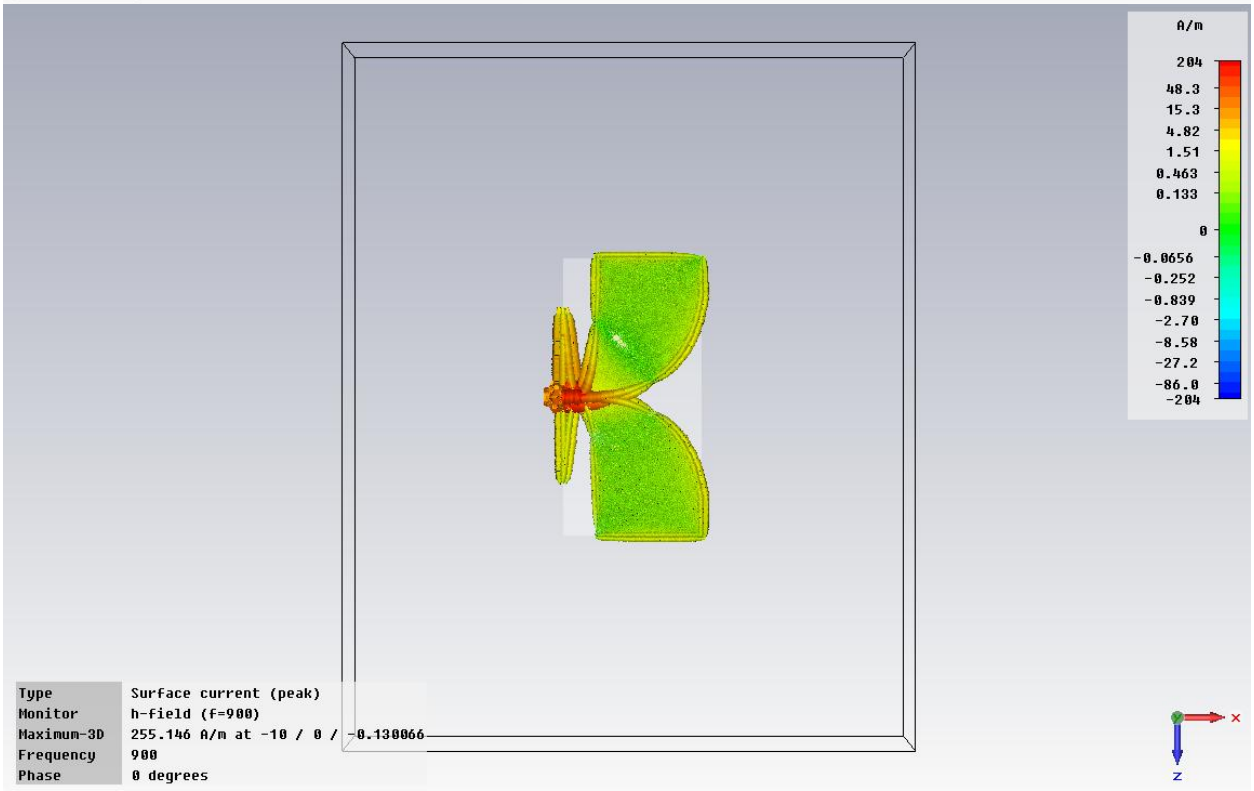
A/m
204
48.3
15.3
4.82
1.51
0.463
0.133
0
-0.0656
-0.252
-0.839
-2.70
-8.58
-27.2
-86.0
-204
Type Surface current (peak)
Monitor h-field (f=900)
Maximum-3D 255.146 A/m at -10 / 0 / -0.130066
Frequency 900
Phase 0 degrees
x
z

Antipodal Chopped Bunny Ears Vivaldi (10cm x 20cm, 100ohm)

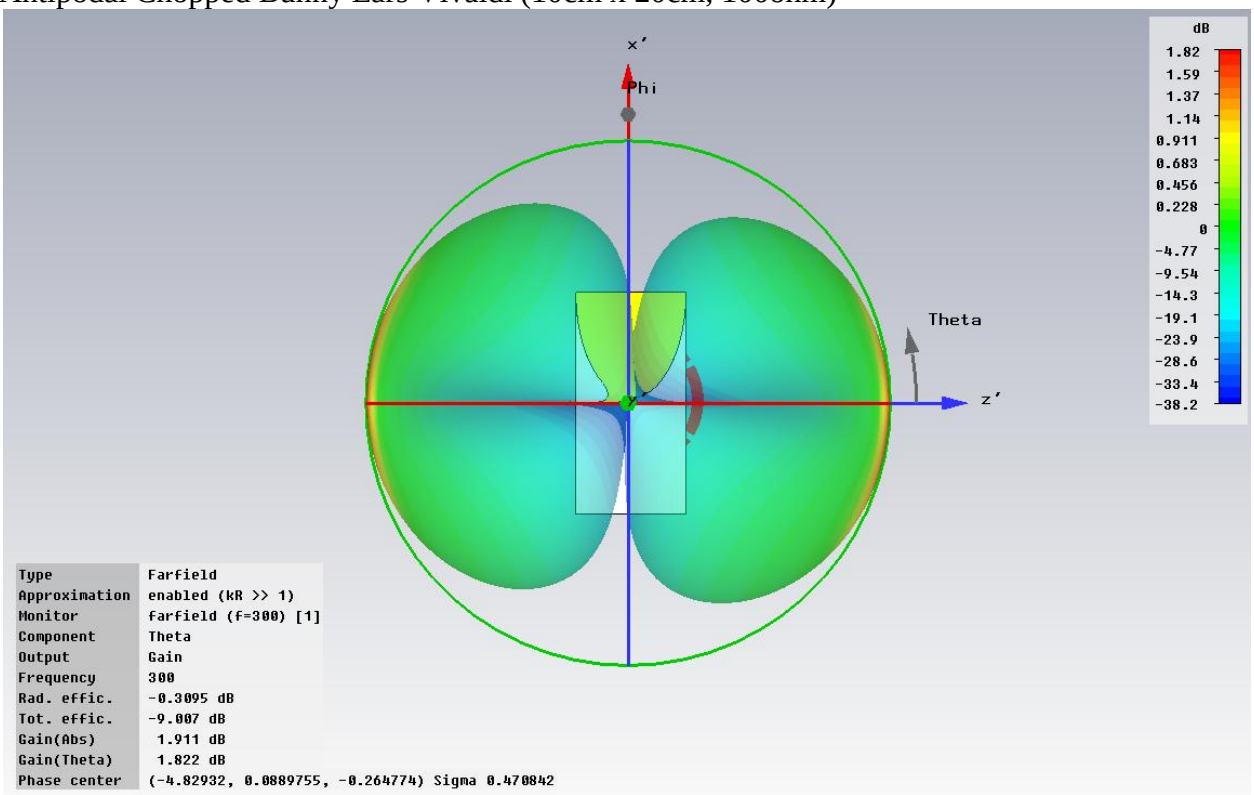

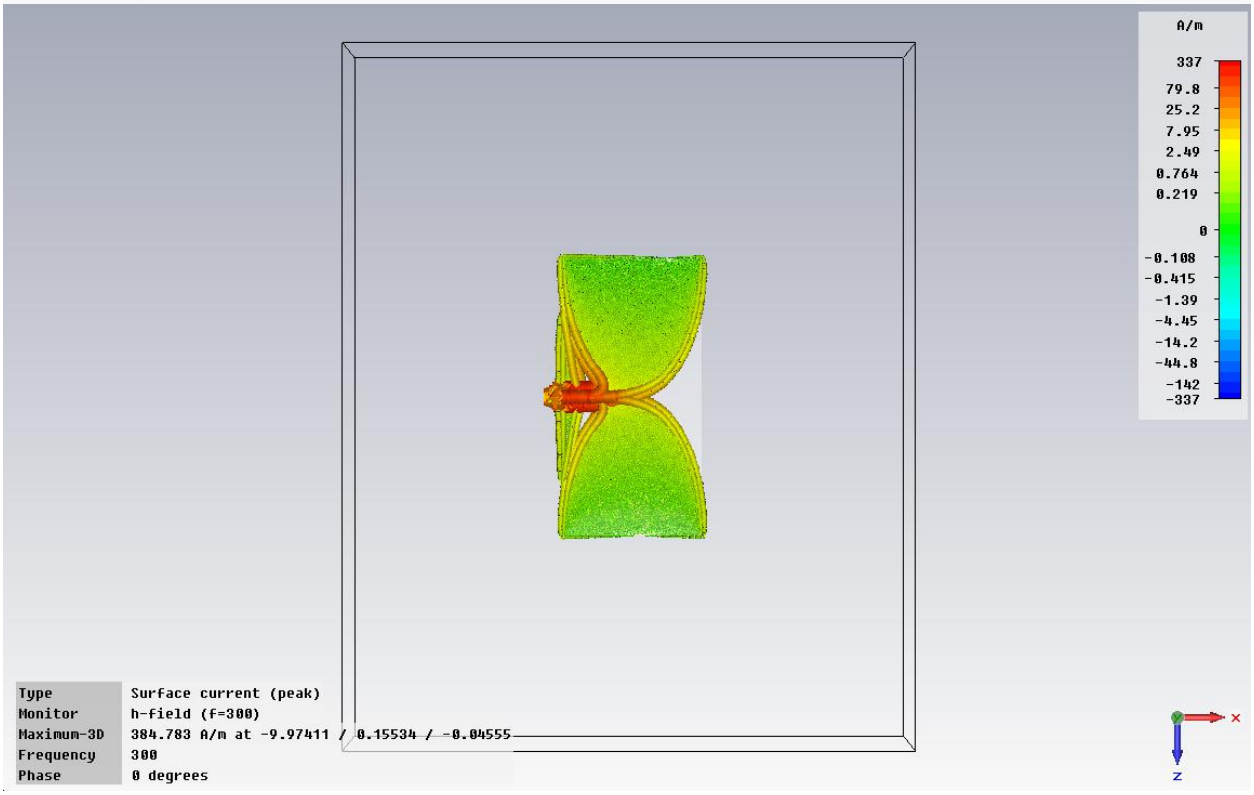

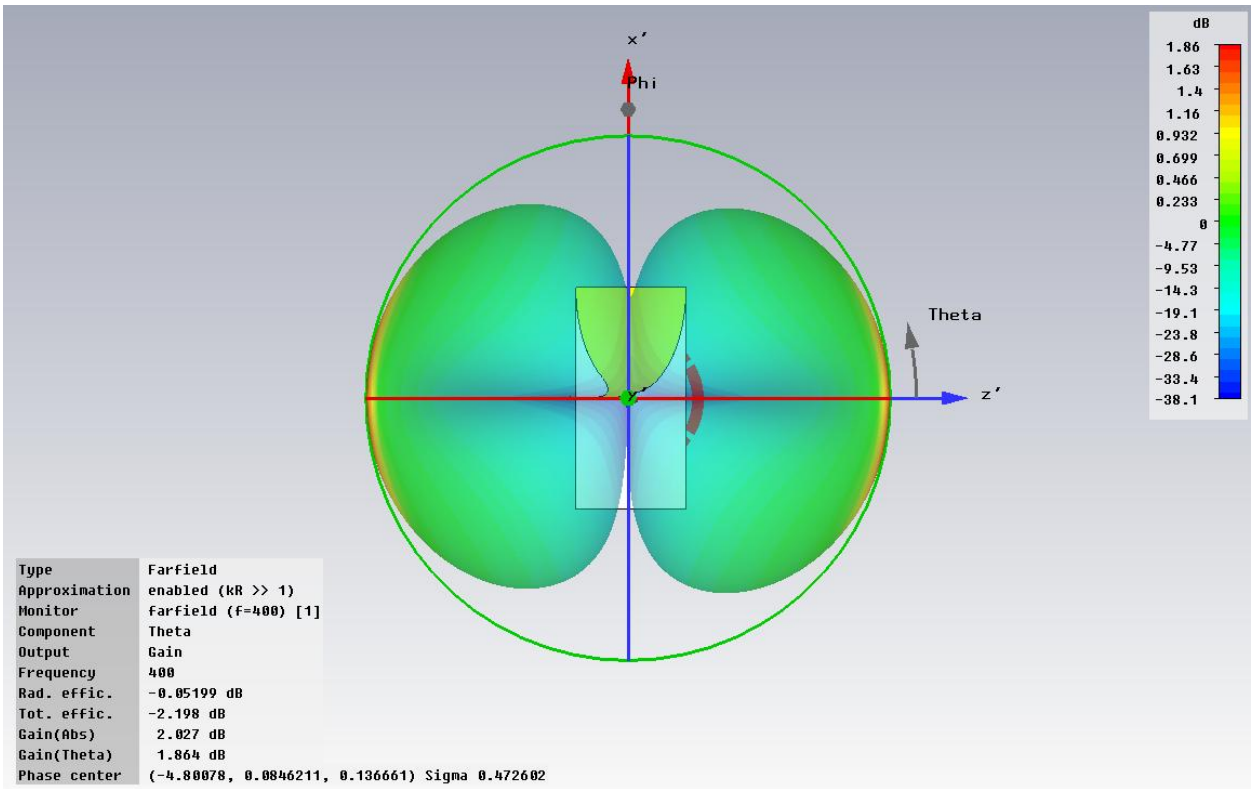

Type	Farfield
Approximation	enabled (kR >> 1)
Monitor	farfield (f=400) [1]
Component	Theta
Output	Gain
Frequency	400
Rad. effic.	-0.05199 dB
Tot. effic.	-2.198 dB
Gain(Abs)	2.027 dB
Gain(Theta)	1.864 dB
Phase center	(-4.80078, 0.0846211, 0.136661) Sigma 0.472602

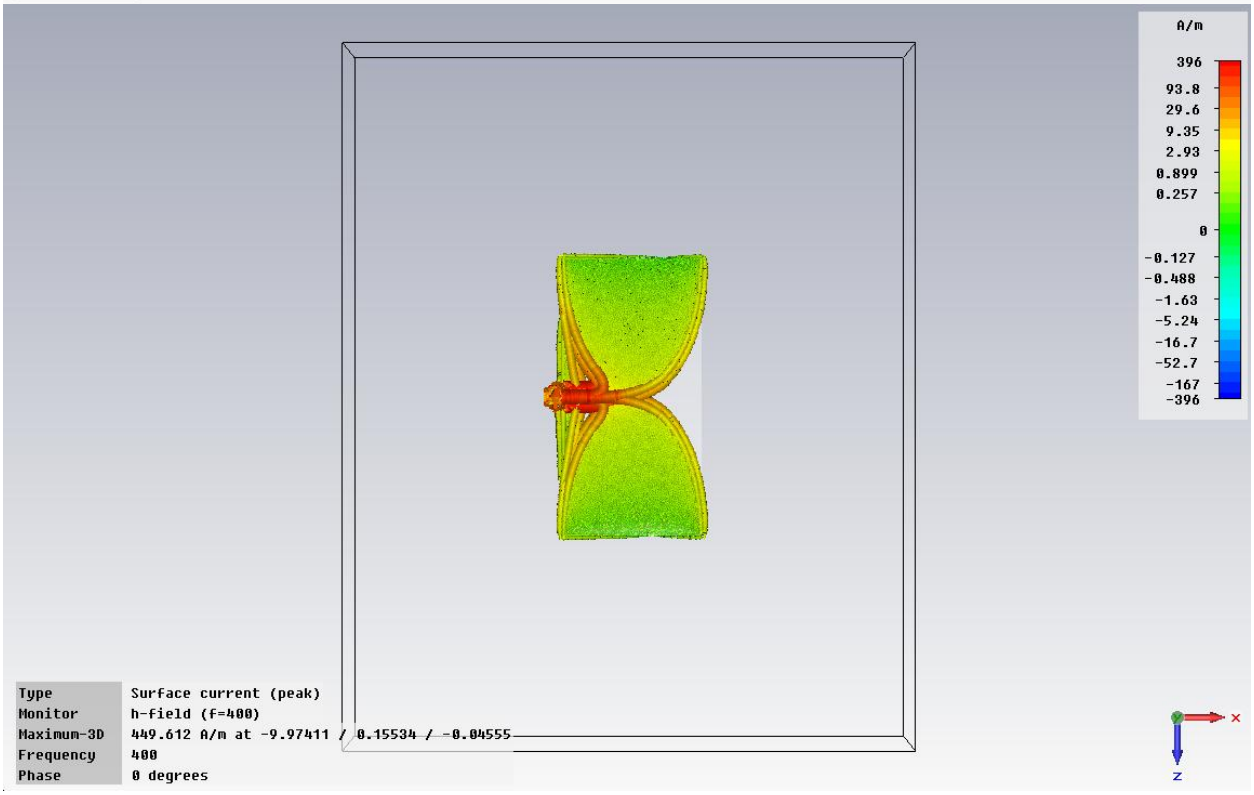

Type	Surface current (peak)
Monitor	h-field (f=400)
Maximum-3D	449.612 A/m at -9.97411 / 0.15534 / -0.04555
Frequency	400
Phase	0 degrees

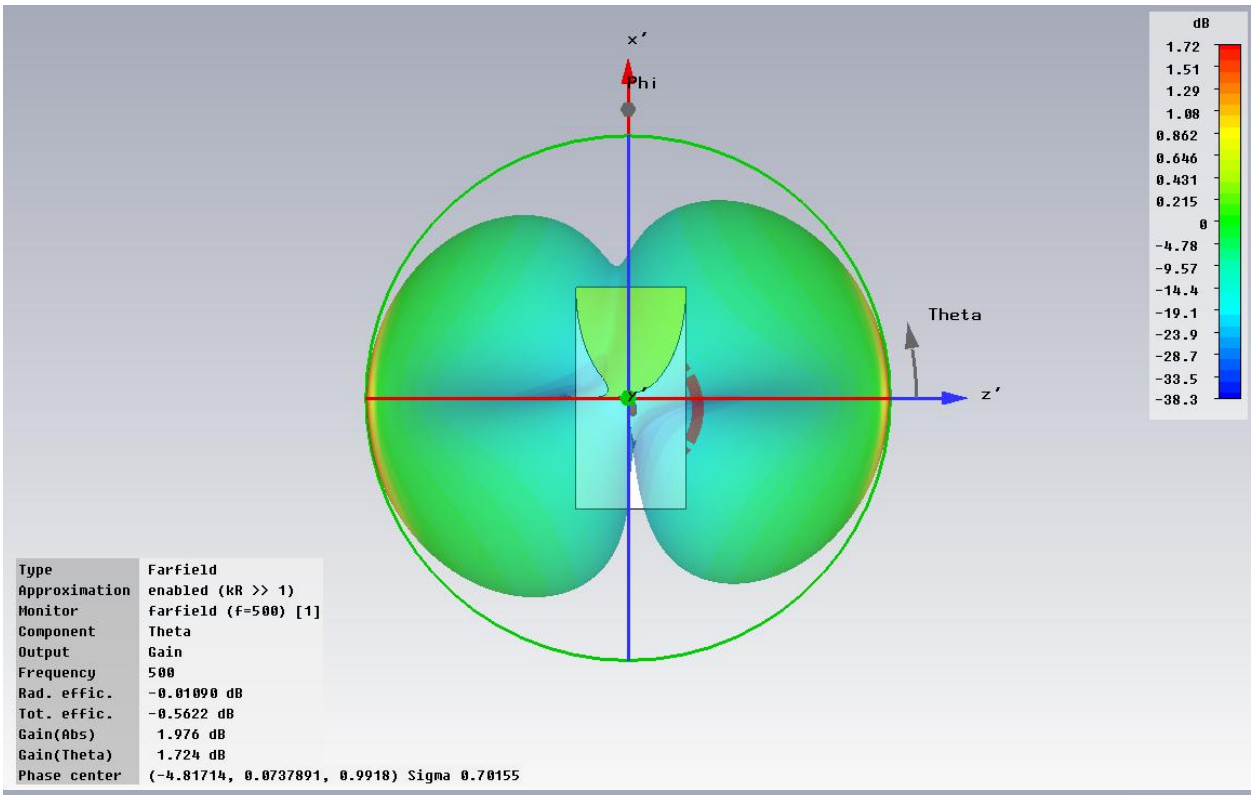

Type	Farfield
Approximation	enabled (kR >> 1)
Monitor	farfield (f=500) [1]
Component	Theta
Output	Gain
Frequency	500
Rad. effic.	-0.01090 dB
Tot. effic.	-0.5622 dB
Gain(Abs)	1.976 dB
Gain(Theta)	1.724 dB
Phase center	(-4.81714, 0.0737891, 0.9918) Sigma 0.70155

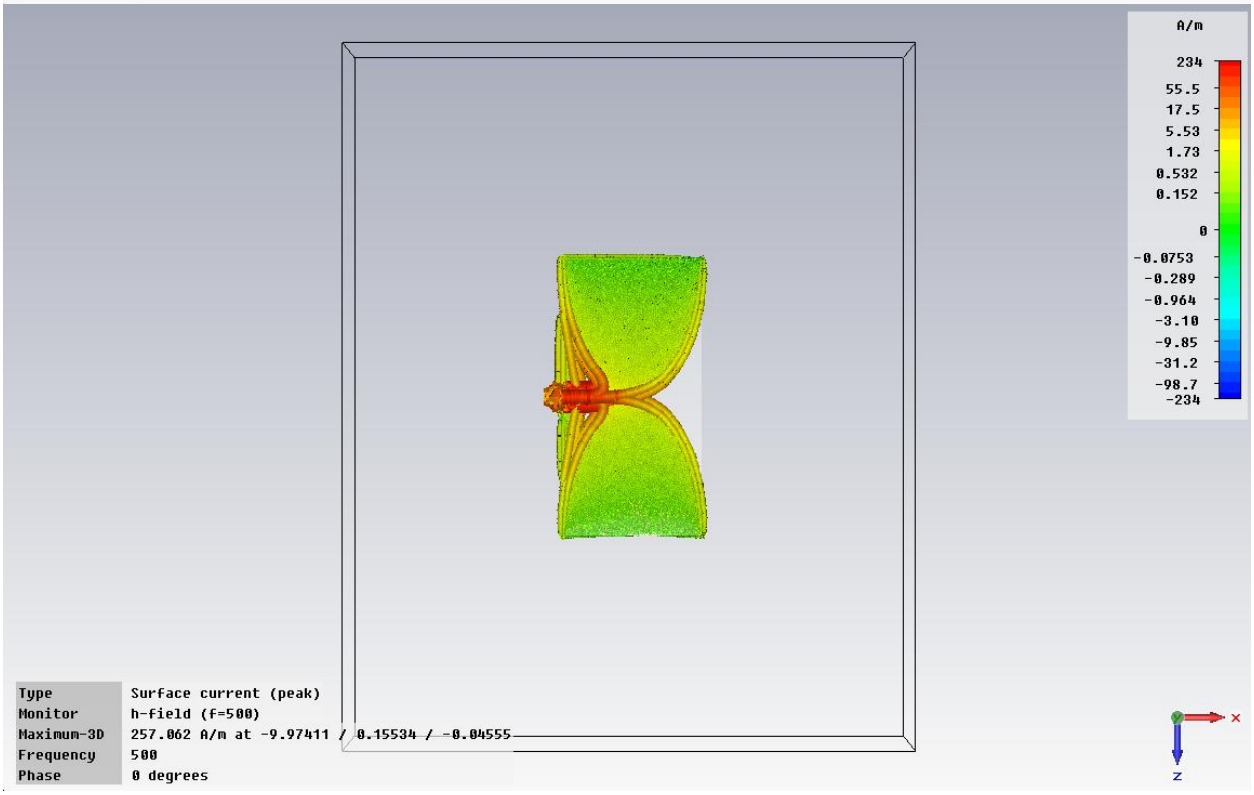

Type	Surface current (peak)
Monitor	h-field (f=500)
Maximum-3D	257.062 A/m at -9.97411 / 0.15534 / -0.04555
Frequency	500
Phase	0 degrees

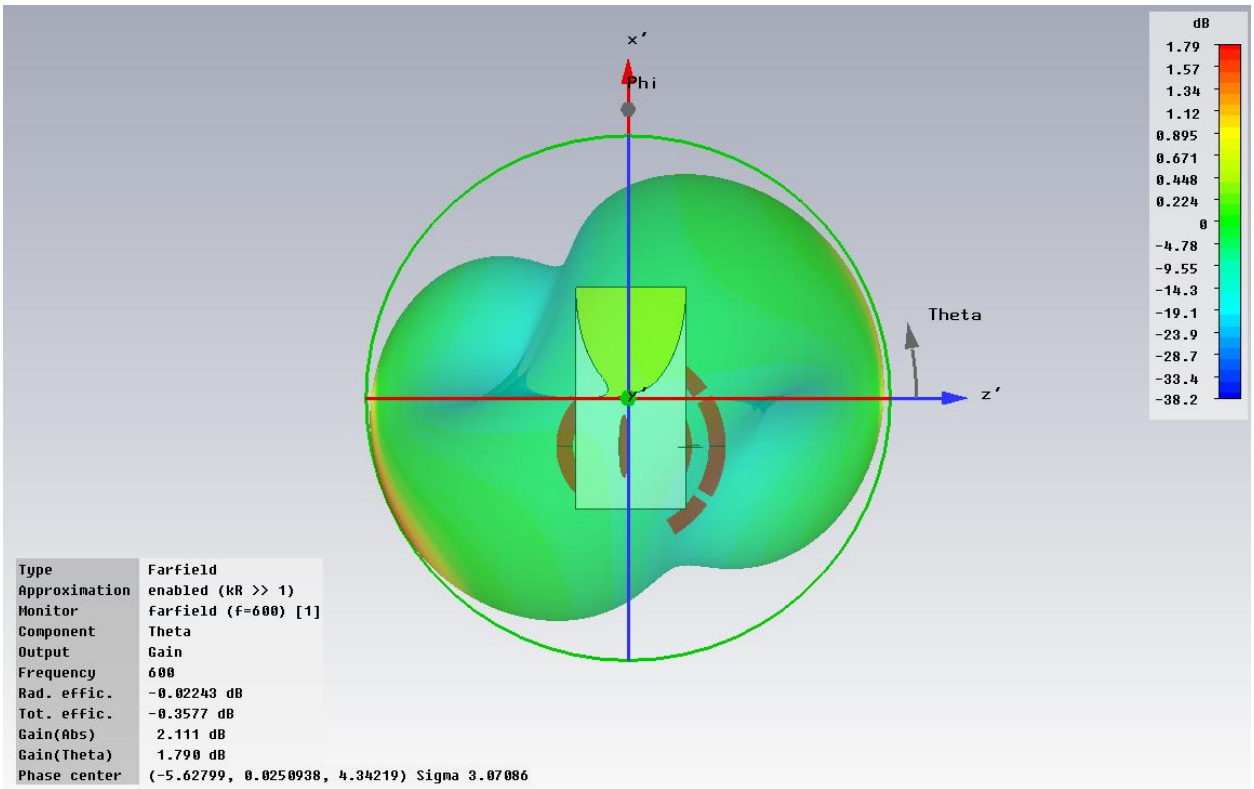
x'
Phi
Theta
z'
dB
1.79
1.57
1.34
1.12
0.895
0.671
0.448
0.224
0
-4.78
-9.55
-14.3
-19.1
-23.9
-28.7
-33.4
-38.2
Type Farfield
Approximation enabled (kR >> 1)
Monitor farfield (f=600) [1]
Component Theta
Output Gain
Frequency 600
Rad. effic. -0.02243 dB
Tot. effic. -0.3577 dB
Gain(Abs) 2.111 dB
Gain(Theta) 1.790 dB
Phase center (-5.62799, 0.0250938, 4.34219) Sigma 3.07086

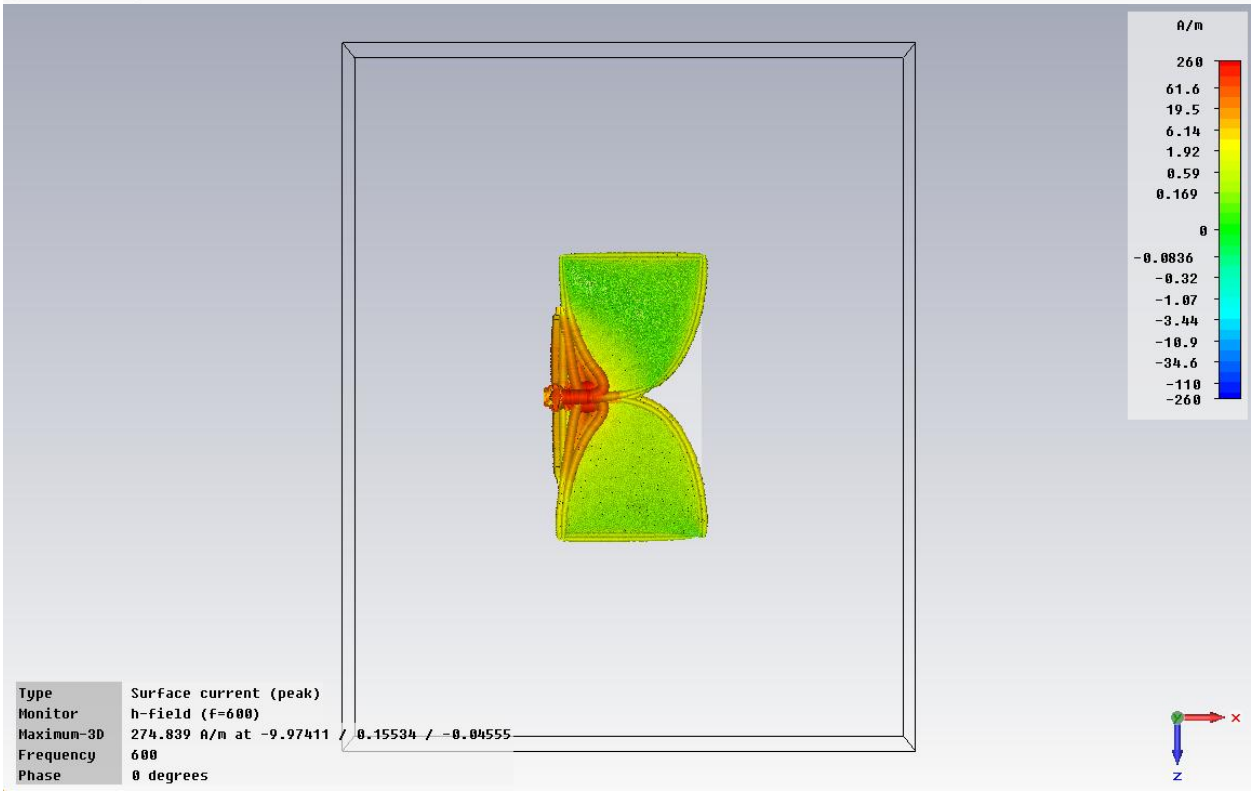
A/m
260
61.6
19.5
6.14
1.92
0.59
0.169
0
-0.0836
-0.32
-1.07
-3.44
-10.9
-34.6
-110
-260
Type Surface current (peak)
Monitor h-field (f=600)
Maximum-3D 274.839 A/m at -9.97411 / 0.15534 / -0.04555
Frequency 600
Phase 0 degrees
x
z

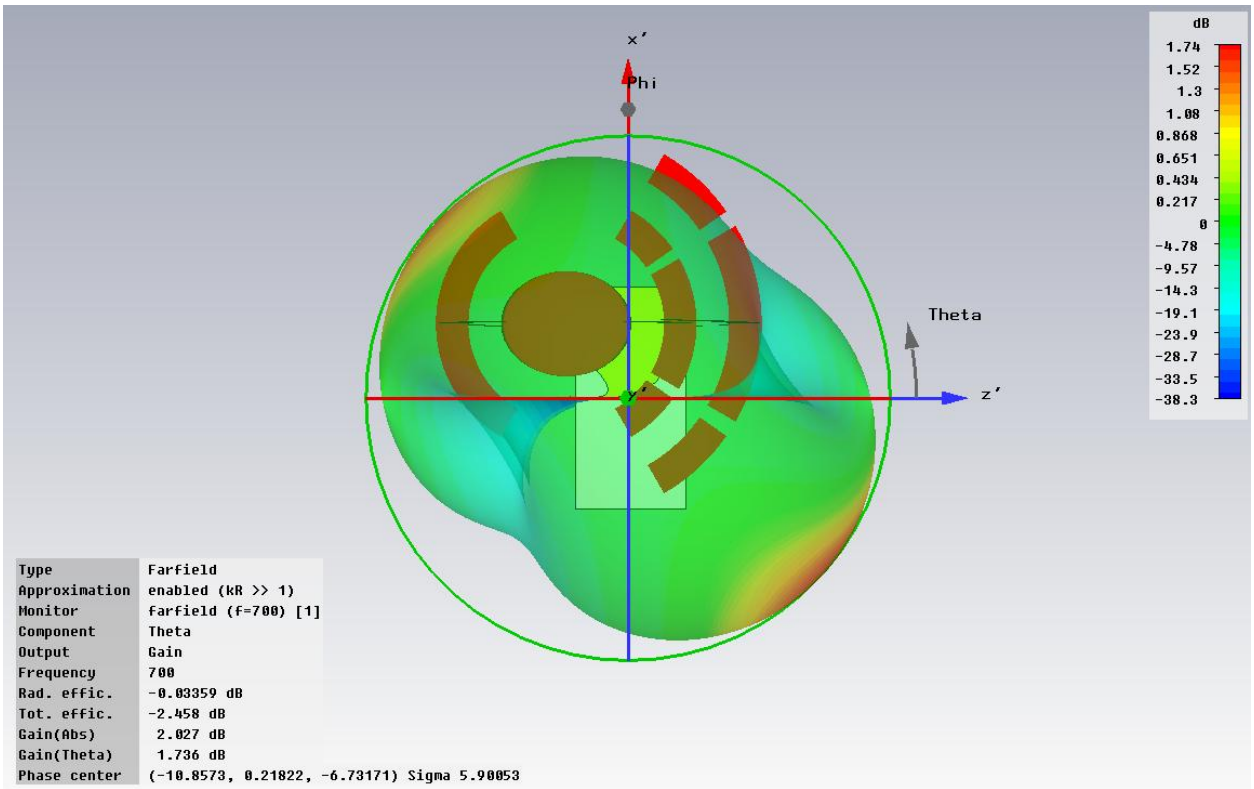
x'
Phi
Theta
z'
dB
1.74
1.52
1.3
1.08
0.868
0.651
0.434
0.217
0
-4.78
-9.57
-14.3
-19.1
-23.9
-28.7
-33.5
-38.3
Type Farfield
Approximation enabled (kR >> 1)
Monitor farfield (f=700) [1]
Component Theta
Output Gain
Frequency 700
Rad. effic. -0.03359 dB
Tot. effic. -2.458 dB
Gain(Abs) 2.027 dB
Gain(Theta) 1.736 dB
Phase center (-10.8573, 0.21822, -6.73171) Sigma 5.90053

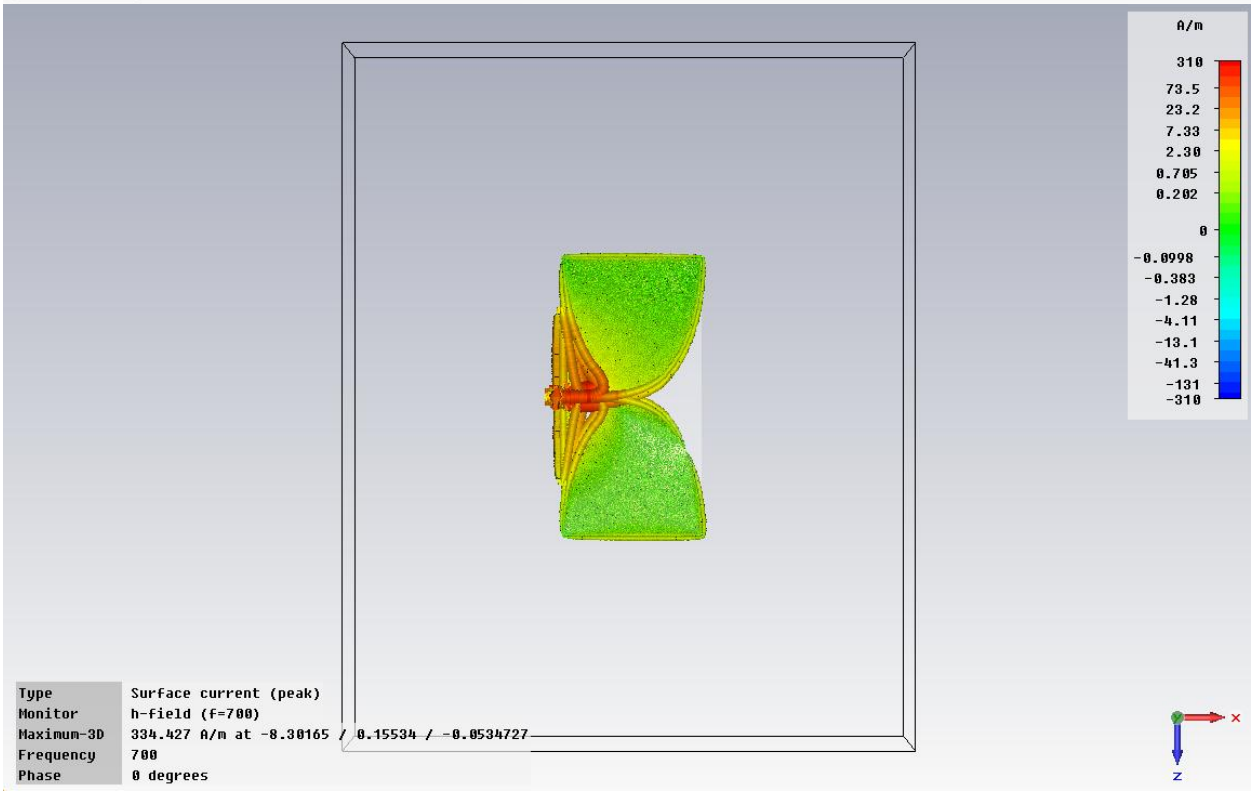
A/m
310
73.5
23.2
7.33
2.30
0.705
0.202
0
-0.0998
-0.383
-1.28
-4.11
-13.1
-41.3
-131
-310
Type Surface current (peak)
Monitor h-field (f=700)
Maximum-3D 334.427 A/m at -8.30165 / 0.15534 / -0.0534727
Frequency 700
Phase 0 degrees
x
z

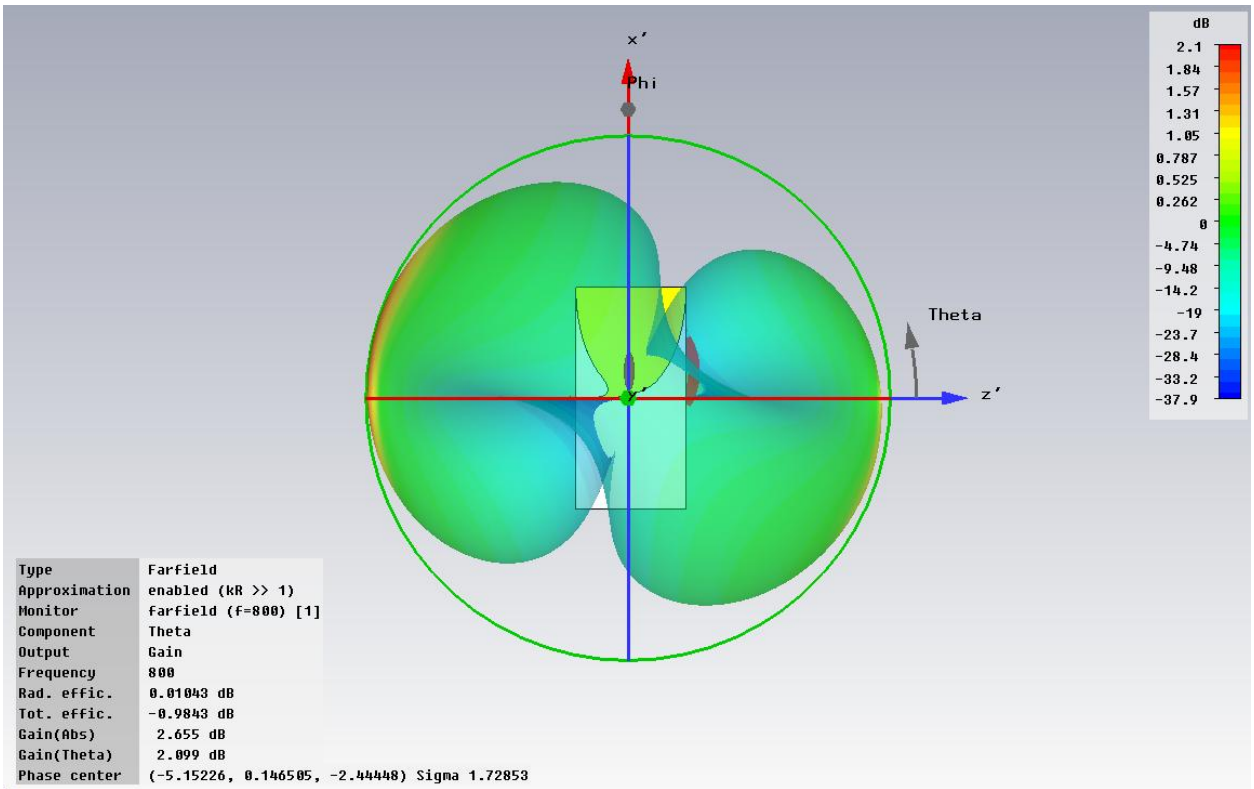
x'
Phi
Theta
z'
dB
2.1
1.84
1.57
1.31
1.05
0.787
0.525
0.262
0
-4.74
-9.48
-14.2
-19
-23.7
-28.4
-33.2
-37.9
Type Farfield
Approximation enabled (kR >> 1)
Monitor farfield (f=800) [1]
Component Theta
Output Gain
Frequency 800
Rad. effic. 0.01043 dB
Tot. effic. -0.9843 dB
Gain(Abs) 2.655 dB
Gain(Theta) 2.099 dB
Phase center (-5.15226, 0.146505, -2.44448) Sigma 1.72853

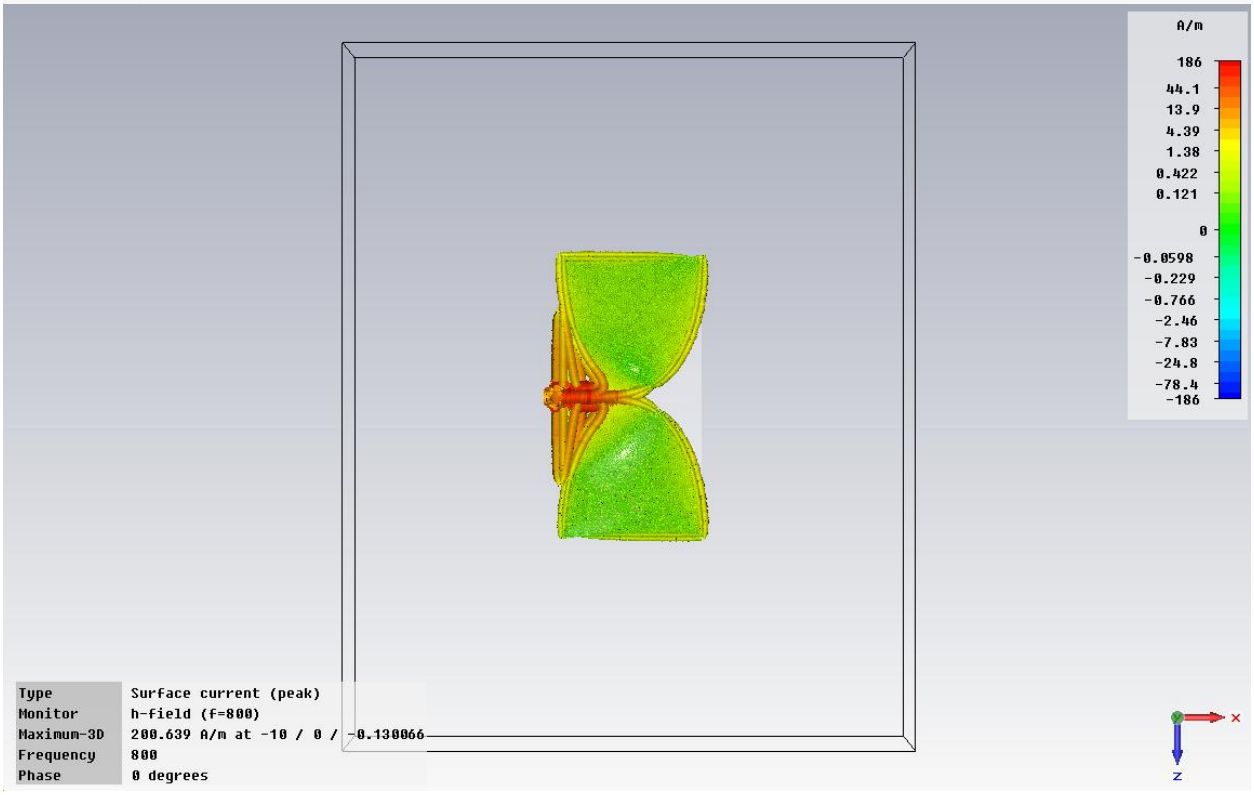
A/m
186
44.1
13.9
4.39
1.38
0.422
0.121
0
-0.0598
-0.229
-0.766
-2.46
-7.83
-24.8
-78.4
-186
Type Surface current (peak)
Monitor h-field (f=800)
Maximum-3D 200.639 A/m at -10 / 0 / -0.130066
Frequency 800
Phase 0 degrees
x
z

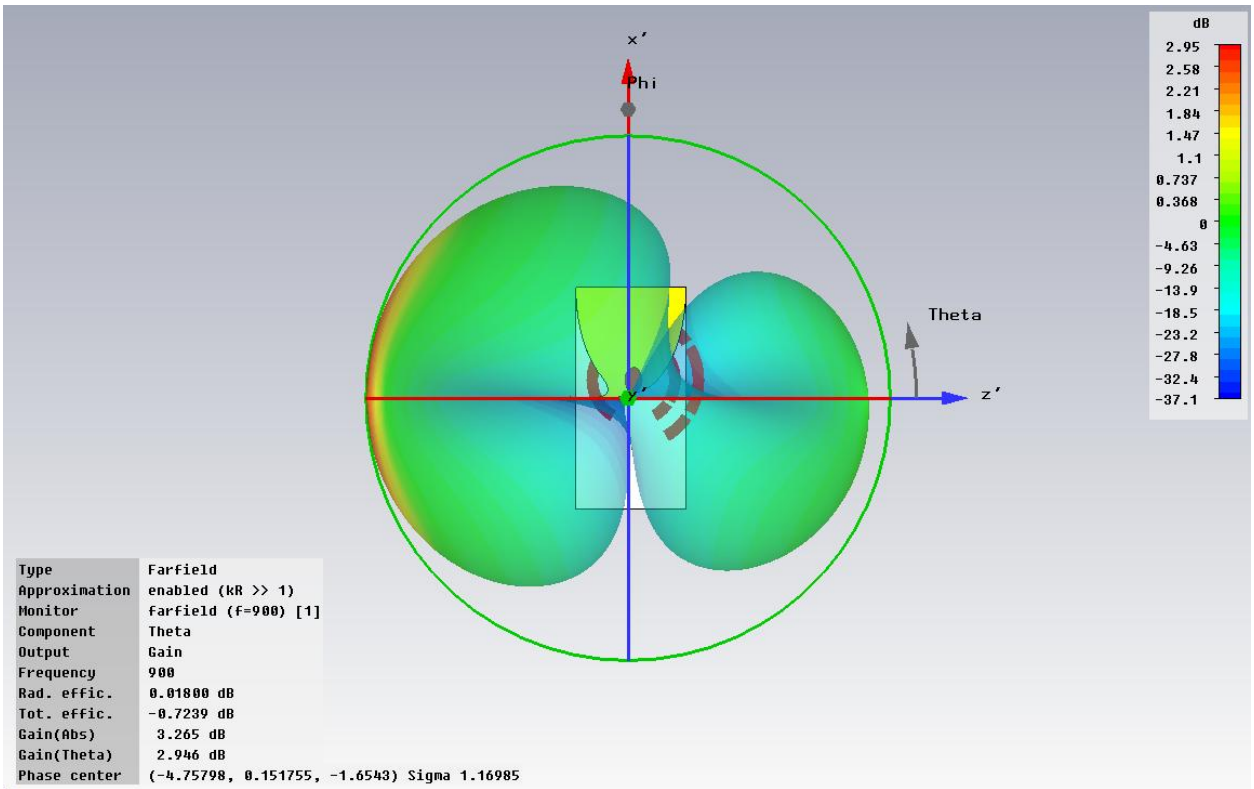
x'
Phi
Theta
z'
dB
2.95
2.58
2.21
1.84
1.47
1.1
0.737
0.368
0
-4.63
-9.26
-13.9
-18.5
-23.2
-27.8
-32.4
-37.1
Type Farfield
Approximation enabled (kR >> 1)
Monitor farfield (f=900) [1]
Component Theta
Output Gain
Frequency 900
Rad. effic. 0.01800 dB
Tot. effic. -0.7239 dB
Gain(Abs) 3.265 dB
Gain(Theta) 2.946 dB
Phase center (-4.75798, 0.151755, -1.6543) Sigma 1.16985

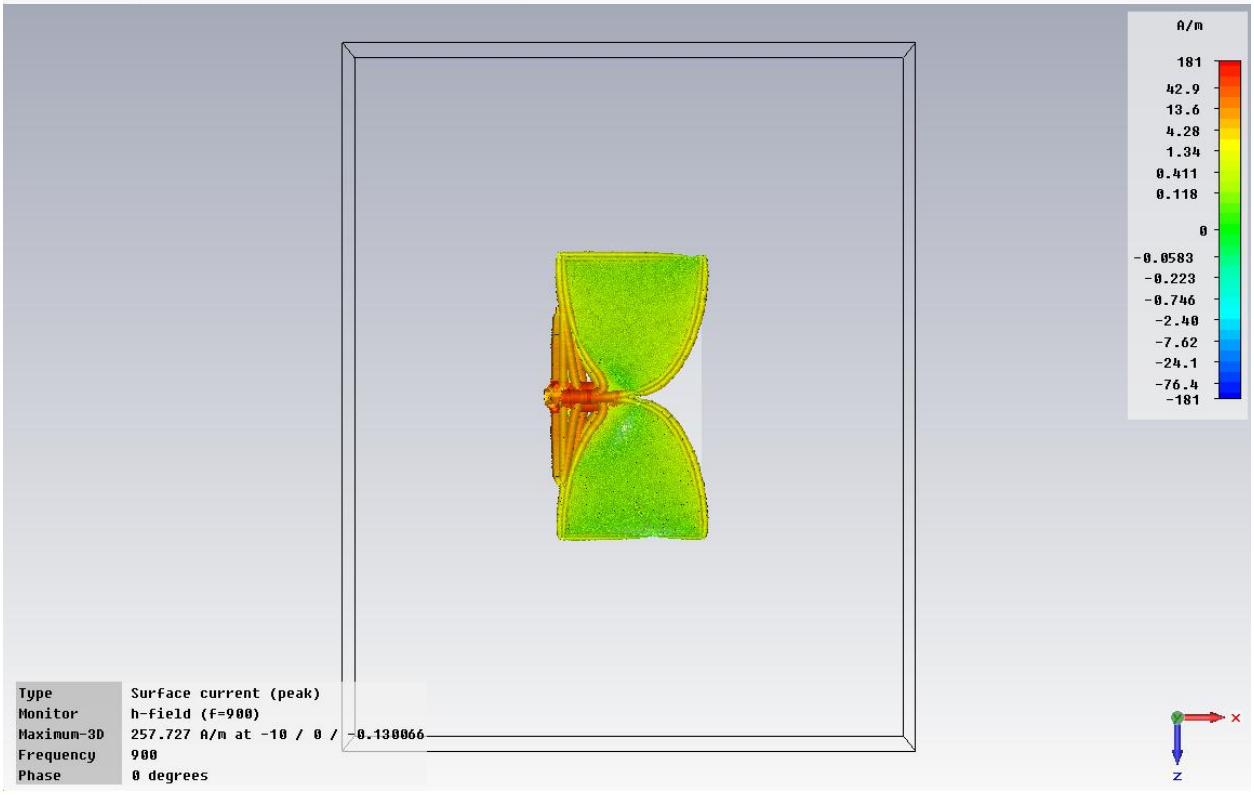
A/m
181
42.9
13.6
4.28
1.34
0.411
0.118
0
-0.0583
-0.223
-0.746
-2.40
-7.62
-24.1
-76.4
-181
Type Surface current (peak)
Monitor h-field (f=900)
Maximum-3D 257.727 A/m at -10 / 0 / -0.130066
Frequency 900
Phase 0 degrees
x
z

Antipodal Bunny Ears Vivaldi (20cm x 15cm, 100ohm)

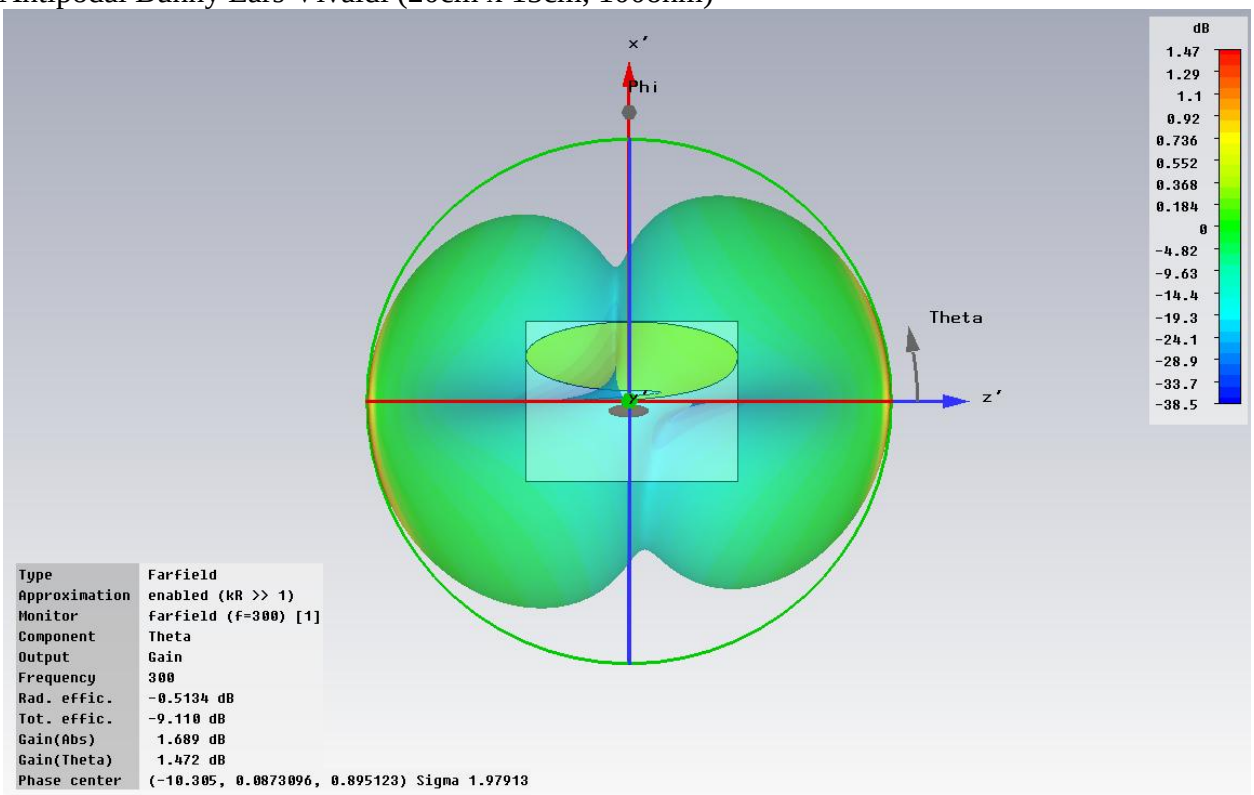

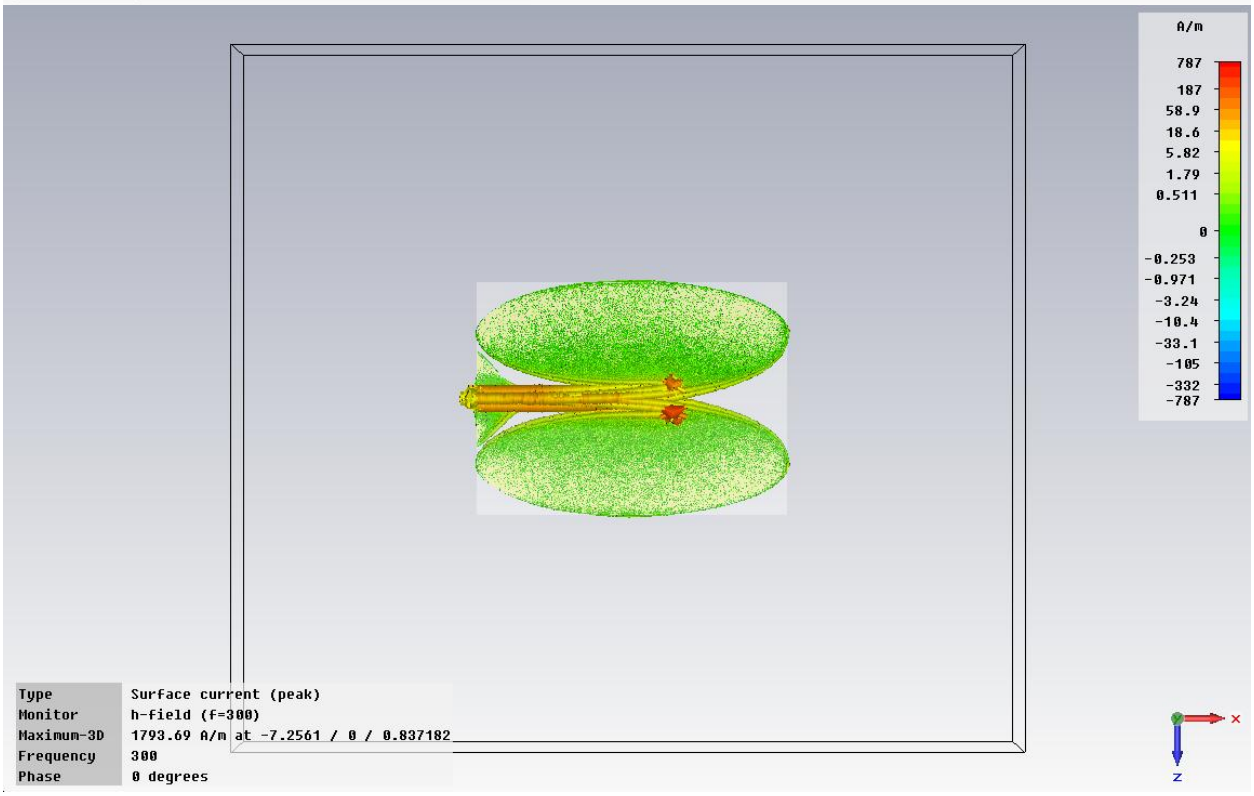

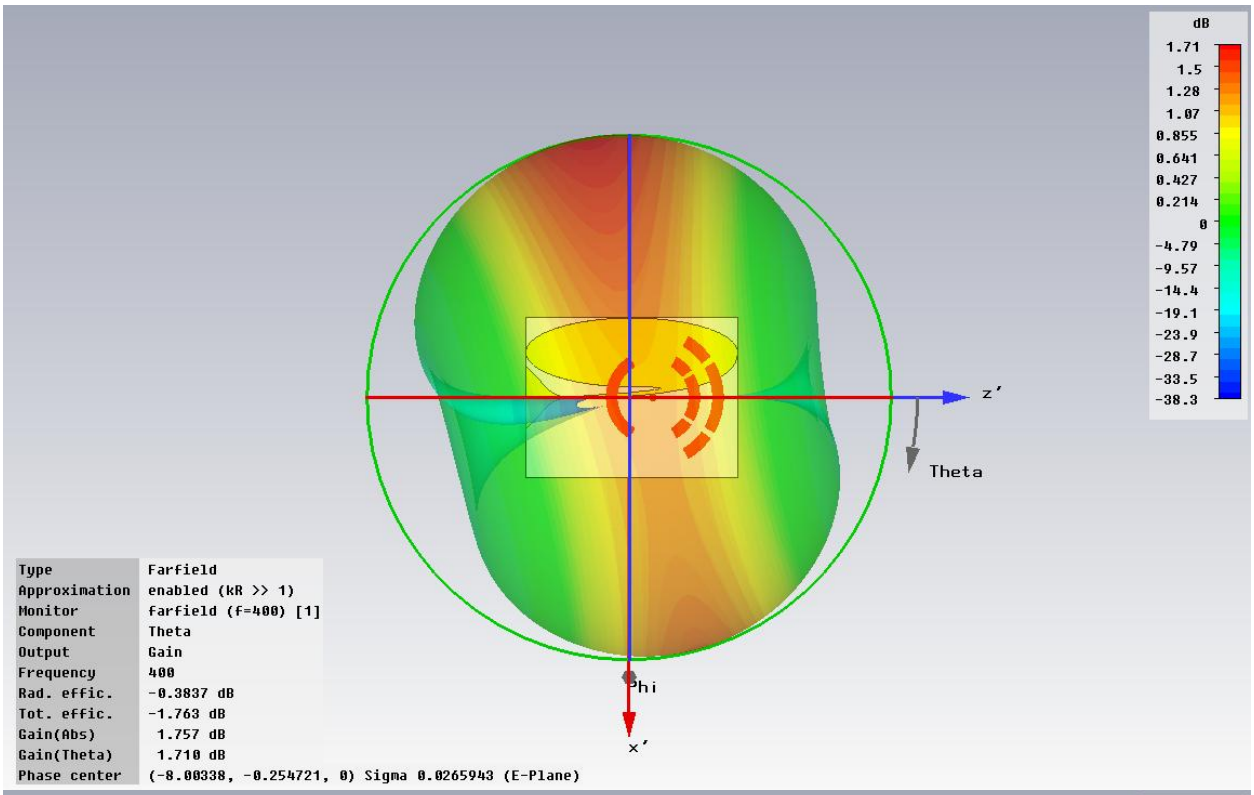
dB
1.71
1.5
1.28
1.07
0.855
0.641
0.427
0.214
0
-4.79
-9.57
-14.4
-19.1
-23.9
-28.7
-33.5
-38.3
z'
Theta
Phi
x'
Type Farfield
Approximation enabled (kR >> 1)
Monitor farfield (f=400) [1]
Component Theta
Output Gain
Frequency 400
Rad. effic. -0.3837 dB
Tot. effic. -1.763 dB
Gain(Abs) 1.757 dB
Gain(Theta) 1.710 dB
Phase center (-8.00338, -0.254721, 0) Sigma 0.0265943 (E-Plane)

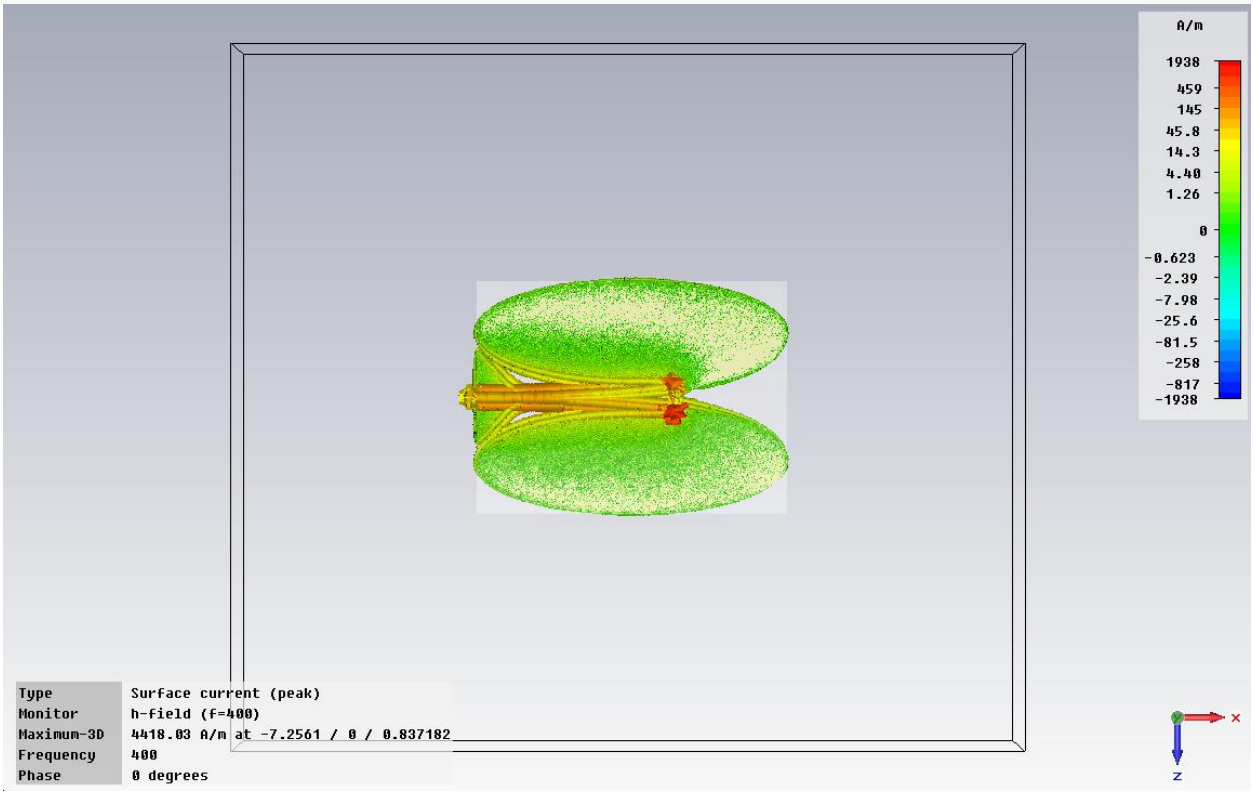
A/m
1938
459
145
45.8
14.3
4.40
1.26
0
-0.623
-2.39
-7.98
-25.6
-81.5
-258
-817
-1938
Type Surface current (peak)
Monitor h-field (f=400)
Maximum-3D 4418.03 A/m at -7.2561 / 0 / 0.837182
Frequency 400
Phase 0 degrees
x
z

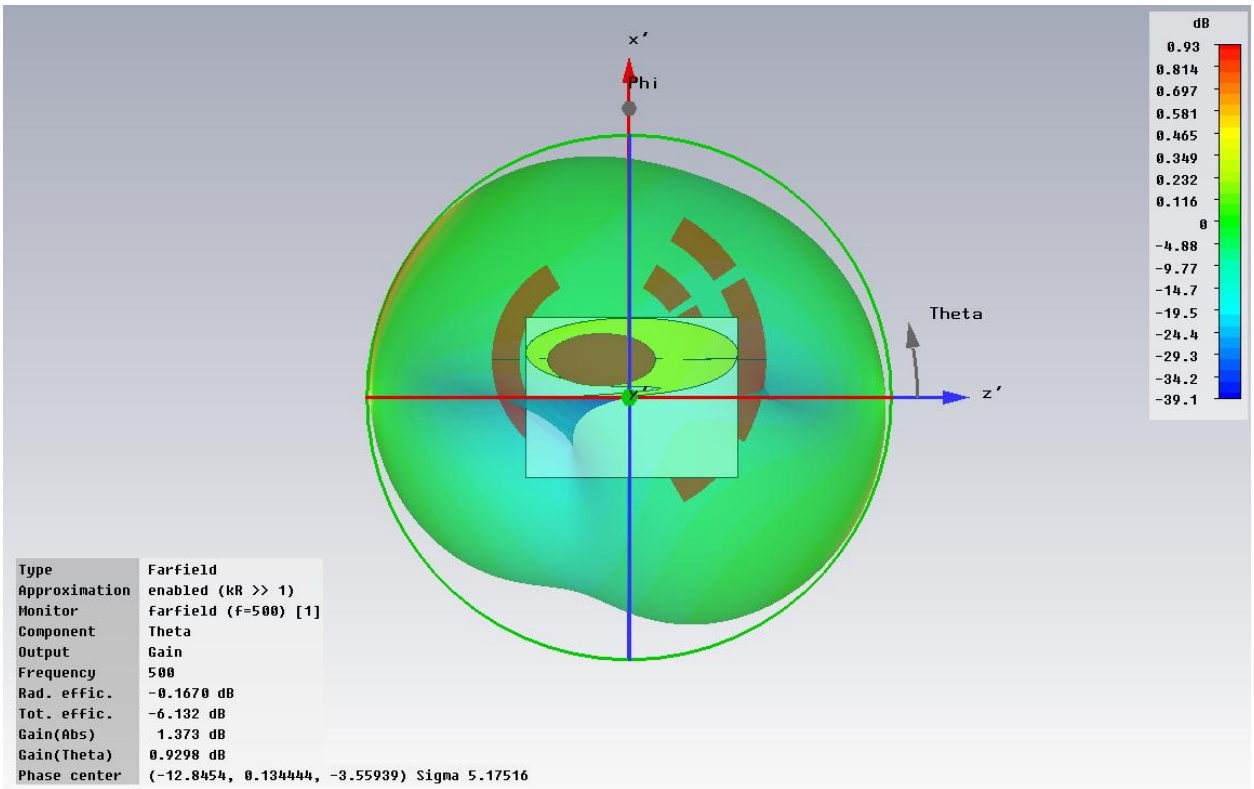

Type	Farfield
Approximation	enabled (kR >> 1)
Monitor	farfield (f=500) [1]
Component	Theta
Output	Gain
Frequency	500
Rad. effic.	-0.1670 dB
Tot. effic.	-6.132 dB
Gain(Abs)	1.373 dB
Gain(Theta)	0.9298 dB
Phase center	(-12.8454, 0.134444, -3.55939) Sigma 5.17516

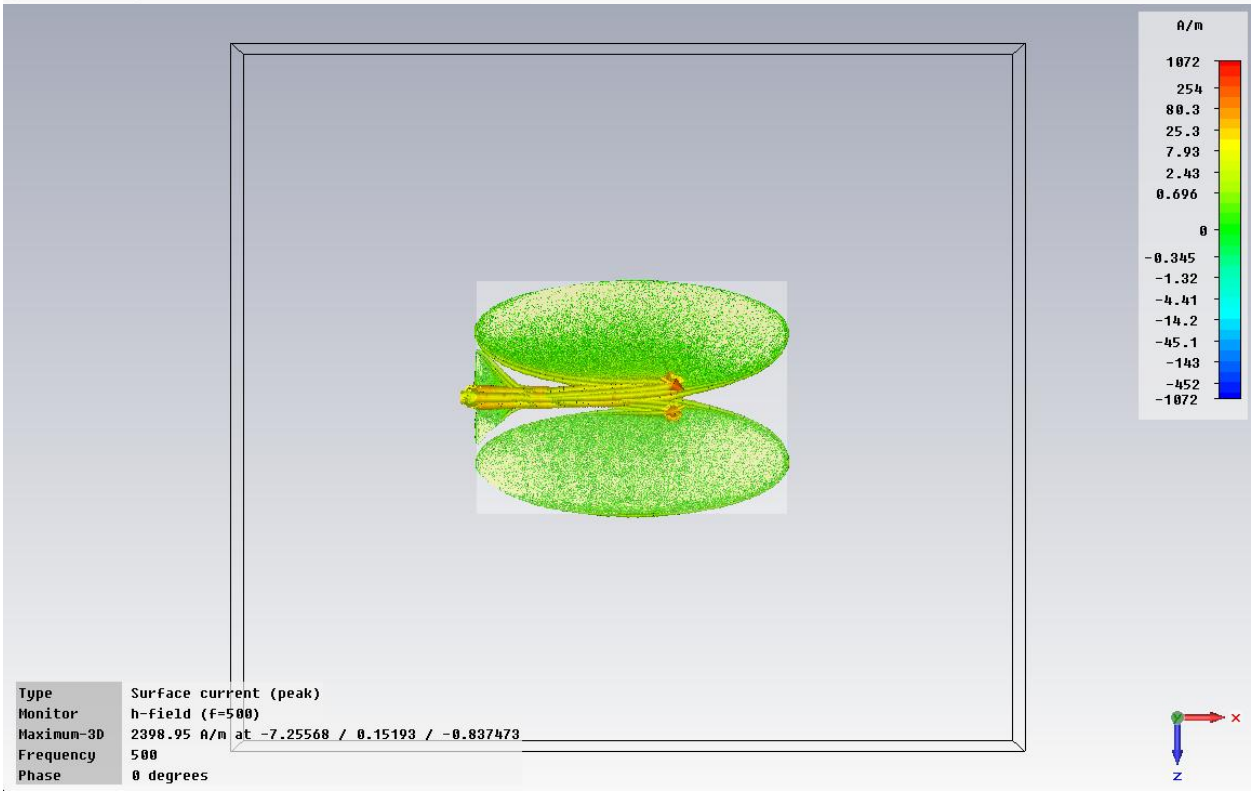

Type	Surface current (peak)
Monitor	h-field (f=500)
Maximum-3D	2398.95 A/m at -7.25568 / 0.15193 / -0.837473
Frequency	500
Phase	0 degrees

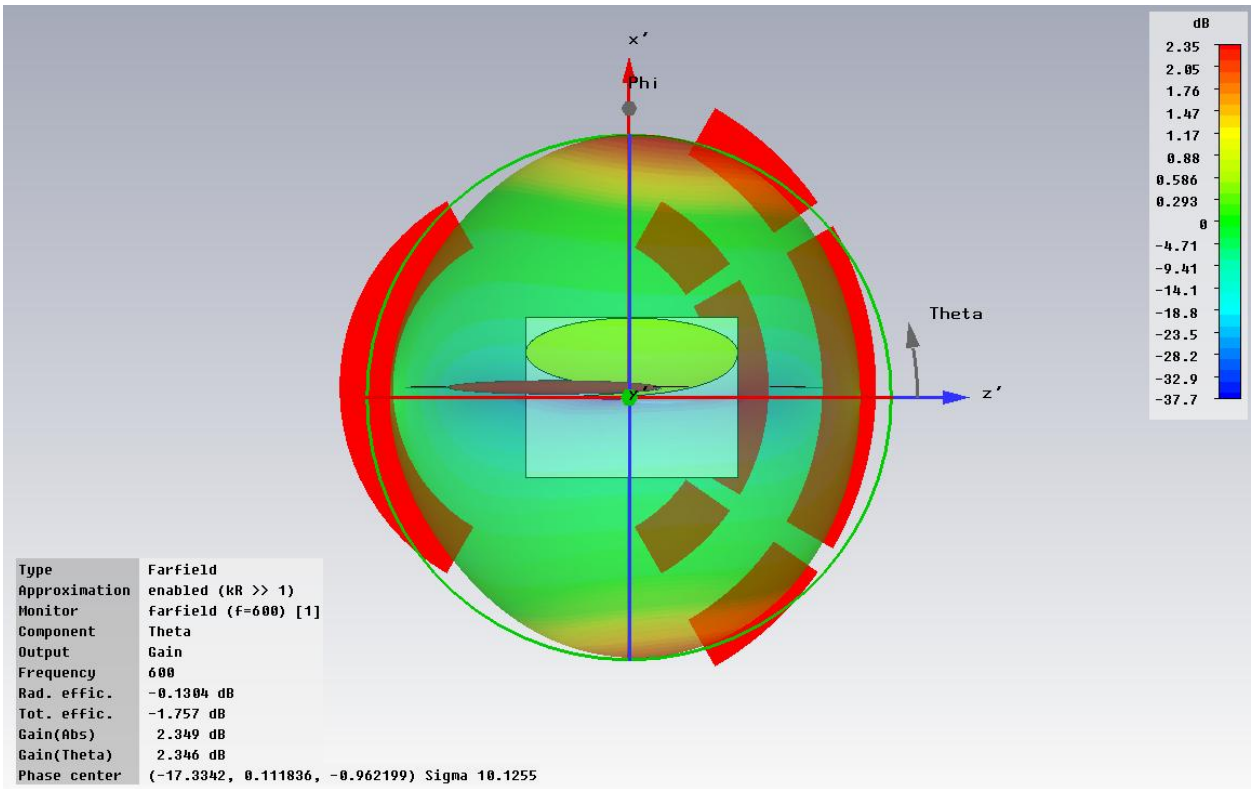
x'
Phi
Theta
z'
dB
2.35
2.05
1.76
1.47
1.17
0.88
0.586
0.293
0
-4.71
-9.41
-14.1
-18.8
-23.5
-28.2
-32.9
-37.7
Type Farfield
Approximation enabled (kR >> 1)
Monitor farfield (f=600) [1]
Component Theta
Output Gain
Frequency 600
Rad. effic. -0.1304 dB
Tot. effic. -1.757 dB
Gain(Abs) 2.349 dB
Gain(Theta) 2.346 dB
Phase center (-17.3342, 0.111836, -0.962199) Sigma 10.1255

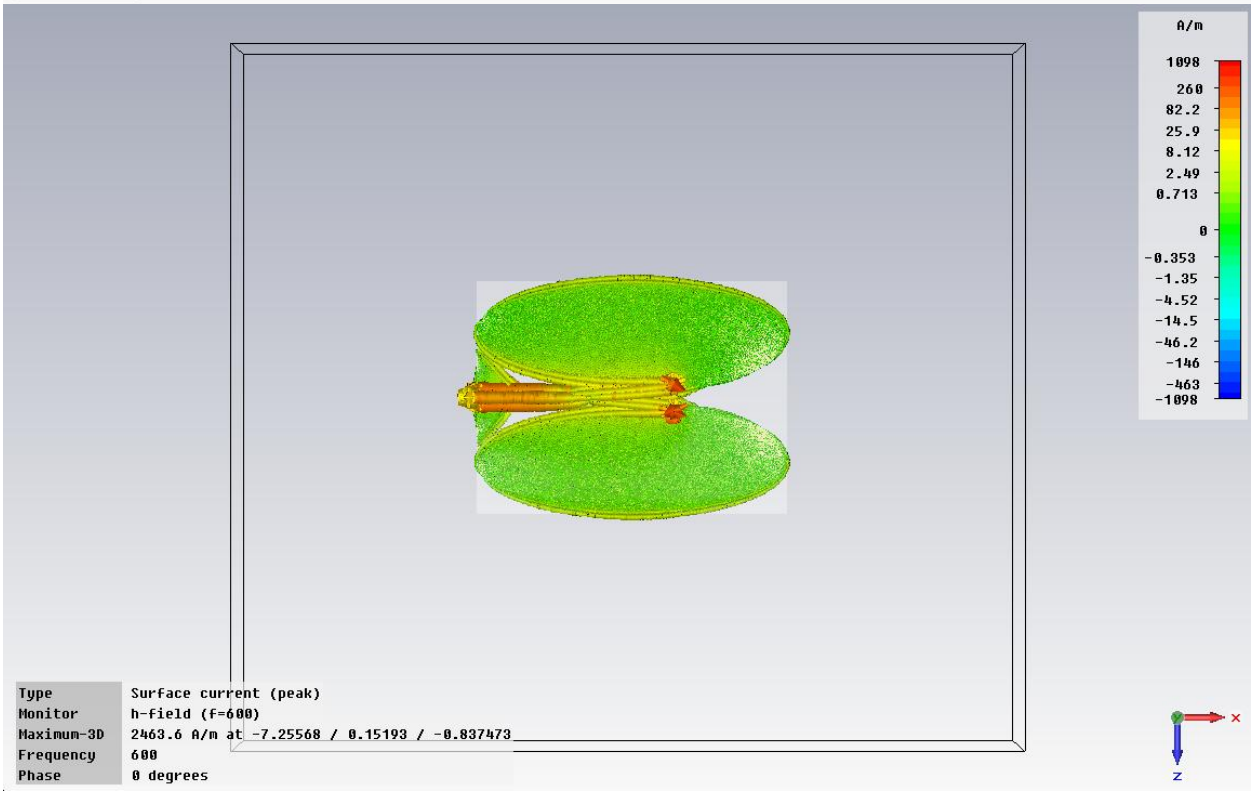
A/m
1098
260
82.2
25.9
8.12
2.49
0.713
0
-0.353
-1.35
-4.52
-14.5
-46.2
-146
-463
-1098
Type Surface current (peak)
Monitor h-field (f=600)
Maximum-3D 2463.6 A/m at -7.25568 / 0.15193 / -0.837473
Frequency 600
Phase 0 degrees
x
z

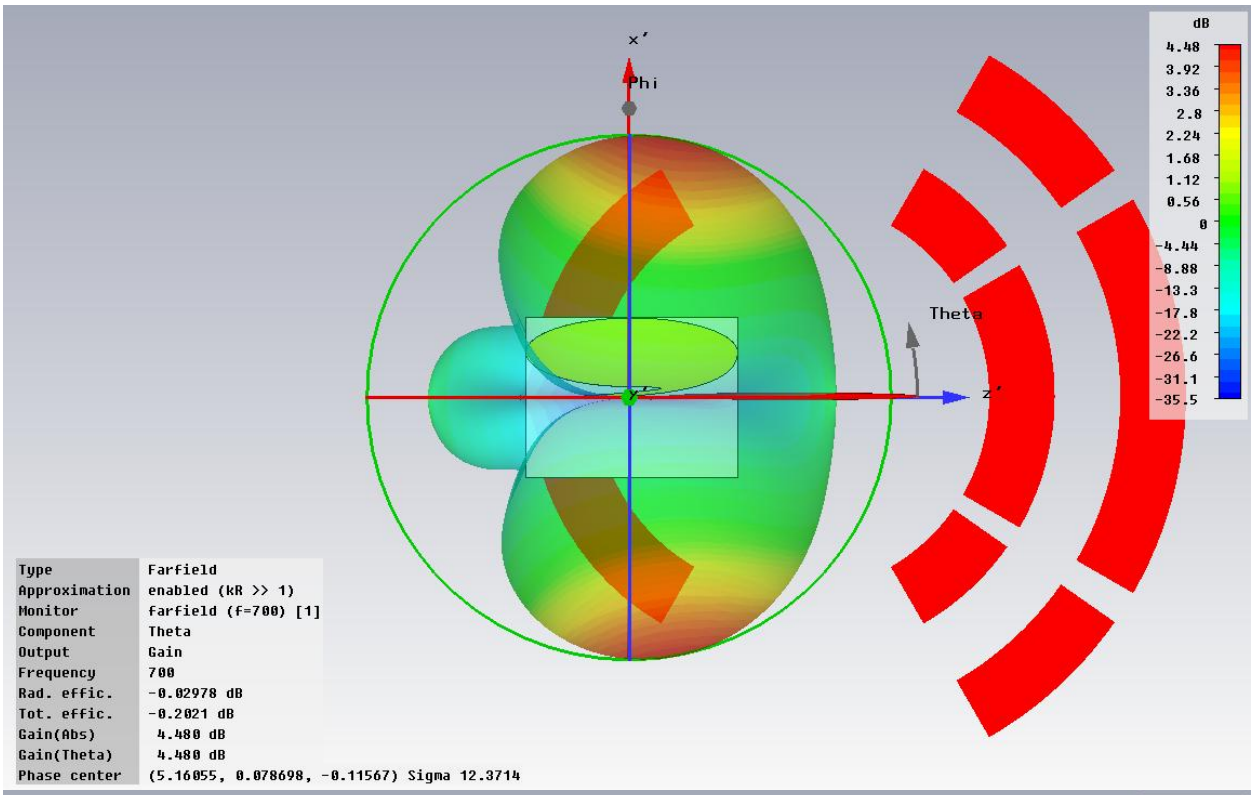

Type	Farfield
Approximation	enabled (kR >> 1)
Monitor	farfield (f=700) [1]
Component	Theta
Output	Gain
Frequency	700
Rad. effic.	-0.02978 dB
Tot. effic.	-0.2021 dB
Gain(Abs)	4.480 dB
Gain(Theta)	4.480 dB
Phase center	(5.16055, 0.078698, -0.11567) Sigma 12.3714

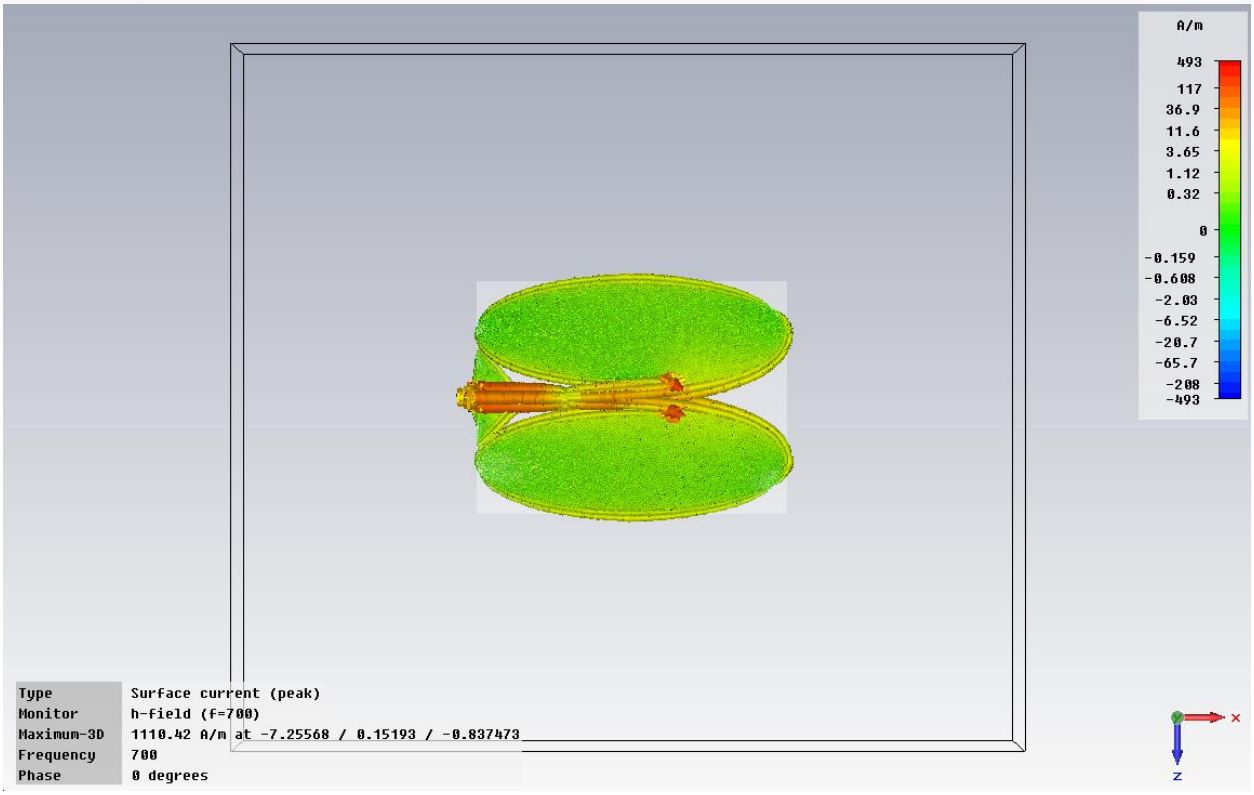

Type	Surface current (peak)
Monitor	h-field (f=700)
Maximum-3D	1110.42 A/m at -7.25568 / 0.15193 / -0.837473
Frequency	700
Phase	0 degrees

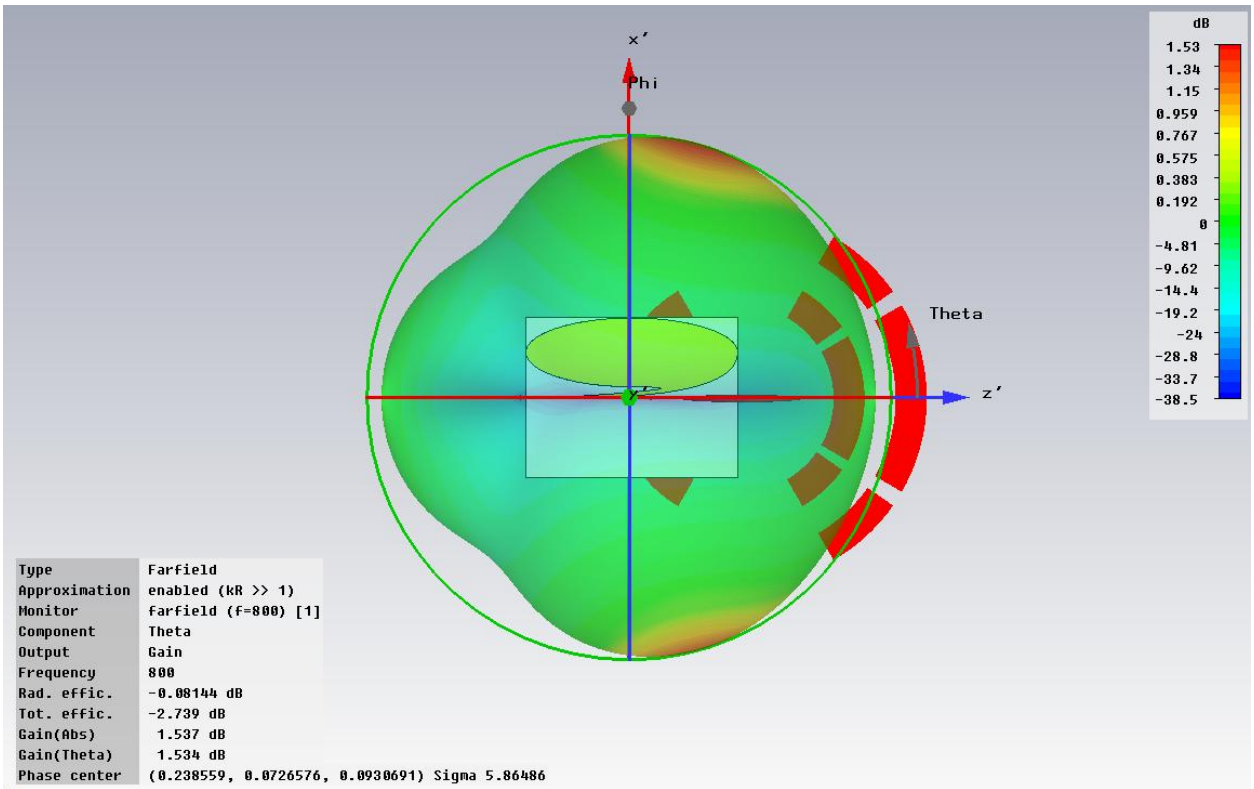

Type	Farfield
Approximation	enabled (kR >> 1)
Monitor	farfield (f=800) [1]
Component	Theta
Output	Gain
Frequency	800
Rad. effic.	-0.08144 dB
Tot. effic.	-2.739 dB
Gain(Abs)	1.537 dB
Gain(Theta)	1.534 dB
Phase center	(0.238559, 0.0726576, 0.0930691) Sigma 5.86486

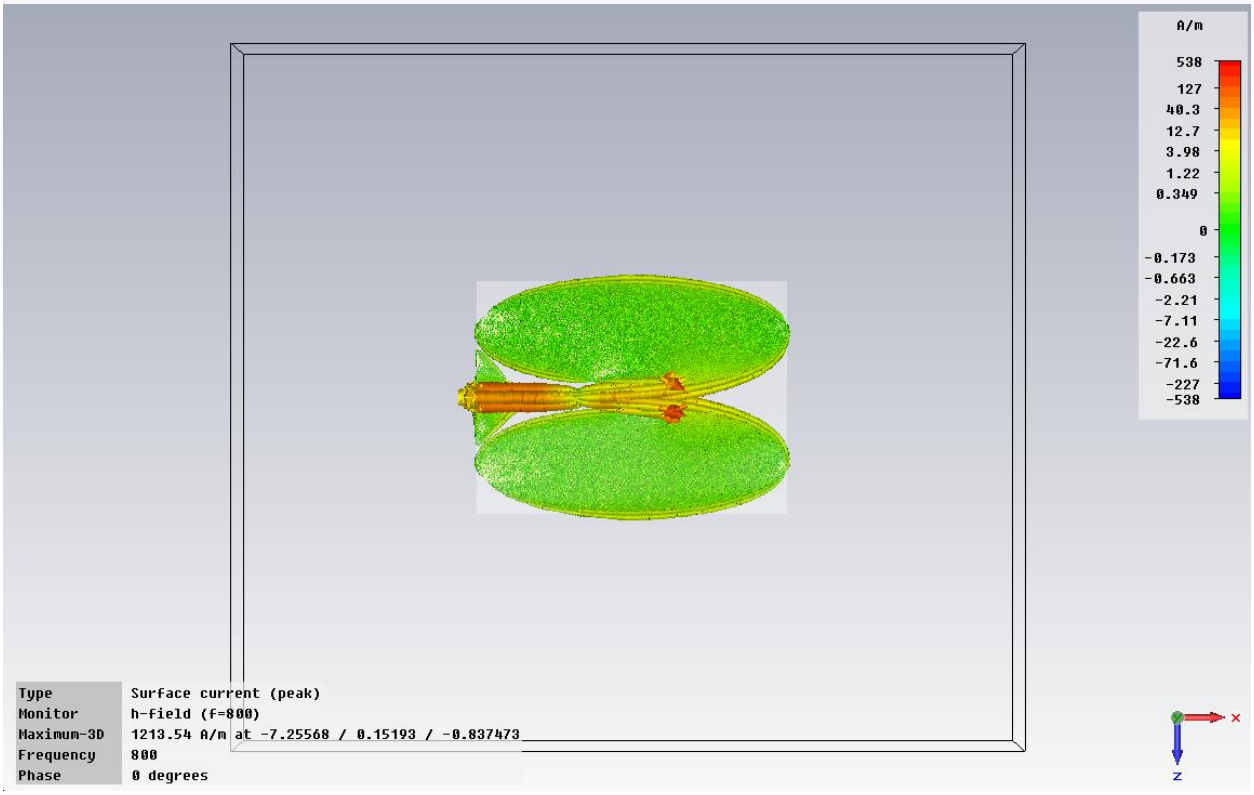

Type	Surface current (peak)
Monitor	h-field (f=800)
Maximum-3D	1213.54 A/m at -7.25568 / 0.15193 / -0.837473
Frequency	800
Phase	0 degrees

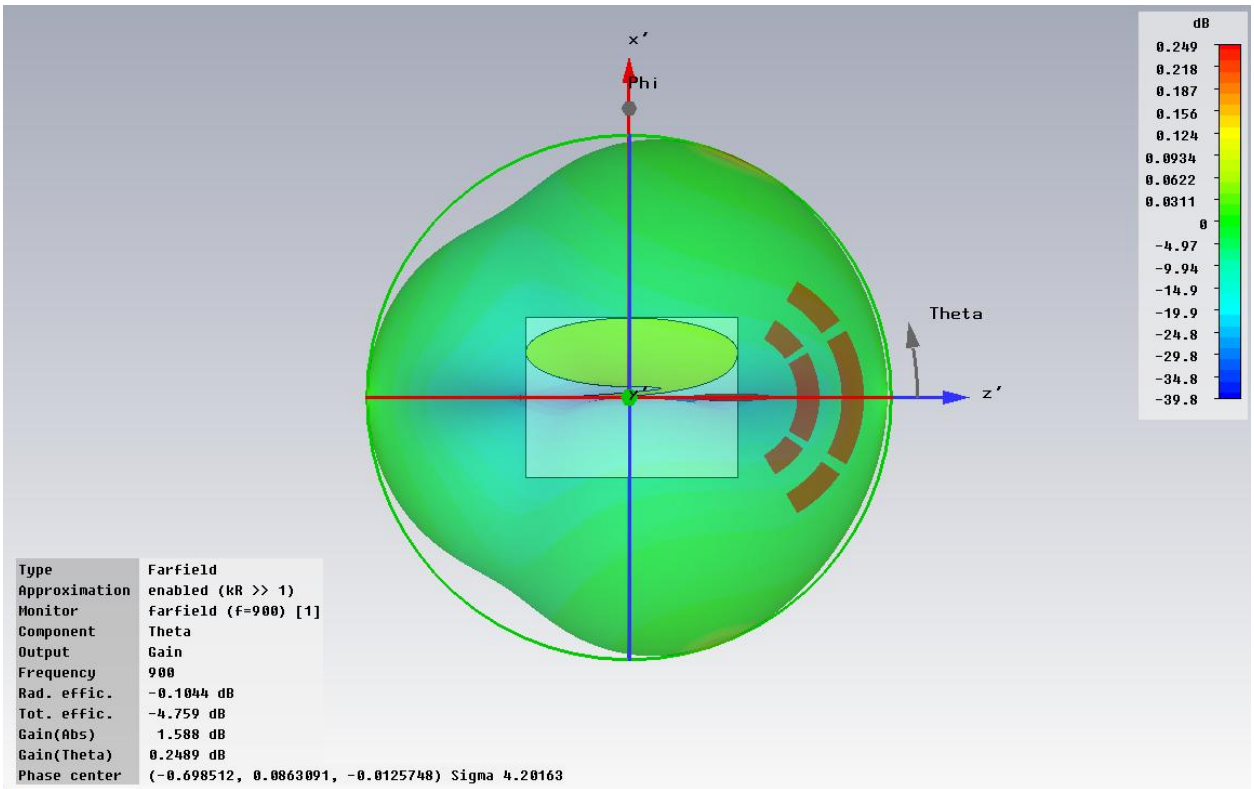

Type	Farfield
Approximation	enabled (kR >> 1)
Monitor	farfield (f=900) [1]
Component	Theta
Output	Gain
Frequency	900
Rad. effic.	-0.1044 dB
Tot. effic.	-4.759 dB
Gain(Abs)	1.588 dB
Gain(Theta)	0.2489 dB
Phase center	(-0.698512, 0.0863091, -0.0125748) Sigma 4.20163

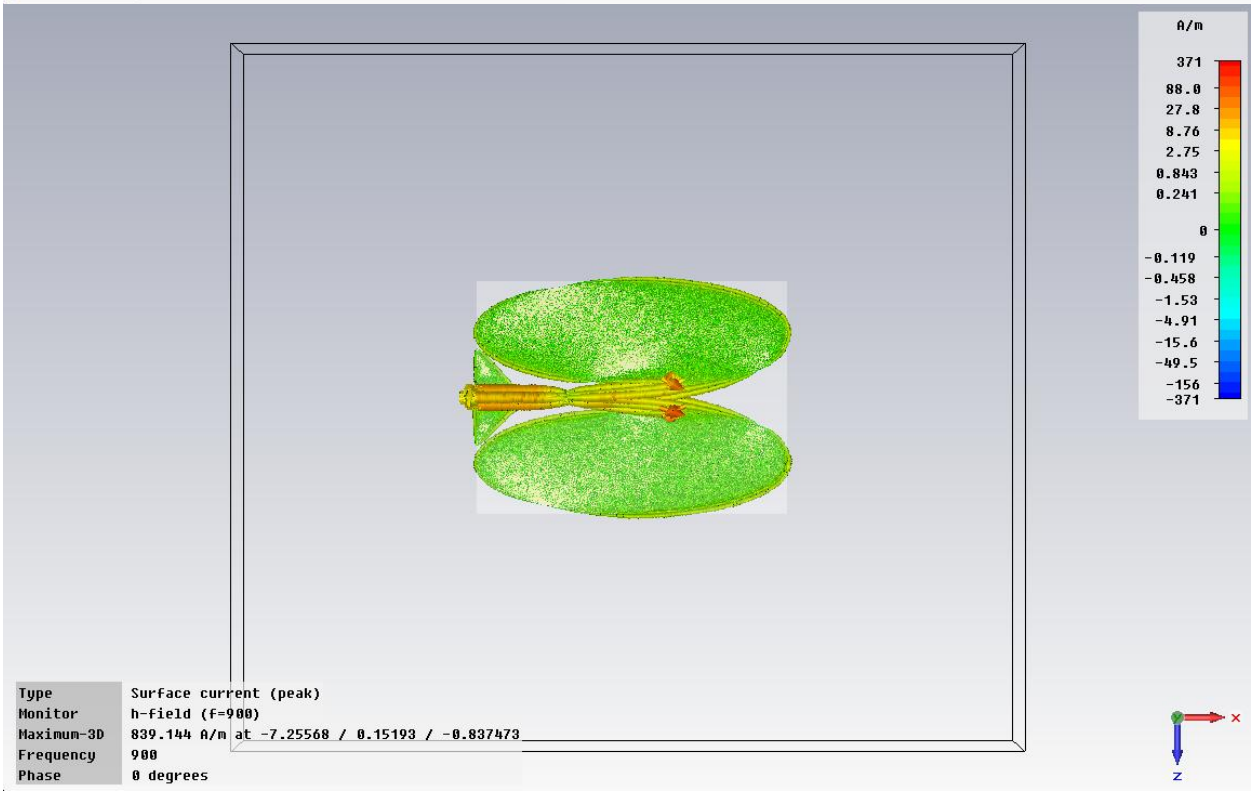

Type	Surface current (peak)
Monitor	h-field (f=900)
Maximum-3D	839.144 A/m at -7.25568 / 0.15193 / -0.837473
Frequency	900
Phase	0 degrees

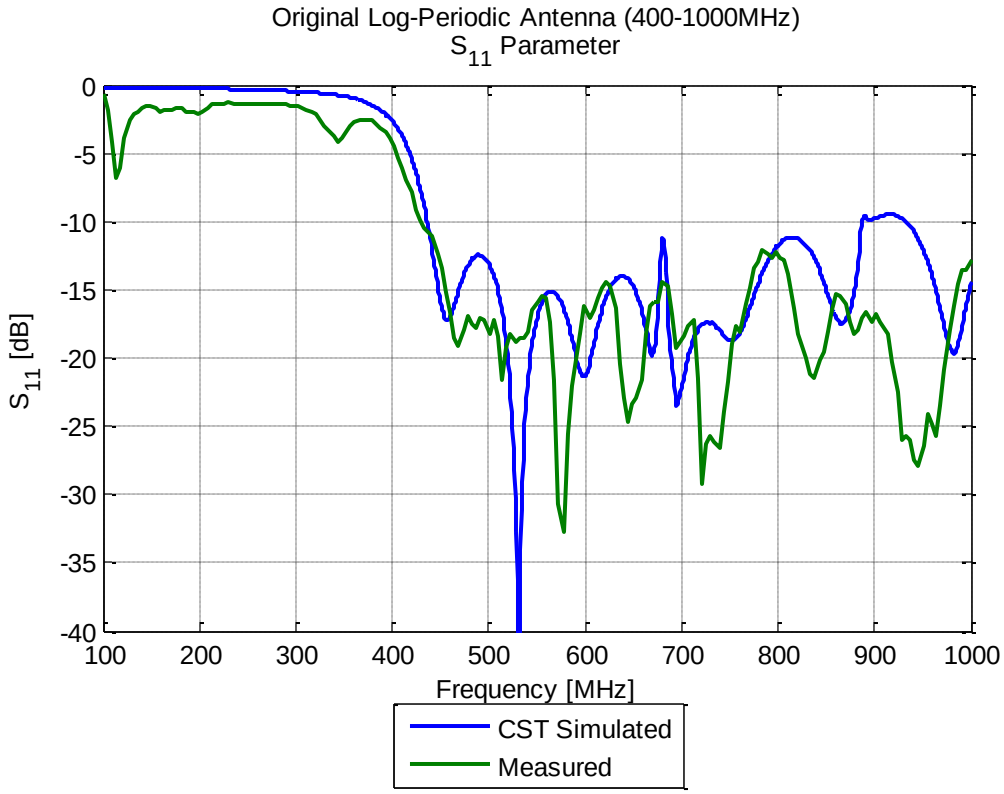
Original Log-Periodic Antenna (400-1000MHz)
S11 Parameter
S11 [dB]
0
-5
-10
-15
-20
-25
-30
-35
-40
100
200
300
400
500
600
700
800
900
1000
Frequency [MHz]
CST Simulated
Measured

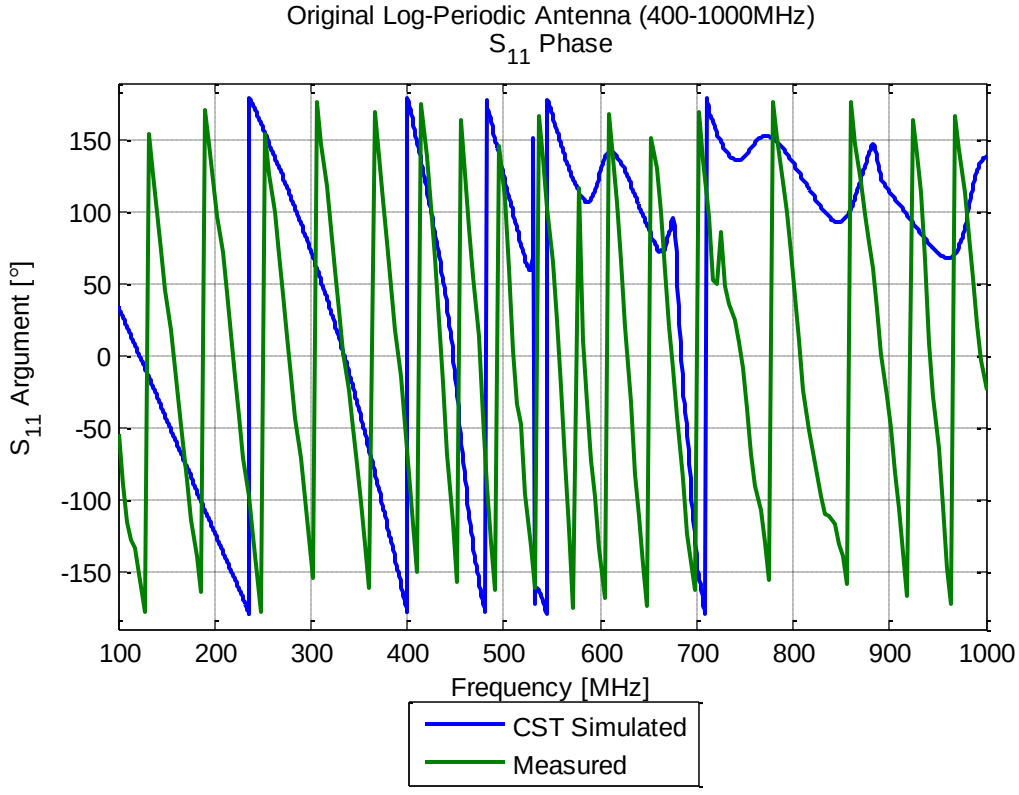
Original Log-Periodic Antenna (400-1000MHz)
S11 Phase
S11 Argument [°]
150
100
50
0
-50
-100
-150
100
200
300
400
500
600
700
800
900
1000
Frequency [MHz]
CST Simulated
Measured

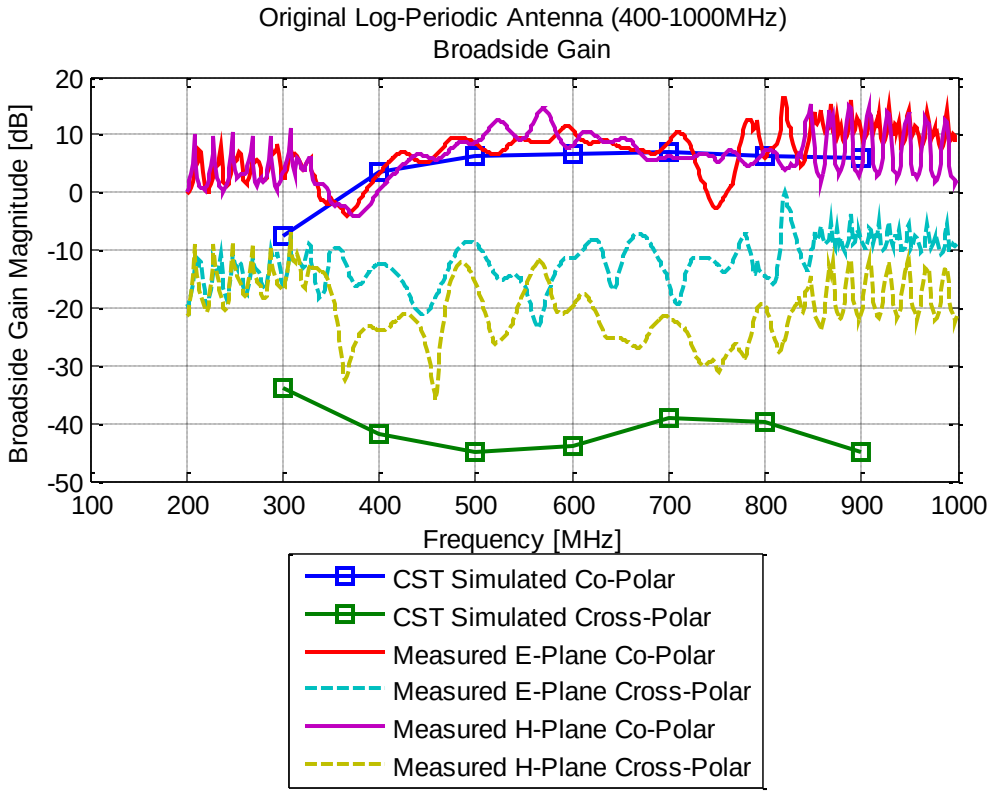
Original Log-Periodic Antenna (400-1000MHz)
Broadside Gain
Broadside Gain Magnitude [dB]
Frequency [MHz]
CST Simulated Co-Polar
CST Simulated Cross-Polar
Measured E-Plane Co-Polar
Measured E-Plane Cross-Polar
Measured H-Plane Co-Polar
Measured H-Plane Cross-Polar

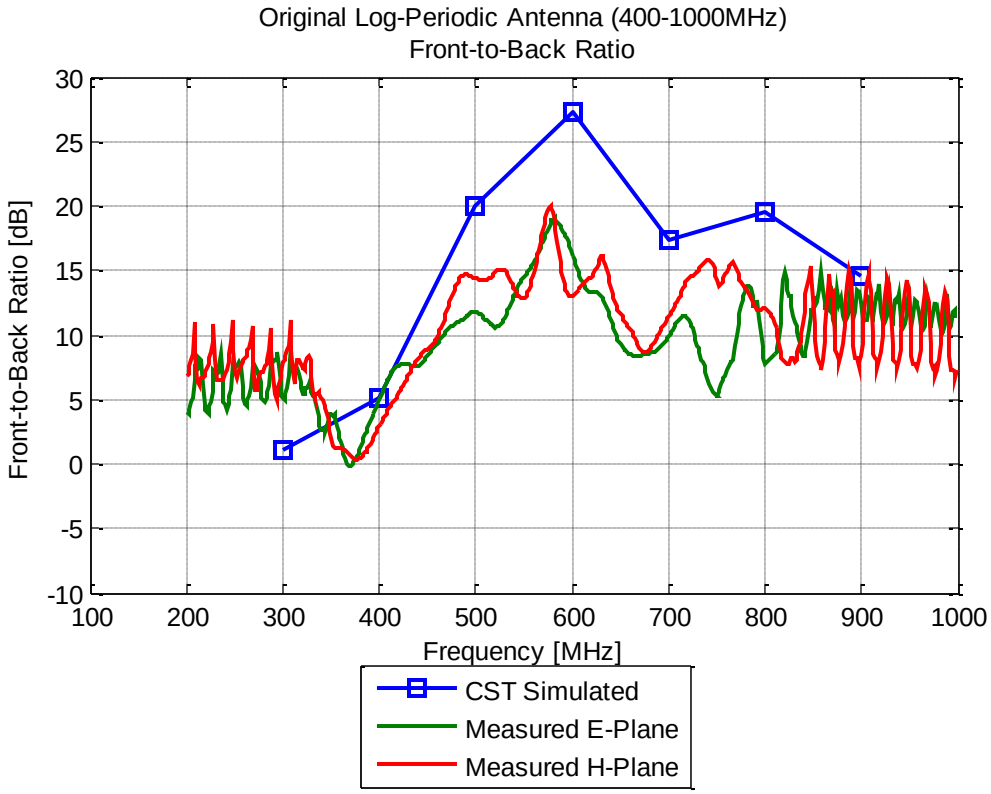
Original Log-Periodic Antenna (400-1000MHz)
Front-to-Back Ratio
Front-to-Back Ratio [dB]
Frequency [MHz]
CST Simulated
Measured E-Plane
Measured H-Plane

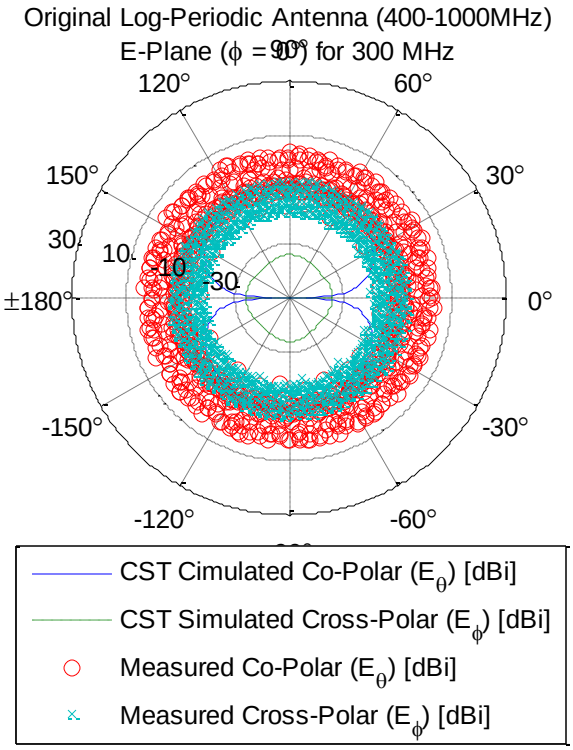
Original Log-Periodic Antenna (400-1000MHz)
E-Plane (ϕ = 90°) for 300 MHz
90°
120°
60°
150°
30°
±180°
0°
-150°
-30°
-120°
-60°
-10
-30
CST Cimulated Co-Polar (Eθ) [dBi]
CST Simulated Cross-Polar (Eϕ) [dBi]
Measured Co-Polar (Eθ) [dBi]
Measured Cross-Polar (Eϕ) [dBi]

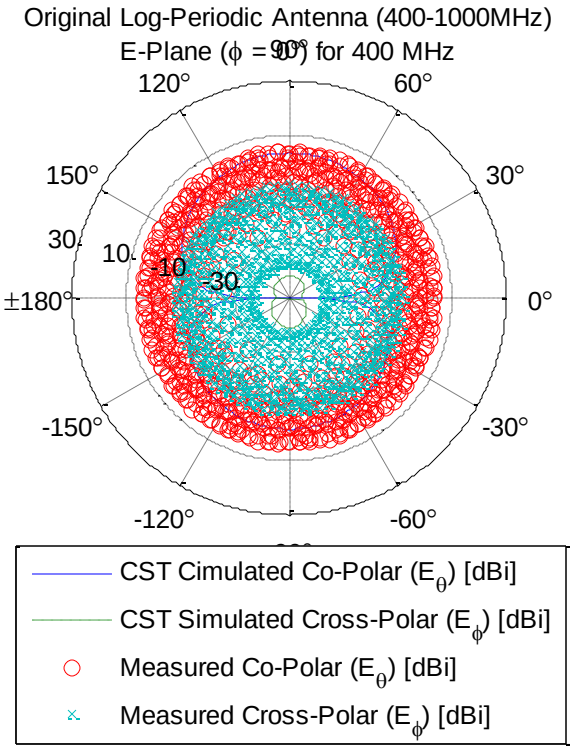
Original Log-Periodic Antenna (400-1000MHz)
E-Plane (ϕ = 90°) for 400 MHz
90°
120°
60°
150°
30°
±180°
0°
-150°
-30°
-120°
-60°
-10
-30
CST Cimulated Co-Polar (Eθ) [dBi]
CST Simulated Cross-Polar (Eϕ) [dBi]
Measured Co-Polar (Eθ) [dBi]
Measured Cross-Polar (Eϕ) [dBi]

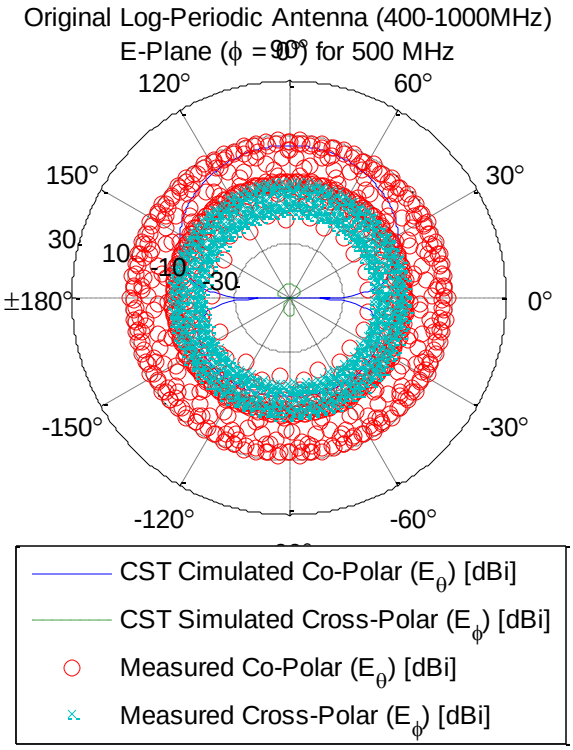
Original Log-Periodic Antenna (400-1000MHz)
E-Plane (ϕ = 90°) for 500 MHz
90°
120°
60°
150°
30°
30
10
-10
-30
±180°
0°
-150°
-30°
-120°
-60°
CST Cimulated Co-Polar (Eθ) [dBi]
CST Simulated Cross-Polar (Eϕ) [dBi]
Measured Co-Polar (Eθ) [dBi]
Measured Cross-Polar (Eϕ) [dBi]

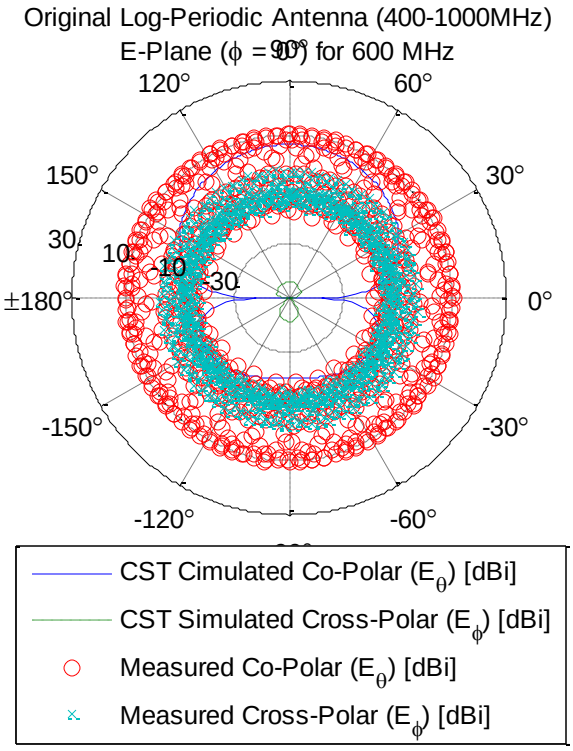
Original Log-Periodic Antenna (400-1000MHz)
E-Plane (ϕ = 90°) for 600 MHz
90°
120°
60°
150°
30°
30
10
-10
-30
±180°
0°
-150°
-30°
-120°
-60°
CST Cimulated Co-Polar (Eθ) [dBi]
CST Simulated Cross-Polar (Eϕ) [dBi]
Measured Co-Polar (Eθ) [dBi]
Measured Cross-Polar (Eϕ) [dBi]

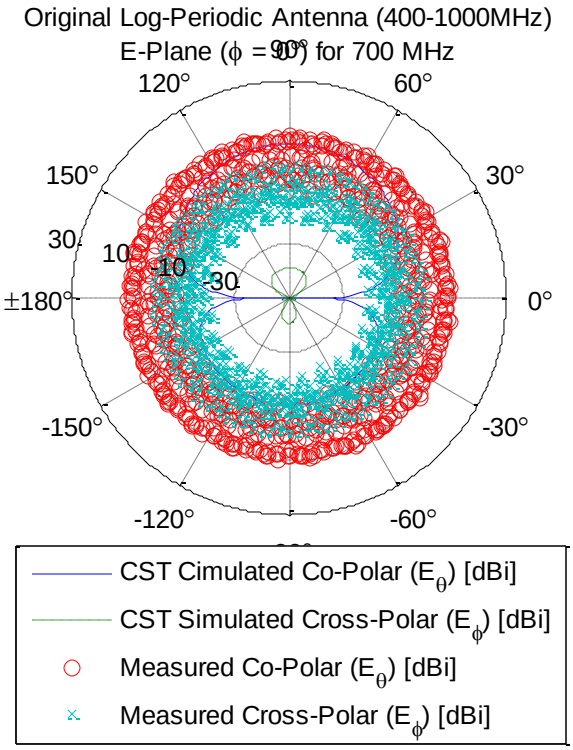
Original Log-Periodic Antenna (400-1000MHz)
E-Plane (ϕ = 90°) for 700 MHz
90°
120°
60°
150°
30°
±180°
0°
-150°
-30°
-120°
-60°
CST Cimulated Co-Polar (Eθ) [dBi]
CST Simulated Cross-Polar (Eϕ) [dBi]
Measured Co-Polar (Eθ) [dBi]
Measured Cross-Polar (Eϕ) [dBi]

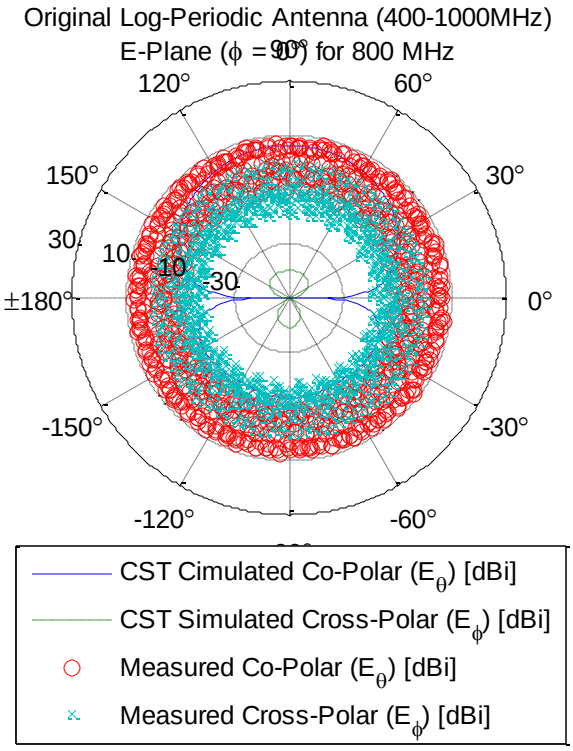
Original Log-Periodic Antenna (400-1000MHz)
E-Plane (ϕ = 90°) for 800 MHz
90°
120°
60°
150°
30°
±180°
0°
-150°
-30°
-120°
-60°
CST Cimulated Co-Polar (Eθ) [dBi]
CST Simulated Cross-Polar (Eϕ) [dBi]
Measured Co-Polar (Eθ) [dBi]
Measured Cross-Polar (Eϕ) [dBi]

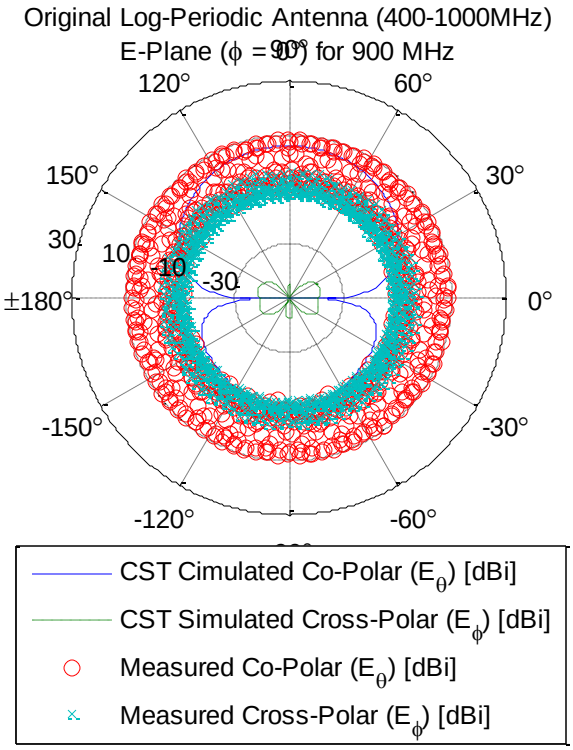
Original Log-Periodic Antenna (400-1000MHz)
E-Plane (ϕ = 90°) for 900 MHz
90°
120°
60°
150°
30°
±180°
0°
-150°
-30°
-120°
-60°
-10
-30
CST Cimulated Co-Polar (Eθ) [dBi]
CST Simulated Cross-Polar (Eϕ) [dBi]
Measured Co-Polar (Eθ) [dBi]
Measured Cross-Polar (Eϕ) [dBi]

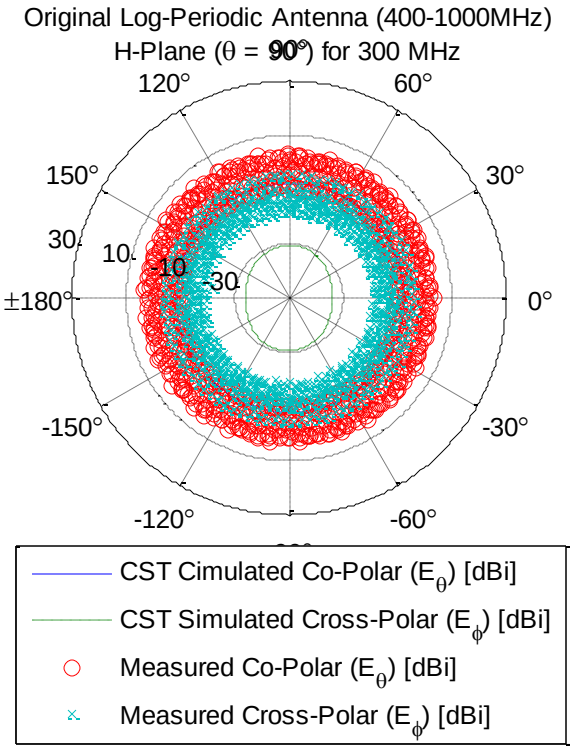
Original Log-Periodic Antenna (400-1000MHz)
H-Plane (θ = 90°) for 300 MHz
90°
120°
60°
150°
30°
±180°
0°
-150°
-30°
-120°
-60°
-10
-30
CST Cimulated Co-Polar (Eθ) [dBi]
CST Simulated Cross-Polar (Eϕ) [dBi]
Measured Co-Polar (Eθ) [dBi]
Measured Cross-Polar (Eϕ) [dBi]

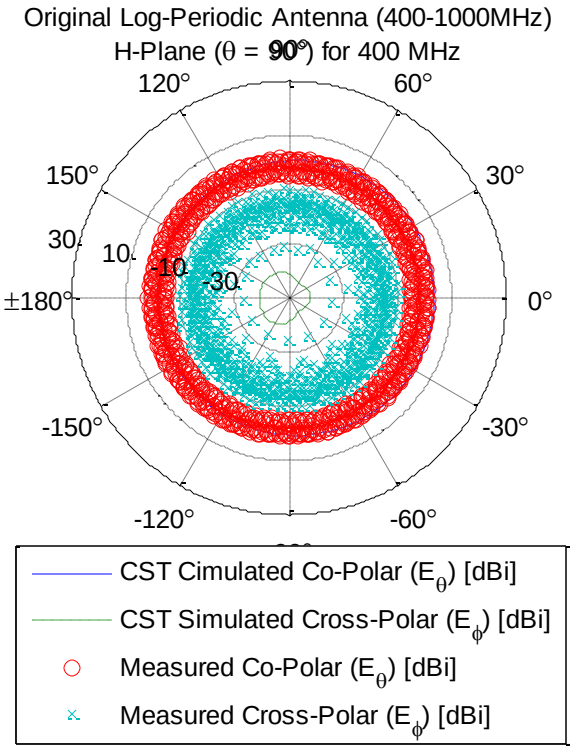
Original Log-Periodic Antenna (400-1000MHz)
H-Plane (θ = 90°) for 400 MHz
120°
60°
150°
30°
±180°
0°
-150°
-30°
-120°
-60°
-10
-30
CST Cimulated Co-Polar (Eθ) [dBi]
CST Simulated Cross-Polar (Eϕ) [dBi]
Measured Co-Polar (Eθ) [dBi]
Measured Cross-Polar (Eϕ) [dBi]

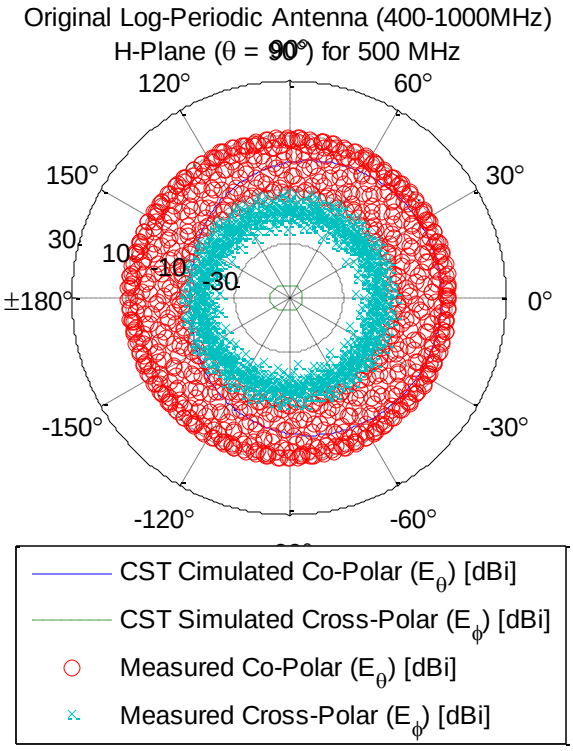
Original Log-Periodic Antenna (400-1000MHz)
H-Plane (θ = 90°) for 500 MHz
120°
60°
150°
30°
±180°
0°
-150°
-30°
-120°
-60°
-10
-30
CST Cimulated Co-Polar (Eθ) [dBi]
CST Simulated Cross-Polar (Eϕ) [dBi]
Measured Co-Polar (Eθ) [dBi]
Measured Cross-Polar (Eϕ) [dBi]

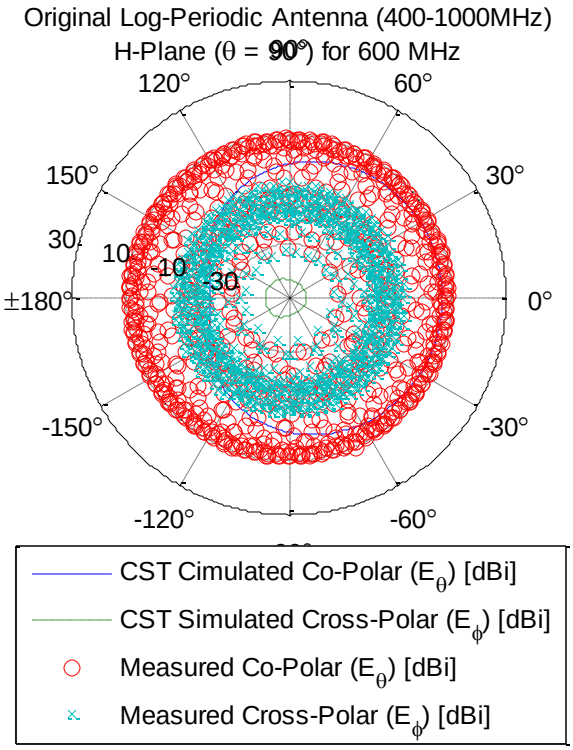
Original Log-Periodic Antenna (400-1000MHz)
H-Plane (θ = 90°) for 600 MHz
120°
60°
150°
30°
10
-10
30
±180°
0°
-150°
-30°
-120°
-60°
CST Cimulated Co-Polar (Eθ) [dBi]
CST Simulated Cross-Polar (Eϕ) [dBi]
Measured Co-Polar (Eθ) [dBi]
Measured Cross-Polar (Eϕ) [dBi]

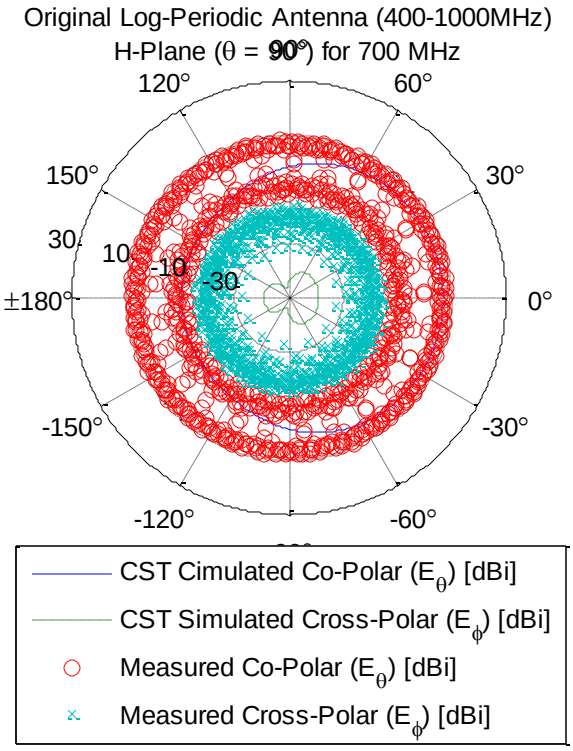
Original Log-Periodic Antenna (400-1000MHz)
H-Plane (θ = 90°) for 700 MHz
120°
60°
150°
30°
10
-10
30
±180°
0°
-150°
-30°
-120°
-60°
CST Cimulated Co-Polar (Eθ) [dBi]
CST Simulated Cross-Polar (Eϕ) [dBi]
Measured Co-Polar (Eθ) [dBi]
Measured Cross-Polar (Eϕ) [dBi]

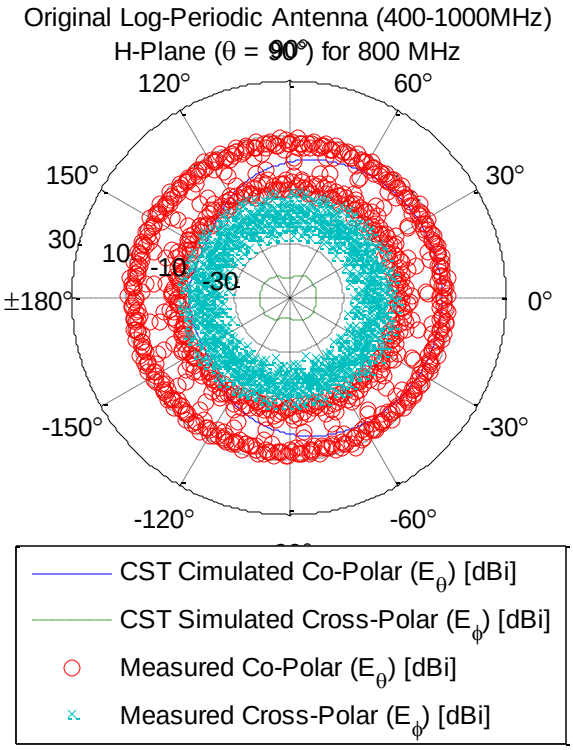
Original Log-Periodic Antenna (400-1000MHz)
H-Plane (θ = 90°) for 800 MHz
120°
60°
150°
30°
10
-10
-30
±180°
0°
-150°
-30°
-120°
-60°
CST Cimulated Co-Polar (Eθ) [dBi]
CST Simulated Cross-Polar (Eϕ) [dBi]
Measured Co-Polar (Eθ) [dBi]
Measured Cross-Polar (Eϕ) [dBi]

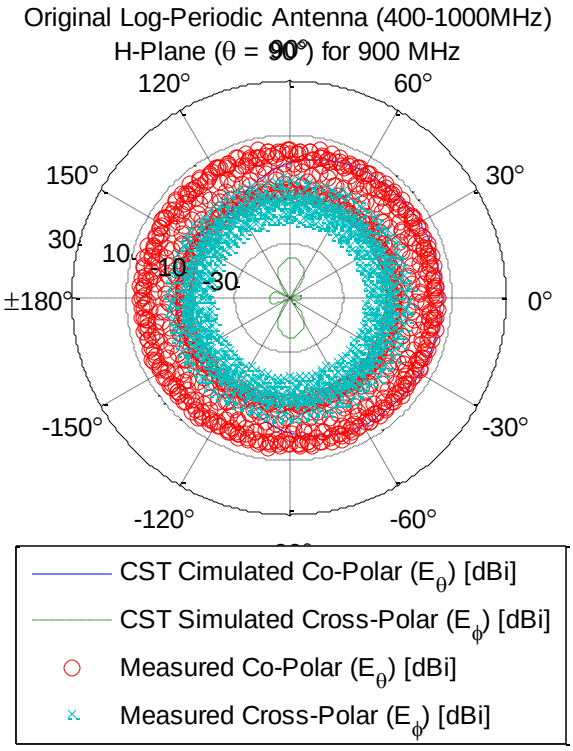
Original Log-Periodic Antenna (400-1000MHz)
H-Plane (θ = 90°) for 900 MHz
120°
60°
150°
30°
10
-10
-30
±180°
0°
-150°
-30°
-120°
-60°
CST Cimulated Co-Polar (Eθ) [dBi]
CST Simulated Cross-Polar (Eϕ) [dBi]
Measured Co-Polar (Eθ) [dBi]
Measured Cross-Polar (Eϕ) [dBi]

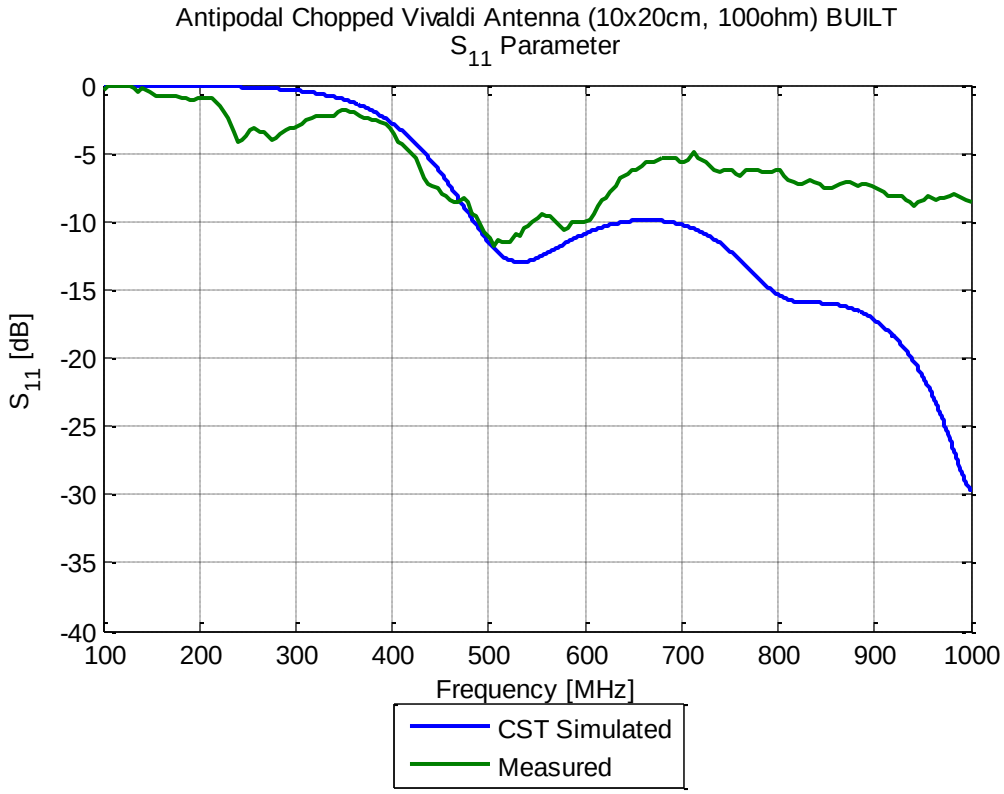
Antipodal Chopped Vivaldi Antenna (10x20cm, 100ohm) BUILT
S11 Parameter
S11 [dB]
0
-5
-10
-15
-20
-25
-30
-35
-40
100
200
300
400
500
600
700
800
900
1000
Frequency [MHz]
CST Simulated
Measured

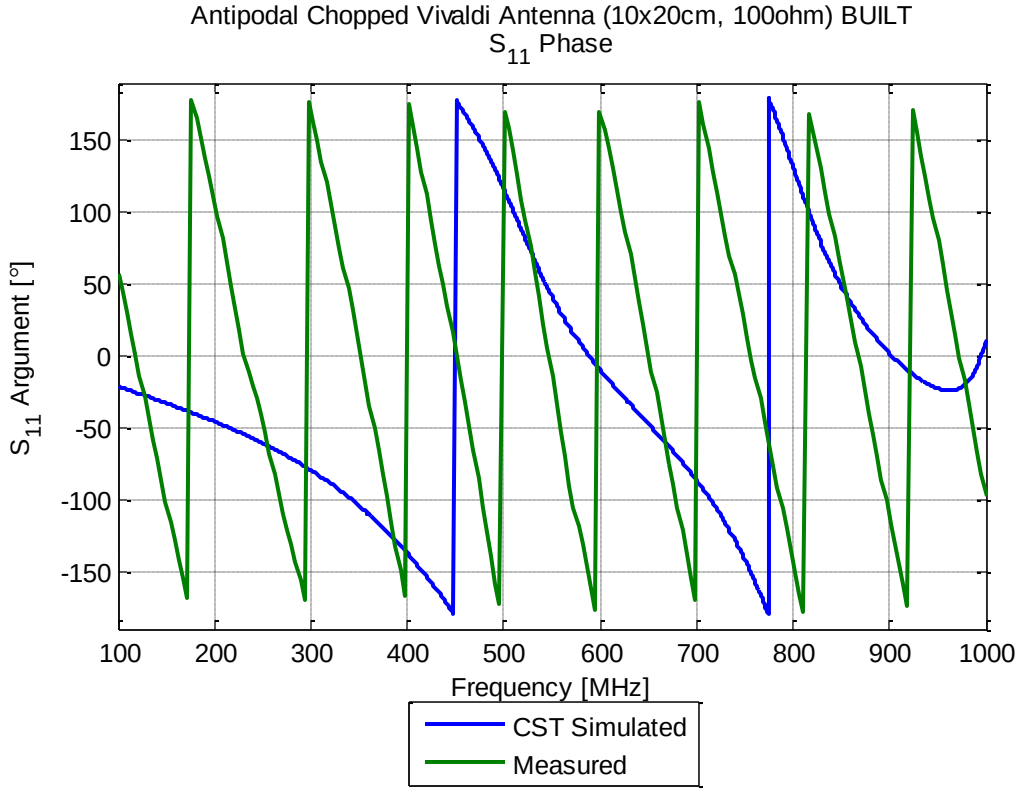
Antipodal Chopped Vivaldi Antenna (10x20cm, 100ohm) BUILT
S11 Phase
S11 Argument [°]
150
100
50
0
-50
-100
-150
100
200
300
400
500
600
700
800
900
1000
Frequency [MHz]
CST Simulated
Measured

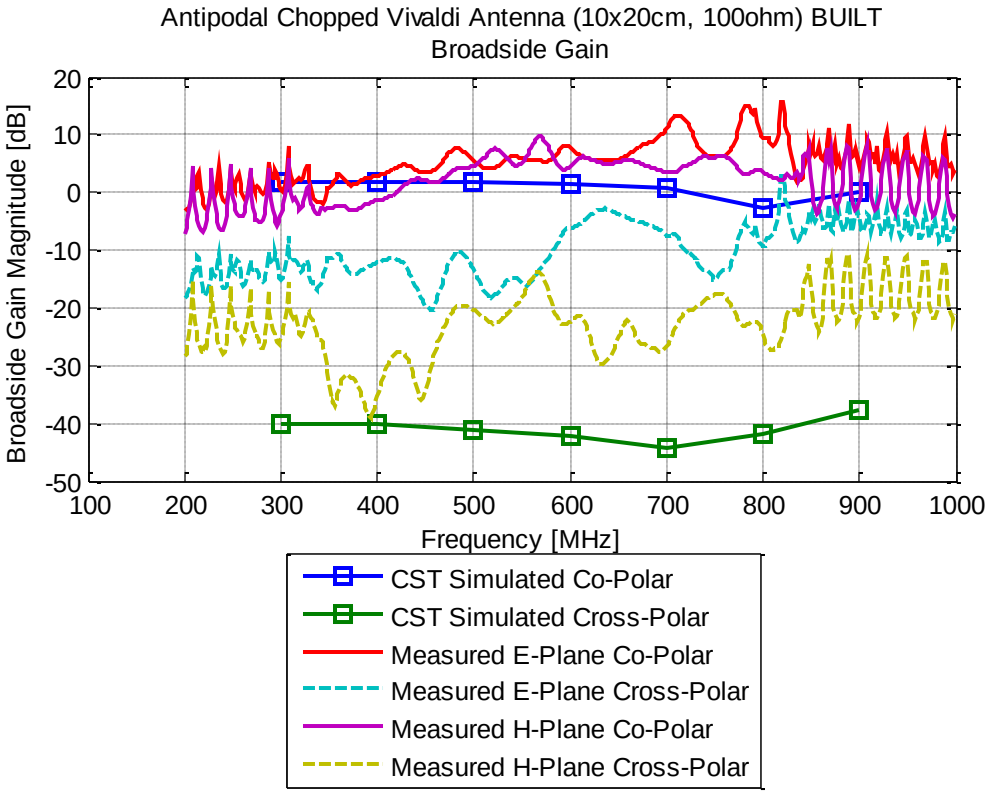
Antipodal Chopped Vivaldi Antenna (10x20cm, 100ohm) BUILT
Broadside Gain
Broadside Gain Magnitude [dB]
20
10
0
-10
-20
-30
-40
-50
100
200
300
400
500
600
700
800
900
1000
Frequency [MHz]
CST Simulated Co-Polar
CST Simulated Cross-Polar
Measured E-Plane Co-Polar
Measured E-Plane Cross-Polar
Measured H-Plane Co-Polar
Measured H-Plane Cross-Polar

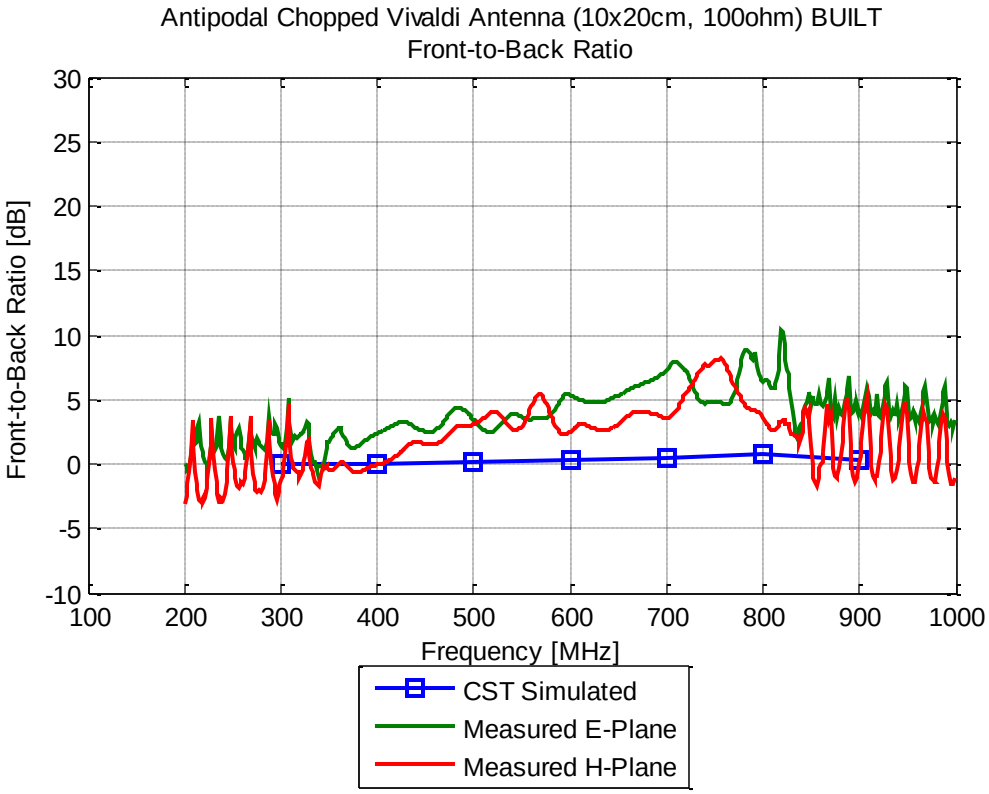
Antipodal Chopped Vivaldi Antenna (10x20cm, 100ohm) BUILT
Front-to-Back Ratio
Front-to-Back Ratio [dB]
30
25
20
15
10
5
0
-5
-10
100
200
300
400
500
600
700
800
900
1000
Frequency [MHz]
CST Simulated
Measured E-Plane
Measured H-Plane

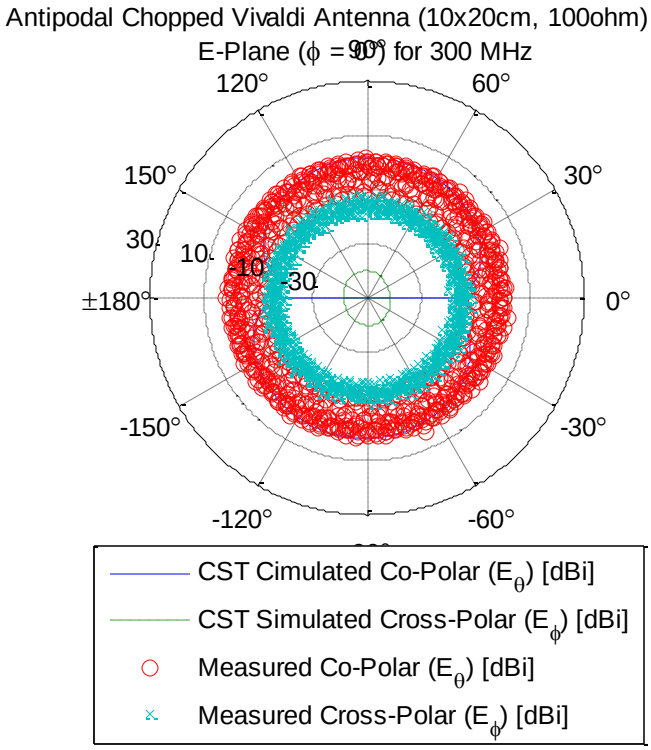
Antipodal Chopped Vivaldi Antenna (10x20cm, 100ohm) BUILT
E-Plane (ϕ = 90°) for 300 MHz
90°
120°
60°
150°
30°
±180°
0°
-150°
-30°
-120°
-60°
-10
-30
CST Cimulated Co-Polar (Eθ) [dBi]
CST Simulated Cross-Polar (Eϕ) [dBi]
Measured Co-Polar (Eθ) [dBi]
Measured Cross-Polar (Eϕ) [dBi]

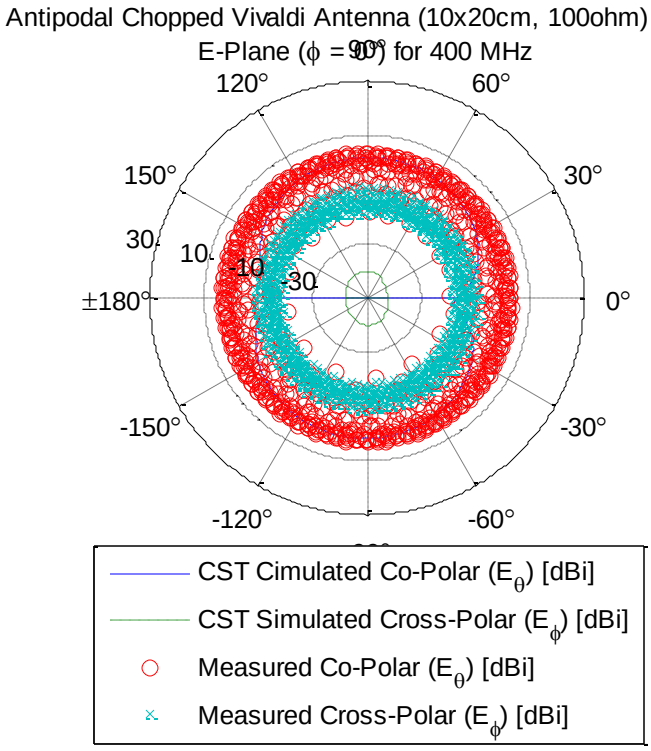
Antipodal Chopped Vivaldi Antenna (10x20cm, 100ohm) BUILT
E-Plane (ϕ = 90°) for 400 MHz
90°
120°
60°
150°
30°
±180°
0°
-150°
-30°
-120°
-60°
-10
-30
CST Cimulated Co-Polar (Eθ) [dBi]
CST Simulated Cross-Polar (Eϕ) [dBi]
Measured Co-Polar (Eθ) [dBi]
Measured Cross-Polar (Eϕ) [dBi]

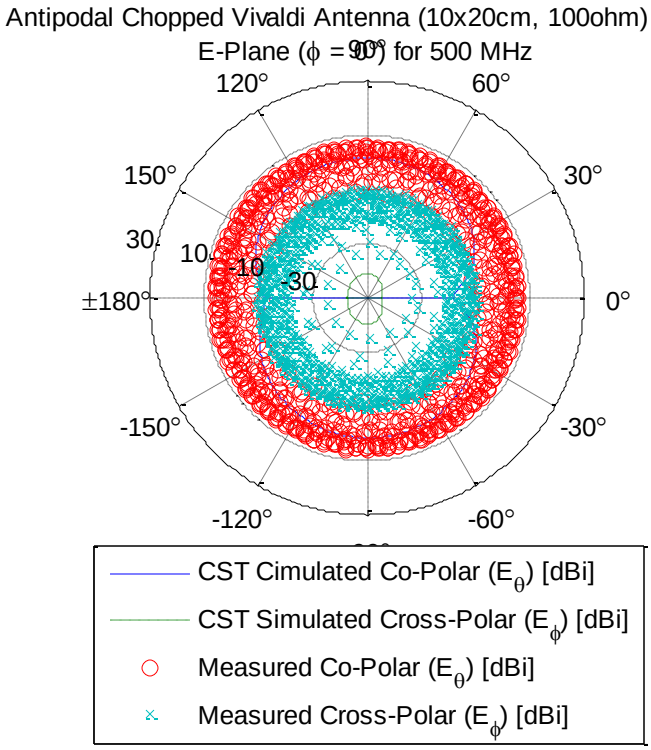
Antipodal Chopped Vivaldi Antenna (10x20cm, 100ohm) BUILT
E-Plane (ϕ = 90°) for 500 MHz
90°
120°
60°
150°
30°
10
-10
-30
±180°
0°
-150°
-30°
-120°
-60°
CST Cimulated Co-Polar (Eθ) [dBi]
CST Simulated Cross-Polar (Eϕ) [dBi]
Measured Co-Polar (Eθ) [dBi]
Measured Cross-Polar (Eϕ) [dBi]

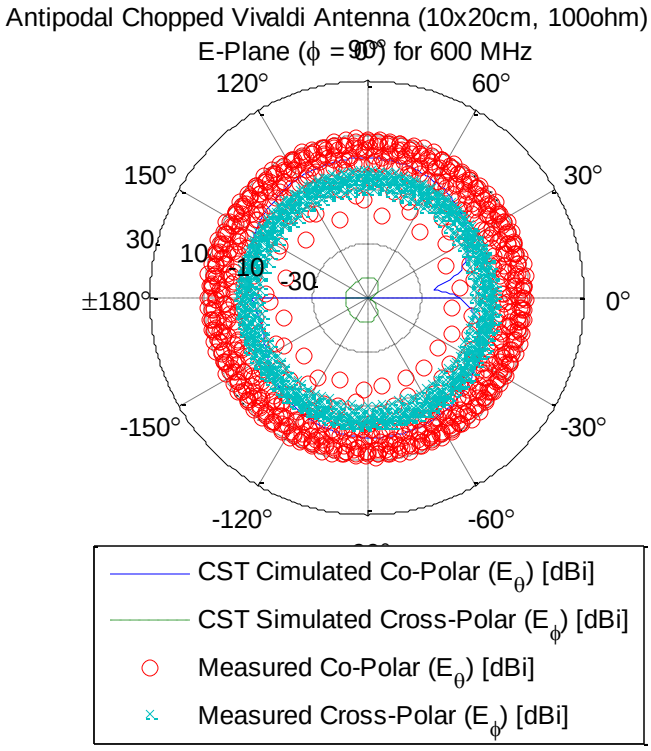
Antipodal Chopped Vivaldi Antenna (10x20cm, 100ohm) BUILT
E-Plane (ϕ = 90°) for 600 MHz
90°
120°
60°
150°
30°
10
-10
-30
±180°
0°
-150°
-30°
-120°
-60°
CST Cimulated Co-Polar (Eθ) [dBi]
CST Simulated Cross-Polar (Eϕ) [dBi]
Measured Co-Polar (Eθ) [dBi]
Measured Cross-Polar (Eϕ) [dBi]

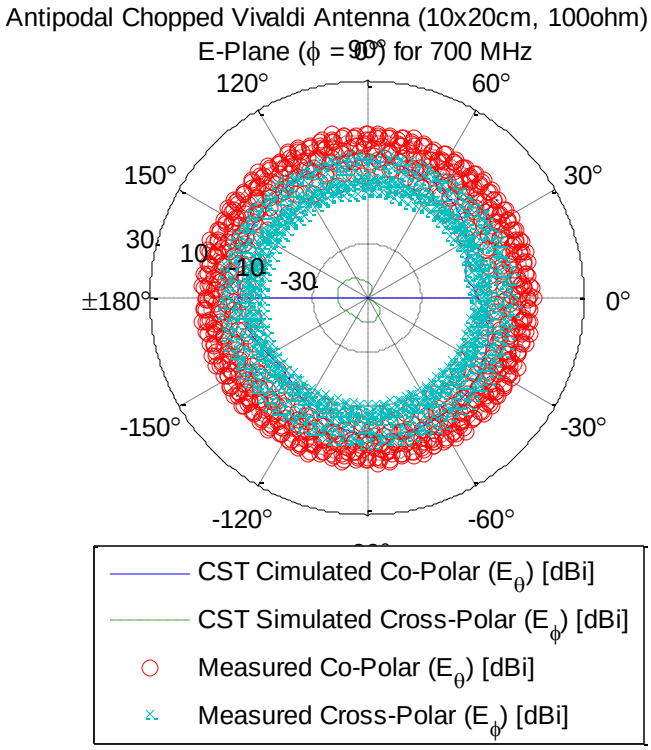
Antipodal Chopped Vivaldi Antenna (10x20cm, 100ohm) BUILT
E-Plane (ϕ = 90°) for 700 MHz
90°
120°
60°
150°
30°
30
10
-10
-30
±180°
0°
-150°
-30°
-120°
-60°
CST Cimulated Co-Polar (Eθ) [dBi]
CST Simulated Cross-Polar (Eϕ) [dBi]
Measured Co-Polar (Eθ) [dBi]
Measured Cross-Polar (Eϕ) [dBi]

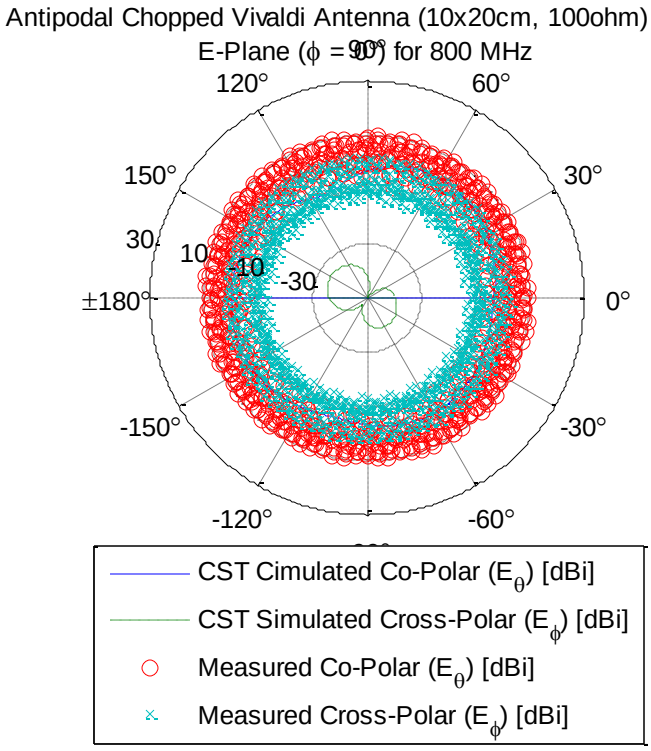
Antipodal Chopped Vivaldi Antenna (10x20cm, 100ohm) BUILT
E-Plane (ϕ = 90°) for 800 MHz
90°
120°
60°
150°
30°
30
10
-10
-30
±180°
0°
-150°
-30°
-120°
-60°
CST Cimulated Co-Polar (Eθ) [dBi]
CST Simulated Cross-Polar (Eϕ) [dBi]
Measured Co-Polar (Eθ) [dBi]
Measured Cross-Polar (Eϕ) [dBi]

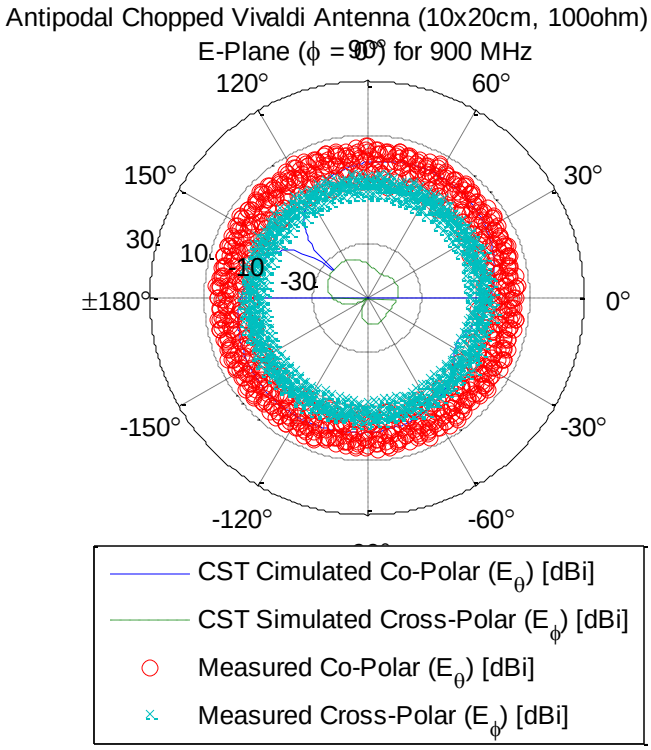
Antipodal Chopped Vivaldi Antenna (10x20cm, 100ohm) BUILT
E-Plane (ϕ = 90°) for 900 MHz
90°
120°
60°
150°
30°
±180°
0°
-150°
-30°
-120°
-60°
-10
-30
CST Cimulated Co-Polar (Eθ) [dBi]
CST Simulated Cross-Polar (Eϕ) [dBi]
Measured Co-Polar (Eθ) [dBi]
Measured Cross-Polar (Eϕ) [dBi]

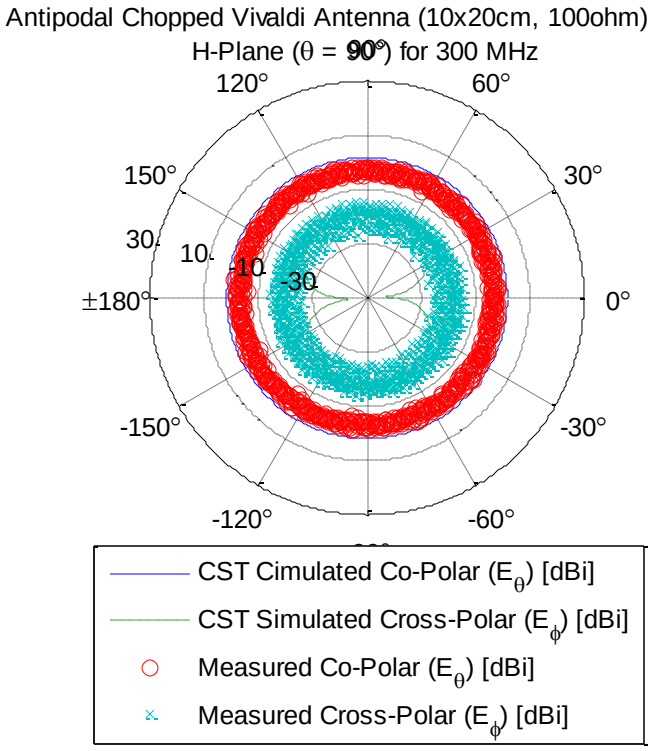
Antipodal Chopped Vivaldi Antenna (10x20cm, 100ohm) BUILT
H-Plane (θ = 90°) for 300 MHz
90°
120°
60°
150°
30°
±180°
0°
-150°
-30°
-120°
-60°
-10
-30
CST Cimulated Co-Polar (Eθ) [dBi]
CST Simulated Cross-Polar (Eϕ) [dBi]
Measured Co-Polar (Eθ) [dBi]
Measured Cross-Polar (Eϕ) [dBi]

Antipodal Chopped Vivaldi Antenna (10x20cm, 100ohm) BUILT
H-Plane (θ = 90°) for 400 MHz

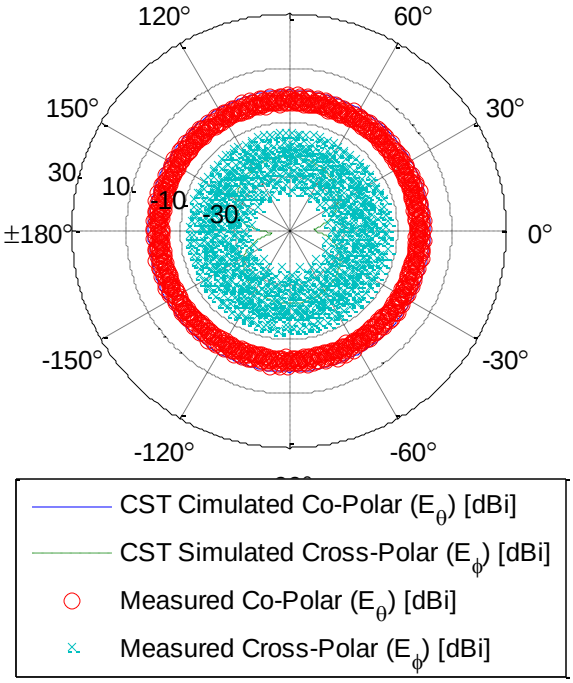

Antipodal Chopped Vivaldi Antenna (10x20cm, 100ohm) BUILT
H-Plane (θ = 90°) for 500 MHz

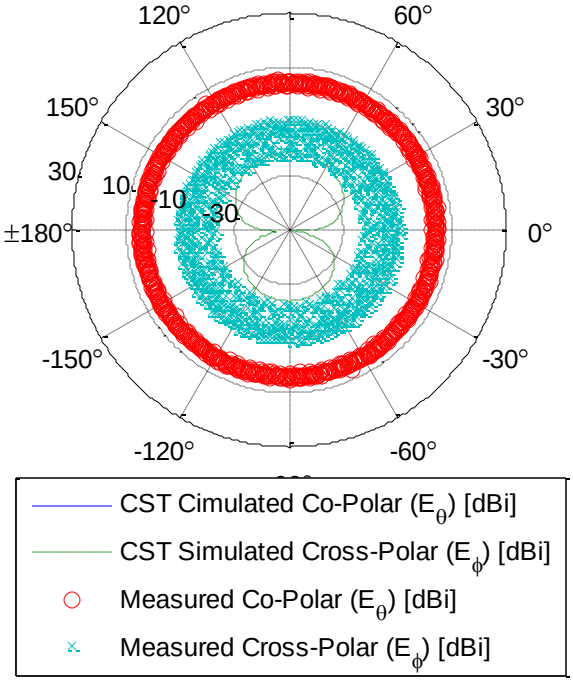

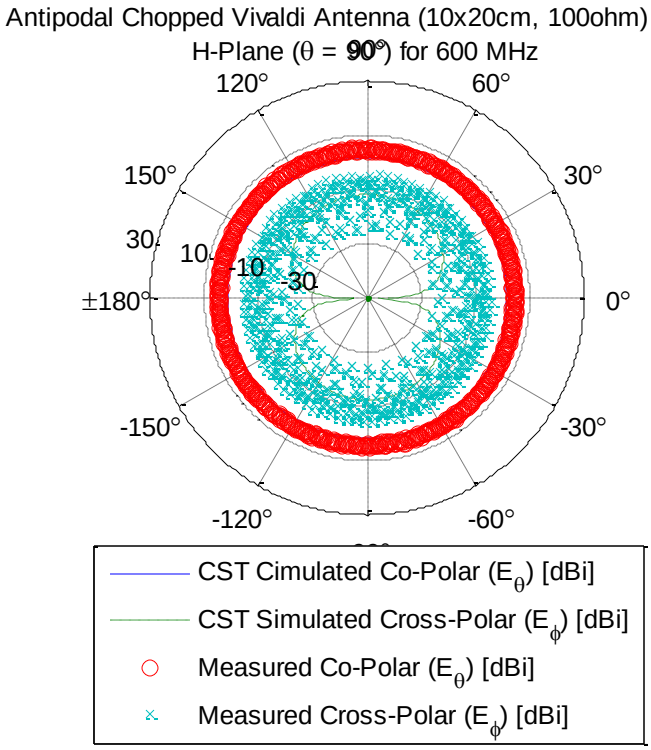
Antipodal Chopped Vivaldi Antenna (10x20cm, 100ohm) BUILT
H-Plane (θ = 90°) for 600 MHz
120°
60°
150°
30°
±180°
0°
-150°
-30°
-120°
-60°
-10
-30
CST Cimulated Co-Polar (Eθ) [dBi]
CST Simulated Cross-Polar (Eϕ) [dBi]
Measured Co-Polar (Eθ) [dBi]
Measured Cross-Polar (Eϕ) [dBi]

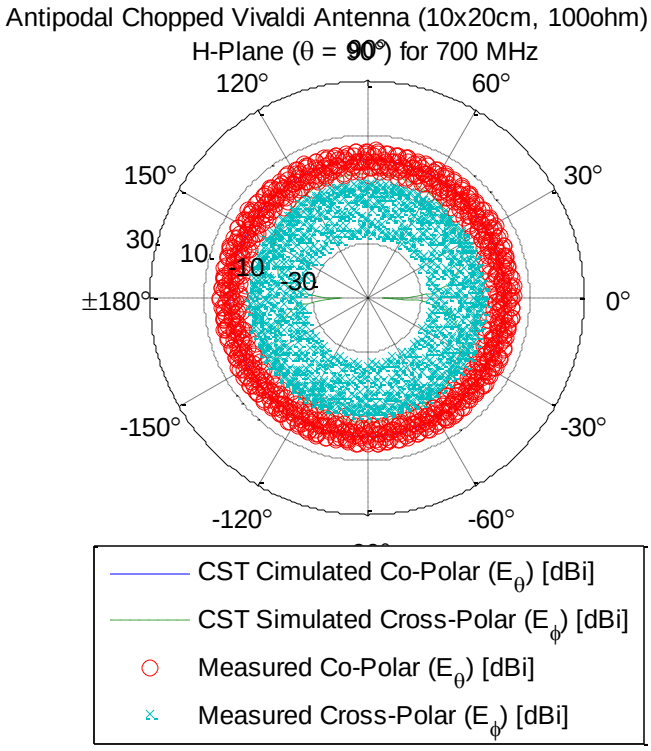
Antipodal Chopped Vivaldi Antenna (10x20cm, 100ohm) BUILT
H-Plane (θ = 90°) for 700 MHz
120°
60°
150°
30°
±180°
0°
-150°
-30°
-120°
-60°
-10
-30
CST Cimulated Co-Polar (Eθ) [dBi]
CST Simulated Cross-Polar (Eϕ) [dBi]
Measured Co-Polar (Eθ) [dBi]
Measured Cross-Polar (Eϕ) [dBi]

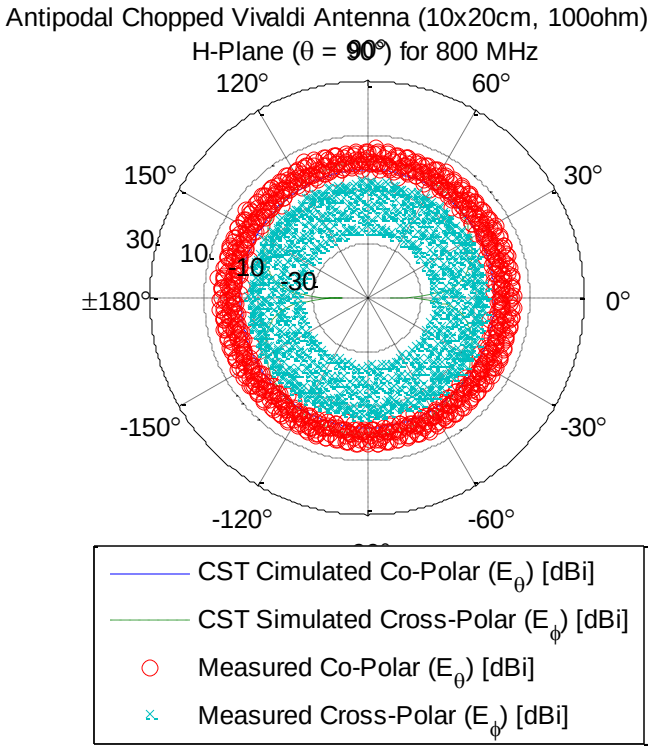
Antipodal Chopped Vivaldi Antenna (10x20cm, 100ohm) BUILT
H-Plane (θ = 90°) for 800 MHz
120°
60°
150°
30°
±180°
0°
-150°
-30°
-120°
-60°
CST Cimulated Co-Polar (Eθ) [dBi]
CST Simulated Cross-Polar (Eϕ) [dBi]
Measured Co-Polar (Eθ) [dBi]
Measured Cross-Polar (Eϕ) [dBi]

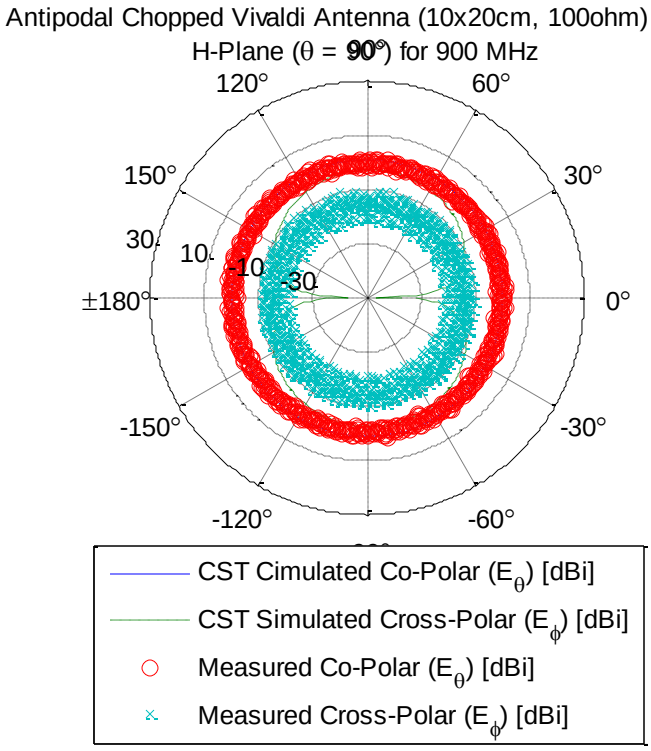
Antipodal Chopped Vivaldi Antenna (10x20cm, 100ohm) BUILT
H-Plane (θ = 90°) for 900 MHz
120°
60°
150°
30°
±180°
0°
-150°
-30°
-120°
-60°
CST Cimulated Co-Polar (Eθ) [dBi]
CST Simulated Cross-Polar (Eϕ) [dBi]
Measured Co-Polar (Eθ) [dBi]
Measured Cross-Polar (Eϕ) [dBi]

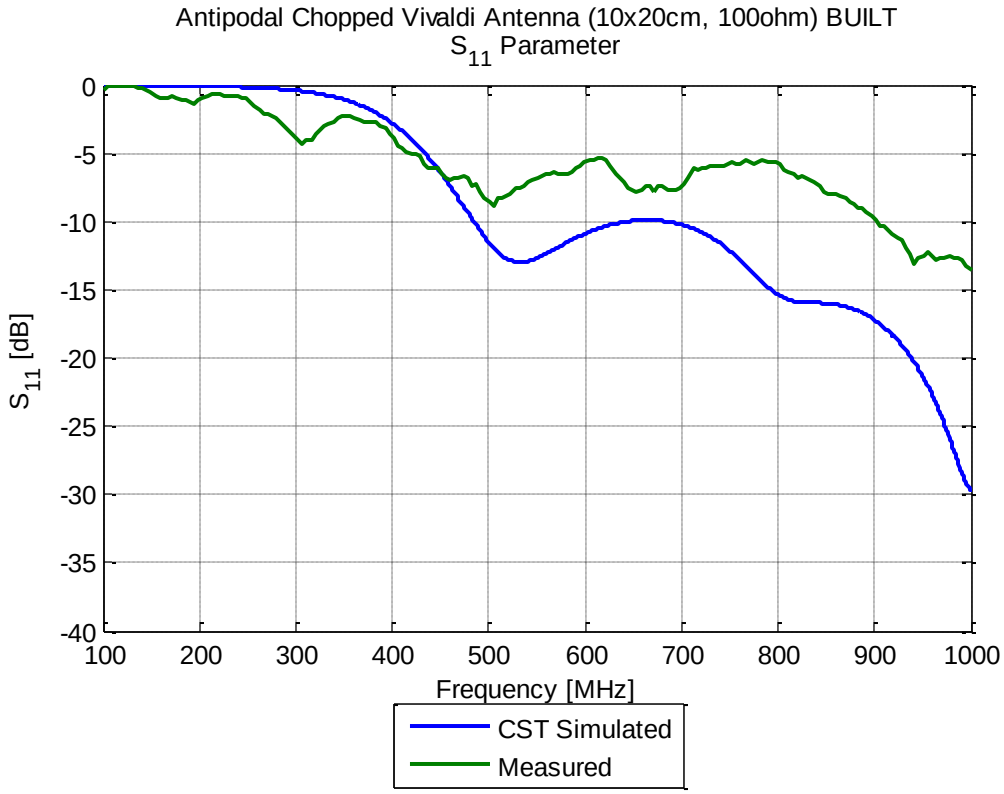
Antipodal Chopped Vivaldi Antenna (10x20cm, 100ohm) BUILT
S11 Parameter
S11 [dB]
0
-5
-10
-15
-20
-25
-30
-35
-40
100
200
300
400
500
600
700
800
900
1000
Frequency [MHz]
CST Simulated
Measured

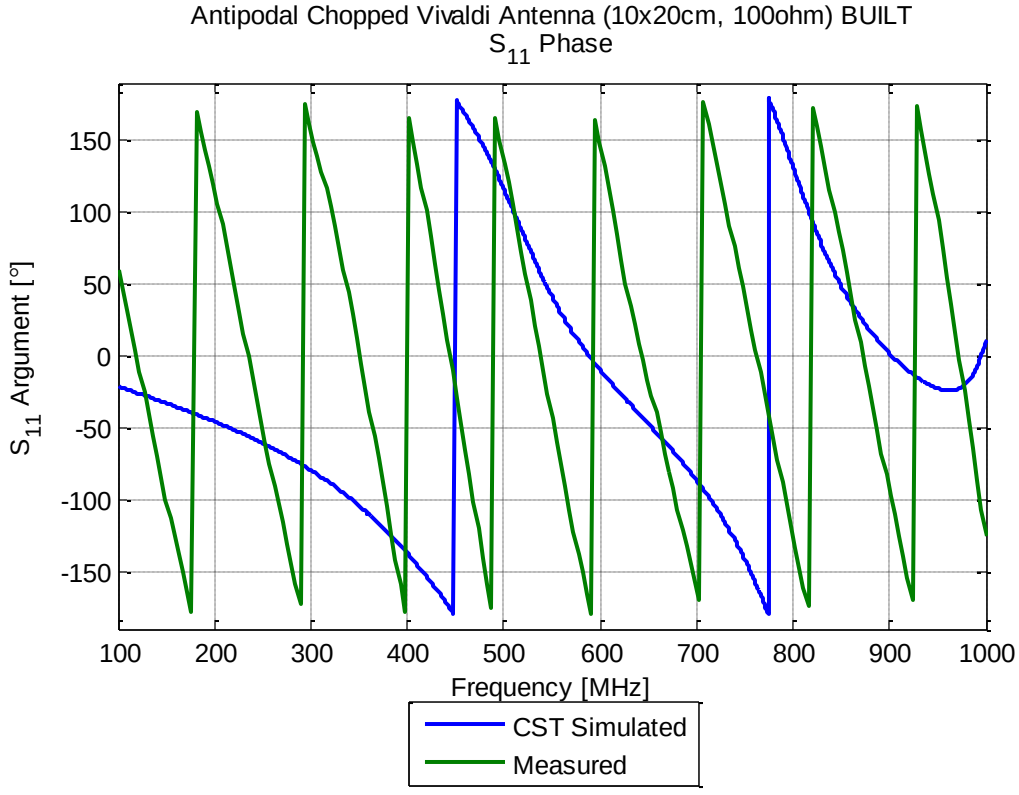
Antipodal Chopped Vivaldi Antenna (10x20cm, 100ohm) BUILT
S11 Phase
S11 Argument [°]
150
100
50
0
-50
-100
-150
100
200
300
400
500
600
700
800
900
1000
Frequency [MHz]
CST Simulated
Measured

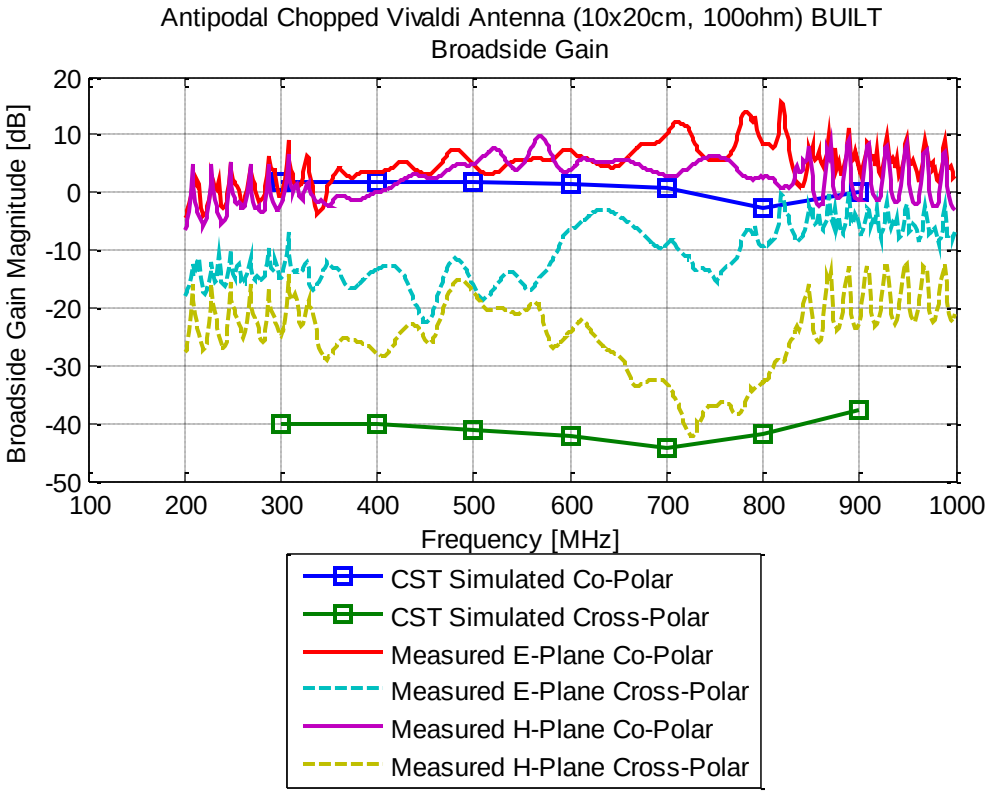
Antipodal Chopped Vivaldi Antenna (10x20cm, 100ohm) BUILT
Broadside Gain
Broadside Gain Magnitude [dB]
20
10
0
-10
-20
-30
-40
-50
100
200
300
400
500
600
700
800
900
1000
Frequency [MHz]
CST Simulated Co-Polar
CST Simulated Cross-Polar
Measured E-Plane Co-Polar
Measured E-Plane Cross-Polar
Measured H-Plane Co-Polar
Measured H-Plane Cross-Polar

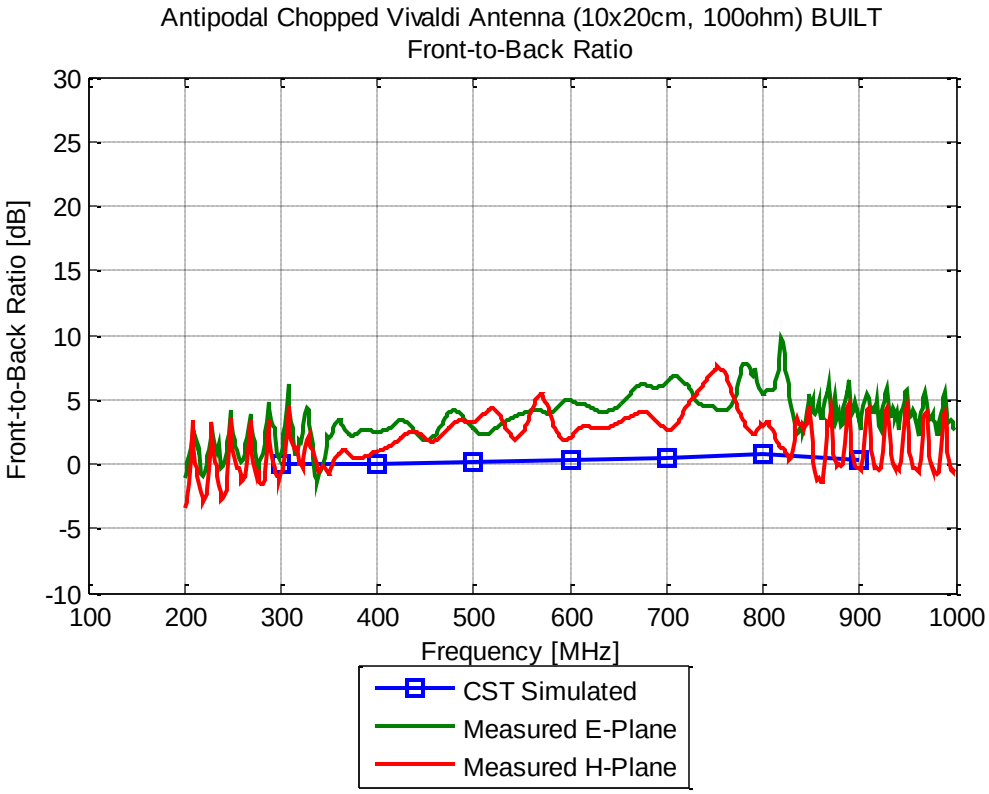
Antipodal Chopped Vivaldi Antenna (10x20cm, 100ohm) BUILT
Front-to-Back Ratio
Front-to-Back Ratio [dB]
30
25
20
15
10
5
0
-5
-10
100
200
300
400
500
600
700
800
900
1000
Frequency [MHz]
CST Simulated
Measured E-Plane
Measured H-Plane

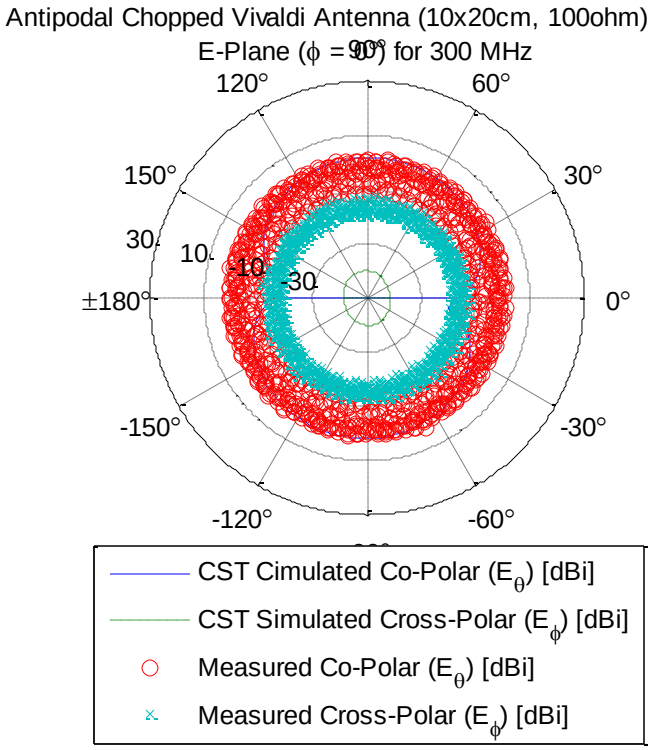
Antipodal Chopped Vivaldi Antenna (10x20cm, 100ohm) BUILT
E-Plane (ϕ = 90°) for 300 MHz
90°
120°
60°
150°
30°
±180°
0°
-150°
-30°
-120°
-60°
-10
-30
CST Cimulated Co-Polar (Eθ) [dBi]
CST Simulated Cross-Polar (Eϕ) [dBi]
Measured Co-Polar (Eθ) [dBi]
Measured Cross-Polar (Eϕ) [dBi]

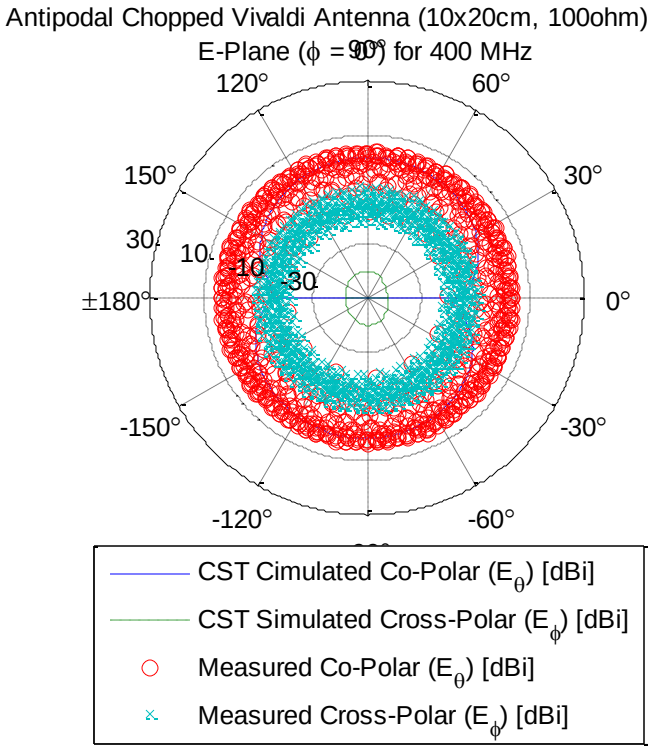
Antipodal Chopped Vivaldi Antenna (10x20cm, 100ohm) BUILT
E-Plane (ϕ = 90°) for 400 MHz
90°
120°
60°
150°
30°
±180°
0°
-150°
-30°
-120°
-60°
-10
-30
CST Cimulated Co-Polar (Eθ) [dBi]
CST Simulated Cross-Polar (Eϕ) [dBi]
Measured Co-Polar (Eθ) [dBi]
Measured Cross-Polar (Eϕ) [dBi]

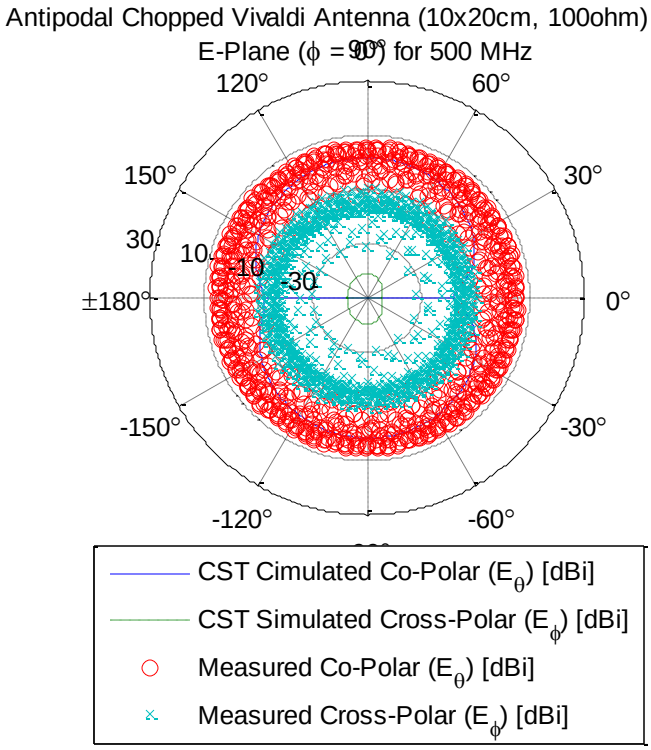
Antipodal Chopped Vivaldi Antenna (10x20cm, 100ohm) BUILT
E-Plane (ϕ = 90°) for 500 MHz
90°
120°
60°
150°
30°
10
-10
-30
±180°
0°
-150°
-30°
-120°
-60°
CST Cimulated Co-Polar (Eθ) [dBi]
CST Simulated Cross-Polar (Eϕ) [dBi]
Measured Co-Polar (Eθ) [dBi]
Measured Cross-Polar (Eϕ) [dBi]

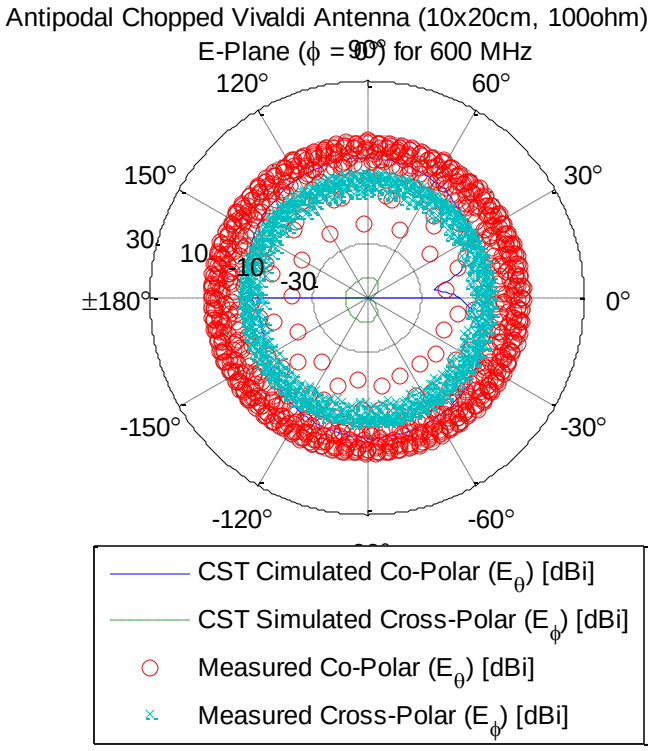
Antipodal Chopped Vivaldi Antenna (10x20cm, 100ohm) BUILT
E-Plane (ϕ = 90°) for 600 MHz
90°
120°
60°
150°
30°
10
-10
-30
±180°
0°
-150°
-30°
-120°
-60°
CST Cimulated Co-Polar (Eθ) [dBi]
CST Simulated Cross-Polar (Eϕ) [dBi]
Measured Co-Polar (Eθ) [dBi]
Measured Cross-Polar (Eϕ) [dBi]

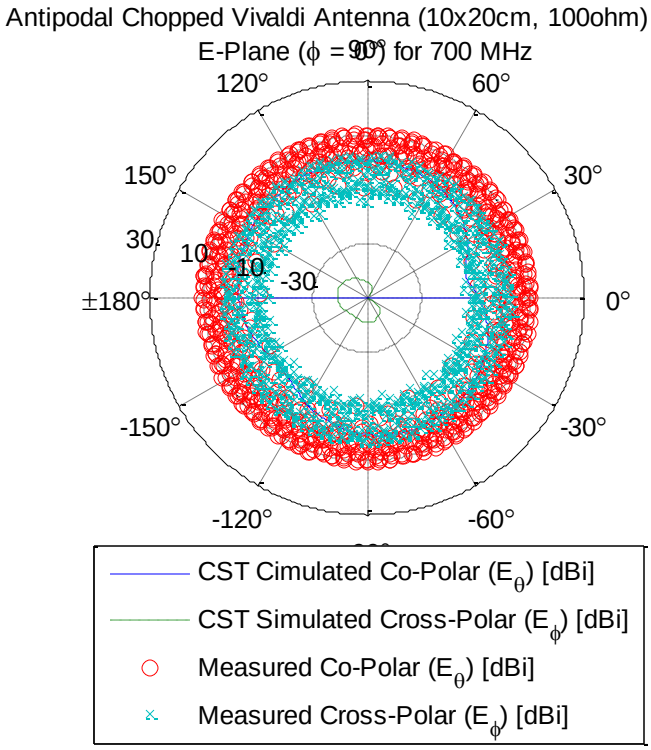
Antipodal Chopped Vivaldi Antenna (10x20cm, 100ohm) BUILT
E-Plane (ϕ = 90°) for 700 MHz
90°
120°
60°
150°
30°
30
10
-10
-30
±180°
0°
-150°
-30°
-120°
-60°
CST Cimulated Co-Polar (Eθ) [dBi]
CST Simulated Cross-Polar (Eϕ) [dBi]
Measured Co-Polar (Eθ) [dBi]
Measured Cross-Polar (Eϕ) [dBi]

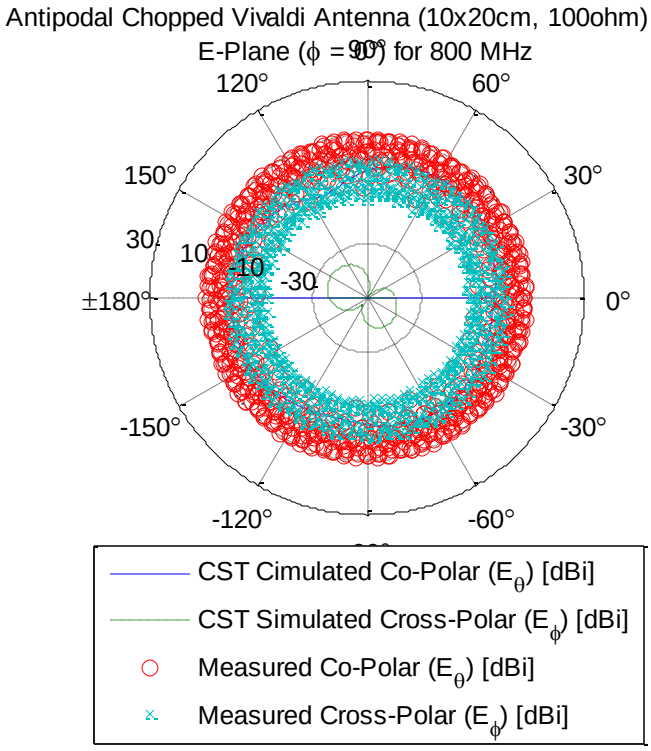
Antipodal Chopped Vivaldi Antenna (10x20cm, 100ohm) BUILT
E-Plane (ϕ = 90°) for 800 MHz
90°
120°
60°
150°
30°
30
10
-10
-30
±180°
0°
-150°
-30°
-120°
-60°
CST Cimulated Co-Polar (Eθ) [dBi]
CST Simulated Cross-Polar (Eϕ) [dBi]
Measured Co-Polar (Eθ) [dBi]
Measured Cross-Polar (Eϕ) [dBi]

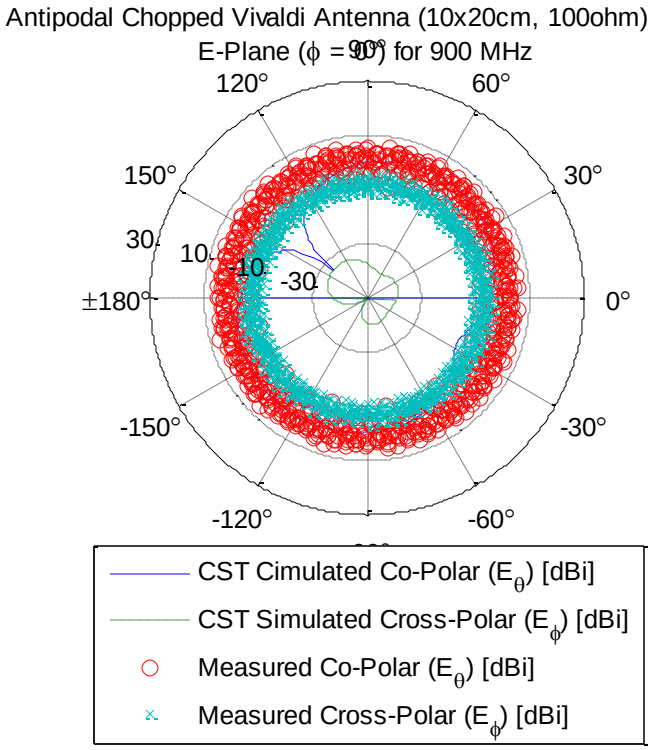
Antipodal Chopped Vivaldi Antenna (10x20cm, 100ohm) BUILT
E-Plane (ϕ = 90°) for 900 MHz
120°
60°
150°
30°
±180°
0°
-150°
-30°
-120°
-60°
-10
-30
CST Cimulated Co-Polar (Eθ) [dBi]
CST Simulated Cross-Polar (Eϕ) [dBi]
Measured Co-Polar (Eθ) [dBi]
Measured Cross-Polar (Eϕ) [dBi]

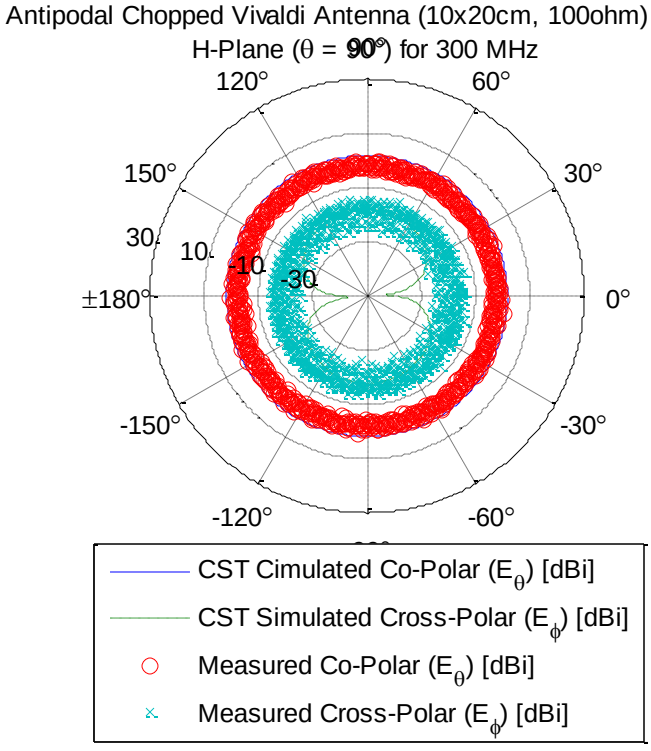
Antipodal Chopped Vivaldi Antenna (10x20cm, 100ohm) BUILT
H-Plane (θ = 90°) for 300 MHz
120°
60°
150°
30°
±180°
0°
-150°
-30°
-120°
-60°
-10
-30
CST Cimulated Co-Polar (Eθ) [dBi]
CST Simulated Cross-Polar (Eϕ) [dBi]
Measured Co-Polar (Eθ) [dBi]
Measured Cross-Polar (Eϕ) [dBi]

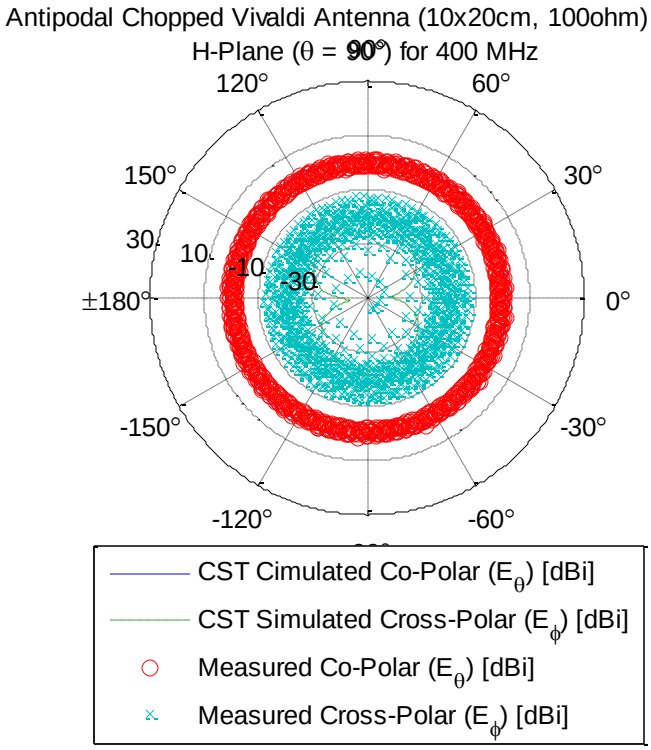
Antipodal Chopped Vivaldi Antenna (10x20cm, 100ohm) BUILT
H-Plane (θ = 90°) for 400 MHz
120°
60°
150°
30°
±180°
0°
-150°
-30°
-120°
-60°
-10
-30
CST Cimulated Co-Polar (Eθ) [dBi]
CST Simulated Cross-Polar (Eϕ) [dBi]
Measured Co-Polar (Eθ) [dBi]
Measured Cross-Polar (Eϕ) [dBi]

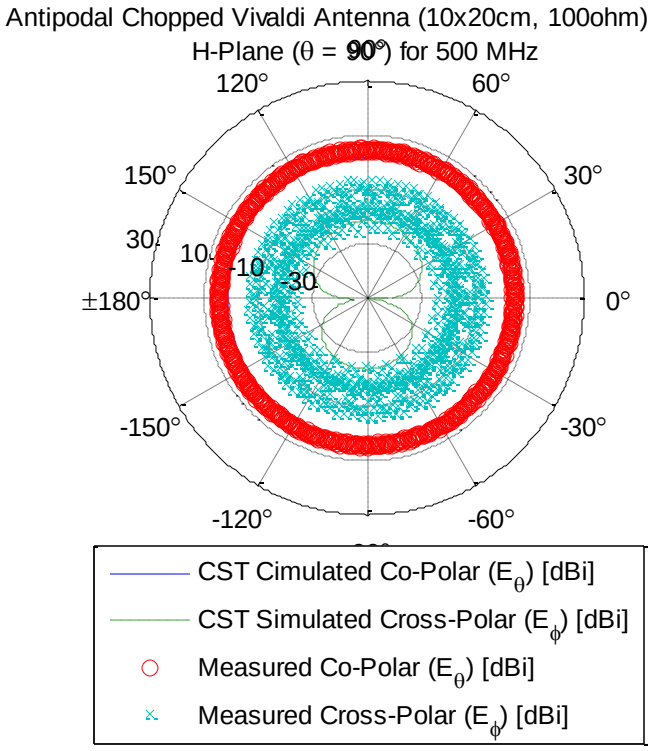
Antipodal Chopped Vivaldi Antenna (10x20cm, 100ohm) BUILT
H-Plane (θ = 90°) for 500 MHz
120°
60°
150°
30°
±180°
0°
-150°
-30°
-120°
-60°
-10
-30
CST Cimulated Co-Polar (Eθ) [dBi]
CST Simulated Cross-Polar (Eϕ) [dBi]
Measured Co-Polar (Eθ) [dBi]
Measured Cross-Polar (Eϕ) [dBi]

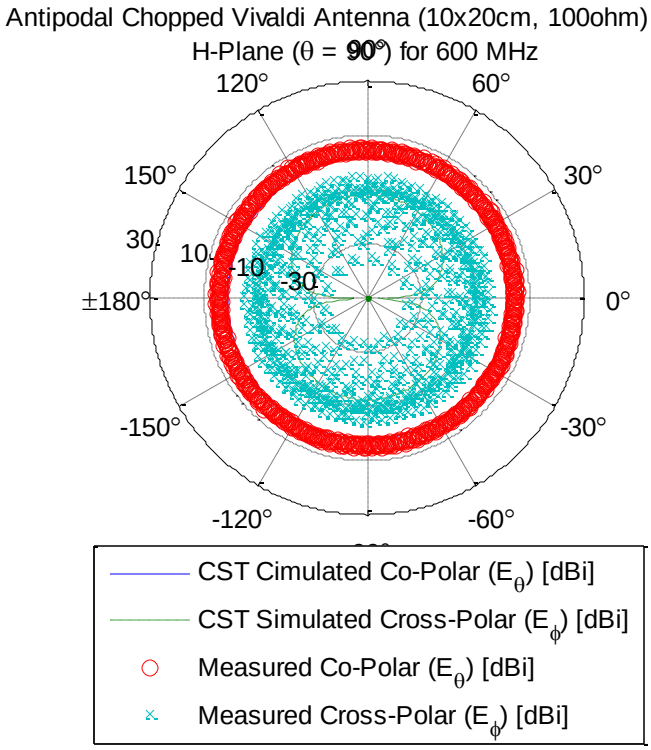
Antipodal Chopped Vivaldi Antenna (10x20cm, 100ohm) BUILT
H-Plane (θ = 90°) for 600 MHz
120°
60°
150°
30°
±180°
0°
-150°
-30°
-120°
-60°
-10
-30
CST Cimulated Co-Polar (Eθ) [dBi]
CST Simulated Cross-Polar (Eϕ) [dBi]
Measured Co-Polar (Eθ) [dBi]
Measured Cross-Polar (Eϕ) [dBi]

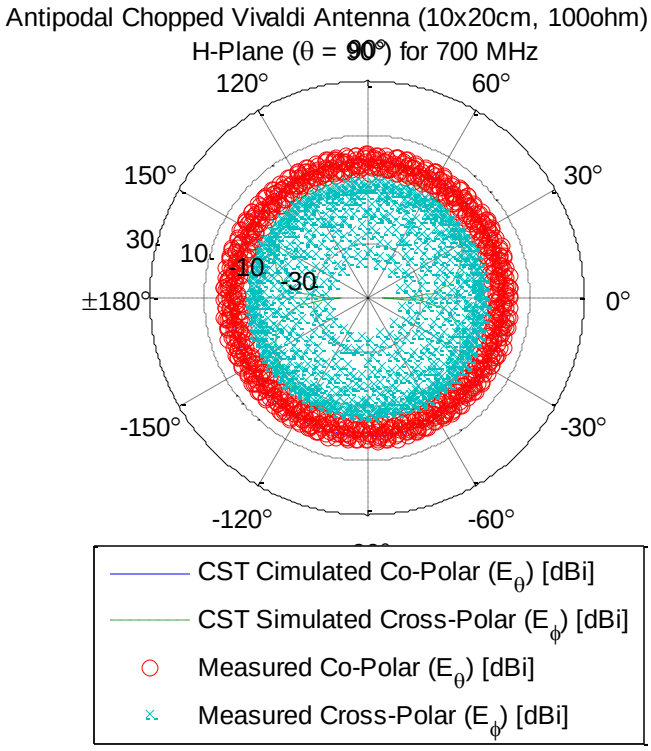
Antipodal Chopped Vivaldi Antenna (10x20cm, 100ohm) BUILT
H-Plane (θ = 90°) for 700 MHz
120°
60°
150°
30°
±180°
0°
-150°
-30°
-120°
-60°
-10
-30
CST Cimulated Co-Polar (Eθ) [dBi]
CST Simulated Cross-Polar (Eϕ) [dBi]
Measured Co-Polar (Eθ) [dBi]
Measured Cross-Polar (Eϕ) [dBi]

Antipodal Chopped Vivaldi Antenna (10x20cm, 100ohm) BUILT
H-Plane (θ = 90°) for 800 MHz

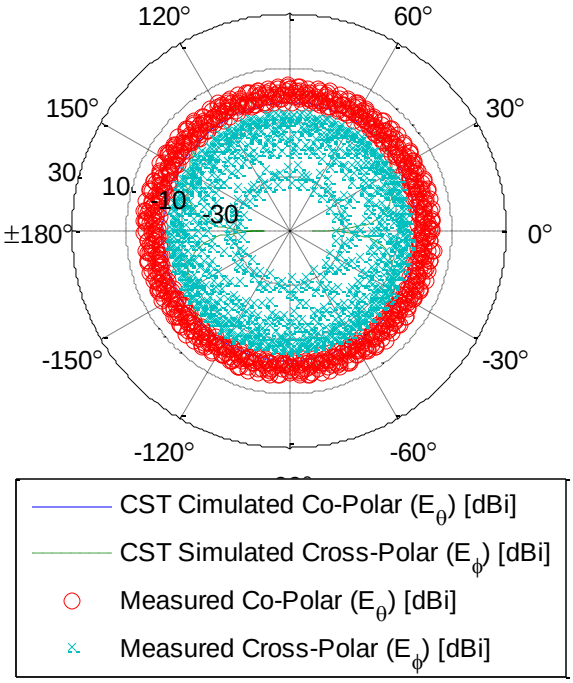

Antipodal Chopped Vivaldi Antenna (10x20cm, 100ohm) BUILT
H-Plane (θ = 90°) for 900 MHz

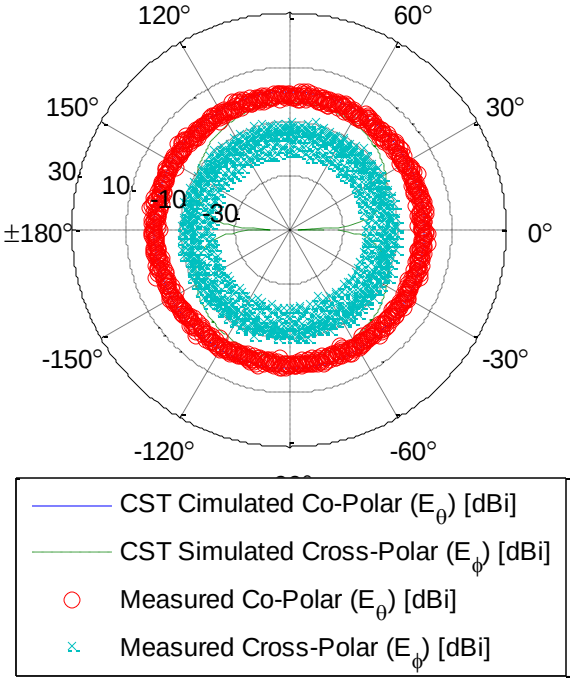

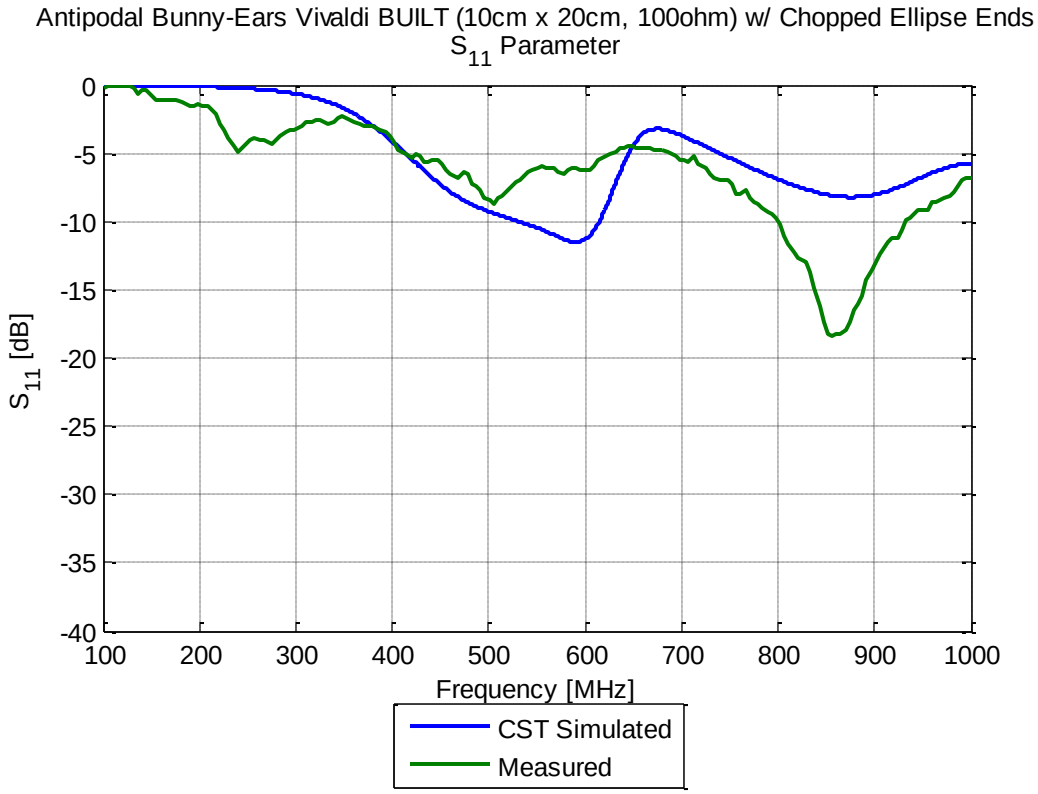
Antipodal Bunny-Ears Vivaldi BUILT (10cm x 20cm, 100ohm) w/ Chopped Ellipse Ends
S11 Parameter
S11 [dB]
0
-5
-10
-15
-20
-25
-30
-35
-40
100
200
300
400
500
600
700
800
900
1000
Frequency [MHz]
CST Simulated
Measured

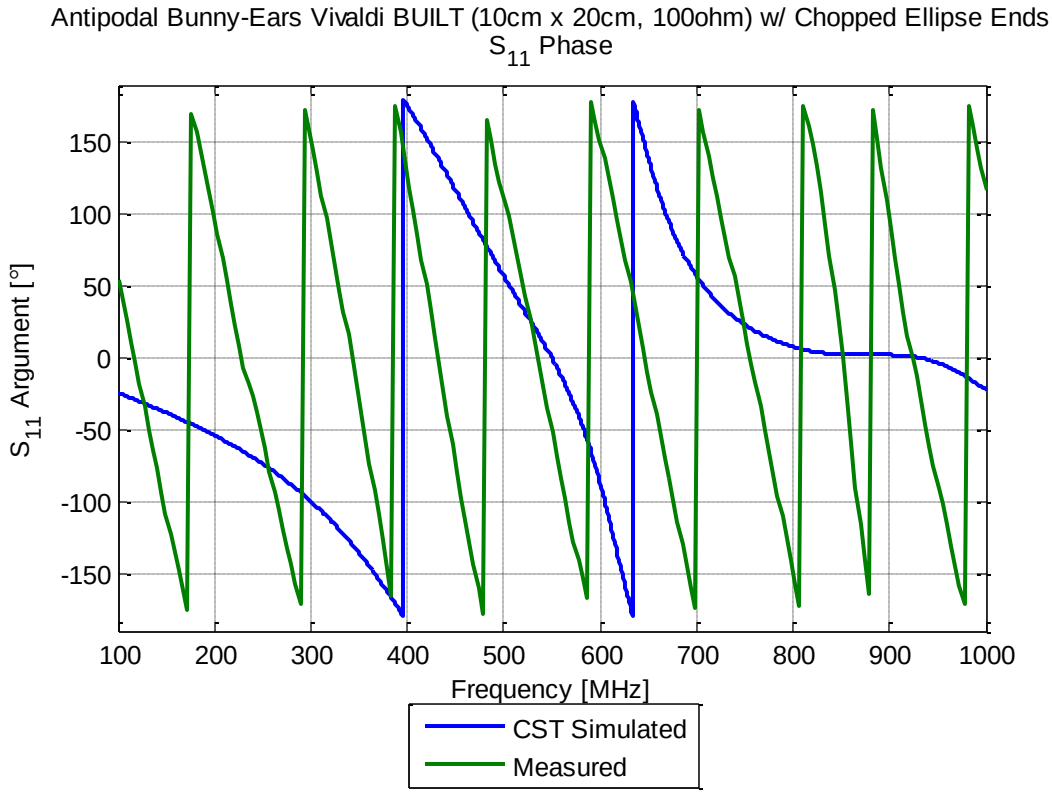
Antipodal Bunny-Ears Vivaldi BUILT (10cm x 20cm, 100ohm) w/ Chopped Ellipse Ends
S11 Phase
S11 Argument [°]
150
100
50
0
-50
-100
-150
100
200
300
400
500
600
700
800
900
1000
Frequency [MHz]
CST Simulated
Measured

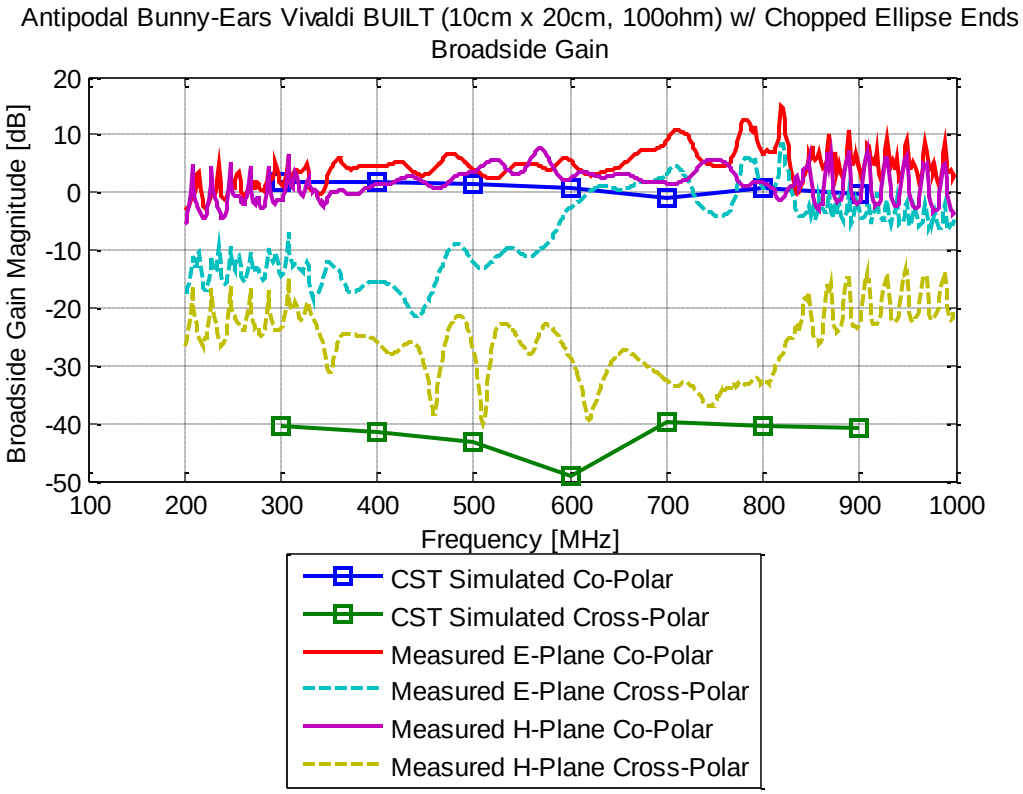
Antipodal Bunny-Ears Vivaldi BUILT (10cm x 20cm, 100ohm) w/ Chopped Ellipse Ends
Broadside Gain
Broadside Gain Magnitude [dB]
20
10
0
-10
-20
-30
-40
-50
100
200
300
400
500
600
700
800
900
1000
Frequency [MHz]
CST Simulated Co-Polar
CST Simulated Cross-Polar
Measured E-Plane Co-Polar
Measured E-Plane Cross-Polar
Measured H-Plane Co-Polar
Measured H-Plane Cross-Polar

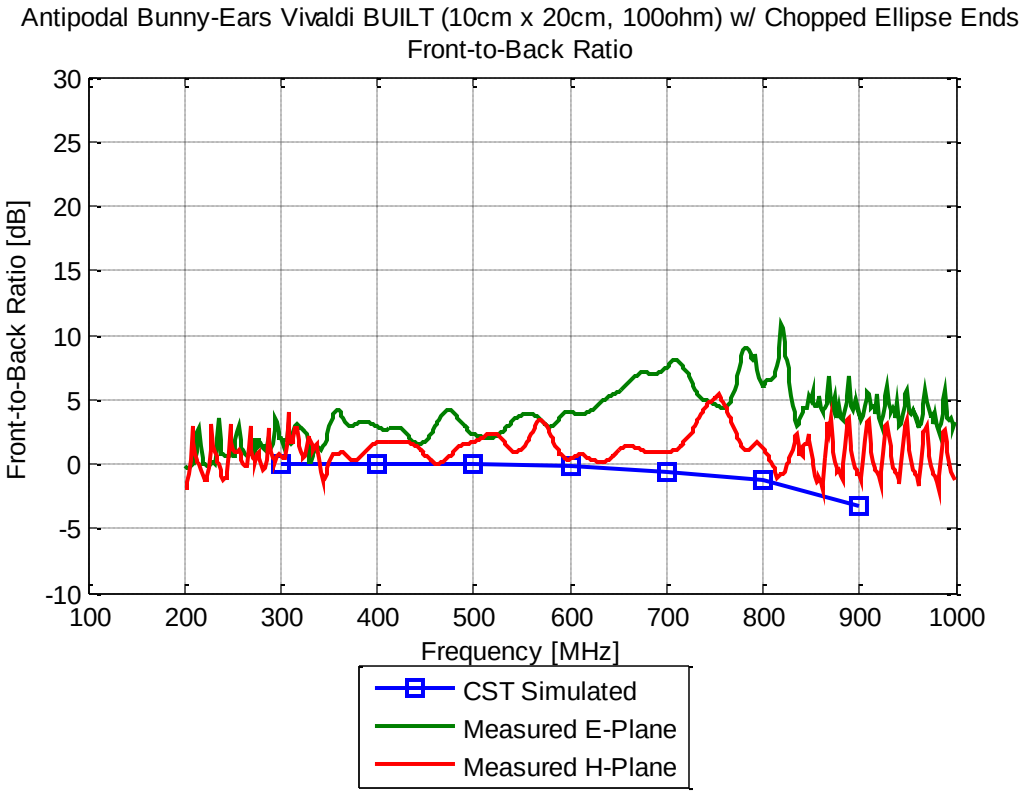
Antipodal Bunny-Ears Vivaldi BUILT (10cm x 20cm, 100ohm) w/ Chopped Ellipse Ends
Front-to-Back Ratio
Front-to-Back Ratio [dB]
30
25
20
15
10
5
0
-5
-10
100
200
300
400
500
600
700
800
900
1000
Frequency [MHz]
CST Simulated
Measured E-Plane
Measured H-Plane

Antipodal Bunny-Ears Vivaldi BUILT (10cm x 20cm, 100ohm) w/ Chopped Ellipse Ends
E-Plane (ϕ = 90°) for 300 MHz

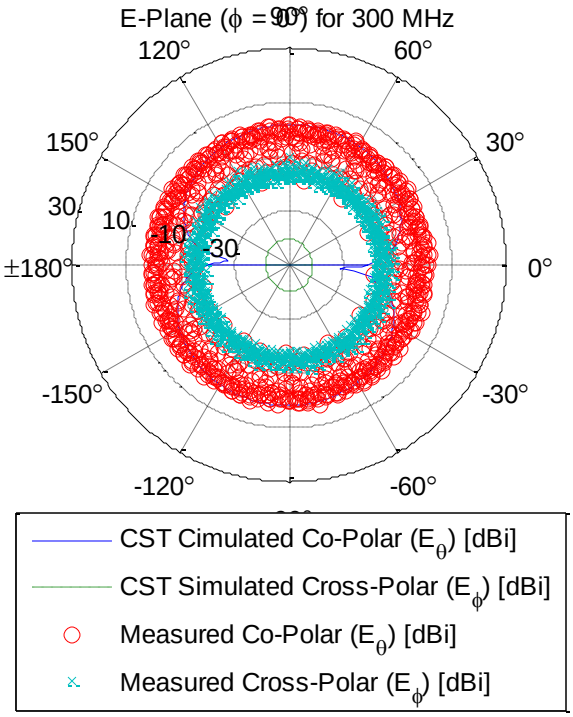

Antipodal Bunny-Ears Vivaldi BUILT (10cm x 20cm, 100ohm) w/ Chopped Ellipse Ends
E-Plane (ϕ = 90°) for 400 MHz

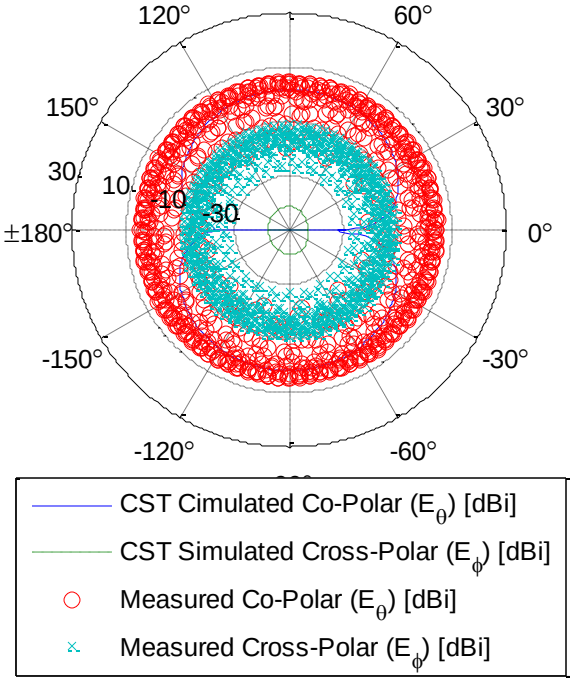

Antipodal Bunny-Ears Vivaldi BUILT (10cm x 20cm, 100ohm) w/ Chopped Ellipse Ends
E-Plane (ϕ = 90°) for 500 MHz

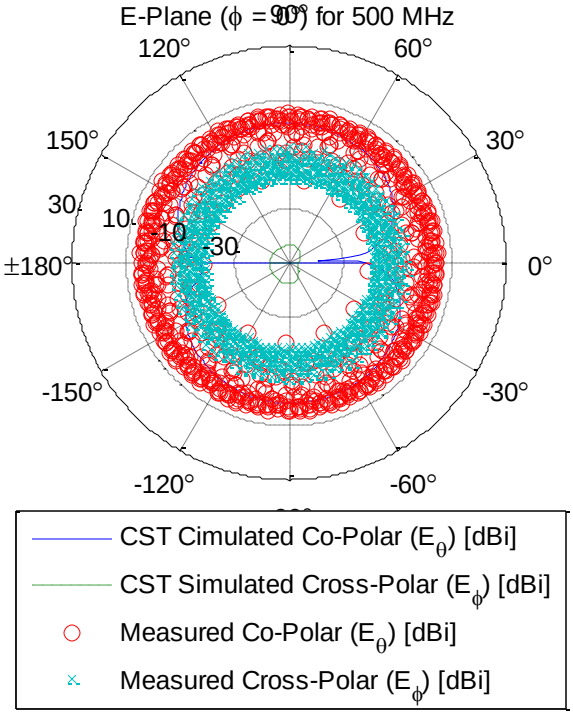

Antipodal Bunny-Ears Vivaldi BUILT (10cm x 20cm, 100ohm) w/ Chopped Ellipse Ends
E-Plane (ϕ = 90°) for 600 MHz

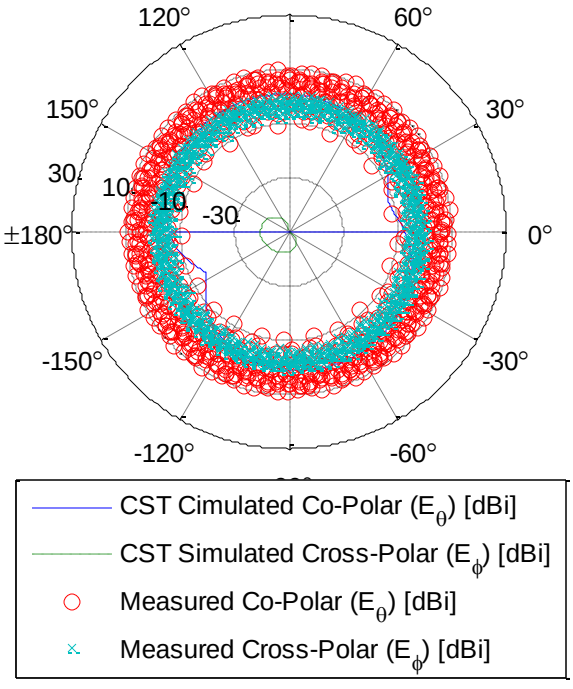

Antipodal Bunny-Ears Vivaldi BUILT (10cm x 20cm, 100ohm) w/ Chopped Ellipse Ends
E-Plane (ϕ = 90°) for 700 MHz

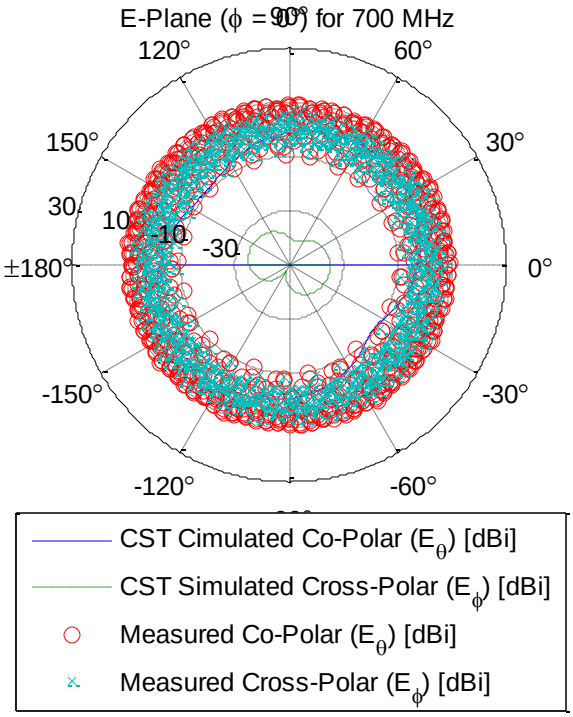

Antipodal Bunny-Ears Vivaldi BUILT (10cm x 20cm, 100ohm) w/ Chopped Ellipse Ends
E-Plane (ϕ = 90°) for 800 MHz

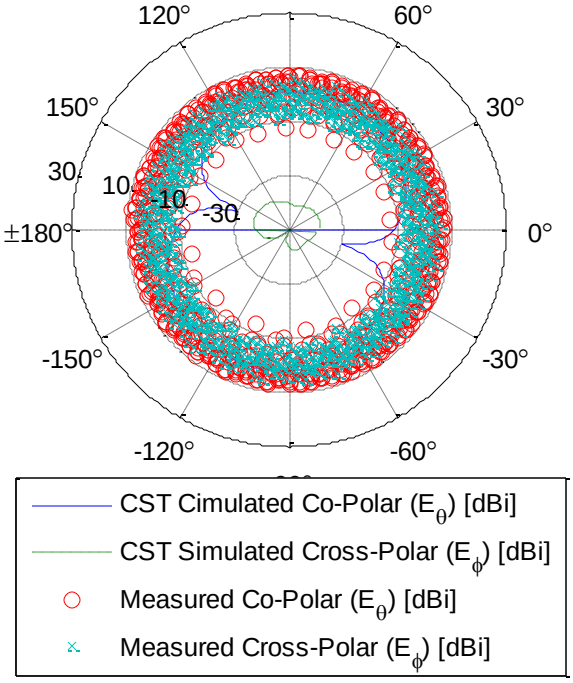

Antipodal Bunny-Ears Vivaldi BUILT (10cm x 20cm, 100ohm) w/ Chopped Ellipse Ends
E-Plane (ϕ = 90°) for 900 MHz

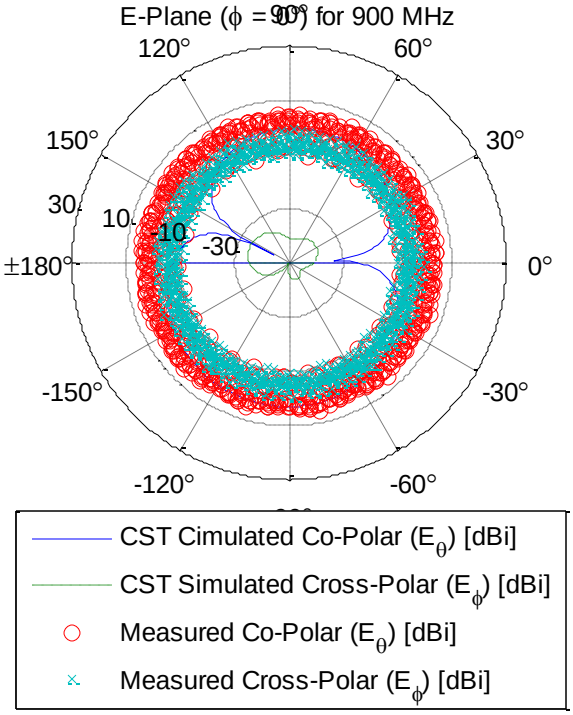

Antipodal Bunny-Ears Vivaldi BUILT (10cm x 20cm, 100ohm) w/ Chopped Ellipse Ends
H-Plane (θ = 90°) for 300 MHz

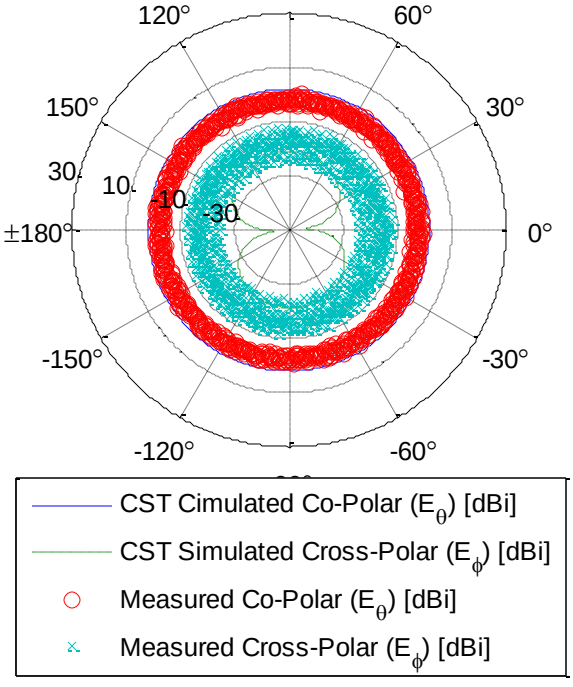

Antipodal Bunny-Ears Vivaldi BUILT (10cm x 20cm, 100ohm) w/ Chopped Ellipse Ends
H-Plane (θ = 90°) for 400 MHz

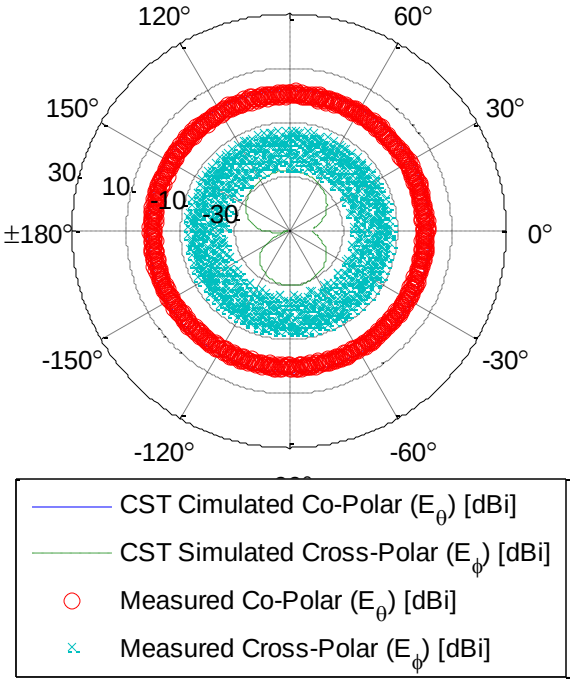

Antipodal Bunny-Ears Vivaldi BUILT (10cm x 20cm, 100ohm) w/ Chopped Ellipse Ends
H-Plane (θ = 90°) for 500 MHz

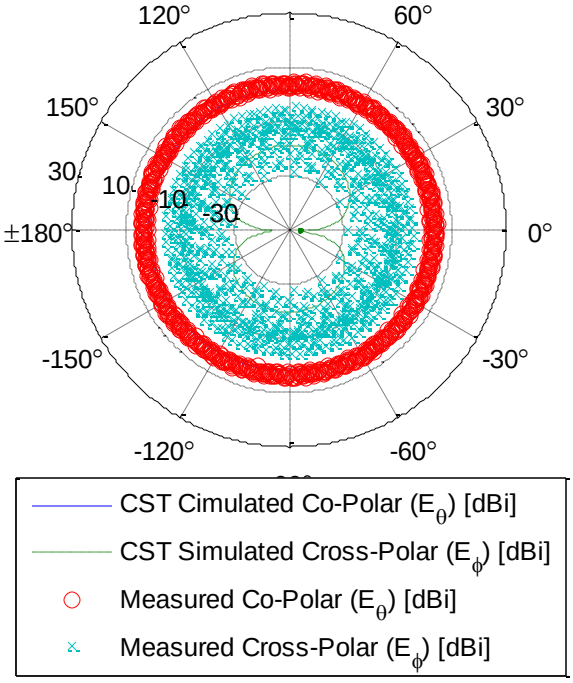

Antipodal Bunny-Ears Vivaldi BUILT (10cm x 20cm, 100ohm) w/ Chopped Ellipse Ends
H-Plane (θ = 90°) for 600 MHz

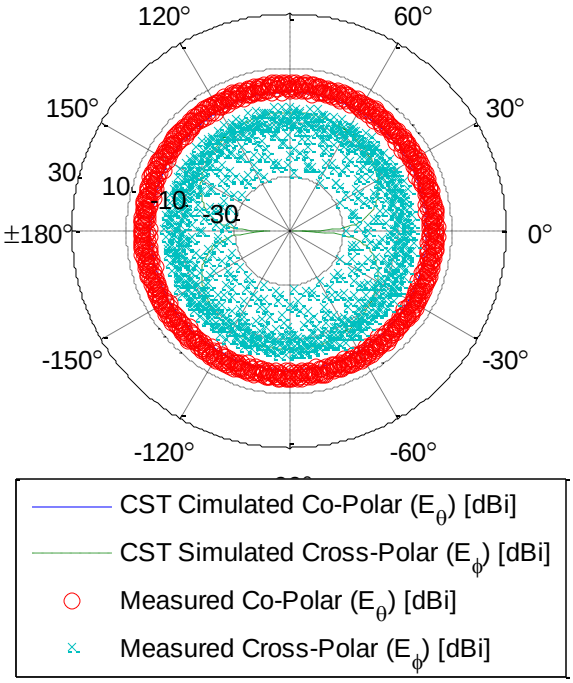

Antipodal Bunny-Ears Vivaldi BUILT (10cm x 20cm, 100ohm) w/ Chopped Ellipse Ends
H-Plane (θ = 90°) for 700 MHz

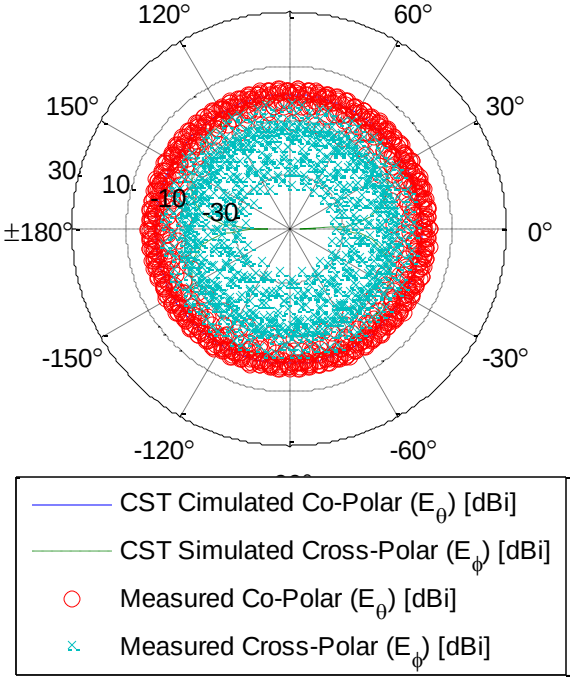

Antipodal Bunny-Ears Vivaldi BUILT (10cm x 20cm, 100ohm) w/ Chopped Ellipse Ends
H-Plane (θ = 90°) for 800 MHz

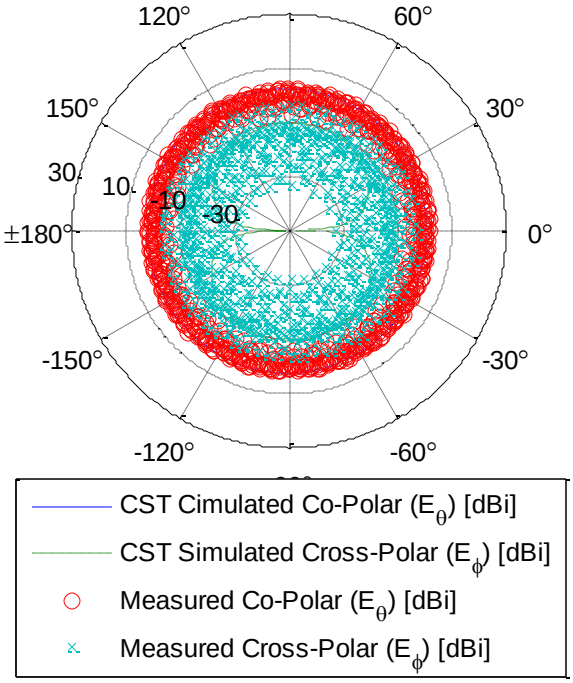

Antipodal Bunny-Ears Vivaldi BUILT (10cm x 20cm, 100ohm) w/ Chopped Ellipse Ends
H-Plane (θ = 90°) for 900 MHz

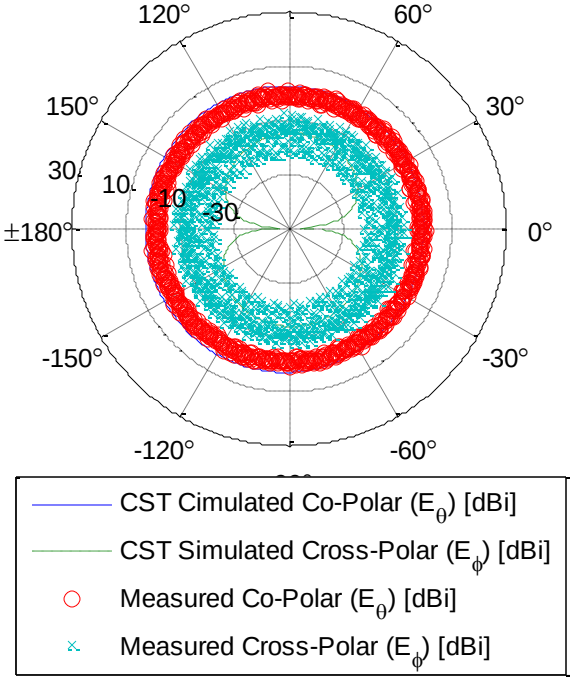

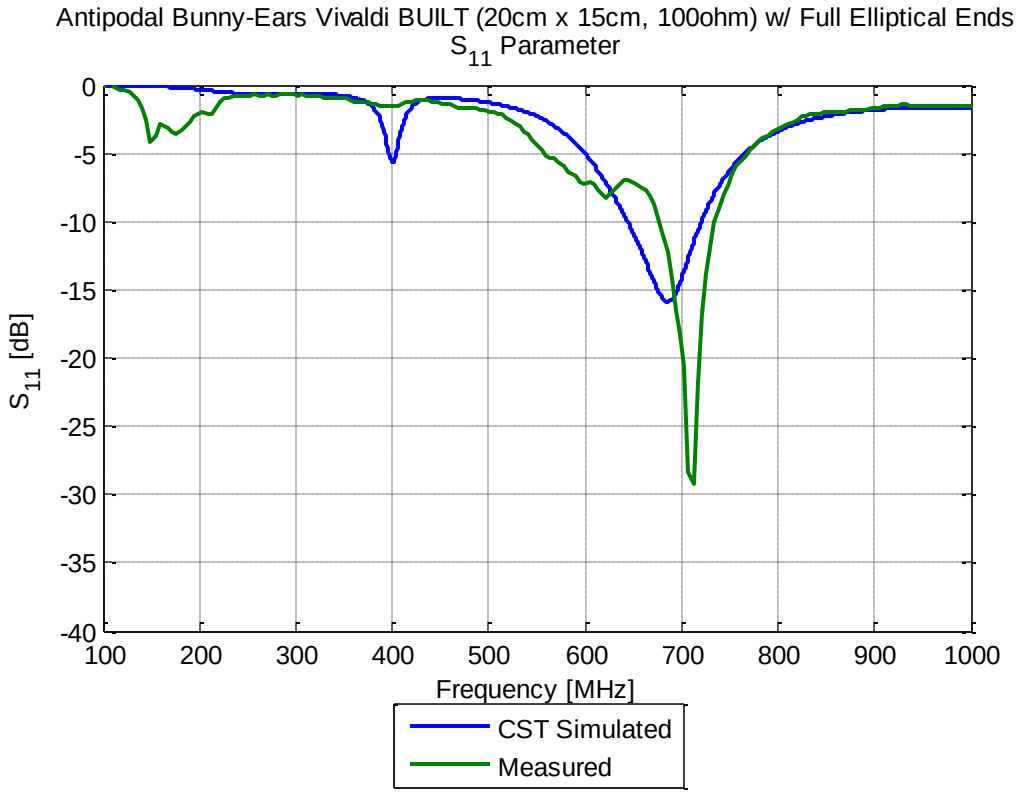
Antipodal Bunny-Ears Vivaldi BUILT (20cm x 15cm, 100ohm) w/ Full Elliptical Ends
S11 Parameter
S11 [dB]
0
-5
-10
-15
-20
-25
-30
-35
-40
100
200
300
400
500
600
700
800
900
1000
Frequency [MHz]
CST Simulated
Measured

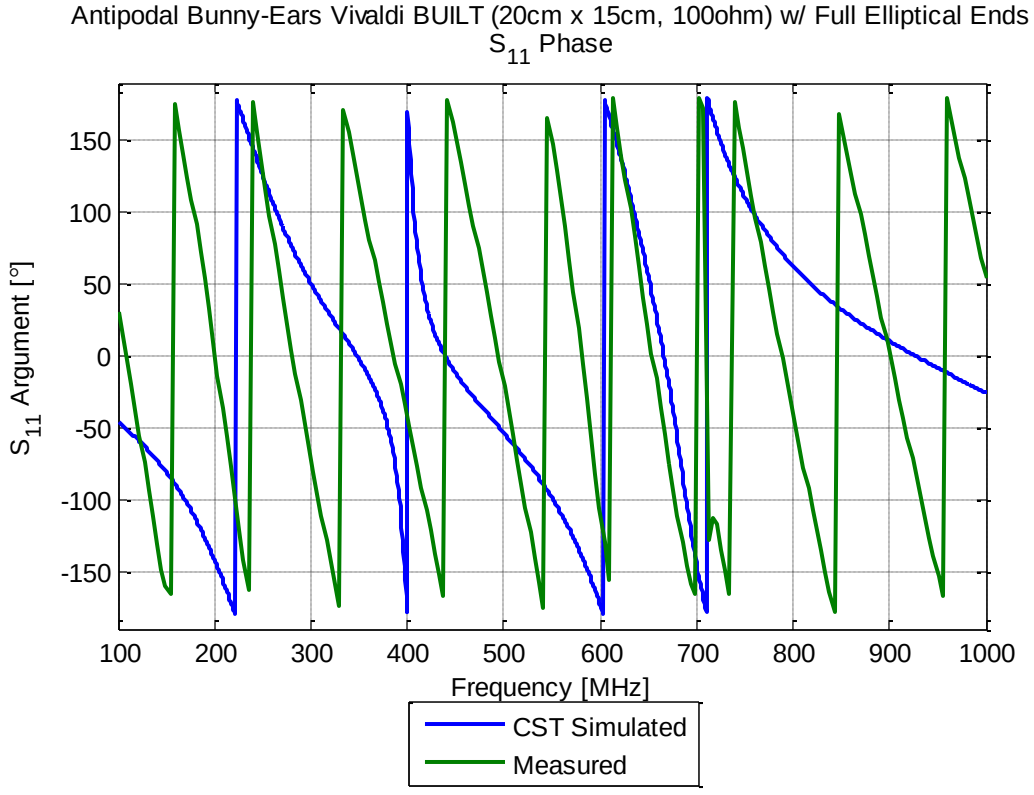
Antipodal Bunny-Ears Vivaldi BUILT (20cm x 15cm, 100ohm) w/ Full Elliptical Ends
S11 Phase
S11 Argument [°]
150
100
50
0
-50
-100
-150
100
200
300
400
500
600
700
800
900
1000
Frequency [MHz]
CST Simulated
Measured

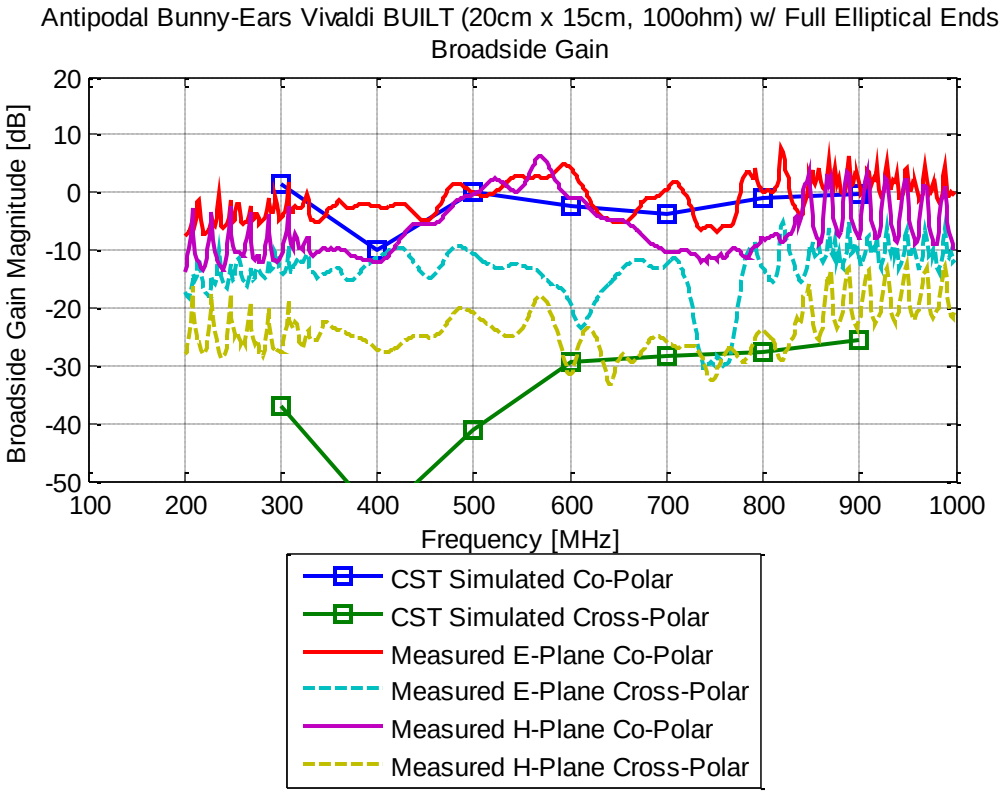
Antipodal Bunny-Ears Vivaldi BUILT (20cm x 15cm, 100ohm) w/ Full Elliptical Ends
Broadside Gain
Broadside Gain Magnitude [dB]
20
10
0
-10
-20
-30
-40
-50
100
200
300
400
500
600
700
800
900
1000
Frequency [MHz]
CST Simulated Co-Polar
CST Simulated Cross-Polar
Measured E-Plane Co-Polar
Measured E-Plane Cross-Polar
Measured H-Plane Co-Polar
Measured H-Plane Cross-Polar

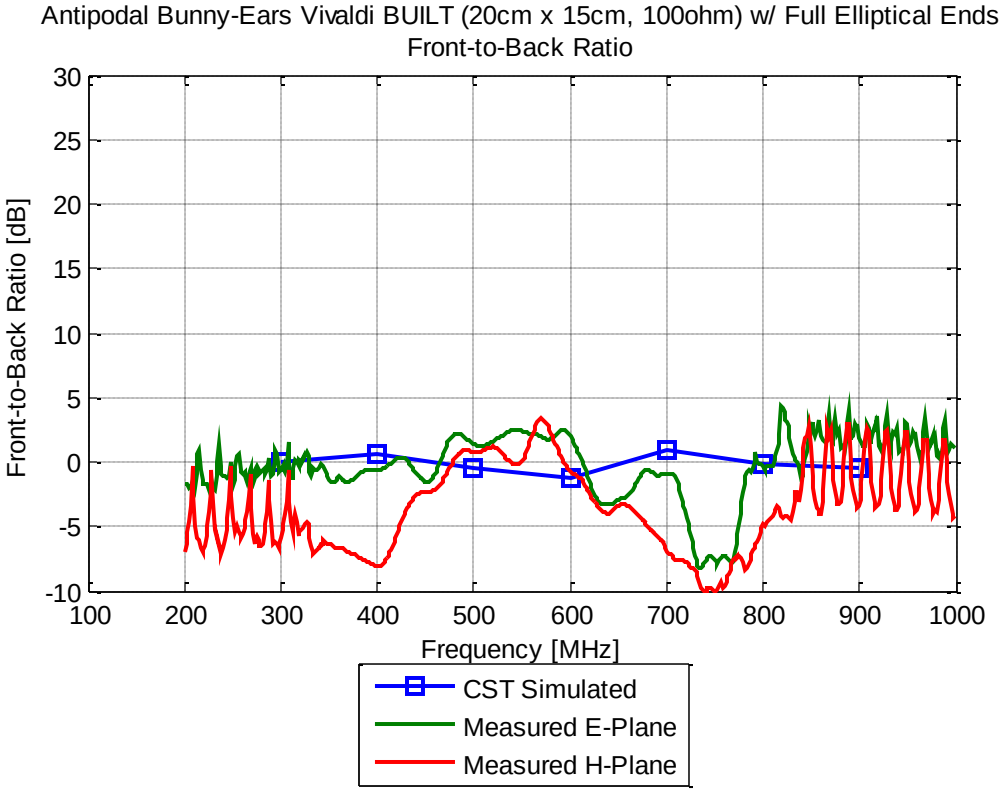
Antipodal Bunny-Ears Vivaldi BUILT (20cm x 15cm, 100ohm) w/ Full Elliptical Ends
Front-to-Back Ratio
Front-to-Back Ratio [dB]
30
25
20
15
10
5
0
-5
-10
100
200
300
400
500
600
700
800
900
1000
Frequency [MHz]
CST Simulated
Measured E-Plane
Measured H-Plane

Antipodal Bunny-Ears Vivaldi BUILT (20cm x 15cm, 100ohm) w/ Full Elliptical Ends
E-Plane (ϕ = 90°) for 300 MHz

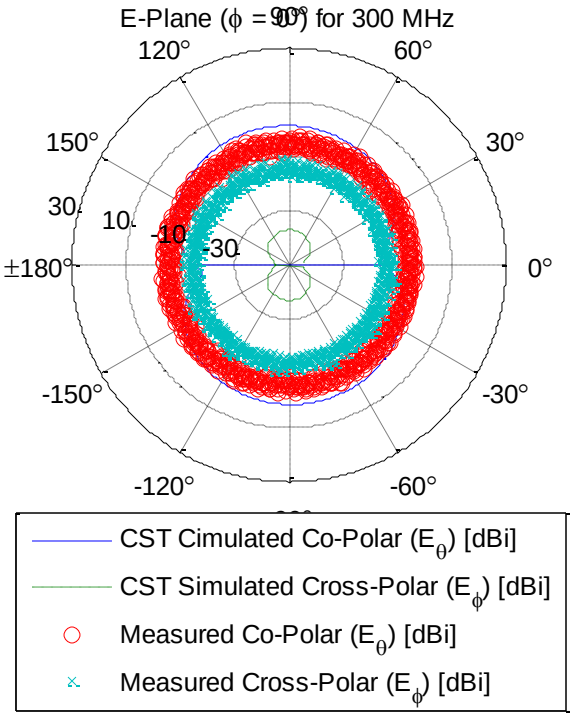

Antipodal Bunny-Ears Vivaldi BUILT (20cm x 15cm, 100ohm) w/ Full Elliptical Ends
E-Plane (ϕ = 90°) for 400 MHz

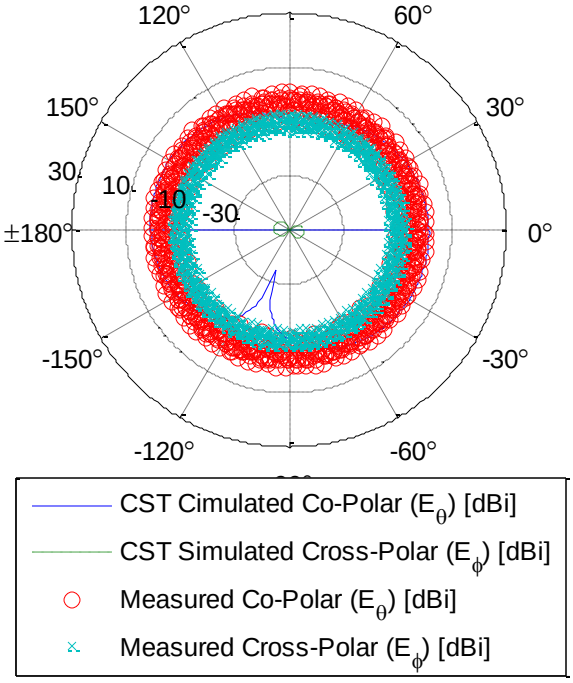

Antipodal Bunny-Ears Vivaldi BUILT (20cm x 15cm, 100ohm) w/ Full Elliptical Ends
E-Plane (ϕ = 90°) for 500 MHz

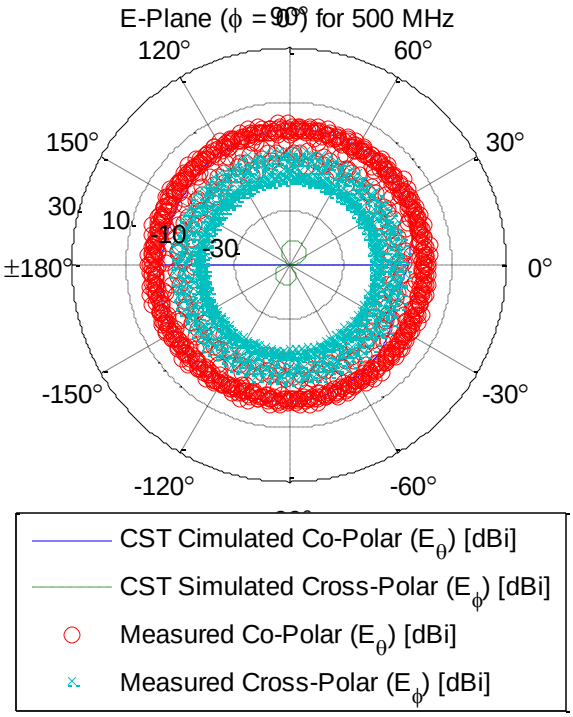

Antipodal Bunny-Ears Vivaldi BUILT (20cm x 15cm, 100ohm) w/ Full Elliptical Ends
E-Plane (ϕ = 90°) for 600 MHz

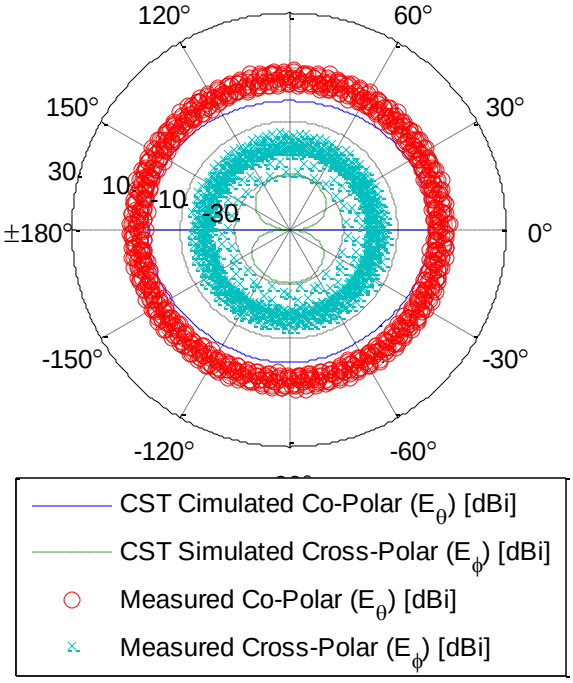

Antipodal Bunny-Ears Vivaldi BUILT (20cm x 15cm, 100ohm) w/ Full Elliptical Ends

E-Plane (ϕ = 90°) for 700 MHz

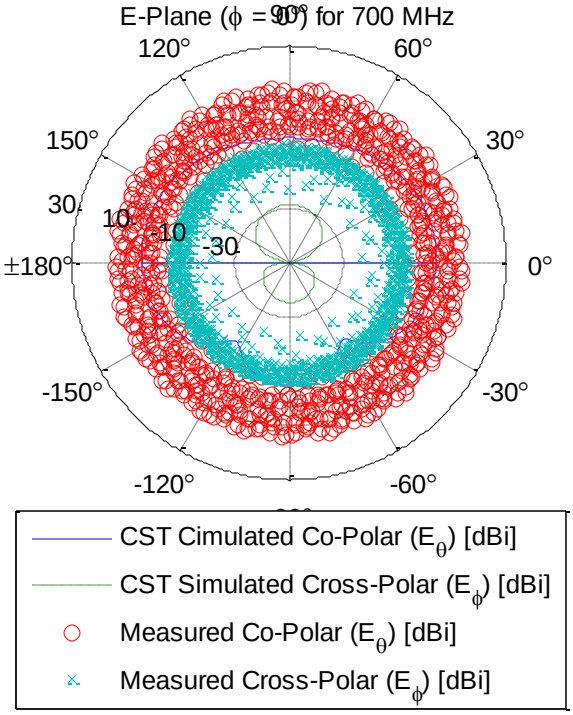

Antipodal Bunny-Ears Vivaldi BUILT (20cm x 15cm, 100ohm) w/ Full Elliptical Ends

E-Plane (ϕ = 90°) for 800 MHz

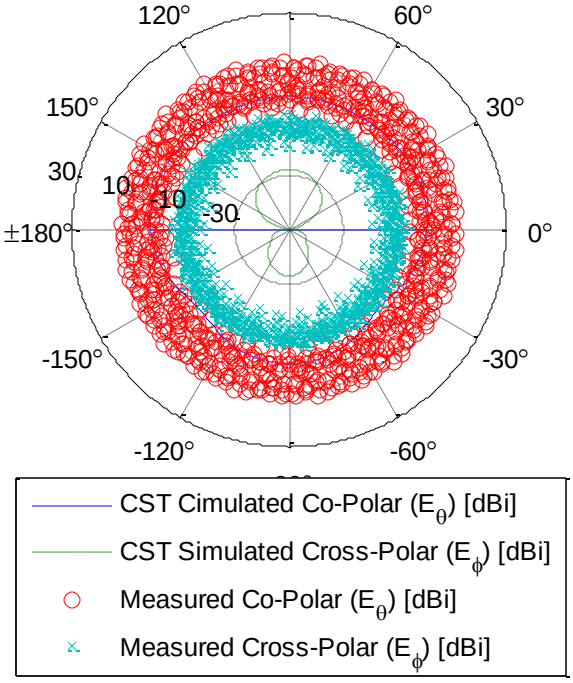

Antipodal Bunny-Ears Vivaldi BUILT (20cm x 15cm, 100ohm) w/ Full Elliptical Ends
E-Plane (ϕ = 90°) for 900 MHz

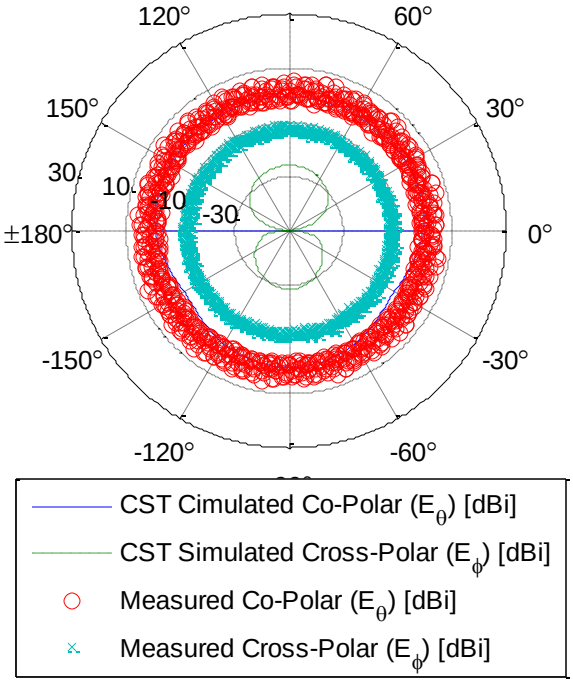

Antipodal Bunny-Ears Vivaldi BUILT (20cm x 15cm, 100ohm) w/ Full Elliptical Ends
H-Plane (θ = 90°) for 300 MHz

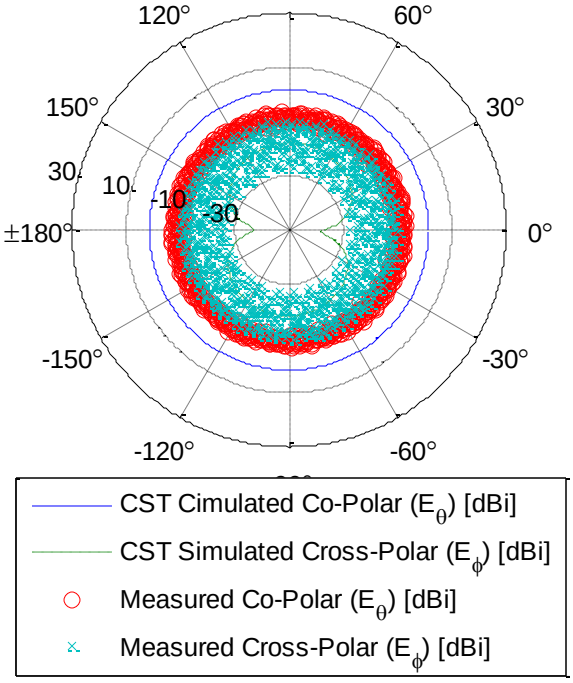

Antipodal Bunny-Ears Vivaldi BUILT (20cm x 15cm, 100ohm) w/ Full Elliptical Ends
H-Plane (θ = 90°) for 400 MHz

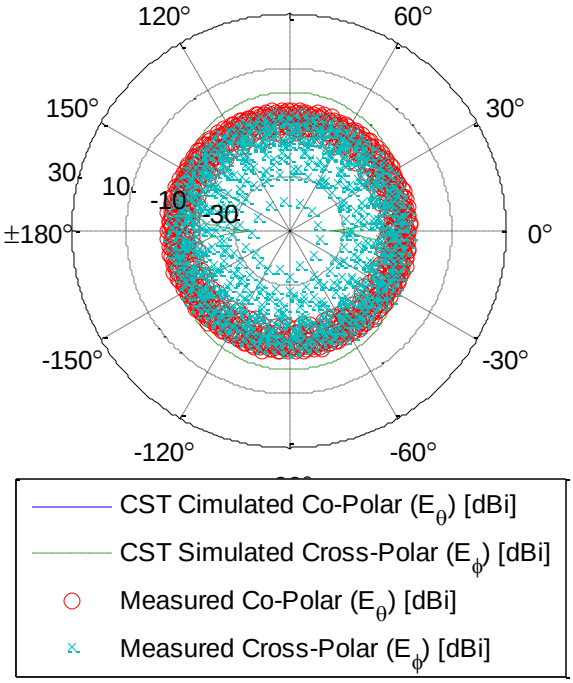

Antipodal Bunny-Ears Vivaldi BUILT (20cm x 15cm, 100ohm) w/ Full Elliptical Ends
H-Plane (θ = 90°) for 500 MHz

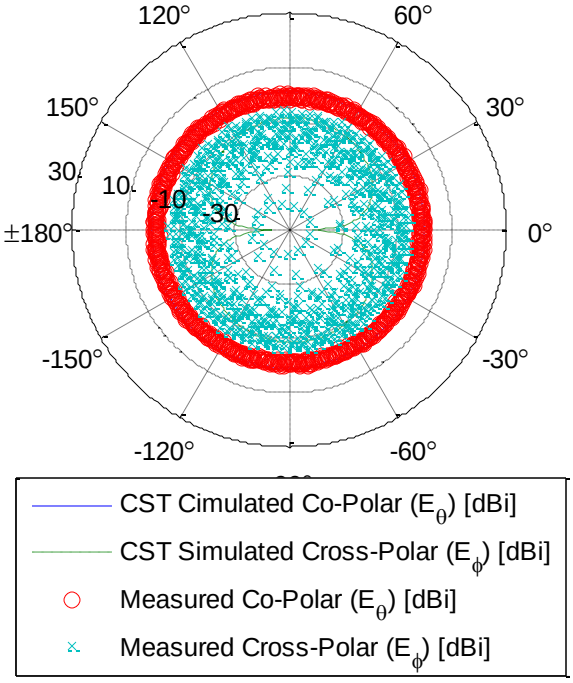

Antipodal Bunny-Ears Vivaldi BUILT (20cm x 15cm, 100ohm) w/ Full Elliptical Ends
H-Plane (θ = 90°) for 600 MHz

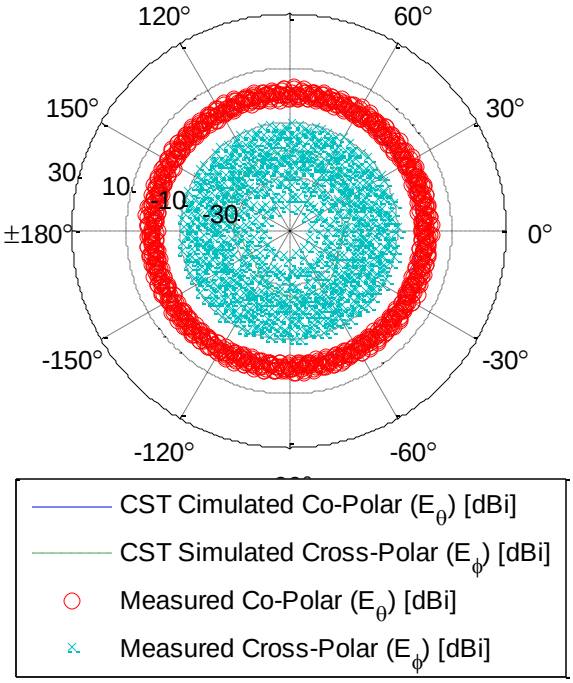

Antipodal Bunny-Ears Vivaldi BUILT (20cm x 15cm, 100ohm) w/ Full Elliptical Ends
H-Plane (θ = 90°) for 700 MHz

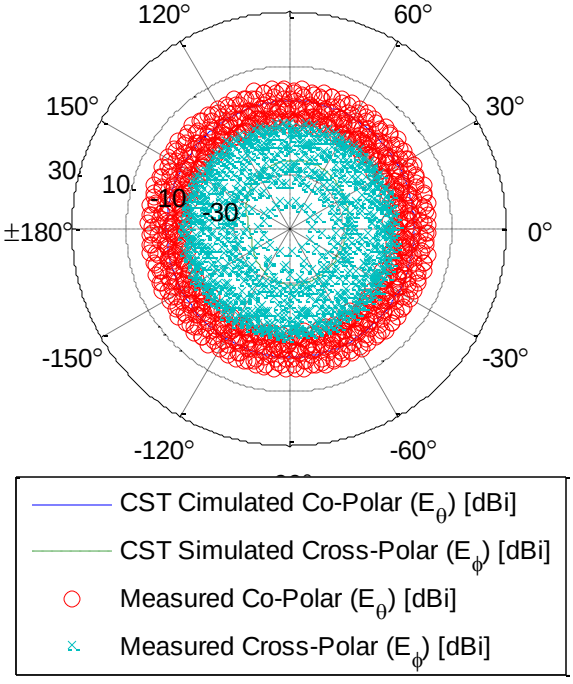

Antipodal Bunny-Ears Vivaldi BUILT (20cm x 15cm, 100ohm) w/ Full Elliptical Ends
H-Plane (θ = 90°) for 800 MHz

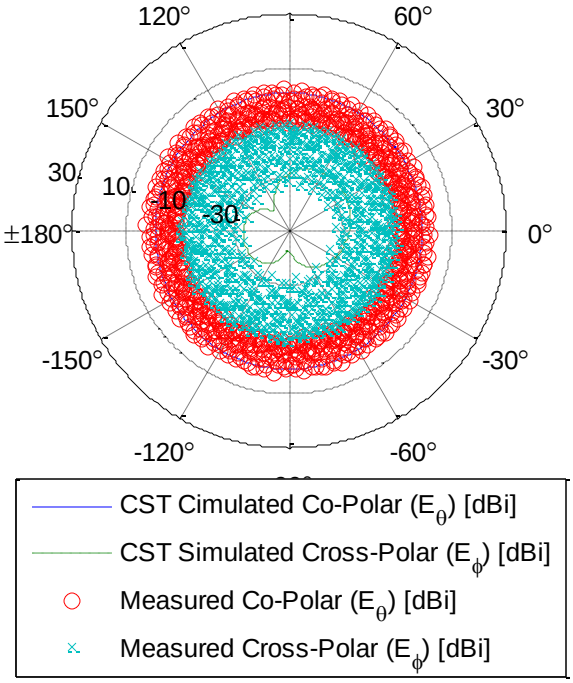

Antipodal Bunny-Ears Vivaldi BUILT (20cm x 15cm, 100ohm) w/ Full Elliptical Ends
H-Plane (θ = 90°) for 900 MHz

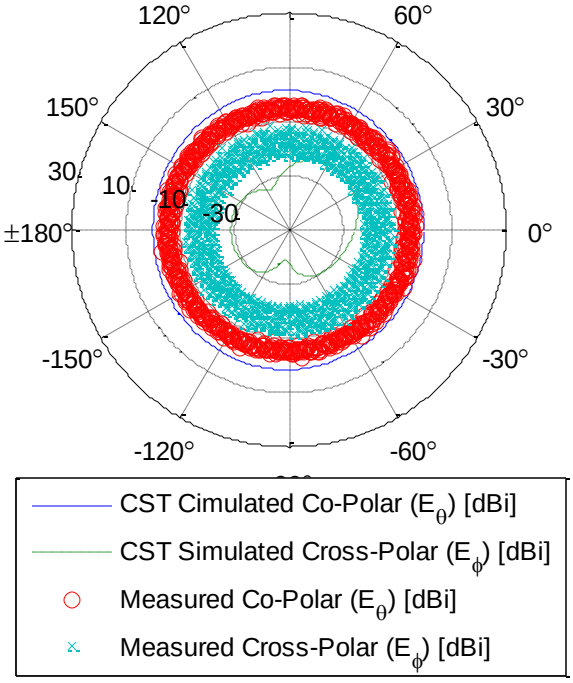

Full 50cm Aperture CVD Performance

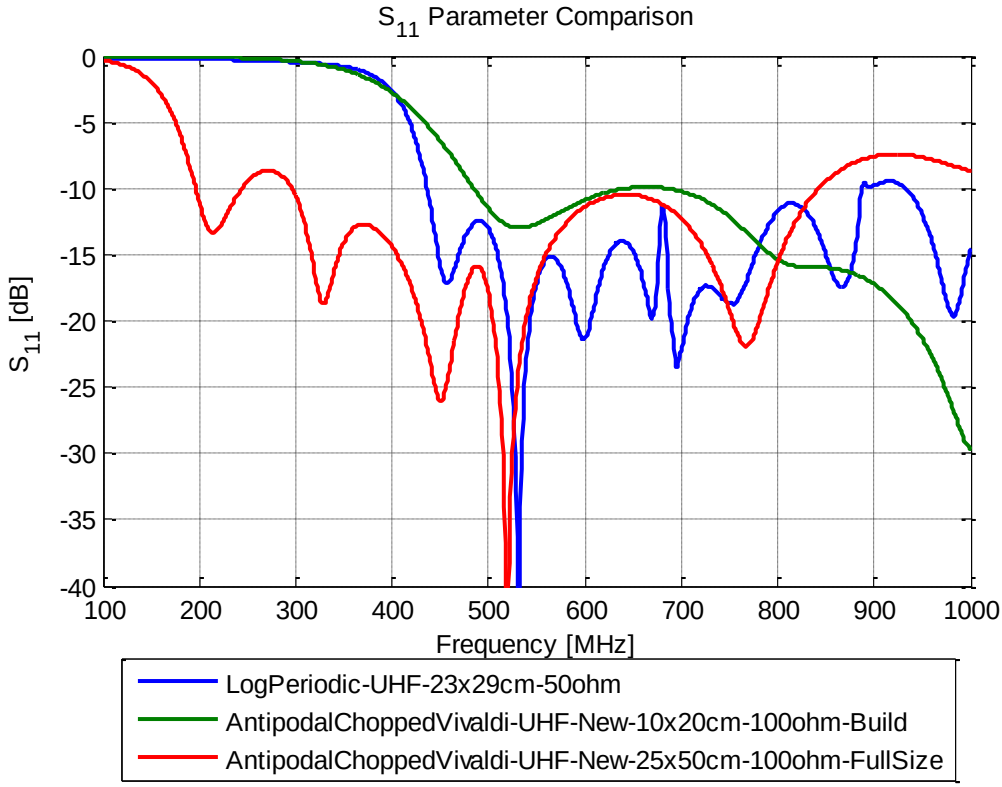

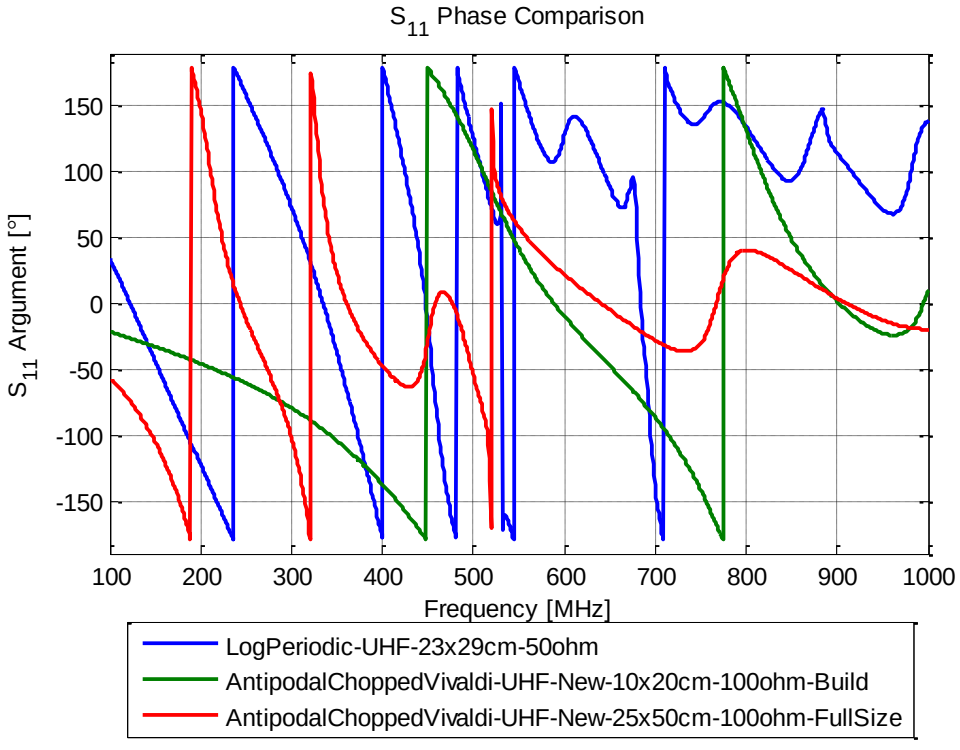

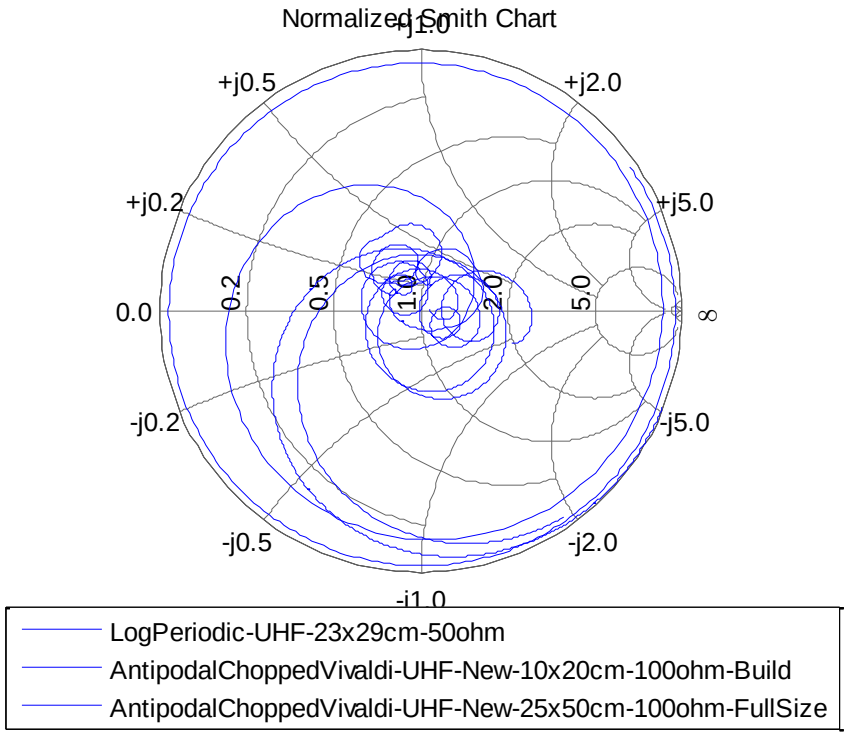
Normalized Smith Chart
+j1.0
+j0.5
+j2.0
+j0.2
+j5.0
0.0
0.2
0.5
1.0
2.0
5.0
∞
-j0.2
-j5.0
-j0.5
-j2.0
-j1.0
LogPeriodic-UHF-23x29cm-50ohm
AntipodalChoppedVivaldi-UHF-New-10x20cm-100ohm-Build
AntipodalChoppedVivaldi-UHF-New-25x50cm-100ohm-FullSize

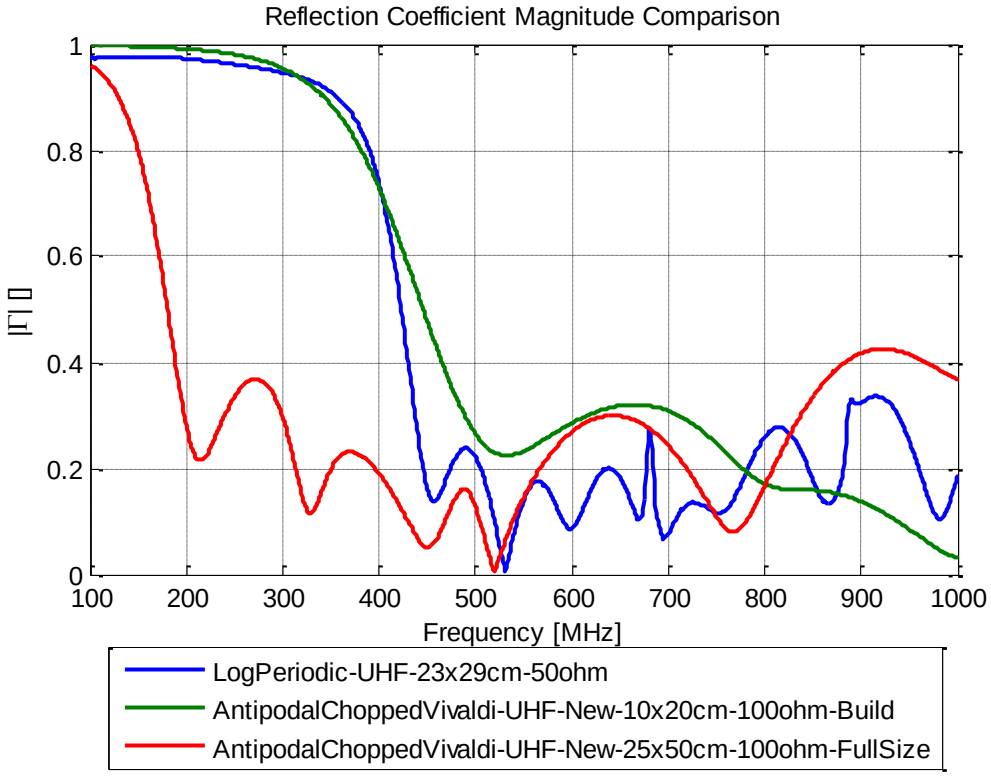
Reflection Coefficient Magnitude Comparison
|Γ| []
1
0.8
0.6
0.4
0.2
0
100
200
300
400
500
600
700
800
900
1000
Frequency [MHz]
LogPeriodic-UHF-23x29cm-50ohm
AntipodalChoppedVivaldi-UHF-New-10x20cm-100ohm-Build
AntipodalChoppedVivaldi-UHF-New-25x50cm-100ohm-FullSize

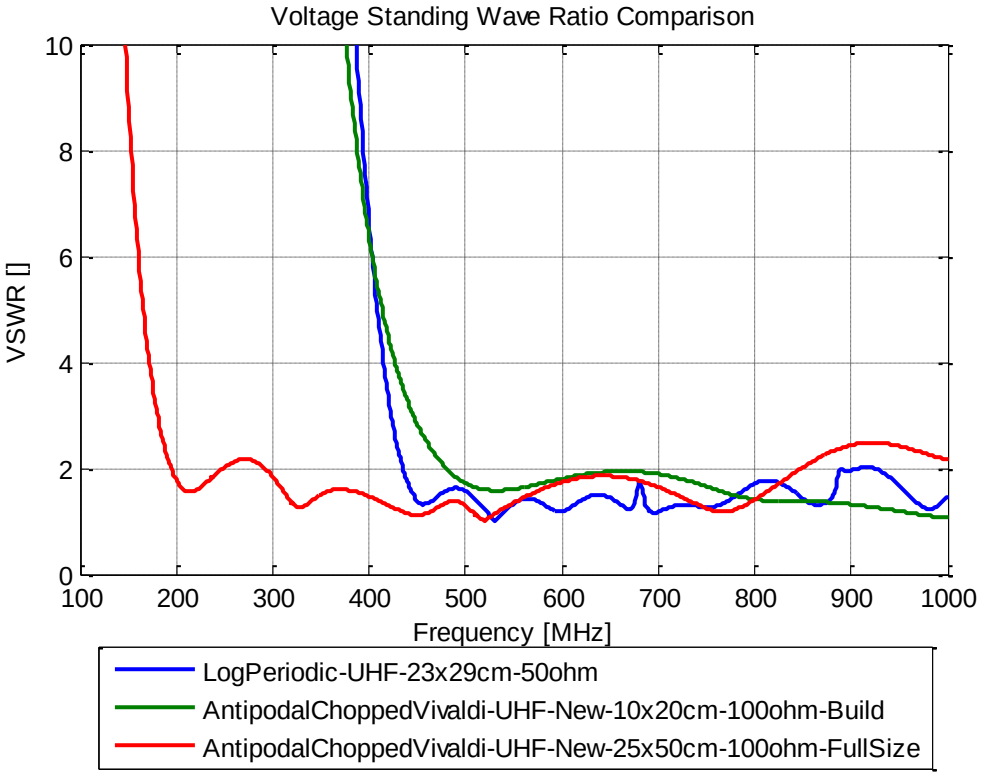
Voltage Standing Wave Ratio Comparison
VSWR []
Frequency [MHz]
10
8
6
4
2
0
100
200
300
400
500
600
700
800
900
1000
LogPeriodic-UHF-23x29cm-50ohm
AntipodalChoppedVivaldi-UHF-New-10x20cm-100ohm-Build
AntipodalChoppedVivaldi-UHF-New-25x50cm-100ohm-FullSize

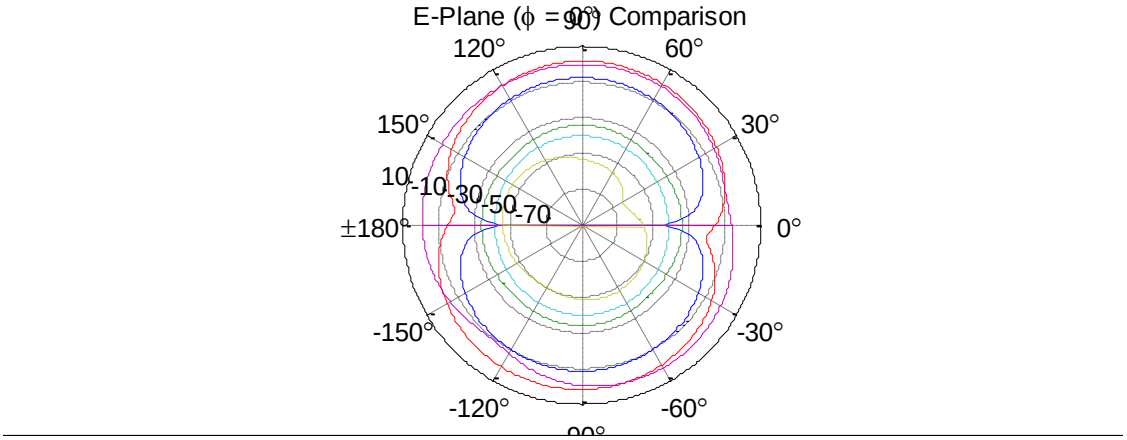
E-Plane (ϕ = 90°) Comparison
90°
120°
60°
150°
30°
±180°
0°
-150°
-30°
-120°
-60°
-90°
-10
-30
-50
-70
LogPeriodic-UHF-23x29cm-50ohm: Co-Polar (Eθ) [dBi] (300 MHz)
LogPeriodic-UHF-23x29cm-50ohm: Cross-Polar (Eϕ) [dBi] (300 MHz)
AntipodalChoppedVivaldi-UHF-New-10x20cm-100ohm-Build: Co-Polar (Eθ) [dBi] (300 MHz)
AntipodalChoppedVivaldi-UHF-New-10x20cm-100ohm-Build: Cross-Polar (Eϕ) [dBi] (300 MH
AntipodalChoppedVivaldi-UHF-New-25x50cm-100ohm-FullSize: Co-Polar (Eθ) [dBi] (300 MH
AntipodalChoppedVivaldi-UHF-New-25x50cm-100ohm-FullSize: Cross-Polar (Eϕ) [dBi] (300

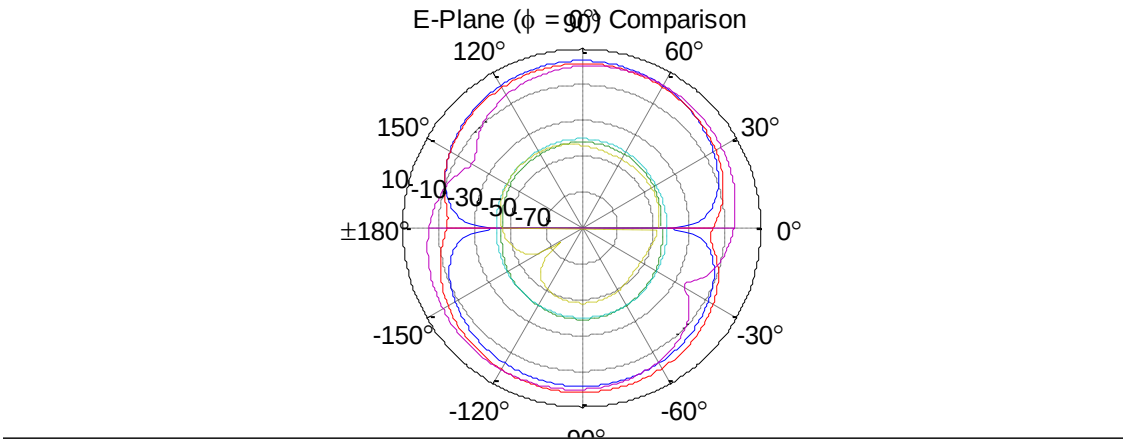

LogPeriodic-UHF-23x29cm-50ohm: Co-Polar (E_θ) [dBi] (400 MHz)

LogPeriodic-UHF-23x29cm-50ohm: Cross-Polar (E_ϕ) [dBi] (400 MHz)

AntipodalChoppedVivaldi-UHF-New-10x20cm-100ohm-Build: Co-Polar (E_θ) [dBi] (400 MHz)

AntipodalChoppedVivaldi-UHF-New-10x20cm-100ohm-Build: Cross-Polar (E_ϕ) [dBi] (400 MH

AntipodalChoppedVivaldi-UHF-New-25x50cm-100ohm-FullSize: Co-Polar (E_θ) [dBi] (400 MH

AntipodalChoppedVivaldi-UHF-New-25x50cm-100ohm-FullSize: Cross-Polar (E_ϕ) [dBi] (400

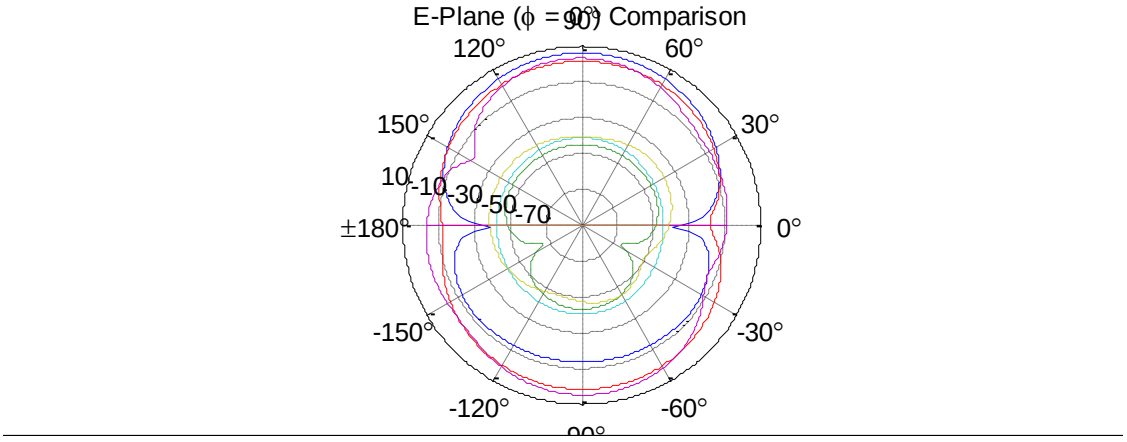

LogPeriodic-UHF-23x29cm-50ohm: Co-Polar (E_θ) [dBi] (500 MHz)

LogPeriodic-UHF-23x29cm-50ohm: Cross-Polar (E_ϕ) [dBi] (500 MHz)

AntipodalChoppedVivaldi-UHF-New-10x20cm-100ohm-Build: Co-Polar (E_θ) [dBi] (500 MHz)

AntipodalChoppedVivaldi-UHF-New-10x20cm-100ohm-Build: Cross-Polar (E_ϕ) [dBi] (500 MH

AntipodalChoppedVivaldi-UHF-New-25x50cm-100ohm-FullSize: Co-Polar (E_θ) [dBi] (500 MH

AntipodalChoppedVivaldi-UHF-New-25x50cm-100ohm-FullSize: Cross-Polar (E_ϕ) [dBi] (500

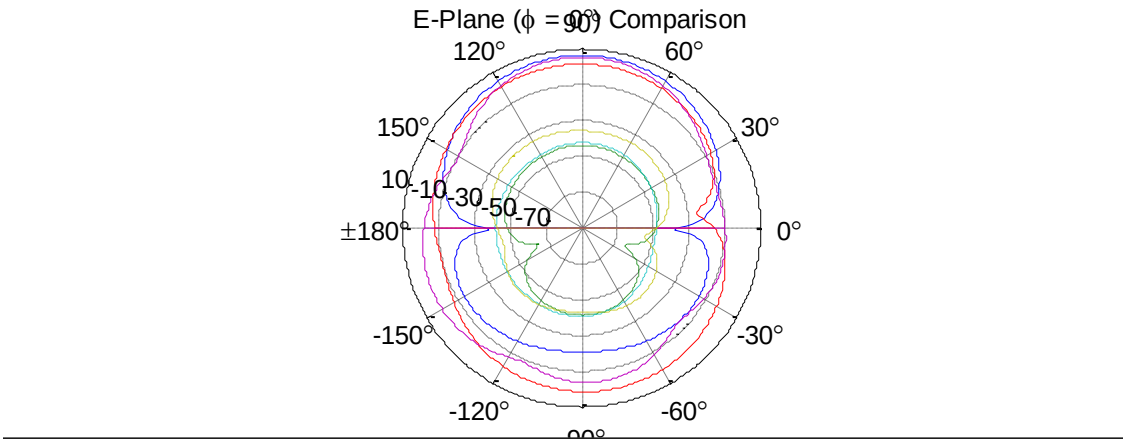
E-Plane (ϕ = 90°) Comparison
90°
120°
60°
150°
30°
-10
-30
-50
-70
±180°
0°
-150°
-30°
-120°
-60°
-90°
LogPeriodic-UHF-23x29cm-50ohm: Co-Polar (Eθ) [dBi] (600 MHz)
LogPeriodic-UHF-23x29cm-50ohm: Cross-Polar (Eϕ) [dBi] (600 MHz)
AntipodalChoppedVivaldi-UHF-New-10x20cm-100ohm-Build: Co-Polar (Eθ) [dBi] (600 MHz)
AntipodalChoppedVivaldi-UHF-New-10x20cm-100ohm-Build: Cross-Polar (Eϕ) [dBi] (600 MH
AntipodalChoppedVivaldi-UHF-New-25x50cm-100ohm-FullSize: Co-Polar (Eθ) [dBi] (600 MH
AntipodalChoppedVivaldi-UHF-New-25x50cm-100ohm-FullSize: Cross-Polar (Eϕ) [dBi] (600

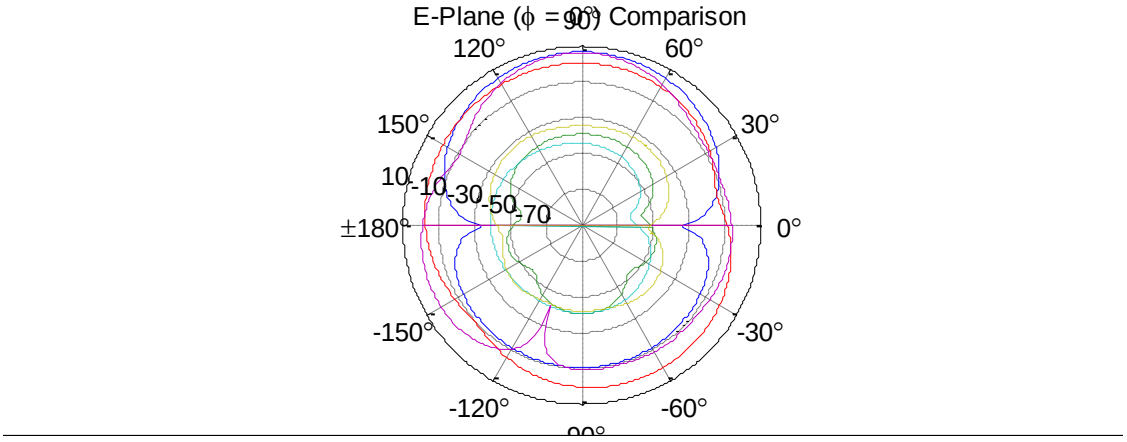
E-Plane (ϕ = 90°) Comparison
90°
120°
60°
150°
30°
-10
-30
-50
-70
±180°
0°
-150°
-30°
-120°
-60°
-90°
LogPeriodic-UHF-23x29cm-50ohm: Co-Polar (Eθ) [dBi] (700 MHz)
LogPeriodic-UHF-23x29cm-50ohm: Cross-Polar (Eϕ) [dBi] (700 MHz)
AntipodalChoppedVivaldi-UHF-New-10x20cm-100ohm-Build: Co-Polar (Eθ) [dBi] (700 MHz)
AntipodalChoppedVivaldi-UHF-New-10x20cm-100ohm-Build: Cross-Polar (Eϕ) [dBi] (700 MH
AntipodalChoppedVivaldi-UHF-New-25x50cm-100ohm-FullSize: Co-Polar (Eθ) [dBi] (700 MH
AntipodalChoppedVivaldi-UHF-New-25x50cm-100ohm-FullSize: Cross-Polar (Eϕ) [dBi] (700

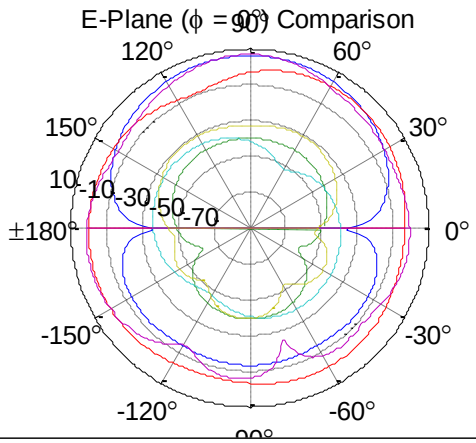

LogPeriodic-UHF-23x29cm-50ohm: Co-Polar (E_θ) [dBi] (800 MHz)

LogPeriodic-UHF-23x29cm-50ohm: Cross-Polar (E_ϕ) [dBi] (800 MHz)

AntipodalChoppedVivaldi-UHF-New-10x20cm-100ohm-Build: Co-Polar (E_θ) [dBi] (800 MHz)

AntipodalChoppedVivaldi-UHF-New-10x20cm-100ohm-Build: Cross-Polar (E_ϕ) [dBi] (800 MH

AntipodalChoppedVivaldi-UHF-New-25x50cm-100ohm-FullSize: Co-Polar (E_θ) [dBi] (800 MH

AntipodalChoppedVivaldi-UHF-New-25x50cm-100ohm-FullSize: Cross-Polar (E_ϕ) [dBi] (800

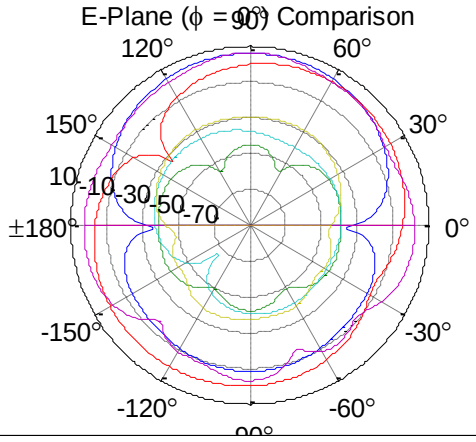

LogPeriodic-UHF-23x29cm-50ohm: Co-Polar (E_θ) [dBi] (900 MHz)

LogPeriodic-UHF-23x29cm-50ohm: Cross-Polar (E_ϕ) [dBi] (900 MHz)

AntipodalChoppedVivaldi-UHF-New-10x20cm-100ohm-Build: Co-Polar (E_θ) [dBi] (900 MHz)

AntipodalChoppedVivaldi-UHF-New-10x20cm-100ohm-Build: Cross-Polar (E_ϕ) [dBi] (900 MH

AntipodalChoppedVivaldi-UHF-New-25x50cm-100ohm-FullSize: Co-Polar (E_θ) [dBi] (900 MH

AntipodalChoppedVivaldi-UHF-New-25x50cm-100ohm-FullSize: Cross-Polar (E_ϕ) [dBi] (900

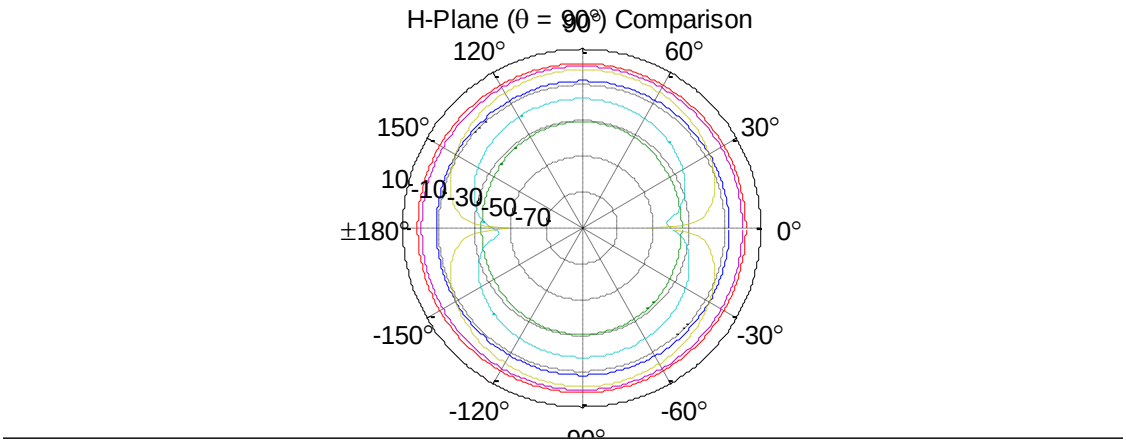
H-Plane (θ = 90°) Comparison
90°
120°
60°
150°
30°
10
-10
-30
-50
-70
±180°
0°
-150°
-30°
-120°
-60°
LogPeriodic-UHF-23x29cm-50ohm: Co-Polar (Eθ) [dBi] (300 MHz)
LogPeriodic-UHF-23x29cm-50ohm: Cross-Polar (Eϕ) [dBi] (300 MHz)
AntipodalChoppedVivaldi-UHF-New-10x20cm-100ohm-Build: Co-Polar (Eθ) [dBi] (300 MHz)
AntipodalChoppedVivaldi-UHF-New-10x20cm-100ohm-Build: Cross-Polar (Eϕ) [dBi] (300 MH
AntipodalChoppedVivaldi-UHF-New-25x50cm-100ohm-FullSize: Co-Polar (Eθ) [dBi] (300 MH
AntipodalChoppedVivaldi-UHF-New-25x50cm-100ohm-FullSize: Cross-Polar (Eϕ) [dBi] (300

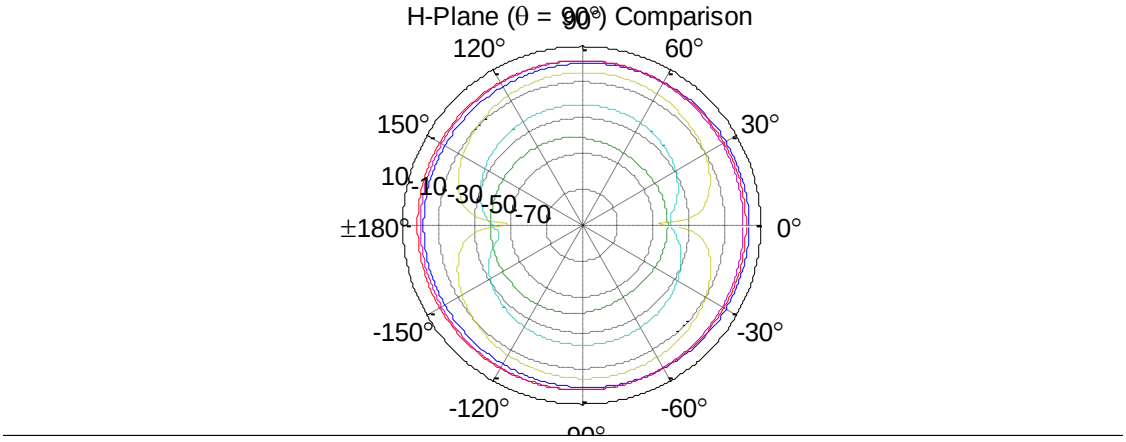
H-Plane (θ = 90°) Comparison
90°
120°
60°
150°
30°
10
-10
-30
-50
-70
±180°
0°
-150°
-30°
-120°
-60°
LogPeriodic-UHF-23x29cm-50ohm: Co-Polar (Eθ) [dBi] (400 MHz)
LogPeriodic-UHF-23x29cm-50ohm: Cross-Polar (Eϕ) [dBi] (400 MHz)
AntipodalChoppedVivaldi-UHF-New-10x20cm-100ohm-Build: Co-Polar (Eθ) [dBi] (400 MHz)
AntipodalChoppedVivaldi-UHF-New-10x20cm-100ohm-Build: Cross-Polar (Eϕ) [dBi] (400 MH
AntipodalChoppedVivaldi-UHF-New-25x50cm-100ohm-FullSize: Co-Polar (Eθ) [dBi] (400 MH
AntipodalChoppedVivaldi-UHF-New-25x50cm-100ohm-FullSize: Cross-Polar (Eϕ) [dBi] (400

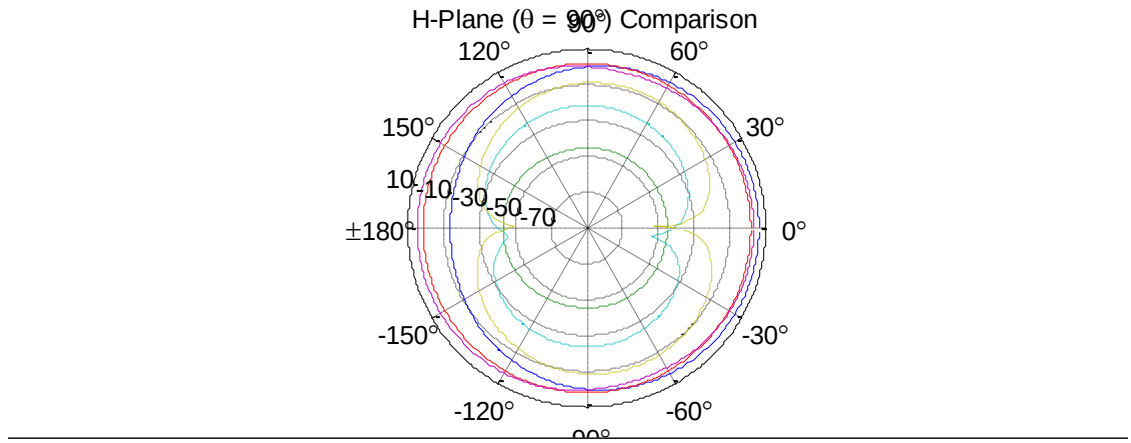
H-Plane (θ = 90°) Comparison
90°
120°
60°
150°
30°
10
-10
-30
-50
-70
±180°
0°
-150°
-30°
-120°
-60°
-90°
LogPeriodic-UHF-23x29cm-50ohm: Co-Polar (Eθ) [dBi] (500 MHz)
LogPeriodic-UHF-23x29cm-50ohm: Cross-Polar (Eϕ) [dBi] (500 MHz)
AntipodalChoppedVivaldi-UHF-New-10x20cm-100ohm-Build: Co-Polar (Eθ) [dBi] (500 MHz)
AntipodalChoppedVivaldi-UHF-New-10x20cm-100ohm-Build: Cross-Polar (Eϕ) [dBi] (500 MH
AntipodalChoppedVivaldi-UHF-New-25x50cm-100ohm-FullSize: Co-Polar (Eθ) [dBi] (500 MH
AntipodalChoppedVivaldi-UHF-New-25x50cm-100ohm-FullSize: Cross-Polar (Eϕ) [dBi] (500

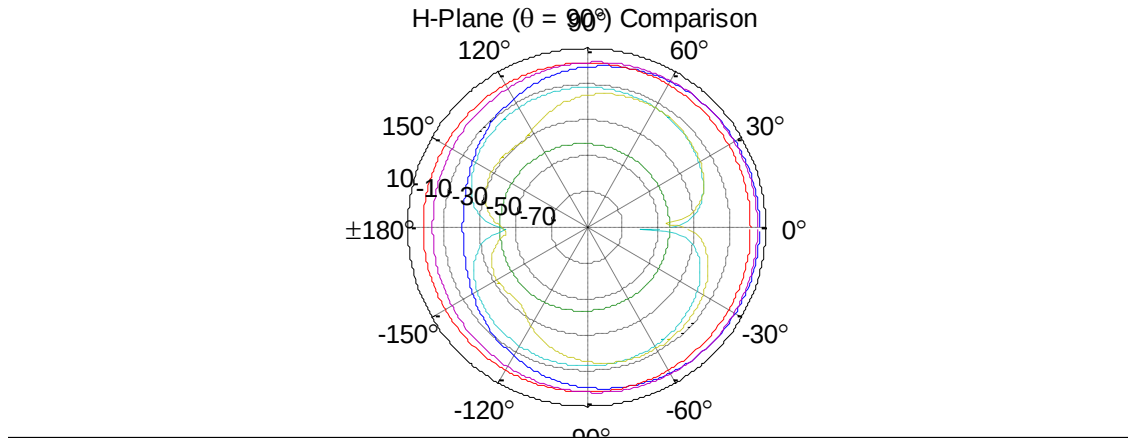
H-Plane (θ = 90°) Comparison
90°
120°
60°
150°
30°
10
-10
-30
-50
-70
±180°
0°
-150°
-30°
-120°
-60°
-90°
LogPeriodic-UHF-23x29cm-50ohm: Co-Polar (Eθ) [dBi] (600 MHz)
LogPeriodic-UHF-23x29cm-50ohm: Cross-Polar (Eϕ) [dBi] (600 MHz)
AntipodalChoppedVivaldi-UHF-New-10x20cm-100ohm-Build: Co-Polar (Eθ) [dBi] (600 MHz)
AntipodalChoppedVivaldi-UHF-New-10x20cm-100ohm-Build: Cross-Polar (Eϕ) [dBi] (600 MH
AntipodalChoppedVivaldi-UHF-New-25x50cm-100ohm-FullSize: Co-Polar (Eθ) [dBi] (600 MH
AntipodalChoppedVivaldi-UHF-New-25x50cm-100ohm-FullSize: Cross-Polar (Eϕ) [dBi] (600

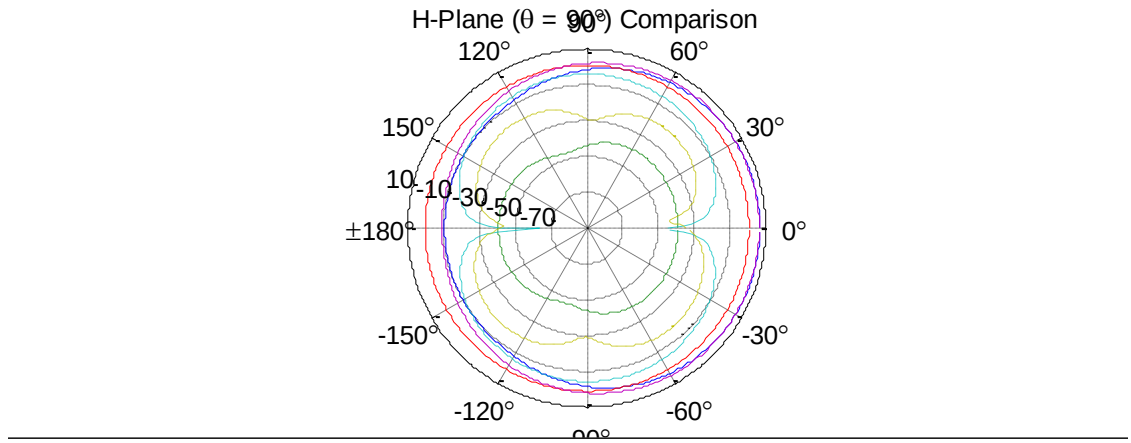
H-Plane (θ = 90°) Comparison
90°
120°
60°
150°
30°
10
-10
-30
-50
-70
±180°
0°
-150°
-30°
-120°
-60°
-90°
LogPeriodic-UHF-23x29cm-50ohm: Co-Polar (Eθ) [dBi] (700 MHz)
LogPeriodic-UHF-23x29cm-50ohm: Cross-Polar (Eϕ) [dBi] (700 MHz)
AntipodalChoppedVivaldi-UHF-New-10x20cm-100ohm-Build: Co-Polar (Eθ) [dBi] (700 MHz)
AntipodalChoppedVivaldi-UHF-New-10x20cm-100ohm-Build: Cross-Polar (Eϕ) [dBi] (700 MH
AntipodalChoppedVivaldi-UHF-New-25x50cm-100ohm-FullSize: Co-Polar (Eθ) [dBi] (700 MH
AntipodalChoppedVivaldi-UHF-New-25x50cm-100ohm-FullSize: Cross-Polar (Eϕ) [dBi] (700

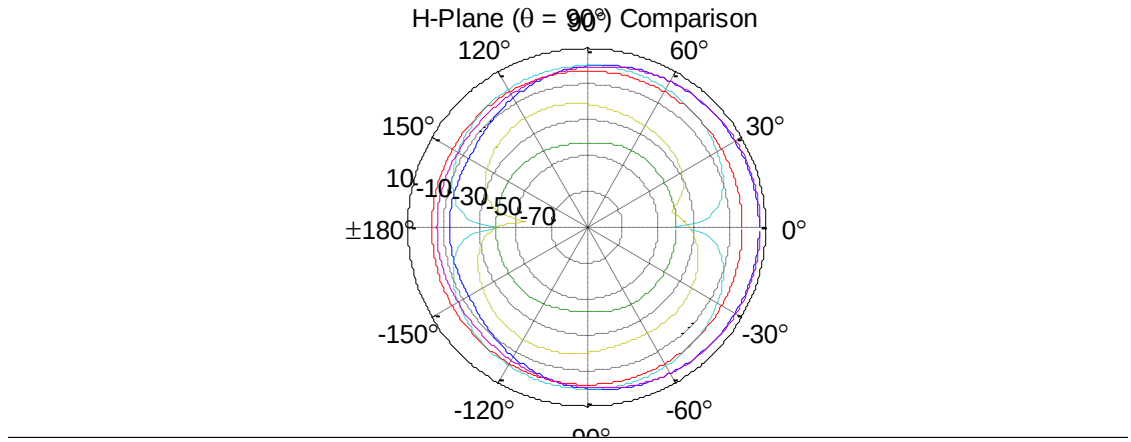
H-Plane (θ = 90°) Comparison
90°
120°
60°
150°
30°
10
-10
-30
-50
-70
±180°
0°
-150°
-30°
-120°
-60°
-90°
LogPeriodic-UHF-23x29cm-50ohm: Co-Polar (Eθ) [dBi] (800 MHz)
LogPeriodic-UHF-23x29cm-50ohm: Cross-Polar (Eϕ) [dBi] (800 MHz)
AntipodalChoppedVivaldi-UHF-New-10x20cm-100ohm-Build: Co-Polar (Eθ) [dBi] (800 MHz)
AntipodalChoppedVivaldi-UHF-New-10x20cm-100ohm-Build: Cross-Polar (Eϕ) [dBi] (800 MH
AntipodalChoppedVivaldi-UHF-New-25x50cm-100ohm-FullSize: Co-Polar (Eθ) [dBi] (800 MH
AntipodalChoppedVivaldi-UHF-New-25x50cm-100ohm-FullSize: Cross-Polar (Eϕ) [dBi] (800

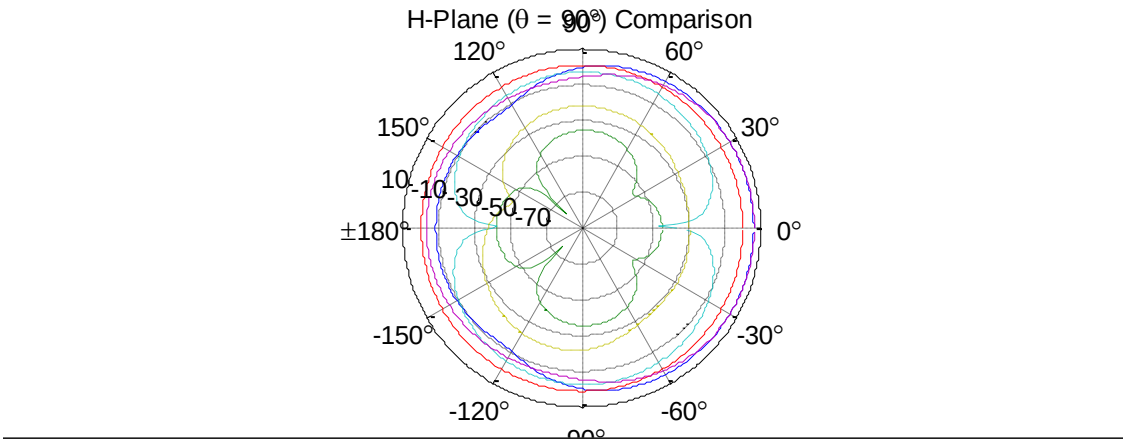
H-Plane (θ = 90°) Comparison
120°
60°
150°
30°
±180°
0°
-150°
-30°
-120°
-60°
-10
-30
-50
-70
LogPeriodic-UHF-23x29cm-50ohm: Co-Polar (Eθ) [dBi] (900 MHz)
LogPeriodic-UHF-23x29cm-50ohm: Cross-Polar (Eϕ) [dBi] (900 MHz)
AntipodalChoppedVivaldi-UHF-New-10x20cm-100ohm-Build: Co-Polar (Eθ) [dBi] (900 MHz)
AntipodalChoppedVivaldi-UHF-New-10x20cm-100ohm-Build: Cross-Polar (Eϕ) [dBi] (900 MH
AntipodalChoppedVivaldi-UHF-New-25x50cm-100ohm-FullSize: Co-Polar (Eθ) [dBi] (900 MH
AntipodalChoppedVivaldi-UHF-New-25x50cm-100ohm-FullSize: Cross-Polar (Eϕ) [dBi] (900

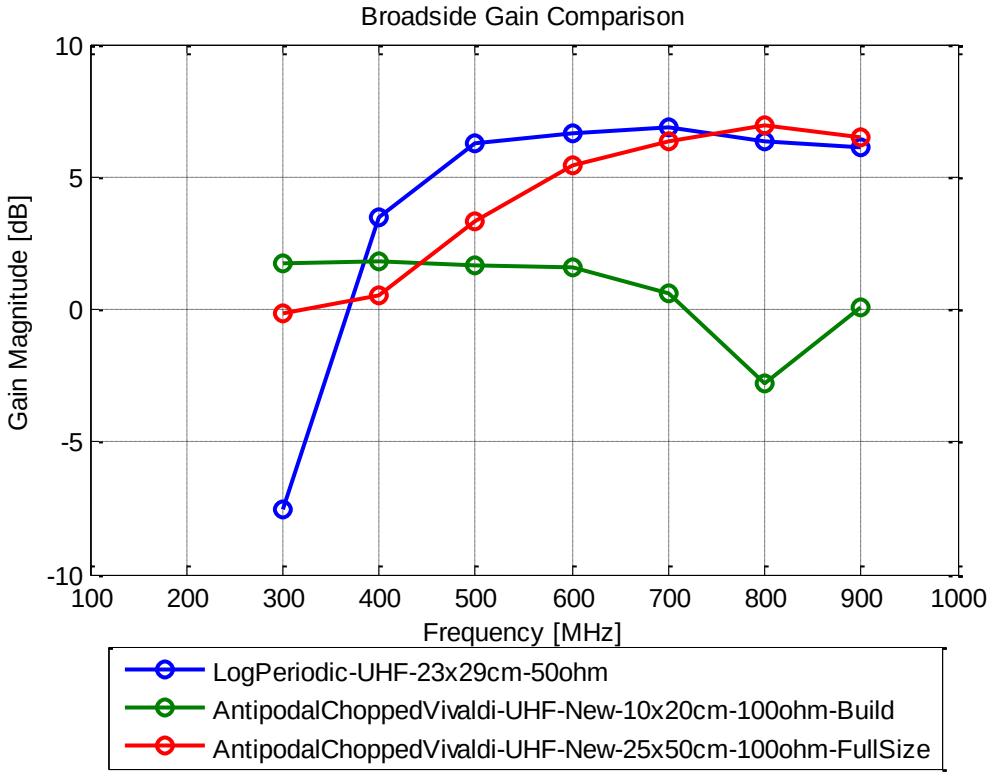
Broadside Gain Comparison
Gain Magnitude [dB]
10
5
0
-5
-10
100
200
300
400
500
600
700
800
900
1000
Frequency [MHz]
LogPeriodic-UHF-23x29cm-50ohm
AntipodalChoppedVivaldi-UHF-New-10x20cm-100ohm-Build
AntipodalChoppedVivaldi-UHF-New-25x50cm-100ohm-FullSize

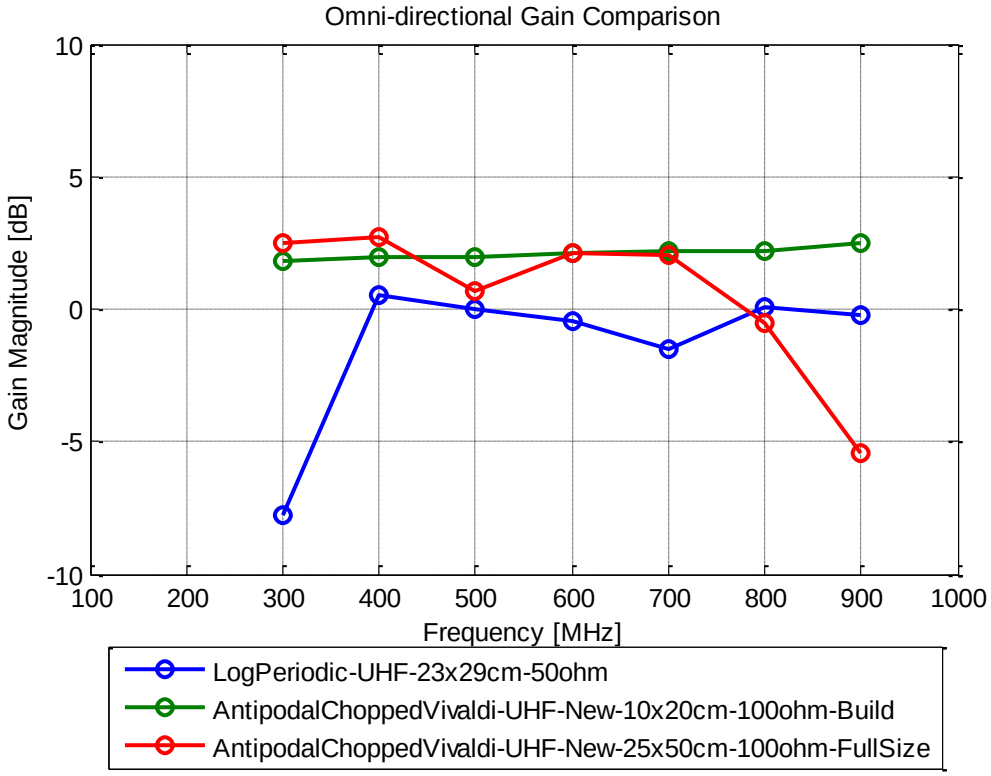
Omni-directional Gain Comparison
Gain Magnitude [dB]
10
5
0
-5
-10
100
200
300
400
500
600
700
800
900
1000
Frequency [MHz]
LogPeriodic-UHF-23x29cm-50ohm
AntipodalChoppedVivaldi-UHF-New-10x20cm-100ohm-Build
AntipodalChoppedVivaldi-UHF-New-25x50cm-100ohm-FullSize

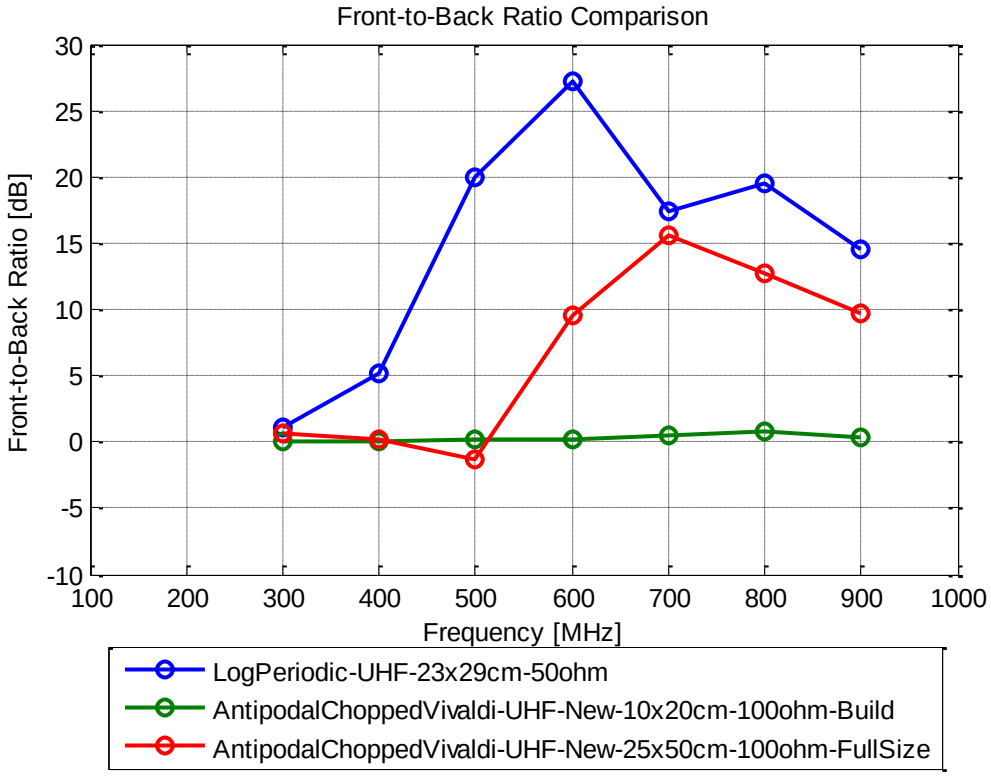
Front-to-Back Ratio Comparison
Front-to-Back Ratio [dB]
30
25
20
15
10
5
0
-5
-10
100
200
300
400
500
600
700
800
900
1000
Frequency [MHz]
LogPeriodic-UHF-23x29cm-50ohm
AntipodalChoppedVivaldi-UHF-New-10x20cm-100ohm-Build
AntipodalChoppedVivaldi-UHF-New-25x50cm-100ohm-FullSize

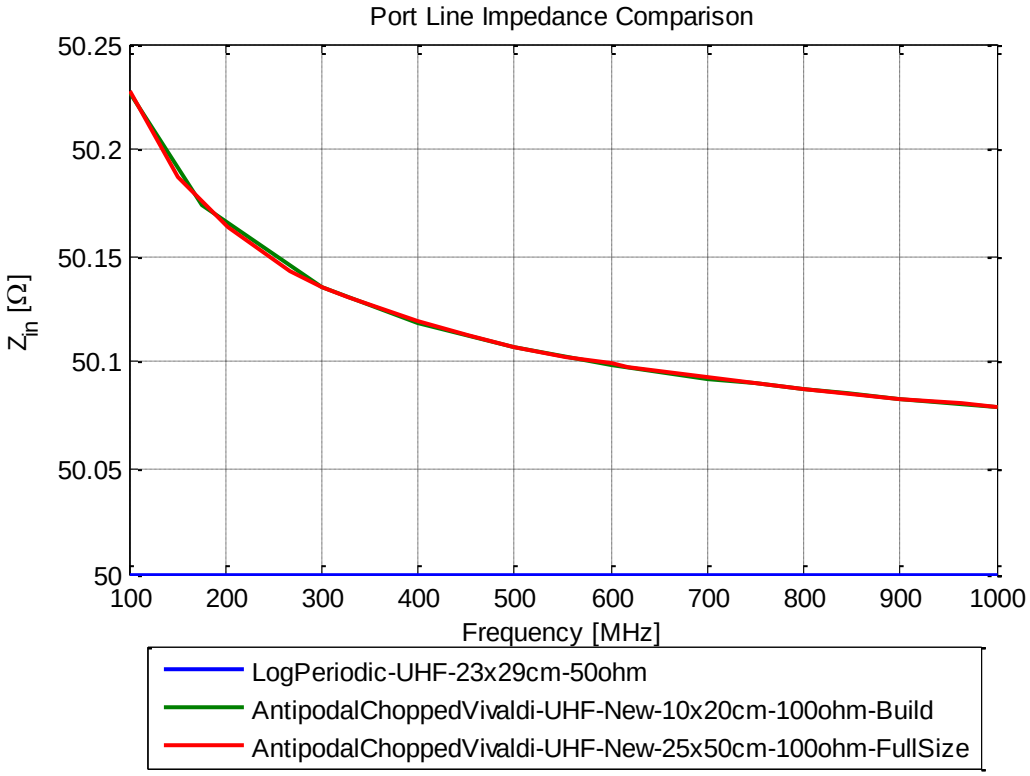
Port Line Impedance Comparison
50.25
50.2
50.15
50.1
50.05
50
Z_{in} [Ω]
100
200
300
400
500
600
700
800
900
1000
Frequency [MHz]
LogPeriodic-UHF-23x29cm-50ohm
AntipodalChoppedVivaldi-UHF-New-10x20cm-100ohm-Build
AntipodalChoppedVivaldi-UHF-New-25x50cm-100ohm-FullSize

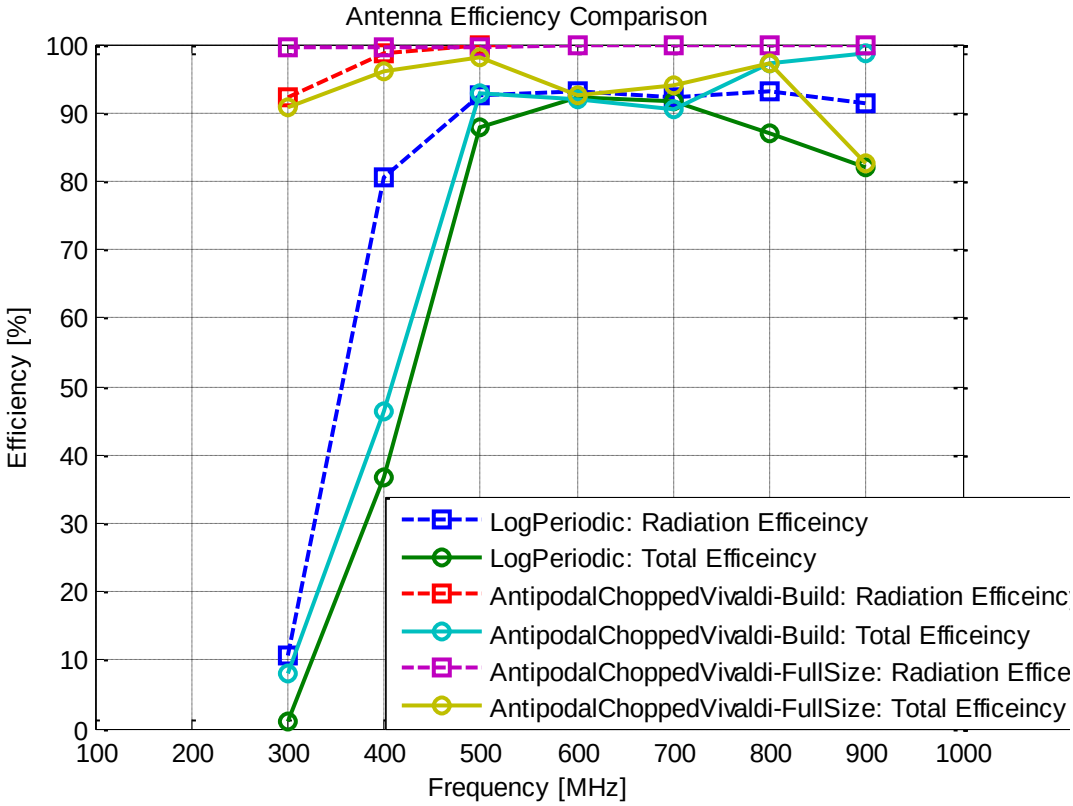
Antenna Efficiency Comparison
100
90
80
70
60
50
40
30
20
10
0
Efficiency [%]
100
200
300
400
500
600
700
800
900
1000
Frequency [MHz]
LogPeriodic: Radiation Efficeincy
LogPeriodic: Total Efficeincy
AntipodalChoppedVivaldi-Build: Radiation Efficeinc
AntipodalChoppedVivaldi-Build: Total Efficeincy
AntipodalChoppedVivaldi-FullSize: Radiation Effice
AntipodalChoppedVivaldi-FullSize: Total Efficeincy

Bibliography

[1] C. A. Balanis, *Antenna Theory: Analysis and Design*, 3rd ed. Hoboken, NJ: John Wiley and Sons Inc., 2005.

[2] M. E. Nelms, *Development and Evaluation of a Multistatic Ultrawideband Random Noise Radar*.: MS Thesis, AFIT/GE/ENG/10-21. Department of Electrical and Computer Engineering, Air Force Institute of Technology (AU), Wright-Patterson AFB, OH, Mar 2010.

[3] Federal Communications Commission (FCC), "Revision of Part 15 of the Commission's Rules Regarding Ultra-wideband Transmission Systems," FCC, First Report and Order ET Docket 98-153, FCC 02-48, Adopted: February 14, 2002; Released April 22, 2002.

[4] X. Chen, J. Liang, S. Wang, Z. Wang, and C. Parini, "Small Ultra Wideband Antennas for Medical Imaging," *Antennas and Propagation Conference, 2008. LAPC 2008. Loughborough*, pp. 28-31, Mar 2008.

[5] I. P. Theron, E. K. Walton, S. Gunawan, and Lixin Cai, "Ultrawide-band noise radar in the VHF/UHF band," *Antennas and Propagation, IEEE Transactions on*, vol. 47, no. 6, pp. 1080-1084, Jun 1999.

[6] K. A. Lukin and R. M. Narayanan, "Fifty Years of Noise Radar," *Physics and Engineering of Microwaves, Millimeter and Submillimeter Waves (MSMW), 2010 International Kharkov Symposium on*, pp. 1-3, Jun 2010.

[7] R. Bourret, "A Proposed Technique for the Improvement of Range Determination with Noise Radar," *Proceedings of the IRE*, vol. 45, no. 12, p. 1744, Dec 1957.

[8] B. M. Horton, "Noise-Modulated Distance Measuring Systems," *Proceedings of the IRE*, vol. 47, no. 5, pp. 821-828, May 1959.

[9] K. Kulpa, "Continuous Wave Radars – Monostatic, Multistatic and Network," in *Advances in Sensing with Security Applications*, NATO Advanced Study Institute, Il Ciocco, Italy, Jul 2005, pp. 1-28.

[10] K. Kulpa, K. Lukin, W. Miceli, and T. Thayaparan, "Signal Processing in Noise Radar Technology," *Radar, Sonar & Navigation, IET*, vol. 2, no. 4, pp. 229-232, Aug 2008.

[11] E. K. Walton, I. P. Theron, S. Gunawan, and L. Cai, "Moving vehicle range profiles measured using a noise radar," *Antennas and Propagation Society International Symposium, 1997. IEEE., 1997 Digest*, vol. 4, pp. 2597-2600, Jul 1997.

[12] I. P. Theron, E. K. Walton, and S. Gunawan, "Compact range radar cross-section measurements using a noise radar," *Antennas and Propagation, IEEE Transactions on*, vol. 46, no. 9, pp. 1285-1288, Sep 1998.

[13] K. Lukin, A. Mogyla, V. Palamarchuck, V. Cherniy, and A. Kravchuk, "Stepped-frequency noise radar with short switching time and high dynamic range," *Radar Symposium (IRS), 2010 11th International*, pp. 1-4, Jun 2010.

[14] K. A. Lukin, V. M. Konovalov, and P. L. Vyplavin, "Stepped delay noise radar with high dynamic range," *Radar Symposium (IRS), 2010 11th International*, pp. 1-3, Jun 2010.

[15] K. A. Lukin, O. V. Zemlyaniy, P. L. Vyplavin, S. K. Lukin, and V. P. Palamarchuk, "High resolution and high dynamic range noise radar," *Microwaves, Radar and Remote Sensing Symposium (MRRS), 2011*, pp. 247-250, Aug 2011.

[16] M. Dawood and R. M. Narayanan, "Receiver operating characteristics for the coherent UWB random noise radar," *Aerospace and Electronic Systems, IEEE Transactions on*, vol. 37, no. 2, pp. 586-594, Apr 2001.

[17] M. Dawood and R. M. Narayanan, "Generalized wideband ambiguity function of a coherent ultrawideband random noise radar," *Radar, Sonar and Navigation, IEE Proceedings*, vol. 150, no. 5, pp. 379-386, Oct 2003.

[18] R. M. Narayanan, Wei Zhou, K. H. Wagner, and Sangtaek Kim, "Acoustooptic correlation processing in random noise radar," *Geoscience and Remote Sensing Letters, IEEE*, vol. 1, no. 3, pp. 166-170, Jul 2004.

[19] R. M. Narayanan, Yi Xu, P. D. Hoffmeyer, and J. O. Curtis, "Design, Performance and Applications of a Coherent UWB Random Noise Radar," in *Ultra-wideband Radar Technology*, Taylor J. D., Ed. Boca Raton: CRC Press, 2000, ch. 8, pp. 181-203.

[20] J. A. Priestly, *AFIT NoNET Enhancements: Software Model Development and Optimization of Signal Processing Architecture*.: MS Thesis, AFIT/GE/ENG/11-34. Department of Electrical and Computer Engineering, Air Force Institute of Technology (AU), Wright-Patterson AFB, OH, Mar 2011.

[21] A. L. Schmitt, *Radar Imaging with a Network of Digital Noise Radar Systems*.: MS Thesis, AFIT/GE/ENG/09-39. Department of Electrical and Computer Engineering, Air Force Institute of Technology (AU), Wright-Patterson AFB, OH, Mar 2009.

[22] J. R. Lievsay, *Simultaneous Range/Velocity Detection with an Ultra-Wideband Random Noise Radar through Fully Digital Cross-Correlation in the Time Domain*.: MS Thesis. AFIT/GE/ENG/11-24. Department of Electrical and Computer Engineering, Air Force Institute of Technology (AU), Wright-Patterson AFB, OH, Mar 2011.

[23] T. J. Thorson, *Simultaneous Range and Velocity Processing and SNR Analysis of the AFIT Random Noise Radar*.: MS Thesis, AFIT/GE/ENG/12-. Department of Electrical and Computer Engineering, Air Force Institute of Technology (AU), Wright-Patterson AFB, OH, Mar 2012.

[24] I. I. Immoreev, "Main Features of UWB Radars and Differences from Common Narrowband Radars," in *Ultra-wideband Radar Technology*, J. D. Taylor, Ed. Boca Raton: CRC Press, 2000, ch. 1, pp. 1-19.

[25] E. Pancera and W. Wiesbeck, "Correlation properties of the pulse transmitted by UWB antennas," *Electromagnetics in Advanced Applications, 2009. ICEAA '09. International Conference on*, pp. 701-704, Sep 2009.

[26] H. Schantz, *The Art and Science of Ultrawideband Antennas*. Boston, MA: Artech House, 2005.

[27] D. Valderas, J. I. Sancho, D. Puente, Cong Ling, and Xiaodong Chen, *Ultrawideband: Antennas Design and Applications*. London: Imperial College Press, 2011.

[28] Qinlong Lu, Lingyun Zhou, Chaoman Tan, and Lu Guanghua, "A Novel Wide Beam UWB Antenna Design for Through-the-Wall Radar," *Microwave and Millimeter Wave Technology (ICMMT), 2010 International Conference on*, pp. 1912-1915, May 2010.

[29] H. A. Wheeler, "Small Antennas," *Antennas and Propagation, IEEE Transactions on*, vol. 23, no. 4, pp. 462-469, Jul 1975.

[30] R. C. Hansen, *Electrically Small, Superdirective, and Superconducting Antennas*. Hoboken, NJ: John Wiley & Sons Inc., 2005.

[31] W. L. Stutzman and G. A. Thiele, *Antenna Theory and Design*, 2nd ed. Hoboken, NJ: John

Wiley and Sons Inc., 1998.

[32] M. A. Richards, J. A. Scheer, and W. A. Holm, Eds., *Principles of Modern Radar: Basic Principles*. Raleigh, NC: Scitech Publishing Inc., 2010.

[33] J. Wisniewski, "Requirements for Antenna Systems in Noise Radars," *Radar Symposium, 2006. IRS 2006. International*, pp. 1-4, May 2006.

[34] Yu-Jiun Ren and Chieh-Ping Lai, "Wideband Antennas for Modern Radar Systems," in *Radar Technology*, G. Kouemou, Ed. Rijeka, Croatia: InTech, 2010, ch. 17.

[35] H. G. Schantz, "Introduction to Ultra-Wideband Antennas," *Ultra Wideband Systems and Technologies, 2003 IEEE Conference on*, pp. 1-9, Nov 2003.

[36] "400-1000 MHz PCB Log Periodic," WA5VJB Antenna Specification Sheet Jul 2002.

[37] Zhiwen Xiao, Jianguo He, and Peiguo Liu, "Study of a Planar Spiral Antenna Used in Ground Penetrating Radar System," *Microwave Conference, 2008 China-Japan Joint*, pp. 250-252, Sep 2008.

[38] Guofeng Lu, S. von der Mark, I. Korisch, L. J. Greenstein, and P. Spasojevic, "Diamond and Rounded Diamond Antennas for Ultrawide-Band Communications," *Antennas and Wireless Propagation Letters, IEEE*, vol. 3, no. 1, pp. 249-252, Dec 2004.

[39] Wang Peng, Wang Anguo, and Dong Jiawei, "Design of the UWB Antenna Using Fractal Concept," *Antennas, Propagation and EM Theory, 2008. ISAPE 2008. 8th International Symposium on*, pp. 189-192, Nov 2008.

[40] H. G. Schantz, "Bottom fed Planar Elliptical UWB Antennas," *Ultra Wideband Systems and Technologies, 2003 IEEE Conference on*, pp. 219-223, Nov 2003.

[41] H. Nazli, E. Bicak, B. Turetken, and M. Sezgin, "An Improved Design of Planar Elliptical Dipole Antenna for UWB Applications," *Antennas and Wireless Propagation Letters, IEEE*, vol. 9, pp. 264-267, 2010.

[42] A. M. Abbosh and M. E. Bialkowski, "Design of UWB Planar Band-Notched Antenna Using Parasitic Elements," *Antennas and Propagation, IEEE Transactions on*, vol. 57, no. 3, pp. 796-799, Mar 2009.

[43] Zhang Chun-Qing, Wang Jun-Hong, and Han Yu-nan, "Coupled Planar Dipole UWB Antenna Design For Wearable Computer," *Microwave and Millimeter Wave Technology, 2007. ICMMT '07. International Conference on*, pp. 1-4, Apr 2007.

[44] Shun-Shi Zhong, Xian-Ling Liang, and Feng-Wei Yao, "Compact Broadband Slot Antenna for UHF-Band Application," *Antennas and Propagation Society International Symposium 2006, IEEE*, pp. 2567-2570, Jul 2006.

[45] M. Leib, M. Frei, D. Sailer, and W. Menzel, "Design and Characterization of a UWB Slot Antenna Optimized for Radiation in Human Tissue," *Ultra-Wideband, 2009. ICUWB 2009. IEEE International Conference on*, pp. 159-163, Sep 2009.

[46] Y. Rahayu, R. Ngah, and T. A. Rahman, "Various Slotted UWB Antenna Design," *Wireless and Mobile Communications (ICWMC), 2010 6th International Conference on*, pp. 107-110, Sep 2010.

[47] M. Ostadrahimi, S. Noghanian, L. Shafai, G. Thomas, and S. Pistorius, "A Novel Broadband Design Procedure for Balanced Compact Planar Tapered Slot Antenna," *Antennas and Propagation Society International Symposium (APSURSI), 2010 IEEE*, pp. 1-4, Jul 2010.

[48] N. V. Venkatarayalu and Yeow-Beng Gan, "Design of a Tapered Slot Array Antenna for UWB Through-Wall RADAR," *Antennas and Propagation Society International Symposium (APSURSI), 2010 IEEE*, pp. 1-4, Jul 2010.

[49] Chao Deng and Yong-jun Xie, "Design of Resistive Loading Vivaldi Antenna," *Antennas and Wireless Propagation Letters, IEEE*, vol. 8, pp. 240-243, 2009.

[50] M. R. Hamid, P. Gardner, P. S. Hall, and F. Ghanem, "Multimode Vivaldi Antenna," *Electronics Letters*, vol. 46, no. 21, pp. 1424-1425, Oct 2010.

[51] Liang Yang, Huiping Guo, Xueguan Liu, Haixia Du, and Gang Ji, "An Antipodal Vivaldi Antenna for Ultra-wideband System," *Ultra-Wideband (ICUWB), 2010 IEEE International Conference on*, vol. 1, pp. 1-4, Sep 2010.

[52] S. Wang, X. D. Chen, and C. G. Parini, "Analysis of Ultra Wideband Antipodal Vivaldi Antenna Design," *Antennas and Propagation Conference, 2007. LAPC 2007. Loughborough*, pp. 129-132, Apr 2007.

[53] R. Mueller, S. Lutz, R. Lorch, and T. Walter, "A UHF Ultrabroadband Vivaldi-Type Direction Finding Antenna," *Antennas and Propagation Society International Symposium (APSURSI), 2010 IEEE*, pp. 1-4, Jul 2010.

[54] Li Ying and Chen Ai-xin, "Design and Application of Vivaldi Antenna Array," *Antennas, Propagation and EM Theory, 2008. ISAPE 2008. 8th International Symposium on*, pp. 267-270, Nov 2008.

[55] Li Tianming, Rao Yuping, and Niu Zhongxia, "Analysis and Design of UWB Vivaldi Antenna," *Microwave, Antenna, Propagation and EMC Technologies for Wireless Communications, 2007 International Symposium on*, pp. 579-581, Aug 2007.

[56] K. Kota and L. Shafai, "Gain and Radiation Pattern Enhancement of Balanced Antipodal Vivaldi Antenna," *Electronics Letters*, vol. 47, no. 5, pp. 303-304, Mar 2011.

[57] H. G. Schantz, "A Brief History of UWB Antennas," in *Proceedings of the IEEE UWBST Conference*, 2003.

[58] Xiaojian Xu and R. M. Narayanan, "Impact of Different Correlation Receiving Techniques on the Imaging Performance of UWB Random Noise Radar," *Geoscience and Remote Sensing Symposium, 2003. IGARSS '03. Proceedings. 2003 IEEE International*, vol. 7, pp. 4525- 4527, Jul 2003.

REPORT DOCUMENTATION PAGE

Form Approved
OMB No. 074-0188

PLEASE DO NOT RETURN YOUR FORM TO THE ABOVE ADDRESS.

1. REPORT DATE *(DD-MM-YYYY)*	2. REPORT TYPE	3. DATES COVERED *(From – To)*
22-03-2012	Master's Thesis	04-10-2010 - 22-03-2012

TITLE AND SUBTITLE

UHF Antenna Design for AFIT Random Noise Radar

5a. CONTRACT NUMBER

5b. GRANT NUMBER

5c. PROGRAM ELEMENT NUMBER

6. AUTHOR(S)

Ludwig, Matthew T., 2Lt, USAF

5d. PROJECT NUMBER
ENG 11G122

5e. TASK NUMBER

5f. WORK UNIT NUMBER

7. PERFORMING ORGANIZATION NAMES(S) AND ADDRESS(S)
Air Force Institute of Technology
Graduate School of Engineering and Management (AFIT/EN)
2950 Hobson Way, Building 640
WPAFB OH 45433-8865

8. PERFORMING ORGANIZATION REPORT NUMBER
AFIT/GE/ENG/12-28

9. SPONSORING/MONITORING AGENCY NAME(S) AND ADDRESS(ES)
Undisclosed sponsor

10. SPONSOR/MONITOR'S ACRONYM(S)
Fill in

11. SPONSOR/MONITOR'S REPORT NUMBER(S)

12. DISTRIBUTION/AVAILABILITY STATEMENT
APPROVED FOR PUBLIC RELEASE; DISTRIBUTION UNLIMITED.

13. SUPPLEMENTARY NOTES

14. ABSTRACT

The design of a small UHF antenna for an UWB RNR system was undertaken in order to improve system bandwidth and reduce overall system size. The Vivaldi dipole antenna class showed the greatest potential for high performance in this specific application. After extensive computer simulation, three designs were built using two printed circuit board antenna construction methods. The antipodal chopped Vivaldi dipole antenna, built with a milling machine, achieved a wider bandwidth and more uniform spectral performance characteristics. Though current results show improvement over the current log-periodic antenna (LPA) used on the system, greater performance could possibly be achieved with higher fidelity construction methods. The chopped Vivaldi dipole antenna can be classified as a highly efficient, electrically small antenna optimized for UWB applications, due to the combination of small size as well as a nearly uniform frequency response and low dispersion in the UHF bandwidth. Though designed for AFIT's Noise Network (NoNET) system, a UHF UWB RNR, the antenna could be applied to a variety of UHF systems looking to optimize the trade-off between size and power budgets.

15. SUBJECT TERMS
Antenna design, UHF antenna, electrically small antennas, UWB, random noise radar

16. SECURITY CLASSIFICATION OF:			17. LIMITATION OF ABSTRACT	18. NUMBER OF PAGES	19a. NAME OF RESPONSIBLE PERSON
a. REPORT	b. ABSTRACT	c. THIS PAGE			Dr. Peter J. Collins (ENG)
U	U	U	UU	238	19b. TELEPHONE NUMBER *(Include area code)* (937) 255-3636, ext 7256 (peter.collins@afit.edu)

Standard Form 298 (Rev. 8-98)
Prescribed by ANSI Std. Z39-18